



**HAL**  
open science

# Nonlinear optical properties of nanostructures, photochromic and lanthanide complexes in solution

Anu Singh

► **To cite this version:**

Anu Singh. Nonlinear optical properties of nanostructures, photochromic and lanthanide complexes in solution. Other [cond-mat.other]. École normale supérieure de Cachan - ENS Cachan, 2012. English. NNT : 2012DENS0081 . tel-00826653

**HAL Id: tel-00826653**

**<https://theses.hal.science/tel-00826653>**

Submitted on 28 May 2013

**HAL** is a multi-disciplinary open access archive for the deposit and dissemination of scientific research documents, whether they are published or not. The documents may come from teaching and research institutions in France or abroad, or from public or private research centers.

L'archive ouverte pluridisciplinaire **HAL**, est destinée au dépôt et à la diffusion de documents scientifiques de niveau recherche, publiés ou non, émanant des établissements d'enseignement et de recherche français ou étrangers, des laboratoires publics ou privés.

ENSC-2012 No.

**THESE DE DOCTORAT  
DE L'ECOLE NORMALE SUPERIEURE DE CACHAN**

Présentée par

**Anu SINGH**

**pour obtenir le grade de  
DOCTEUR DE L'ECOLE NORMALE SUPERIEURE DE CACHAN**

Domaine:  
**SCIENCES PHYSIQUES**

Sujet de la thèse:

***Propriétés optiques non linéaires de nanostructures, de  
complexes photochromes et de complexes de lanthanides  
en solution***

Thèse présentée et soutenue à Cachan le 11 Décembre 2012 devant le jury composé de:

Prof. PIERRE-FRANÇOIS BREVET  
Prof. BOUCHTA SAHRAOUI  
Prof. JOSEPH ZYSS  
Prof. HUBERT LE BOZEC  
Dr. HYND REMITA  
Prof. ISABELLE LEDOUX-RAK

Rapporteur  
Rapporteur  
Examineur  
Examineur  
Examineur  
Directrice de thèse

Laboratoire de Photonique Quantique et Moléculaire (LPQM)  
ENS Cachan / CNRS / UMR 8537  
61, Avenue du Président Wilson 94235 Cachan, Cedex- France

*Nonlinear optical properties of  
nanostructures, photochromic and  
lanthanide complexes in solution*

By

Anu Singh

A thesis submitted to École Normale Supérieure De Cachan in **fulfillment of  
the requirement for the degree of**

Laboratoire de Photonique Quantique et Moléculaire (LPQM)  
Institut d'Alembert - École Normale Supérieure de Cachan  
CNRS/UMR 8537  
61, Avenue du Président Wilson  
94235 Cachan, Cedex- France

*Dedicated To*  
*My Beloved Parents*

# *Declaration*

The research work presented in this thesis titled “*Nonlinear optical properties of nanostructures, photochromic and lanthanide complexes in solution*” was carried out by me independently in this institute under the supervision of Prof. Isabelle Ledoux-Rak, LPQM, ENS Cachan, Cachan. This work is original and has not been submitted in part or full for any other degree or diploma of this or any other university.

Anu Singh

Laboratoire de Photonique Quantique et Moléculaire (LPQM)  
Institut d'Alembert - École Normale Supérieure de Cachan  
CNRS/UMR 8537  
61, Avenue du Président Wilson  
94235 Cachan, Cedex- France

## Résumé

L'Optique non linéaire est un outil très puissant pour étudier les propriétés des matériaux. Dans cette thèse, nous avons utilisé deux techniques d'optique non linéaire pour l'étude des non linéarités moléculaires: la génération de seconde harmonique induite sous champ électrique (EFISH) et la diffusion harmonique de la lumière (DHL). Tout d'abord, nous avons mis en évidence la conjugaison des groupements donneurs  $\pi$  dans les complexes d'iridium cyclométallés. Nous avons également exploré une série de molécules trinuécléaires organométalliques (triaryle-1, 3, 5-triazinane-2, 4, 6-triones) fonctionnalisées par des acétylures métalliques avec des complexes des métaux de transition à leur périphérie; l'hyperpolarisabilité est beaucoup plus élevée que celles des dérivés purement organiques équivalents. D'autre part une série de complexes métalliques dipolaires et octupolaires contenant des ligands 2, 2'-bipyridine photochromes à base de dithiényléthène (DTE) ont été synthétisés et caractérisés. L'étude révèle une forte augmentation de Les hyperpolarisabilités après irradiation UV correspondant à la fermeture de cycle associée au DTE. Cette forte exaltation reflète bien la délocalisation du système d'électrons  $\pi$  et la formation de chromophores push-pull dans les formes fermées. Troisièmement, nous avons étudié les propriétés optiques non linéaires de complexes de bis (phthalocyaninato) lanthanide (III) en sandwich, avec 2 phthalocyanines substituées en ABAB (alternance de donneurs d'électrons et d'accepteurs d'électrons), AB<sub>3</sub> (3 groupes de donneurs), A<sub>4</sub> (4 groupes d'accepteurs) et B<sub>4</sub> (aucun groupe de donneur). L'hyperpolarisabilité du 1<sup>er</sup> ordre  $\beta$  mesurées sont les plus élevées jamais enregistrées pour des molécules octupolaires. La contribution directe d'électrons  $f$  dans les ions lanthanides complexés est également observée sur l'activité non linéaire du second ordre. Enfin, des nanosphères (AuNSs) et des nanotubes d'or (AuNRs) avec différents rapports d'aspect (AR) allant de 1,7 à 3,2 nm ont été synthétisés par la méthode de radiolyse. Le signal de deuxième harmonique émis par des AuNRs est nettement supérieur à celui des nanosphères et révèle leur dépendance à l'AR. Nous avons également mélangé un dérivé du chromophore 4-diméthylamino-N-méthyl-4-stilbazolium tosylate (DAST) avec les AuNRs et observé une influence des AuNRs sur l'amélioration des propriétés ONL du DAST. Une nette augmentation de l'hyperpolarisabilité (par un facteur 8) du dérivé de DAST en est la preuve.

**Mots clefs:** Optique non linéaire, Photochromisme, Nanoplasmonique, Ingénierie moléculaire

## Abstract

Nonlinear optics is well known to be a highly powerful tool to investigate the properties of the materials. In this thesis we used two important nonlinear optical techniques known as Electric Field Induced Second Harmonic Generation (EFISH) and Harmonic Light Scattering (HLS) to study the first hyperpolarizability of various molecular objects. Firstly, we evidenced the  $\pi$  donor conjugation in cyclometalated Ir complexes. We have also explored the series of trinuclear organometallic triaryl-1, 3, 5-triazinane-2, 4, 6-triones functionalized by  $d^6$ -transition metal acetylides complexes at their periphery; large hyperpolarizabilities, far higher than those of related purely organic derivatives are reported. Secondly, a series of dipolar and octupolar dithienylethene (DTE)-containing 2, 2'-bipyridine ligands with different metal ions featuring two, four and six photochromic dithienylethene units have been synthesized and fully characterized. The study reveals a large increase in the hyperpolarizability after UV irradiation and subsequent formation of ring-closed isomers. This efficient enhancement clearly reflects the delocalization of the  $\pi$ -electron system and the formation of strong push-pull chromophores in the closed forms. Thirdly, we have investigated NLO properties of bis (phthalocyaninato) lanthanide-(III) double-decker complexes with crosswise ABAB (phthalocyanine bearing alternating electron-donor and electron-acceptor groups), AB<sub>3</sub> (3 donor groups), A<sub>4</sub> (without donor groups) and B<sub>4</sub> (4 donor groups) ligands. First-order hyperpolarizability ( $\beta$ ) is measured and display the highest quadratic hyperpolarizability ever reported for an octupolar molecule. The direct contribution of *f*-electrons in coordinated lanthanides ions is also observed on second order nonlinear activity. Finally, gold nanospheres (AuNSs) and gold nanorods (AuNRs) with different aspect ratios (AR) ranging from 1.7 to 3.2 nm have been synthesized by Radiolysis method. Second harmonic intensity collected from AuNRs is clearly higher than that of the nanospheres and reveals their dependence on the AR. We have also mixed the chromophore 4-dimethylamino-*N*-methyl-4-stilbazolium tosylate (DAST) derivative with AuNRs and observed the enhancement of DAST NLO properties in the presence of AuNRs. A clear increase in the hyperpolarizability (by a factor of 8) of DAST derivatives has been evidence.

**Keywords:** Nonlinear optics, Electric Field Induced Second Harmonic Generation (EFISH), Harmonic Light Scattering (HLS), photochromism, lanthanides, and gold nanoparticles.

## Acknowledgments

*On the occasion of the completion of the thesis, it is my pleasure to express my sincere gratitude for all those whose support and encouragement made my research journey much easier.*

*Foremost, I am grateful to my supervisor Prof. Isabelle Ledoux-Rak for giving me a chance to join her research group to start my Ph.D. I would like to express my thanks and gratitude for her invaluable suggestions, incessant encouragement and enthusiasm to explore the new field. I am pleased to express that my PhD experience has been extremely positive since making that move. I really appreciate her constant support and fruitful discussions from the bottom of my heart. Without her, I could not achieve so much today. I also appreciate her patience and confidence in me. I am fortunate and proud to be part of her group.*

*As well, I would like to express my sincere thanks and immense pleasure to Madam Hynd Remita. It is beyond my capacity to describe how valuable her guidance is and how much I have learned from her. I would also like to thank her dedicated scientific guidance, consistent support, and encouragement throughout the duration of my Ph.D.*

*I would like to offer my sincere thanks to Prof. Hubert Le Bozec, Dr. Yann Bretonnière, and Dr. Frederic Paul for their numerous discussions during my Ph.D. Most of my research has been done in close cooperation with them.*

*My deepest gratitude is also to Prof. Pierre-François Brevet and Prof. Bouchta Sahraoui for reviewing my thesis. I am very thankful for Prof. Joseph Zyss and Prof. P.F Brevet for their valuable suggestions and discussions. Their suggestions helped me to develop an appropriate approach towards my results.*

*I would like to express my gratitude to Mr. Colin Lopez, Research Engineer, LPQM, ENS CACHAN who improved our experimental set-up and help me to get used of it.*

*My heartiest thank to Mr. Arnaud Brosseau, PPSM laboratory, ENS de Cachan for helping me time to time. My sincere thanks are also extended to all my colleagues, labmates, friends and well-wishers for helping me throughout the research.*

*I would like to offer my sincere thanks to Ginette puyhaubert for her valuable help in organizing order de mission and my defense.*

*I gratefully wish to acknowledge the C'NANO IDF for their excellent financial supports. I am also indebted to the ENS Cachan for giving me an opportunity to conduct my PhD thesis at this prestigious institute.*

*Finally, I cannot express my gratitude in mere to my parents for their affectionate support, love and encouragement that they've given me over the years, without which I would not have had the confidence to pursue a career in science. I am indebted to express my gratefulness to my sisters and brother, for their love, support and encouragement. At last but not the least I am thankful to my husband for considering my dream as his dream and providing me the strength and enthusiasm to reach my goals. I am grateful to him for always being there for me. Thanks are due to rest of the family members for all the love, care and pride.*

***Thanks***

***ANU***

# Table of contents

|  |              |
|--|--------------|
| Résumé.....  | v            |
| Abstract.....  | vi           |
| Acknowledgments.....   | vii-viii     |
| Table of Contents.....   | iv-vii       |
| List of Tables.....  | viii-xii     |
| List of Figures.....   | xiii.-xiv    |
| List of Schemes.....   | xv-xx        |
| List of Abbreviations.....   | xxi-xxii     |
| <br>   |              |
| <b>Introduction.....</b>   | <b>1-4</b>   |
| <br>   |              |
| <b>Chapter 1: Presentation of materials and investigation tools.....</b> | <b>5-95</b>  |
| <br>   |              |
| <b>Part A: Introduction to NLO materials.....</b>                        | <b>5-33</b>  |
| 1.1 Definition of nonlinear optics .....                                 | 5-6          |
| 1.2 Historical background of nonlinear optics.....                       | 6-7          |
| 1.3 Origin of NLO.....   | 8-9          |
| 1.4 Various types of second-order NLO effects.....                       | 10-10        |
| 1.5: Materials for NLO.....  | 11-12        |
| 1.6 Molecular engineering of dipolar and octupolar molecules.....        | 13-16        |
| 1.7 Various Models for molecular Hyperpolarizability.....                | 17-18        |
| 1.7.1 Additivity model   |              |
| 1.7.2 Valence bond charge transfer model                                 |              |
| 1.7.3 Equivalent field model   |              |
| 1.7.4 Two level dispersion model   |              |
| 1.8 Multifunctional systems: Photochromism.....                          | 19-20        |
| 1.9 Multifunctional systems: Lanthanides and Lanthanide complexes.....   | 21-25        |
| 1.9.1: Photophysical properties and applications                         |              |
| 1.9.2: Porphyrins and phthalocyanine complexes                           |              |
| <br>   |              |
| <b>References.....</b>   | <b>26-33</b> |
| <br>   |              |
| <b>Part B: Gold nanoparticles for nonlinear optics.....</b>              | <b>34-63</b> |
| 1.10 Introduction.....   | 34           |
| 1.11 Historical background.....  | 35-36        |

|  |               |
|--|---------------|
| 1.12 Synthesis: Bottom up and Bottom down methods.....                             | 37-37         |
| 1.13 Deposition methods: Electron scattering phenomena with material.....          | 38-39         |
| 1.14 Solution growth methods.....  | 40-43         |
| 1.14.1 Türkevich Methods   |               |
| 1.14.2 Electrochemical methods   |               |
| 1.14.3 Seeding method  |               |
| 1.14.4 Photochemical method  |               |
| 1.14.5 Radiolysis  |               |
| 1.15 Physical, chemical and optical properties.....                                | 44-49         |
| 1.15.1 General Physico-chemical and catalytic properties of_AuNPs                  |               |
| 1.15.1.1 Physical  |               |
| 1.15.1.2 Chemical  |               |
| 1.15.1.3 Catalytic properties  |               |
| 1.15.2 Optical properties: Surface Plasmon Resonance                               |               |
| 1.16 Nanoparticles and quadratic second order nonlinear Optics.....                | 50-52         |
| 1.17 Applications of Gold nanoparticles.....                                       | 53-55         |
| <b>References.....</b>   | <b>56-63</b>  |
| <b>Part C: Investigation tools for Experimental details.....</b>                   | <b>64-95</b>  |
| 1.18 Radiolysis.....   | 64-65         |
| 1.18.1 Principles: Radiolytic reducing species                                     |               |
| 1.18.2 Irradiation facilities  |               |
| 1.19 Characterization methods.....   | 66-69         |
| 1.19.1 UV-Vis Spectroscopy   |               |
| 1.19.2 Transmission Electron Microscopy (TEM) images                               |               |
| 1.19.3 Dynamic Light Scattering (DLS)  |               |
| 1.20 Instrumentation NLO techniques for molecular engineering.....                 | 70-82         |
| 1.20.1 EFISH at 1.907 $\mu\text{m}$  |               |
| 1.20.2 Third harmonic generation   |               |
| 1.20.3 Harmonic Light Scattering at 1.907 $\mu\text{m}$                            |               |
| 1.20.4 Harmonic Light Scattering at 1.064 $\mu\text{m}$                            |               |
| 1.21 Variable incident polarization in Harmonic Light Scattering .....             | 83-85         |
| 1.22 Improved version of HLS and EFISH experimental set-up .....                   | 86-93         |
| <b>References.....</b>   | <b>94-95</b>  |
| <b>Chapter 2: New developments in molecular engineering for quadratic NLO.....</b> | <b>96-144</b> |
| <b>Part A: Novel metal complexes.....</b>  | <b>96-106</b> |
| 2.1 <u>Platinum complexes</u> .....  | 96-98         |
| 2.1.1 Characterization of Platinum (II) complexes                                  |               |

|   |                |
|---|----------------|
| 2.1.2 NLO properties of Platinum (II) complexes                               |                |
| 2.2 <u>Cyclometalated Iridium (III) complexes</u> .....                       | 99-102         |
| 2.2.1 NLO properties  |                |
| 2.3 <u>New Organometallic octupolar chromophores</u> .....                    | 103-106        |
| 2.3.1 Characterization of octupolar molecules                                 |                |
| 2.3.2 NLO properties of octupolar molecules                                   |                |
| <b>Part B: Photochromic molecules</b> .....                                   | <b>107-123</b> |
| 2.4 Characterization of photoswitching molecules.....                         | 108            |
| 2.5 Experimental procedure.....   | 109            |
| 2.6 Properties and characterization of newly synthesized dipolar molecules... | 110-116        |
| 2.6.1 Luminescent properties  |                |
| 2.6.2 NLO properties  |                |
| 2.7 Properties and characterization of tetrahedral Copper metal complexes...  | 117-118        |
| 2.7.1 Characterization of newly synthesized Tetrahedral Cu complexes          |                |
| 2.7.2 NLO properties  |                |
| 2.8 Properties and characterization of Octahedral Iron metal complexes.....   | 119-121        |
| 2.8.1 Characterization of the newly synthesized Octahedral Fe complexes       |                |
| 2.8.2 NLO properties  |                |
| 2.9 Role of MLCT transition with respect to NLO activity.....                 | 122-123        |
| <b>Part C: Lanthanide Series</b> .....  | <b>124-137</b> |
| 2.10 Crystal structure.....   | 124-125        |
| 2.11 Linear properties.....   | 126-127        |
| 2.12 NLO properties.....  | 128-131        |
| <b>References</b> .....   | <b>138-144</b> |
| <b>Chapter 3: Second harmonic generation from AuNPs</b> .....                 | <b>145-176</b> |
| 3.1 Introduction.....   | 145            |
| 3.2 Materials.....  | 146            |
| 3.3 Synthesis of Gold Nanorods.....   | 146            |
| 3.3.1 Synthesis of Au spherical particles                                     |                |
| 3.3.2. Nanoparticles in thin polymeric films                                  |                |
| 3.4 Principles.....   | 147-148        |
| 3.5 Mechanism of reduction and formation of AuNRs.....                        | 149-150        |
| 3.6 Aspect Ratio.....   | 151            |

|   |                |
|---|----------------|
| 3.7 Characterization.....                                   | 151-153        |
| 3.7.1 UV-Visible absorption spectra                         |                |
| 3.7.2 TEM images  |                |
| 3.8 NLO properties of AuNRs and AuNSs.....                  | 154-162        |
| 3.9 Nonlinear Microscopy.....                               | 163-167        |
| 3.9.1 Nonlinear scanning microscopy                         |                |
| 3.9.2 Results   |                |
| 3.10 Mixture of AuNRs with DAST derivative.....             | 168-173        |
| 3.10.1 Preparation  |                |
| 3.10.2 Linear properties                                    |                |
| 3.10.3 NLO properties                                       |                |
| <b>References.....</b>                                      | <b>174-176</b> |
| <b>Conclusions and perspectives.....</b>                    | <b>177-179</b> |
| <b>List of Publications and Conference Proceedings.....</b> | <b>180-182</b> |

## List of Tables

|  |            |
|--|------------|
| <b>Table 1.1</b> General characteristics of the gold.....  | <b>45</b>  |
| <b>Table 2.1</b> Experimental electronic spectra, HLS $\beta$ values, related dipolar and octupolar contributions.....   | <b>99</b>  |
| <b>Table 2.2</b> UV–Vis absorption spectra for Cyclometalated Ir (III) complexes.....  | <b>102</b> |
| <b>Table 2.3</b> HLS $\beta$ values determined at 1.907 $\mu\text{m}$ incident wavelength.....   | <b>106</b> |
| <b>Table 2.4</b> UV-Vis absorption spectra for complexes in the open and closed (PSS) forms...   | <b>112</b> |
| <b>Table 2.5</b> $\mu\beta$ values determined at 1.910 $\mu\text{m}$ incident wavelength of Zn (II) and Re (I) complexes.....  | <b>115</b> |
| <b>Table 2.6</b> $\beta$ values determined at 1.907 $\mu\text{m}$ incident wavelength of Re (I) and Ru (II) complexes.....   | <b>116</b> |
| <b>Table 2.7</b> UV–Vis absorption spectra for Cu (L) <sub>2</sub> PF <sub>6</sub> complexes.....  | <b>118</b> |
| <b>Table 2.8</b> HLS $\beta$ and $\beta_{xyz}$ values determined at 1.907 $\mu\text{m}$ incident wavelength of [Cu (L <sub>o,o</sub> ) <sub>2</sub> ]PF <sub>6</sub> complexes.....        | <b>119</b> |
| <b>Table 2.9</b> Electronic absorption data for complexes in the open and closed (PSS) forms...  | <b>121</b> |
| <b>Table 2.10</b> HLS $\beta$ values of Fe complexes determined at 1.907 $\mu\text{m}$ incident wavelength...  | <b>122</b> |
| <b>Table 2.11</b> UV-Vis absorption spectra of neutral, oxidised and reduced form of Ln (Eu, Dy, and Lu) (ABAB) <sub>2</sub> bis-phthalocyanine in chloroform ( $1 \times 10^{-5}$ M)..... | <b>129</b> |
| <b>Table 2.12</b> $\beta$ values of the neutral form of ABAB, A <sub>4</sub> , B <sub>4</sub> and AB <sub>3</sub> complexes.....   | <b>133</b> |
| <b>Table 2.13</b> $\beta$ values of ABAB complexes in neutral, oxidized and reduced forms.....   | <b>135</b> |
| <b>Table 2.14</b> $\beta$ values of A <sub>4</sub> complexes in neutral, oxidized and reduced forms.....   | <b>136</b> |
| <b>Table 2.15</b> $\beta$ values of B <sub>4</sub> complexes in neutral, oxidized and reduced forms.....   | <b>136</b> |
| <b>Table 3.1</b> Parameters of the AuNRs synthesized after total reduction of the gold ions by radiolysis as a function of silver concentration.....                                       | <b>153</b> |
| <b>Table 3.2</b> $\beta$ of Au per atom and per particle for NSs and NRs are calculated.....   | <b>157</b> |

|   |            |
|---|------------|
| <b>Table 3.3</b> Comparison between the previously observed $\beta$ values of Au per particle and our AuNSs sample.....   | <b>158</b> |
| <b>Table 3.4</b> Depolarization ratio (D), norms of the dipolar and octupolar tensor components of hyperpolarizability along with their squared nonlinear anisotropy $\rho^2$ ..... | <b>160</b> |
| <b>Table 3.5</b> $\beta$ of Au per atom obtained from DAST, NR-4 and mixture of NR4 with DAST.....  | <b>171</b> |
| <b>Table 3.6</b> $\beta$ of Au per atom obtained from DAST, NR-1 and mixture of NR1 with DAST.....  | <b>172</b> |
| <b>Table 3.7</b> $\beta$ of Au per atom obtained from DAST, NR-3 and mixture of NR3 with DAST.....  | <b>173</b> |

## List of Figures

|   |    |
|---|----|
| <b>Figure 1.1</b> Dr. T. Maiman, Hughes Research Laboratories.....  | 6  |
| <b>Figure 1.2</b> (a) Plot of the polarization response $P$ to an incident electromagnetic wave of field strength $E(\omega)$ at frequency $\omega$ in a non-centrosymmetric $D-\pi-A$ molecule. (b) To (d) Fourier components of $P$ at frequencies for $\omega$ , $2\omega$ , and $0$ .....                             | 9  |
| <b>Figure 1.3</b> (a) Geometry of second-harmonic generation. (b) Energy-level diagram describing second-harmonic generation. (c) Sum frequency generation (d) Pockels effect (e) Optical rectification.....  | 11 |
| <b>Figure 1.4</b> Examples of the structure of nonlinear, dipolar push-pull molecules.....  | 13 |
| <b>Figure 1.5</b> Examples of donor and acceptor groups together with conjugated path.....  | 14 |
| <b>Figure 1.6</b> Schematic representation of octupolar symmetries.....   | 15 |
| <b>Figure 1.7</b> Benzene-like (left) and central atom (right) strategy for 2D octupolar engineering.....   | 16 |
| <b>Figure 1.8</b> 3D octupolar engineering schemes as derived from the cubic octupolar template (a) Covalent tetrahedral Sn derivative (b) Tetrahedral metal complex (c) Substituted biphenyl derivative (d) Paracyclophane derivative.....   | 17 |
| <b>Figure 1.9</b> The Lanthanide element series.....  | 21 |
| <b>Figure 1.10</b> Authentic Euro banknotes are believed to contain europium chelates that emit red luminescence under ultraviolet light.....   | 22 |
| <b>Figure 1.11</b> Sizes of nanoparticles in comparison with other biological entities.....   | 34 |
| <b>Figure 1.12</b> (a) Stained glasses (b) The Lycurgus Cup, British Museum, 1958 (c) Stained-glass windows in Milan Cathedral, Italy.....  | 35 |
| <b>Figure 1.13</b> (a) Portrait of Michael Faraday. (b) Michael Faraday in his lab, by Harriet Moore (Wikipedia) (c) Reproduced by Courtesy of the Royal Institution of Great Britain Faraday's colloidal ruby gold. (d) First publication of gold Nanoparticles by reduction of gold chloride with white phosphorus..... | 36 |
| <b>Figure 1.14</b> Methods of nanoparticle production: top-down and bottom-up.....  | 38 |

|   |           |
|---|-----------|
| <b>Figure 1.15</b> Magnetron sputtering technique.....  | <b>39</b> |
| <b>Figure 1.16</b> Laser vaporization technique .....   | <b>40</b> |
| <b>Figure 1.17</b> Origin of surface plasmon resonance due to coherent interaction of the electrons in the conduction band with electromagnetic field.....  | <b>46</b> |
| <b>Figure 1.18</b> Application of AuNPs in depollution.....   | <b>53</b> |
| <b>Figure 1.19</b> Applications of AuNPs.....   | <b>55</b> |
| <b>Figure 1.20</b> Scheme of metal ion reduction in solution by ionizing radiation.....   | <b>65</b> |
| <b>Figure 1.21</b> Illustration of Beer-Lambert law.....  | <b>67</b> |
| <b>Figure 1.22</b> (a) Schematic outline of a TEM (b) Electron source of a TEM (c) The imaging system of a TEM (d) Photograph of TEM.....   | <b>68</b> |
| <b>Figure 1.23</b> (a) EFISH Experimental Set-up at 1.907 $\mu\text{m}$ . (b) EFISH measurement cell (c) Plot of the SHG signal from the DCM solvent as a function of cell displacement.....          | <b>72</b> |
| <b>Figure 1.24</b> Geometry of Third harmonic generation.....   | <b>76</b> |
| <b>Figure 1.25</b> Schematic representation of Harmonic Light Scattering at 1.907 $\mu\text{m}$ .....   | <b>78</b> |
| <b>Figure 1.26</b> Second harmonic intensity recorded from ETV is plotted with respect to the SH intensity collected from the NPP powder (frequency doubler) at 1907 nm fundamental wavelength.....   | <b>79</b> |
| <b>Figure 1.27</b> Second harmonic intensity recorded from water is plotted with respect to the SH intensity collected from the NPP powder (frequency doubler) at 1064 nm fundamental wavelength..... | <b>83</b> |
| <b>Figure 1.28</b> Schematic representation of Variable incident polarization in Harmonic Light Scattering (VIP-HLS) at 1.064 $\mu\text{m}$ .....   | <b>83</b> |
| <b>Figure 1.29</b> Fundamental incoming beam propagating along Z and polarized in the (X, Y) plane. The observation direction is along Y, and polarization state of SH along X or Z plane.....        | <b>84</b> |
| <b>Figure 1.30</b> New version of Experimental set-up.....  | <b>87</b> |
| <b>Figure 1.31</b> Plot of the SHG signal from the DCM solvent as a function of cell displacement observed from the old system of the experimental set-up.....  | <b>88</b> |

|  |                |
|--|----------------|
| <b>Figure 1.32</b> (a) SHG signal from the DCM solvent as a function of cell displacement observed from the new system of the experimental set-up. (b) Excel plot of the SHG signal from the DCM solvent as a function of cell displacement observed from the old system of the experimental set-up.....       | <b>89</b>      |
| <b>Figure 1.33</b> Second harmonic intensity recorded from ETV is plotted with respect to the SH intensity collected from the NPP powder (frequency doubler) at 1907 nm fundamental wavelength from the old version.....   | <b>90</b>      |
| <b>Figure 1.34</b> (a) SH intensity recorded from ETV and NPP powder is shown in red and green colors respectively at 1907 nm using the new version. (b) Excel plot of the SH intensity recorded from ETV with respect to the SH intensity collected from the NPP powder at 1907 nm using the new version..... | <b>91</b>      |
| <b>Figure 1.35</b> Second harmonic intensity recorded from water is plotted with respect to the SH intensity collected from the NPP powder (frequency doubler) at 1064 nm fundamental wavelength the (old version).....  | <b>92</b>      |
| <b>Figure 1.36</b> Plot of the SH intensity recorded from water plotted with respect to the SH intensity collected from the NPP powder at 1064 nm fundamental wavelength (new version).....  | <b>93</b>      |
| <b>Figure 2.1</b> The Jablonski diagram describes the energy levels and different transitions between states.....  | <b>97</b>      |
| <b>Figure 2.2</b> UV-Visible absorption change of Lig NMe <sub>2</sub> .....   | <b>109</b>     |
| <b>Figure 2.3</b> Chemical structure of photochromic bipyridine Zn (II), Re (I), and Ru (II) complexes.....  | <b>110-111</b> |
| <b>Figure 2.4</b> UV/Vis absorption change of ZnCl <sub>2</sub> (D = NBU <sub>2</sub> ) in CH <sub>2</sub> Cl <sub>2</sub> (1.5 × 10 <sup>-5</sup> M) upon irradiation.....  | <b>111</b>     |
| <b>Figure 2.5</b> UV-vis absorption spectra changes of (a) (dmbipy) <sub>2</sub> Ru](PF <sub>6</sub> ) <sub>2</sub> [D = NMe <sub>2</sub> ] and (b) Re(CO) <sub>3</sub> Br [D = NMe <sub>2</sub> ]in dichloromethane upon excitation at 350 nm.....  | <b>113</b>     |
| <b>Figure 2.6</b> (Left) Emission spectrum of (dmbipy) <sub>2</sub> Ru(PF <sub>6</sub> ) <sub>2</sub> at 77 K (blue line) upon excitation into the lowest energy absorption band (490 nm) (Right) Corresponding spectra of Re (CO) <sub>3</sub> Br open and its PSS form.....                                  | <b>114</b>     |

|   |            |
|---|------------|
| <b>Figure 2.7</b> Comparison between the SH intensity collected from open and closed form of $ZnCl_2$ [D= NBU <sub>2</sub> ] and $CHCl_2$ .....   | <b>114</b> |
| <b>Figure 2.8</b> (Left) Chemical structure of $[Cu(L_{0,0})_2]PF_6$ . (Right) Experimental UV-vis absorption spectra change of $[Cu(L_{0,0})_2]PF_6$ in $CH_2Cl_2$ upon excitation at 350 nm.....  | <b>117</b> |
| <b>Figure 2.9</b> (Left) Chemical structure of photochromic bipyridine Fe (II) (D = H, NMe <sub>2</sub> and NBU <sub>2</sub> ) complexes (Right) UV-Vis absorption spectra changes in $CH_2Cl_2$ upon irradiation excitation at 350 nm..... | <b>120</b> |
| <b>Figure 2.10</b> Constructive or antagonist interactions between the MLCT and ILCT transitions.....   | <b>122</b> |
| <b>Figure 2.11</b> Bis (phthalocyanine) lutetium complex $[Pc_2Lu]$ as a point-charge template for an octupole.....   | <b>125</b> |
| <b>Figure 2.12</b> (a) X-ray crystal structure of M= LU, Dy, Y and Eu (H atoms and the solvent molecule have been omitted for clarity) and (b) coordination polyhedron around the $La^{3+}$ ion.....  | <b>127</b> |
| <b>Figure 2.13</b> (a) Absorption spectra of newly synthesized bis (phthalocyaninato) - lanthanide (III) ABAB complexes in neutral form in chloroform.....  | <b>128</b> |
| <b>Figure 2.13</b> (b) Absorption spectra of newly synthesized bis (phthalocyaninato) - lanthanide (III) ABAB complexes in oxidized form in chloroform.....   | <b>130</b> |
| <b>Figure 2.13</b> (c) Absorption spectra of newly synthesized bis (phthalocyaninato) - lanthanide (III) ABAB complexes in reduced form in chloroform.....  | <b>131</b> |
| <b>Figure 2.14</b> Second harmonic intensity recorded from bis-(phthalocyaninato) lutetium complexes with respect to the SH intensity from NPP.....   | <b>132</b> |
| <b>Figure 2.15</b> Plot of the hyperpolarizability coefficient $\beta$ vs f orbital filling for neutral forms.....  | <b>134</b> |
| <b>Figure 2.16</b> Plot of the hyperpolarizability coefficient $\beta$ from neutral, oxidized, and reduced forms of ABAB type.....  | <b>135</b> |
| <b>Figure 2.17</b> Plot of the hyperpolarizability coefficient $\beta$ from neutral, oxidized, and reduced forms of A <sub>4</sub> type.....  | <b>136</b> |

|   |            |
|---|------------|
| <b>Figure 2.18</b> Plot of the hyperpolarizability coefficient $\beta$ from neutral, oxidized, and reduced forms of B <sub>4</sub> type.....  | <b>137</b> |
| <b>Figure 3.1</b> Schematic representation of synthesis of gold nanoparticles.....  | <b>148</b> |
| <b>Figure 3.2</b> Image of the vials containing the solutions with the synthesized AuNSs and different aspect ratios of AuNRs.....  | <b>152</b> |
| <b>Figure 3.3</b> UV-Visible absorption spectra of Au <sup>III</sup> solution, AuNSs (without AgNO <sub>3</sub> precursor) and Au Nanorods containing different amounts of AgNO <sub>3</sub> precursor..... | <b>153</b> |
| <b>Figure 3.4</b> TEM images of the Au NS and Au NRs of different aspect ratios synthesized with different amounts of silver ions (A) NR1, (B) NR2, (C) NR3, (D) NR4, and (E) NR5.....                      | <b>154</b> |
| <b>Figure 3.5</b> Comparison between the second harmonic intensity recorded from pure water and NR4 water solution.....   | <b>156</b> |
| <b>Figure 3.6</b> Absolute value of the first hyperpolarizability ( $\beta$ ) calculated per Au atom and per Au particle in the solution versus the aspect ratio of AuNPs.....                              | <b>159</b> |
| <b>Figure 3.7</b> Experimental harmonic scattered intensities $I^{2\omega}$ for Nanospheres and Nanorods solution in water, as a function of the incident polarization angle $\varphi$ .....                | <b>160</b> |
| <b>Figure 3.8</b> Plot of depolarization ratio (D) against the aspect ratio (AR) of the AuNPs.....  | <b>161</b> |
| <b>Figure 3.9</b> Plot of dipolar and octupolar values with respect to aspect ratios of the AuNPs.....  | <b>162</b> |
| <b>Figure 3.10</b> Plot of ( $\rho$ ) ratio against the aspect ratio of the AuNPs.....  | <b>163</b> |
| <b>Figure 3.11</b> Zoom of the SHG detected during a typical scan of the NR2 dispersed on a glass coverslip.....  | <b>164</b> |
| <b>Figure 3.12</b> Photostability of the SHG signal scattering from a single NR2, recorded as two polarization components along x (red trace) and y (black trace), respectively.....                        | <b>165</b> |
| <b>Figure 3.13</b> Spectral dependence of the SHG process. Typical spectrum emitted by the SHG NR2 excitation wavelengths at 1280 nm.....   | <b>166</b> |
| <b>Figure 3.14</b> Experimentally obtained polarization analysis of the emission observed for NR2.....  | <b>166</b> |
| <b>Figure 3.15</b> Zoom of the sample after measurements of the spectra.....  | <b>167</b> |

|   |            |
|---|------------|
| <b>Figure 3.16</b> DAST used to mix it with AuNRs.....  | <b>169</b> |
| <b>Figure 3.17</b> UV-Visible absorption spectra of DAST, NR4 and mixture of NR4 with DAST.....                         | <b>170</b> |
| <b>Figure 3.18</b> UV-Visible absorption spectra of DAST, NR1 and mixture of NR1 with DAST.....                         | <b>171</b> |
| <b>Figure 3.19</b> UV-Visible absorption spectra of DAST, NR3 and mixture of NR3 with DAST.....                         | <b>172</b> |
| <b>Figure 3.20:</b> $\beta_{\text{DAST}}^{\text{attached}}$ with NRs and enhancement factor vs the AR of the AuNRs..... | <b>173</b> |

## List of Schemes

|   |            |
|---|------------|
| <b>Scheme 1.1</b> Photochromic interconversion of a dithienylethene (DTE) unit.....   | <b>20</b>  |
| <b>Scheme 2.1</b> Structures of the Pt (II) complexes investigated.....   | <b>98</b>  |
| <b>Scheme 2.2</b> Newly synthesized Cyclometalated Ir (III) complexes with different donor groups.....  | <b>101</b> |
| <b>Scheme 2.3</b> Compounds 1-X and 2.....  | <b>103</b> |
| <b>Scheme 2.4</b> Compounds 3, 6, 7, 8 and 9 ([Fe] = ( $\eta^2$ -dppe) ( $\eta^5$ -C <sub>5</sub> Me <sub>5</sub> ) Fe and [Ru] = trans-( $\eta^2$ -dppe) <sub>2</sub> Ru)..... | <b>104</b> |
| <b>Scheme 2.5</b> DTE-based bipyridines with ML <sub>n</sub> dipolar complex.....   | <b>107</b> |
| <b>Scheme 2.6</b> Newly synthesized DTE-based bipyridines with different metal complexes and donor group.....   | <b>108</b> |
| <b>Scheme 2.7</b> Bis (phthalocyanine) (Ln = Eu, Dy, and Lu) complex [Pc <sub>2</sub> Eu] [Pc <sub>2</sub> Dy] and [Pc <sub>2</sub> Lu] template for an octupole.....           | <b>125</b> |
| <b>Scheme 2.8</b> The structure of phthalocyanine ABAB.....   | <b>127</b> |
| <b>Scheme 3.1</b> Summarizing the reduction and growth mechanism leading to the formation of AuNRs by Radiolysis.....   | <b>150</b> |

## List of Abbreviations

|                                 |   |
|---------------------------------|---|
| AuNPs                           | Gold nanoparticles  |
| AuNRs                           | Gold nanorods   |
| AuNSs                           | Gold nanospheres  |
| AgNO <sub>3</sub>               | Silver nitrate  |
| AR                              | Aspect ratio  |
| Au                              | Gold  |
| Ag                              | Silver  |
| Cu                              | Copper  |
| CTAB                            | Cetyl trimethyl ammonium bromide                          |
| CHCl <sub>3</sub>               | Chloroform  |
| CH <sub>2</sub> Cl <sub>2</sub> | Dichloromethane   |
| CCD                             | Charged coupled device                                    |
| DLS                             | Dynamic light scattering                                  |
| DAST                            | 4-dimethylamino- <i>N</i> -methyl-4-stilbazolium tosylate |
| DAE                             | Diarylethene  |
| Dy                              | Dysprosium  |
| DMF                             | Dimethylformamide   |
| D                               | Depolarization ratio                                      |
| DTE                             | Dithienylethene   |
| EFISH                           | Electric field induced second harmonic generation         |
| EDFA                            | Erbium doped fiber amplifiers                             |
| Eu                              | Europium  |
| Fe                              | Iron  |
| HOMO                            | Highest occupied molecular orbital                        |
| HLS                             | Harmonic Light scattering                                 |
| ICT                             | Intramolecular charge transfer                            |
| IR                              | Infrared  |
| Ir                              | Iridium   |
| ILCT                            | Intraligand charge transfer                               |
| KDP                             | Potassium dihydrogen phosphate                            |
| LUMO                            | lowest unoccupied molecular orbital                       |
| LiNbO <sub>3</sub>              | Lithium niobate   |
| Ln                              | Lanthanide  |
| Ln(Pc) <sub>2</sub>             | Lanthanide phthalocyanine                                 |
| LgSPR                           | Longitudinal surface plasmon resonance                    |
| Lu                              | Lutetium  |
| MLCT                            | Metal-to-ligand charge transfer                           |
| MQ                              | Mille-Q   |

|                  |                                      |
|------------------|--------------------------------------|
| NIR              | Near infrared                        |
| NMR              | Nuclear magnetic resonance           |
| NSs              | Nanosphere                           |
| NRs              | Nanorods                             |
| NLO              | Nonlinear optical                    |
| NPP              | N-4-nitrophenyl-L-prolinol           |
| Pt               | Platinum                             |
| PSS              | Photostationary state                |
| Pc               | Phthalocyanines                      |
| PAA              | Polyacrylic acid                     |
| Re               | Rhenium                              |
| Ru               | Ruthenium                            |
| SFG              | Sum Frequency Generation             |
| SPR              | Surface plasmon resonance            |
| SHG              | Second Harmonic Generation           |
| SH               | Second harmonic                      |
| THF              | Tetrahydrofuran                      |
| THG              | Third-harmonic generation            |
| TrSPR            | Transverse surface plasmon resonance |
| TOAB             | Tetraoctyl ammonium bromide          |
| TEM              | Transmission electron microscopy     |
| UV               | Ultraviolet                          |
| VB-CT            | Valence-bond charge transfer         |
| Vis              | Visible                              |
| Zn               | Zinc                                 |
| $\chi$ (Khi/Chi) | Electric susceptibility              |
| $\beta$          | Hyperpolarizability                  |

## Introduction

The importance of molecular and nanomaterials engineering for science and technology has highly increasing during the last 10 years. Materials with NLO activity may be used as electro-optic switching elements for telecommunication and optical information processing. Therefore, the design of nonlinear optical (NLO) molecules has become a focus of current research. The NLO process requires materials that control the amplitude, phase, polarization and frequency of optical waves. In this context, a variety of dipolar and octupolar complex materials such as organometallic, photochromic, lanthanides and lanthanide complexes are synthesized and studied by powerful tools, e.g. Harmonic Light Scattering (HLS) and Electric Field Induced Second Harmonic Generation (EFISH) to determine their first hyperpolarizability ( $\beta$ ). The NLO properties of these materials are tailored by using different donor and acceptor groups, metals and  $\pi$ -conjugation backbones. Apart from these materials, gold nanoparticles are also studied because of their large optical second and third-order nonlinearities. Huge hyperpolarizabilities have been reported in relation with their surface plasmon resonance. For this reason, in the context of this thesis gold nanorods and spherical particles have been synthesized by Radiolysis and their first hyperpolarizabilities have been measured by HLS at 1064 nm. In particular, we have investigated the role of the surface plasmon resonance on the first hyperpolarizabilities ( $\beta$ ) for gold nanorods, with a strong emphasis on the role of their aspect ratio. Moreover, the NLO properties of nanorods functionalized with highly nonlinear DAST dyes have been characterised in order to evidence interactions between plasmon resonance and the optical properties of organic conjugated molecules.

**Chapter 1:** This chapter contains three parts. **Part A** provides brief introduction about Nonlinear Optics, and various types of NLO effects. The main principles of molecular engineering for quadratic NLO are discussed. We therefore discussed the NLO materials based on the concept of charge transfer between donor and acceptor groups separated by a spacer (D-Spacer-A) and how the nonlinearity varies by changing the conjugation length, donor and acceptor groups and their position in the molecules. The extension of this concept to octopolar structures is also presented. Various models to determine molecular hyperpolarizability has been discussed. At the end of this part, multifunctional systems such

as photochromism, lanthanides and lanthanide complexes along with their applications are discussed.

**Parts B** contains the information about gold nanoparticles (AuNPs), starting with the introduction, history, and different methods available for the synthesis of AuNPs. Then the physical, chemical, catalytic and optical properties of AuNPs are discussed. At the end of this part we tried to show the importance of AuNPs for quadratic second order NLO and their applications in the different domain.

**Pact C** contains the information about investigation tools used to characterize the linear and nonlinear optical properties of our newly synthesized molecules and AuNPs. It includes the radiolysis technique that we used to synthesize the AuNPs (rods and spheres). The absorption spectra of the different molecules and nanoparticles are taken by UV-Vis-IR spectroscopy. The transmission electron microscopy is used to observe the images of nanoparticles and to evaluate their size and aspect ratios. Along with the TEM, we also used the dynamic light scattering technique to confirm the size and shape of the nanoparticles. After linear characterization, optical nonlinear studies are done by using the powerful second- and third-harmonic generation tools known as EFISH, HLS and THG. We used two different wavelengths, at 1.064  $\mu\text{m}$  for AuNPs and at 1.907  $\mu\text{m}$  for the other newly synthesized molecules.

**Chapter 2:** This chapter has also been divided into 3 parts. **Part A** includes newly synthesized cyclometallated 1, 3-di (2-pyridyl) benzene platinum (II) complexes. The effect of the nature of the substituent on the quadratic hyperpolarizability has been investigated. Then we report on newly synthesized compounds of tris-cyclometallated Ir complexes incorporating various  $\pi$ -donor conjugated groups inducing strong charge transfers. At the end of this part, the NLO response of the octupolar triaryl-1, 3, 5-triazinanes-2, 4, 6-triones functionalized with electron-rich Fe (II) and Ru (II) acetylide complexes has been reported.

**Part B** of this chapter starts with a basic introduction about photochromic molecules and the previously reported hyperpolarizability of dithienylethene containing 2, 2'-bipyridine ligands. We present here a new series of chromophores in which DTE-based bipyridines combine with different donor groups (D) such as H, OMe, NMe<sub>2</sub>, and NBu<sub>2</sub>, and with

different metallic centers, namely the strong Lewis acid  $\text{ZnCl}_2$  as well as the  $\text{Ru}(\text{bipy})_2^{2+}$ ,  $\text{Re}(\text{CO})_3\text{Br}$ , Ru, Cu, and Fe moieties. In this part we describe their optical, especially luminescence properties, and their quadratic hyperpolarizability for the open and photocyclized closed forms, as measured by the EFISH and HLS techniques. In particular, the investigation of the role of metal centers on the photochromic and NLO activity is also reported.

**Part C** of this chapter reports on lanthanide complexes which a preliminary presentation of previous results in NLO properties of rare-earth derivatives. The newly synthesised bis (phthalocyaninato) lanthanide double-decker complexes are extensively studied. In this respect, Eu, Dy, and Lu bis- (phthalocyaninato) sandwich complexes with a crosswise ABAB phthalocyanine bearing electron-donor (thioalkyl) group grafted on the two opposite phthalocyanine (Pc) rings were synthesized and their first molecular hyperpolarizability ( $\beta$ ) measured. Similarly, AB<sub>3</sub> (3 electron-donor groups on the two opposite Pc rings), A<sub>4</sub> (no electron donor groups), and B<sub>4</sub> (4 electron-donor groups on each opposite Pc ring) double-decker complexes are synthesized and characterized by UV-Vis-IR spectroscopy and by the HLS technique for their NLO properties. The  $\beta$  values of bis- (phthalocyaninato) lanthanide sandwich complexes with ABAB, AB<sub>3</sub>, A<sub>4</sub>, and B<sub>4</sub> and oxidized  $[(\text{Lu}(\text{Pc})_2)^+]$  and reduced  $[(\text{Lu}(\text{Pc})_2)^-]$  rare earth centres are reported. The role of *f* electrons on the hyperpolarizability is presented.

**Chapter 3:** This chapter contains the synthesis of gold nanoparticles (spherical and rod shapes) made in this work in order to study their linear and nonlinear optical properties for their application in photonics. We discussed the principles and mechanisms underlying the radiolytic reduction process of gold nanoparticles. We evidenced transverse and longitudinal SPR bands of our synthesized gold nanospheres (AuNSs) and gold nanorods (AuNRs) along with their TEM images. With this information, we calculated the average diameter of AuNSs and AuNRs. HLS at 1.064  $\mu\text{m}$  is used and the  $\beta$  value is determined for AuNSs and AuNRs with different aspect ratios. The observed value is then compared with respect to the aspect ratio. The observed  $\beta$  value is compared with the previous reported ones. Variable incident polarization measurements on HLS are also performed, resulting in the determination of the depolarization ratio. We can then extract from depolarization data the relative dipolar and

octupolar contributions to the AuNRs  $\beta$  tensor and their dependence with AuNRs aspect ratios. We also used the nonlinear optical microscopy to observe SHG from the AuNRs. Finally, we performed functionalization of AuNRs with DAST derivatives, and we investigated the effect of SPR from AuNRs on the DAST derivative NLO response.

# **Chapter 1: Presentation of materials and investigation tools**

## **Part A: Nonlinear optics and molecular engineering**

### **A-1.1: Nonlinear optics (NLO)**

Nonlinear optical phenomena are “nonlinear” in the sense that they occur when the response of a material system to an applied optical field depends in a nonlinear manner on the strength of the optical field. For example, second-harmonic generation occurs as a result of the part of the atomic response that scales quadratically with the amplitude of the applied optical field. Consequently, the intensity of the light generated at the second-harmonic frequency increases as the square of the intensity of the applied laser light. NLO plays an important role in the development of photonics, an emerging field offering attractive performances in data transmission and processing as compared to electronics [1]. In photonics, photons replace electrons to acquire, store, process and transmit information. There are, in some cases, similarities between photonics and electronics circuits. For example, light can be switched from one channel to other using passive or active functionalities. For optical switching, it requires a material that allows the manipulation of photons by an electric field or a laser beam. Therefore, [2-5] materials which allowing manipulating light at the switching points must display optical nonlinearities. It is not surprising that these materials are gaining importance in technologies for several decades as a promising field with important potential applications in optical signal processing, switching and frequency generation (such as harmonic generation, frequency mixing, and optical parametric oscillation), and may also contribute to optical data storage, development of high-bit- rate communication, and dynamic image processing. If we compare photonics and electronics, photonics has many distinguishable merits over electronics. The most important advantage is a higher speed, because photons are massless particles, travelling much faster than electron in matter. Another important advantage in optical communications is the absence of mutual electromagnetic perturbations between optical wave propagating in a linear medium like a silica optical fiber, then allowing the transmission of numerous optical information channels, differing e.g. by their wavelength, in the same optical fiber (wavelength multiplexing).

### **A-1.2: Historical Background**

Under normal conditions the response of a medium to light is linear and as a consequence most optical phenomena can be described in terms of a linear refractive index and linear absorption. NLO appeared experimentally only with the invention of lasers in the early 1960, when Maiman constructed the first operating optical ruby laser shown in figure 1.1. Lasers provide high, coherent optical waves, with strong electromagnetic field amplitude reaching a level where the response of the medium starts to deviate from the linear behavior. It was found that at sufficiently high light intensities the optical response of the material depends on light intensity. This led to the new field of nonlinear optics and to the discovery of various fascinating phenomena such as second and third harmonic, sum- and difference frequency generation, nonlinear refraction saturable absorption, and four-wave mixing [2]. Shortly after the first experimental evidence of a NLO phenomenon,  $10^8$  V/m laser fields could be easily gained from Q-switched nanosecond solid state laser sources. Today, picosecond, and femtosecond lasers are commercially available and attracted the interest of scientist and researchers from various fields.

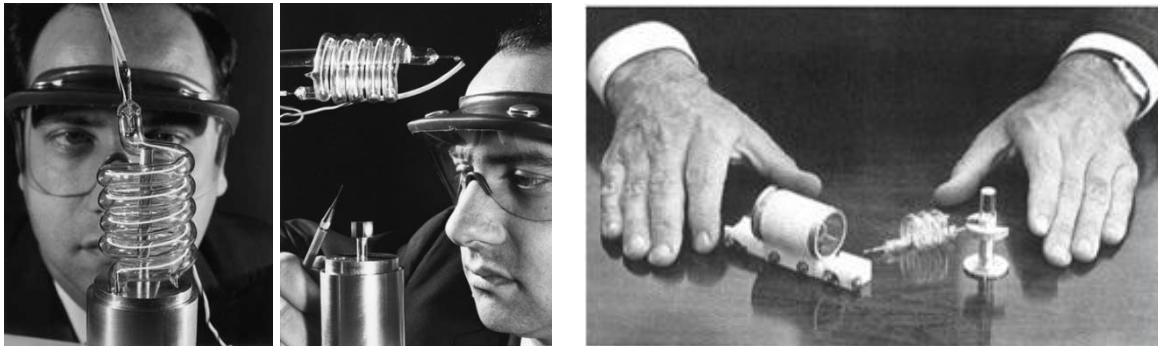


*Figure 1.1: Dr. T. Maiman from Hughes Research Laboratories looking at a ruby cylinder the core of his first laser experiment (Photo: HRL Laboratories, LLC and a publicity shot by Hughes Aircraft Co., July 1960).*

In 1960, T. Maiman built the first ruby laser, and Ali Javan invented the first He-Ne laser. One year later, Peter Franken et al. 1961, performed an experiment where a quartz crystal was irradiated with a laser beam from a ruby laser at a 694.2 nm wavelength to generate the second harmonic wavelength at 347.1 nm. This was the first evidence of a purely optical nonlinear effect in the history of optics [6]. Afterwards, several other optical frequency mixing effects were demonstrated including optical sum-frequency generation (1962), optical

third harmonic generation (1962), optical rectification (1962), optical difference frequency generation (1963) and optical parametric amplification and oscillation (1965) [2]. In 1965, Terhune, Maker and Savage discovered Harmonic light scattering in liquids [7].

Even before the invention of lasers, there were few reports of experimental nonlinear optical phenomena, all of them requiring the use of a quasi-static electric or magnetic field. First, Michael Faraday discovered the Faraday Effect in 1845. He found that an intense magnetic field changes the polarization of the light along its propagation direction [8]. The Kerr Electro-Optic effect was discovered by John Kerr in 1875. He applied an electric field instead of a magnetic field, perpendicular to the propagation direction and found that that the refractive index of the material was proportional to the second power of the electric field [9]. In 1893, Friedrich Pockels discovered the “linear” Pockels Effect. He noticed that the refractive index of a non centrosymmetric medium is modified by an applied electric field, and displays a linear dependence with respect to this applied field. Later on 1922, Leon Brillouin theoretically predicted Brillouin scattering (interaction of a photon with acoustic mode) an effect that was experimentally demonstrated by E. Gross in 1930 [10]. Raman scattering (interaction of a photon with molecular vibration mode) was predicted by A. Smekal in 1923 and observed by C.V. Raman in 1928. Raman was awarded by Nobel physics prize in 1930 for the discovery of the Raman Effect [11]. In the case of Brillouin and Raman scattering the frequency of light is modified by a light matter interaction process, but involving only one optical photon.

The discovery of Stimulated Raman scattering by Woodbury and Ng (1962) [12] was another important discovery in the history of nonlinear optics, a more detailed description of this effect is reported by Eckhardt et al. (1962) [13]. The importance of this discovery is that, for the first time, the ‘stimulated’ nature of light scattering under excitation by an intense laser was revealed. The properties of stimulated Raman scattering have been reviewed by Bloembergen (1967) [14], Kaiser and Maier (1972) [15], Penzkofer et al. (1979) [16], and Raymer and Walmsley (1990) [17]. In 1964, Chiao et al used powerful new lasers for the first time to experimentally observe stimulated Brillouin Scattering phenomena [18]. Afterwards, in 1966, Stimulated Rayleigh-wing scattering was discovered both theoretically

and experimentally by Bloembergen, Chao, Cho and other researchers [19-21]. There are still many early phases of the development of nonlinear process that are not mentioned here, but they have been reviewed in the most illuminating way in classical nonlinear optics books (e.g. by *Bloembergen* [4] and *Akhmanov* and *Khokhlov* [22]). New physical phenomena along with comprehensive overview of nonlinear optical novel concepts and applications have been discussed textbooks by *Boyd* [2], *Shen* [3], and others.

### **A-1.3: Origin and Theory**

In order to describe more precisely the concept of an optical nonlinearity, let us consider how the dipole moment per unit volume (polarization P) depends on the electric field strength  $E^\omega$  of an applied optical wave at frequency  $\omega$ . In case of linear material, P is a linear function of E, i.e. P oscillates at the same frequency  $\omega$  as  $E^\omega$

$$P^\omega = \epsilon_0 \chi^{(1)} E^\omega \quad (1.1)$$

Where,  $\chi^{(1)}$  is the linear electric susceptibility of the dielectric and  $\epsilon_0$  is the permittivity of free space.

NLO phenomena (i.e. involving at least two optical fields) occur at intense fields. As the applied field strength increases (e.g. by using, lasers) the polarization response of the medium is no longer linear. The optical response can often be described by Eq. (1.2) developing the induced polarization (P) in a series of increasing powers of  $E^\omega$ , and given by [3]

$$P = \epsilon_0 \chi^{(1)} E^\omega + \chi^{(2)} E^\omega E^\omega + \chi^{(3)} E^\omega E^\omega E^\omega \quad (1.2)$$

Where  $\chi^{(1)}$  is the linear, second-rank susceptibility tensor of the material, and  $\chi^{(2)}$  and  $\chi^{(3)}$  are the second-order (third-rank) and third-order, (4<sup>th</sup>-rank) non-linear optical susceptibility tensors, respectively.

At the molecular level eq. (1.2) is expressed as

$$P = \sum_j \alpha_{ij} E^\omega + \sum_{j < k} \beta_{ijk} E^{\omega^2} + \sum_{j < k < l} \gamma_{ijkl} E^{\omega^3} + \dots \dots \dots (1.3)$$

Where,

$\alpha_{ij}$  = linear polarizabilities

$\beta_{ijk}$  = First hyperpolarizability (second order effects)

$\gamma_{ijkl}$  = Second hyperpolarizability (third order effects)

i,j,k,l correspond to the molecular coordinates

Nonlinearities of molecules and materials depend on their symmetry. If molecules or materials are centrosymmetric, then their quadratic NLO response cancel out as it is the case for any quadratic physical property.

Oudar [4], Yariv [24] and later Williams [23] proposed a chemically oriented picture to describe the connection between the nonlinear propagation response and the applied electric field in medium. This description considers an individual molecular unit rather than a collection of molecular units to describe the NLO optical phenomena.

A prototypical noncentrosymmetric electron donor (D) and acceptor (A) molecule exhibits an asymmetric polarization response with respect to the applied electric field from laser, as shown in figure 1.2 (a).

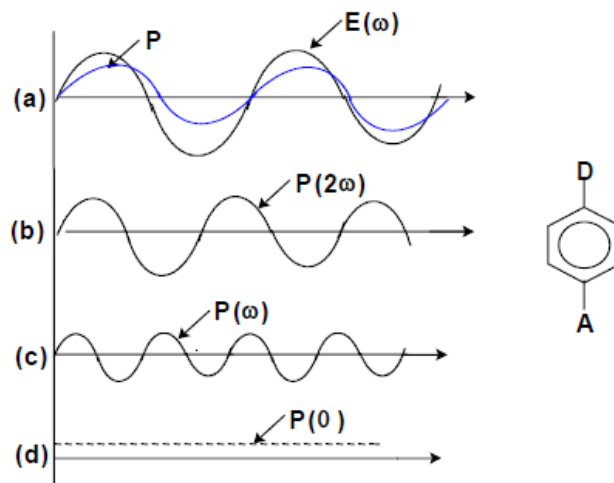


*Figure 1.2: (a) Plot of the polarization response  $P$  to an incident electromagnetic wave of field strength  $E(\omega)$  at frequency in a non-centrosymmetric D- $\pi$ -A molecule. (b) to (d) Fourier components of  $P$  at frequencies for  $\omega$ ,  $2\omega$ , and  $0$ .*

The polarization takes place from D (electron rich substituent) to the A (electron deficient substituent). The asymmetric polarization induced by the oscillating optical field can be described as a superimposition of the Fourier components of frequencies  $0$ ,  $\omega$ ,  $2\omega$ , and  $3\omega$  etc., as shown in Figure 1.2 (b). The harmonic components of polarization, such as  $P(2\omega)$ , will produce an optical electric field of harmonic frequency  $E(2\omega)$ . An ensemble of asymmetric microscopic units organized in a non-centrosymmetric arrangement produces in a similar way a macroscopic harmonic response.

#### **A-1.4: Various types of Second-order NLO effects**

In a quadratic NLO medium, four types of second-order NLO effects can be observed experimentally. These are Second Harmonic Generation (SHG), Sum or difference Frequency Generation (or Parametric Generation (SFG), linear electro-optic effect or Pockels effect and optical rectification.

Second harmonic generation (SHG also known as “frequency doubling”) is a nonlinear optical process in which two incident photons at frequency  $\omega$  interacting with a nonlinear material are effectively “combined” to form one new photon at frequency  $2\omega$ , i.e therefore half the wavelength of the initial photons. According to figure 1.3 (b), two photons of frequency  $\omega$  are destroyed, and a photon of frequency  $2\omega$  is simultaneously created in a single quantum-mechanical process. The solid line in the figure represents the atomic ground state, and the thin lines represent virtual levels. These levels are not necessarily eigen energies of the free atom or molecule.

Figures 1.3 (c), (d) and (e) show SFG, Pockels effect and optical rectification. **SFG** is the transformation of a light wave with frequency  $\nu$  into two new photons with frequencies  $\nu_1$  and  $\nu_2$ . The **Pockels effect** is a linear with respect to an applied electric field change in the refractive index of a medium in the presence of an external low-frequency electric field. The change in the polarization due to the presence of these two interacting optical and electrical

field components alters the refractive index of the medium [2]. **Optical rectification** is defined as the ability to induce a DC voltage between the electrodes placed on the surface of

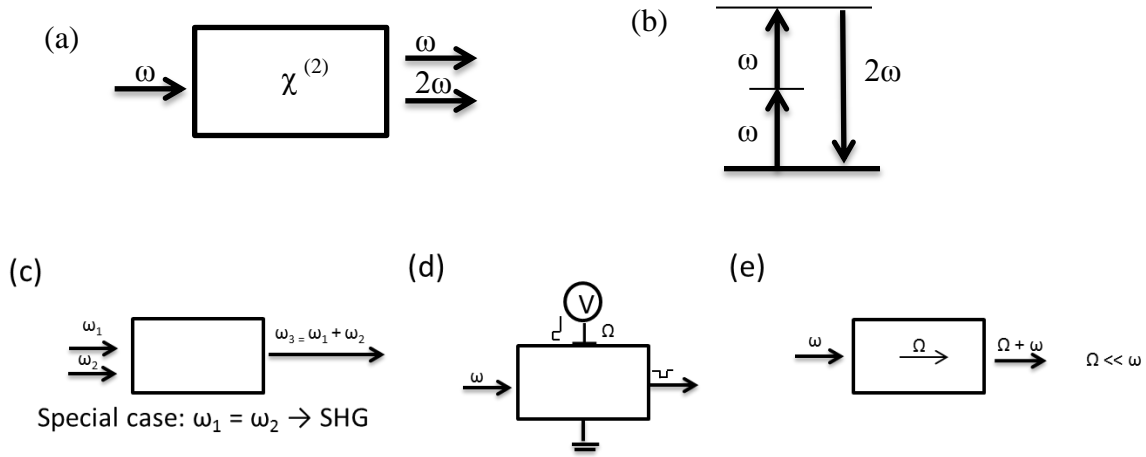


Figure 1.3: (a) Geometry of second-harmonic generation. (b) Energy-level diagram describing second-harmonic generation. (c) Sum frequency generation (d) Pockels effect (e) Optical rectification.

the crystal when two intense laser beams at the same frequency  $\omega$  are directed into the crystal [25].

### A-1.5: Materials for Nonlinear optics

Over the past few decades, continuous progress has been reported in the domain of NLO materials as the result of the so-called molecular engineering schemes. These NLO materials display potential applications in various fields, such as optical data storage, telecommunications, and optical information processing. This has attracted numerous chemists to perform chemical synthesis, and physicists to target and characterize their functional properties for a wide choice of materials; organic, inorganic, semiconductors and polymers [26 (a)]. Fair choices of inorganic optical materials are commercially available for use as electro-optic devices, frequency doubler or parametric oscillators. Examples for inorganic materials are lithium niobate ( $\text{LiNbO}_3$ ), potassium dihydrogen phosphate (KDP), Baryum Boron oxide (BBO). NLO Semiconductor materials are gallium arsenide [26 (b)] or Cadmium selenide [26 (c)] (these being used as quantum dots). Organic materials may be

used in a crystalline form, such as (POM [26 (d)], NPP [26 (e)], and DAST [26 (f)],) or in polymers (for electro-optic applications) [34].

Inorganic materials may be covalent or ionic. Indium antimonide (InSb) has one of the largest known  $\chi^{(2)}$  value, but being a semiconductor, it is highly absorbing in the visible region of the optical spectrum and therefore cannot be used for most laser applications.  $\text{LiNbO}_3$  is the most extensively studied material for electro-optic device applications (26 (g)). Potassium dihydrogen phosphate (KDP) [26 (h)] has been used widely for phase matched SHG of high-powered near-IR lasers. Both inorganic and semiconductor materials are used in commercial applications such as modulators, optical switches etc., [27] but they also show some drawbacks. For example, these crystals face a ‘trade-off’ problem between the response time and magnitude of optical nonlinearity. Semiconductors are costly and difficult to produce, furthermore they absorb strongly in the visible region, then preventing them for use in the visible range [28]. To date inorganic transparent oxides, such as  $\text{LiNbO}_3$ ,  $\text{KH}_2\text{PO}_4$ , or BBO are the most widely spread NLO materials at the commercial level.

Earlier investigations focused on purely organic systems [29] and then on organometallic derivatives have gradually intensified in the last fifteen years [30]. Organic materials are molecular materials that consist of chemically bonded molecular units interacting in the bulk media through weak van der Waals interactions. Organic materials are emerging as an alternative to inorganic materials because of their specific advantages over inorganic materials for applications in optoelectronic devices, such as fast response times, cost effective, and intrinsic tailorability and versatility from the chemical synthesis point of view, [31-32]. Organic materials display low dielectric constants, high optical damage thresholds in a pulsed regime, and very large NLO responses over a broad frequency range as comparable to those of semiconductor materials, and are thus suitable for high-frequency modulation applications for the linear electro-optic effect [33-34]. The most important feature of organic molecules is a typical push-pull structure, i.e.,  $\pi$ -conjugated systems connecting an electron-donating group and an electron-withdrawing group [35]. However, organics display several disadvantages such as thermal degradation. Their long-term stability has been questioned until now, in spite of recent systematic studies [31-32].

Organometallic complexes are similar to organic molecules in that they can possess conjugated ligands and display high molecular hyperpolarizabilities. The presence of the metal results in a greater design flexibility, e.g. by variation in metal oxidation state, ligand environment and geometry; metals coordinated with NLO chromophores result in molecules of much greater complexity than for the first generation of “push-pull” organic molecules and can give rise to tuneable optical properties [36-37]. The metal center may be an extremely strong electron donor or acceptor, a requirement for electron asymmetry and hence second-order nonlinearity.

#### **A-1.6: Molecular Engineering: Dipoles and Octupoles**

The NLO properties of molecular materials are mainly governed by the NLO characteristics of the individual molecular units. Chromophores containing electron donor (D) and electron acceptor (A) substituents linked through a conjugated  $\pi$ -backbone (Figure 1.4) show high NLO responses, according to the classical molecular engineering scheme restricted to dipolar compound with one dimensional charge-transfer transitions.

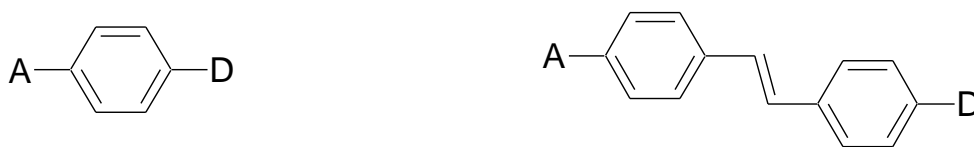


*Figure 1.4: Examples of the structure of nonlinear, dipolar push-pull molecules (A=Acceptor group, D= Donor group.)*

Nonlinearities can be enhanced by either *increasing the conjugation length between the donor and acceptor group* (improving delocalization) or by *increasing the strength of donor or acceptor groups* (improving electron asymmetry). The *position and number of acceptor and donor groups* in the molecule play also an important role [29].

Various examples of donor or acceptor groups and of the conjugated backbone are shown in Figure 1.5. Special attention has been paid to the nature, the symmetry and length of the conjugated path. Traditional classification strategies of quadratic nonlinear molecules have been governed, for a long time, by the prevailing two level quantum model of  $\beta$  [38] and the electric-field- induced second-harmonic generation (EFISH) experimental technique [63] which, by nature, are suitable only for dipolar contributions to the  $\beta$  tensor.

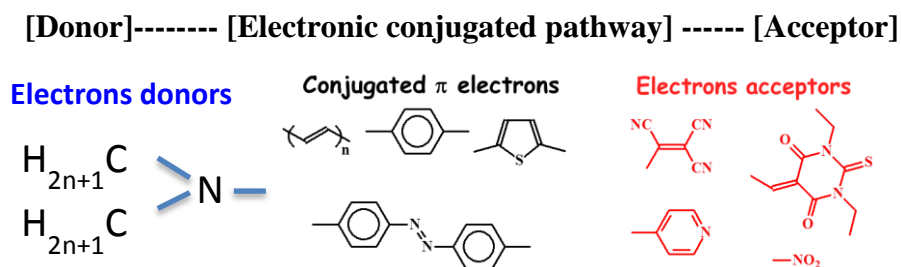


Figure 1.5: Examples of donor and acceptor groups together with conjugated path.

The two-level model, valid for 1D intramolecular charge-transfer molecules, will be discussed later in more details [38]. The combination of strong electron donor and strong acceptors yields a high  $\beta$  value. However when donor and acceptor groups are very strong the ground state tends to become a charge-separated state, displaying a poor polarizability and hence lowering the NLO value. Moreover, the difference in dipole moments between this ground state and the charge transfer excited state may become small, resulting in poor  $\beta$  values. As the investigated response is nonlinear, a small variation in the molecular architecture can lead to large modification in the NLO response.

In the early 1990s the concept of octupolar molecules has emerged as a new field of research and expanded the scope of molecular engineering for nonlinear optics. Such octupolar compounds with multi-directional (two or three dimensional) charge-transfer transitions are able to improve the efficiency/transparency and stability as compare to classical dipolar compounds [39]. The vector part of the molecular hyperpolarizability tensor  $\beta_{J=1}$ , corresponding to the dipolar contribution, being cancelled out. Only the octupolar contribution  $\beta_{J=3}$  contributes to the 3<sup>rd</sup> rank  $\beta$  tensor. The most general octupolar distribution of positive and negative charges (corresponding to electron donor D and electron acceptor A, respectively) is a cube, D and A substituents being alternatively located at its edges. Another 3D octupolar distribution is represented by a tetrahedron with a central A (or D) unit connected to 4 peripheral D (or A) groups. 2D structures can be derived from the cubic one by projecting the A and D groups on a plane perpendicular to the  $C_3$  axis of the cubes giving rise to  $D_3$  and  $C_3$  symmetries (Figure 1.6).

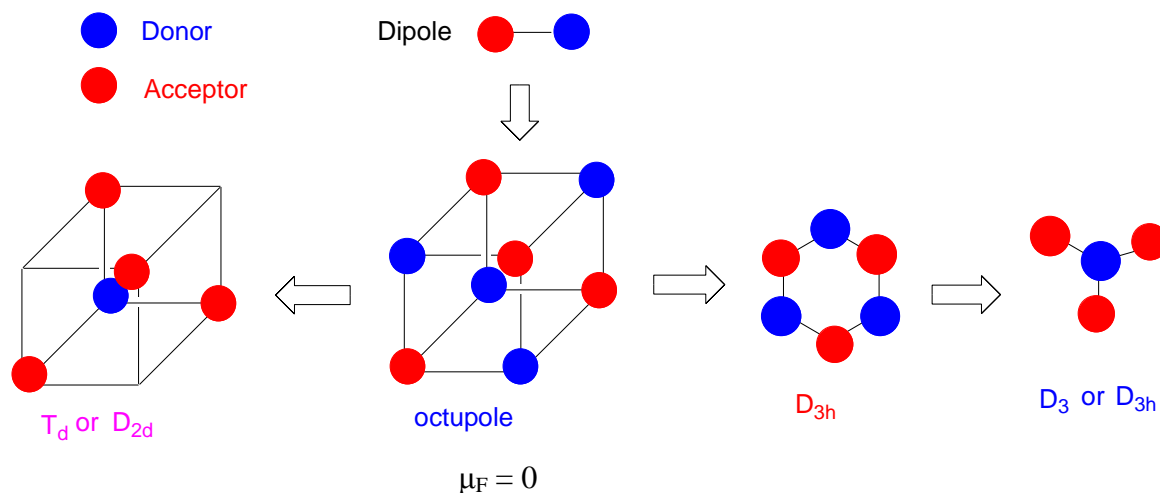
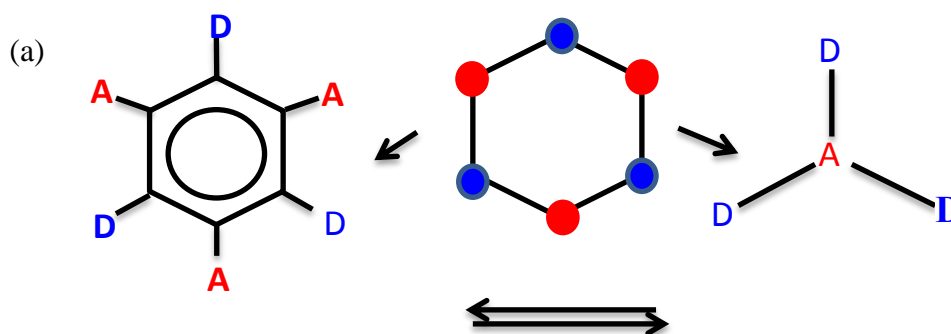


Figure 1.6: Schematic representation of octupolar symmetries [40]

The two important advantages of using nondipolar chromophores as compared to dipolar ones are an easier noncentrosymmetric arrangement and an improved nonlinearity tradeoff. The concept of octupolar non-linearity has been widely demonstrated at the molecular level and numerous examples of octupolar molecules exhibit large hyperpolarizability, with the same order of magnitude than that of the best dipoles, as reported in [41]. Afterwards, an increasing number of 2-D and 3-D scheme octupolar have recently appeared in the literature [40]. Zyss [39] proposed general 2D and 3D strategies for the optimization of  $\beta_{J=3}$ . The two main approaches in the realm of 2D structures are:

- 1) A central  $\pi$ -electron reservoir mediating intramolecular charge transfer (ICT) interactions between peripheral electro-active side groups (Figure 1.7 a) like, 1,3,5 benzene [42], triazine derivatives [43], and 1,3,5-triamino-2,4,6-trinitrobenzene (TATB) derivative [44].



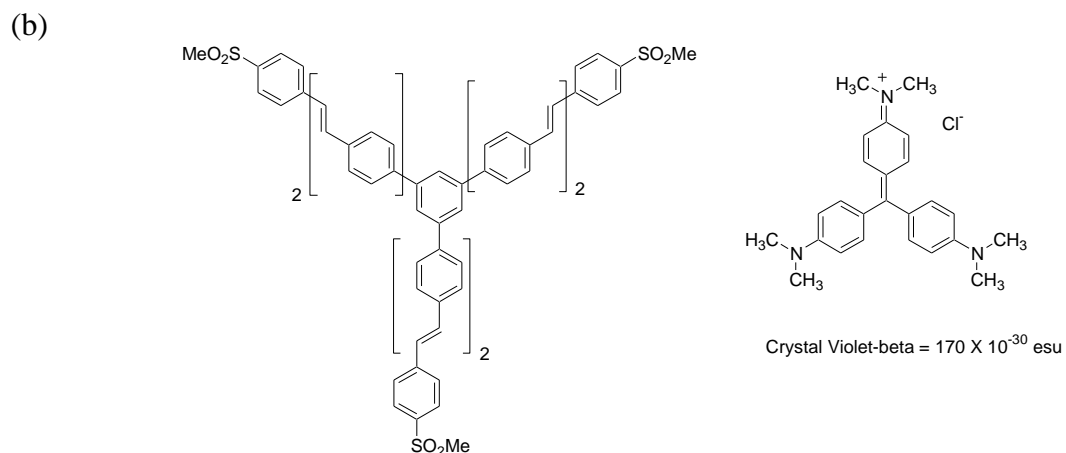


Figure 1.7: Benzene-like (left) and central atom (right) strategy for 2D octupolar engineering [45].

- 2) A donor (acceptor) atom occupying a central position at the cornerstone of the molecular structure mediating a multipolar ICT interaction with three accepting (donating) groups through a conjugated system (figure 1.7 (b)) like, Crystal Violet [46], trisubstituted amines, cyanine salts and biphenyl derivatives [47], oligothieryl analogues [48], or ruthenium<sup>II</sup> (2,2'-bipyridine)<sub>3</sub> complexes [49], or subphthalocyanines [50].

The design of efficient 3D structures is mainly illustrated by metal complexes and provides attractive possibilities for the octupolar engineering of 3D molecules, in view of their potentially available electronic properties, such as metal core oxidation potential, open shell electronic structures, as well as the existence of built-in chirality. Tetrahedral covalent bonding or complexation are derived from the very general 3D cubic octupolar scheme, on the basis of complex donor or acceptor tetrahedral substructures resulting in efficient *Td* octupolar systems such as tetra substituted tin derivatives [51] as shown in Figure 1.8 (a), or tetrahedral copper bipyridine complexes as shown in Figure 1.8 (b) [52]. Purely organic alternatives based on functionalized biphenyls [47] [Figure 1.8 (c)] or paracyclophane derivatives [Figure 1.8 (d)] [53] are also very promising.

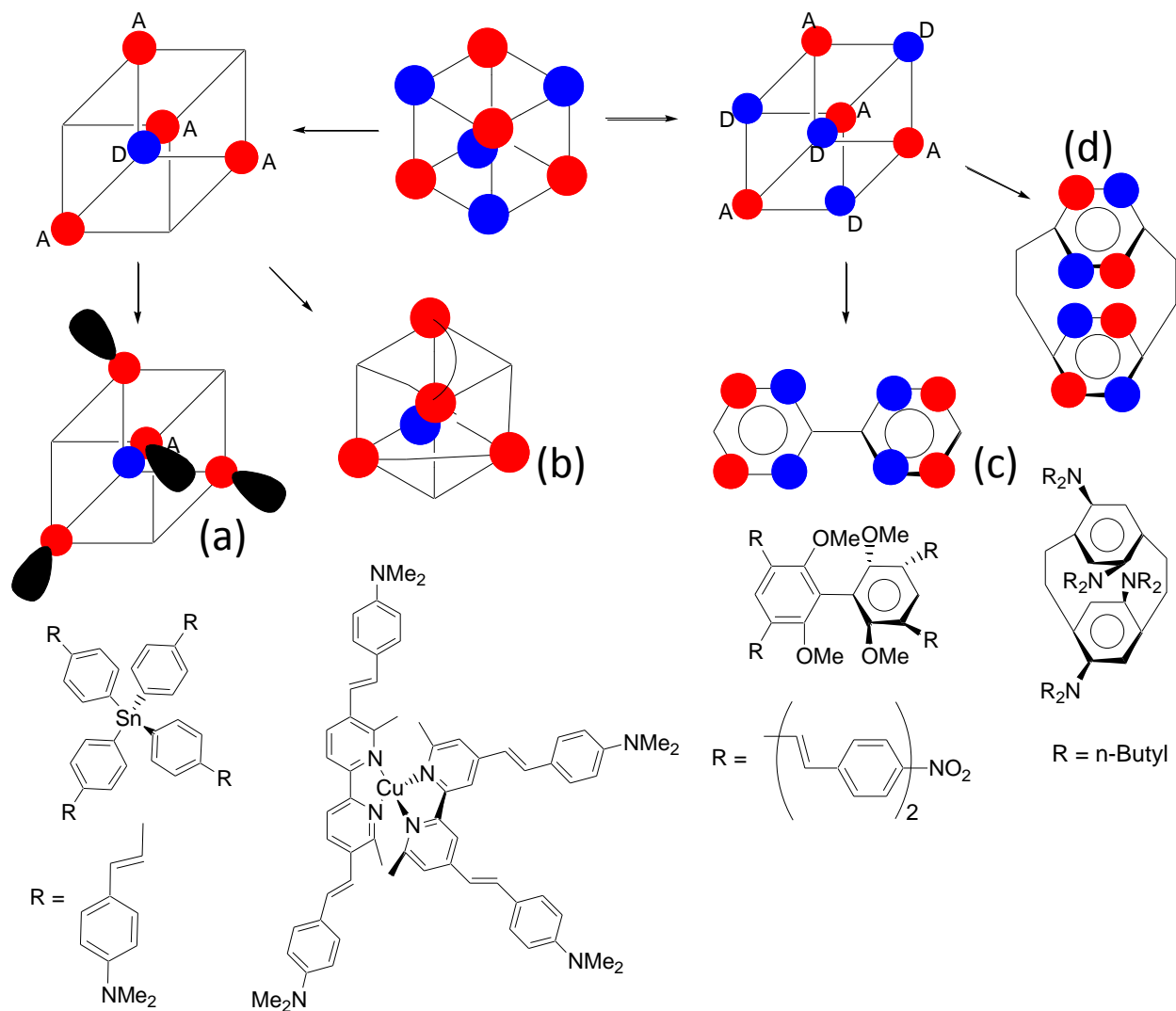


Figure 1.8: 3D octupolar engineering schemes as derived from the cubic octupolar template [40]. (a) Covalent tetrahedral Sn derivative. (b) Tetrahedral metal complex. (c) Substituted biphenyl derivative. (d) Paracyclophane derivative.

## A-1.7: Various models for molecular hyperpolarizabilities

### A-1.7.1: Additivity model

This is a simple, “naive” model to predict the second-order response of disubstituted organic molecules. It is proposed that the total molecular nonlinearity for a complex molecule is the vector sum of the contributions from each of the main structural elements of the molecule [58-59]. Such an additivity model can be successful to predicting the scalar portions of molecular polarizabilities in complicated systems [60]. Later this model used vector addition for experimental NLO responses for small molecules to predict responses of more complicated structure [61-62]. Zyss has found that this additivity model works well for

weakly coupled systems, such as D and A  $\sigma$ -networks [55-56], but, in generally fails for strongly coupled disubstituted systems [38, 63-64]. This model cannot account for the high  $\beta$ -values observed for highly asymmetric  $\pi$ -networks.

#### **A-1.7.2: The valence bond charge transfer model**

The valence-bond charge transfer (VB-CT) model is one of the simplest and extensively studied models in order to provide well-defined for the structure/NLO-property relationship of various multipolar molecules. The VB and CT states correspond to 1D dipoles, 1D linear quadrupoles, 2D planar octupoles, and 3D tetrahedral octupoles. The four-state model consisting of a single valence-bond (VB) configuration and three charge-transfer (CT) configurations, describes two-dimensional octupolar molecules, whereas a five-state model is needed to tetrahedral, three-dimensional species [45].

#### **A-1.7.3: Equivalent Field Model (EIF)**

Oudar and Chemla [54] developed the equivalent field model to describe the second-order responses of dipolar molecules. The EIF model sought to understand trends in  $\beta$  by quantifying the ground state asymmetry of a  $\pi$ -network in a systematic fashion. It is proposed that a major part of the second order response in  $\pi$ -organic chromophores could be predicted from the ground state deformation of an initially symmetric  $\pi$ -electron distribution by an internal (equivalent) electric field induced by donor and acceptor substituents. A generalization of this concept to octupolar structure has been proposed by Zyss [55-56]. The “equivalent” field is replaced by an equivalent electrical potential induced by an octupolar distribution of positive and negative charges, featuring donor and acceptor group grafted to a central benzene ring [57].

#### **A-1.7.4: Two level dispersion model**

In order to account for the frequency-dependence of quadratic hyperpolarizability ( $\beta$ ) for push/pull  $\pi$ -organic chromophores, Oudar and Chemla [38] proposed a two-state dispersion model, derived from the complex developments of hyperpolarizabilities as proposed by Orr and Ward [65]. In particular, the molecule must be polarizable (for example with a wide  $\pi$  electronic conjugation), must have an asymmetric charge distribution (i.e. a push-pull system

with charge transfer), must have one or more excited states and must display a great difference between the ground and excited state dipole moment. They proposed that the large NLO response of these systems is due to an intermolecular charge transfer (CT) between D and A. The  $\beta$  is given as the sum of two contributions, one ( $\beta_{\text{add}}$ ) accounting for the interaction between each individual substituents and the conjugated  $\pi$ -network (additivity model) and the other ( $\beta_{\text{CT}}$ ) being the contribution arising from charge transfer due to the interaction of D and A moieties through the conjugated path.

$$\beta = \beta_{\text{CT}} + \beta_{\text{add}} \quad (1.4)$$

$\beta_{\text{CT}}$ , describing the charge transfer, is described in terms of a two-level dispersion model of  $\beta$  between the ground state (g) and the first excited state (n) as follows:

$$\beta_{\text{CT}} = \frac{3e^2}{2m} \frac{h\omega_{\text{gn}} f_{\text{gn}} \Delta\mu_{\text{gn}}}{[(h\omega_{\text{gn}})^2 - (2h\omega)^2][(h\omega_{\text{gn}})^2 - (h\omega)^2]} \quad (1.5)$$

$h\omega$  is the energy of the incident, fundamental photon

$h\omega_{\text{gn}}$  is the energy difference between the ground state (g) and the first excited state (n)

$f_{\text{gn}}$  is the oscillator strength of a g-n transition.

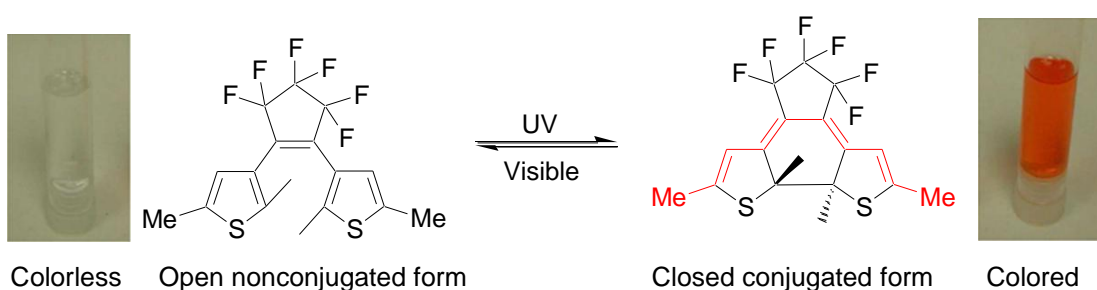
$\Delta\mu_{\text{gn}}$  is the difference in dipole moments between the ground and first excited state.

Theoretically, Zyss [56] confirmed the conclusions of Oudar and Chemla. Thus, the high- $\beta$  values of push/pull  $\pi$ -organic chromophores are intrinsically related to charge-transfer excited states, and therefore any method that seeks to accurately predict the  $\beta$  must adequately represent the energy and the charge distribution of these states [66].

### **A-1.8: Multifunctional Systems: Photochromism**

Photochromism refers to the reversible color change of a compound induced by light irradiation, due to a photo induced structural transformation of a molecule, resulting in a new form with an absorption spectra differing from that of the non-irradiated form. This prospect attracts much attention for the construction of molecular photonic devices. Reversible

changes of luminescence are interesting from the viewpoint of applications such as erasable memory media, optical switches and luminescent probes. During the past decade, there has been a growing interest in the synthesis and applications of organic photochromic materials because of their special properties [65-71]. Switching from a transparent to a colored form is known as photocoloration or photocyclization by illumination with UV light, the back switching from colored to transparent is known as photobleaching or photocycloreversion which occurs by illumination with visible light. Typically, upon photoisomerization, the conjugated pathway in the molecule is modified. The structural modification in photochromic molecules is accompanied by an energy shift of the highest occupied molecular orbital (HOMO) and/or of the lowest unoccupied molecular orbital (LUMO). The longer the conjugated pathway of the colored form, the smaller the HOMO-LUMO gap will be. Photochromic materials have been the focus of intensive investigations, at both fundamental and applied levels for their potential applications to optically rewritable data storage, optical switching, and chemical sensing. Photochromic transformations are generally based on unimolecular processes involving the interconversion of two isomers, such as cis/trans isomerization, ring opening/closing or intramolecular proton transfer. Combining a photochromic moiety with an organometallic or coordination compound provides new design parameters deriving from the combination of redox, optical and magnetic properties of the metal complexes with the photochromic reaction.



*Scheme 1.1: Photochromic interconversion of a dithienylethene (DTE) unit.*

The derivatives of Diarylethene (DAE) have recently received much attention because DAE have been used as ligand in transition-metal complexes. Coordination of DAE ligands opens up new perspectives for the design of photoswitchable molecules. Another similar family, 1,

2-dithienylcyclopentene (DTE) derivatives, is most promising because of their remarkable thermal stability of isomers, their fast response time and good fatigue-resistance properties, not only in solution but also in the single-crystalline phase, which are prerequisite conditions for practical applications [72-74]. Typically, DTE derivatives undergo reversible interconversion between a non-conjugated colorless open form to a  $\pi$ -conjugated, colored, closed form when irradiated in the UV range, the colored form being in the visible range (Scheme 1.1) [68,74]. The reaction is reversible by irradiation.

To open-up new perspectives for the design of metal-based photoswitchable molecules, chemists successfully combine the ligand or DTE with transition metals. The photochromic properties could be readily tuned by changing the nature of the transition metal system such as Re, Fe, Zn, Ru, Cu, etc. Metal complexes featuring photoresponsive ligands are an interesting alternative to pure organic photochromes. In the following chapter we will discuss more about newly synthesized photochromic molecules with the same DTE ligand and different transition metals. Their hyperpolarizabilities have also been studied and compared.

### **A-1.9: Multifunctional Systems: Lanthanides and Lanthanide Complexes**

The lanthanide series, made of fourteen elements starting with atomic number 58 (Cerium) to 71 (lutetium) is shown in Figure 1.9 (which also induced Lanthanum) and is characterized by the progressive filling of their 4*f* shells [75]. These fourteen lanthanide elements are often collectively known as rare earth elements. In general, lanthanides are most stable in the form of Ln<sup>3+</sup> ions and their electronic configuration is [Xe] 5*d* 6*s*<sup>2</sup> *nf*, *n* being the number of 4*f* electrons [76-77]. The outer 5*d* and 6*s* electrons shield the inner 4*f* electrons. As a result, the 4*f* energy levels are expected to be relatively insensitive to host media and are weakly mixed with the higher energy levels. They are considered as non-reactive and in fact chemical and linear optical absorption properties of lanthanide derivatives are very similar, for any value of *n*.

|   |                                      |  |   |  |                                       |  |   |   |  |   |                                      |   |   |   |
|---|--------------------------------------|--|---|--|---------------------------------------|--|---|---|--|---|--------------------------------------|---|---|---|
| 57<br><b>La</b><br>Lanthanum<br>138.90547 | 58<br><b>Ce</b><br>Cerium<br>140.116 | 59<br><b>Pr</b><br>Praseodymium<br>140.90765 | 60<br><b>Nd</b><br>Neodymium<br>144.242 | 61<br><b>Pm</b><br>Promethium<br>(145) | 62<br><b>Sm</b><br>Samarium<br>150.36 | 63<br><b>Eu</b><br>Europium<br>151.964 | 64<br><b>Gd</b><br>Gadolinium<br>157.25 | 65<br><b>Tb</b><br>Terbium<br>158.92535 | 66<br><b>Dy</b><br>Dysprosium<br>162.500 | 67<br><b>Ho</b><br>Holmium<br>164.93032 | 68<br><b>Er</b><br>Erbium<br>167.259 | 69<br><b>Tm</b><br>Thulium<br>168.93421 | 70<br><b>Yb</b><br>Ytterbium<br>173.054 | 71<br><b>Lu</b><br>Lutetium<br>174.9668 |
|---|--------------------------------------|--|---|--|---------------------------------------|--|---|---|--|---|--------------------------------------|---|---|---|

*Figure 1.9: The Lanthanide element series.*

### A-1.9.1: Photophysical properties and applications

Most of the interesting and useful photophysical properties of lanthanides ions are due to the  $4f$  electrons. The most impressive feature of lanthanide ions spectra is the sharpness of absorption and emission peaks, and the long lifetime of excited states, due to forbidden  $f-f$  electronic transitions. The optical properties of the lanthanides were first discovered in 1908 by Becquerel [78]. Lanthanides are usually incorporated in crystals as divalent or trivalent cations for the realization of optically active materials for photonic and optoelectronic applications. For example, optical lenses made with lanthanum oxide are used in special cameras and binoculars. Europium is widely used in phosphor based devices, and erbium as an efficient light amplifier at the  $1.55 \mu\text{m}$  optical fiber telecommunication wavelength.

Most  $\text{Ln}^{\text{III}}$  ions are luminescent. Ermolaev *et al.* reported luminescent lifetimes of a number of lanthanide ions emitting visible and near infrared light in solution [79]. Lanthanide luminescent derivatives have found a variety of uses in both biological and non-biological systems [80]. One of the most interesting and appropriate “real world” application of lanthanides is the red color that show up on the euro banknote under ultraviolet light, as shown in figure 1.10 [81]. The television industry also uses lanthanides, like europium and yttrium oxides to produce red colors on the television screen.



Figure 1.10: Authentic Euro banknotes are believed to contain europium chelates that emit red luminescence under ultraviolet light.

It has been more than 40 years since the first lanthanide lasers were reported [82]. A wide variety of lanthanide lasers and amplifiers have been investigated.  $\text{Nd}^{\text{III}}$ ,  $\text{Ho}^{\text{III}}$ ,  $\text{Er}^{\text{III}}$  and  $\text{Yb}^{\text{III}}$  have special interest because they emit in the near infrared spectral range which makes them very useful in the design of lasers (especially  $\text{Nd}^{\text{III}}$  with its line at  $1.06 \mu\text{m}$ ), amplification

and telecommunication devices [83]. Lanthanide ions are very stable under laser action because the luminescence originates from internal transitions that do not involve chemical bonds. Another reason is the long-lived excited state of the ions that facilitate laser action. In addition, by using various ions, the whole spectral range from UV to IR can be covered almost completely for laser emission.  $\text{Nd}^{3+}$  ions are widely used in active media for high power solid-state lasers, such as Yttrium Aluminum Garnet doped with  $\text{Nd}^{3+}$  (Nd:YAG). In this laser the lowest threshold occurs at 1064 nm, but laser effect can also be obtained at 946, 1319 and 1839 nm [84].

In optical telecommunications, lanthanide ions are of high importance because a number of ions display optical transitions at telecommunication wavelengths in the near-infrared (NIR) region [85]. Therefore, they are employed in optical amplifiers in order to compensate for intensity losses, caused by for instance absorption or scattering in long optical fibers. In particular,  $\text{Er}^{3+}$  doped fibers amplifiers (EDFA) operating at 1.55  $\mu\text{m}$  has reached a stage of practical applications for optical telecommunications. In the field of solid state light-emitting devices, an increasing interest is devoted to semiconductors activated with lanthanide ions [86-89]. Thulium is a blue emitter and is used in electroluminescent devices [90]. Erbium doped silicon nano-structures are investigated for 1.54  $\mu\text{m}$  laser emission [86-87], while organic-lanthanide ion complexes are studied as promising materials for new electroluminescent devices or amplifiers [82, 88-89]. Apart from these applications, lanthanides are used to regulate and to control the rods of the nuclear reactor. This is due to their ability to absorb neutrons. They have also been used as shielding materials, and as structural components in reactors. Some lanthanides have unusual magnetic properties [91]. Another important field of application of lanthanide doped materials concerns the realization of scintillators for high-energy radiation detectors for medical, industrial and scientific purposes. Scintillators absorb the energy from the high-energy particle, or radiation, and convert it into visible light that is detected by means of photomultiplier tubes or photodiodes [92]. The number of applications of rare earth doped optical materials constantly increases, together with the continuous improvement in the knowledge of their physical properties.

### **A-1.9.2: Porphyrins and phthalocyanine complexes:**

Among several new organic molecules, porphyrins and phthalocyanines have deserved special attention, not only because of their potential usefulness for nonlinear optical applications and photonic devices [93], but for other applications such as molecular thermometers [94], light-emitting diodes [95-96], magnets [97], solar cells [98-99], photodynamic therapy [100], and passive optical limiters [101-102]. Their applications as drugs are commonly used in photodynamic therapy [103-104] for cancer treatment and bacterial reduction.

Phthalocyanines have been widely used in industry for more than 50 years as pigments and dyes because of their high thermal and chemical stability. Phthalocyanines also draw interest as materials for optical recording media, light absorption, electric conduction, photoconduction, energy conversion, electrode, and catalysis (105-109). Phthalocyanines have highly polarizable  $\pi$ -systems, and therefore display very good NLO properties, second order ions when unsymmetrically substituted, and of course large third-order susceptibilities [110-111]. Phthalocyanines compounds with various substituted groups, such as alkyl, alkoxy, or alkoxymethyl chains have been synthesized [112-116]. When substituents are placed on a Phthalocyanines ring, not only the solubility of the compound increases, but supramolecular organization can be achieved too. To further enhance the nonlinear optical properties, one can increase the number of conjugated electrons by adding peripheral rings or by constructing sandwich compounds, known as bis-phthalocyanines, where two phthalocyanine rings are coordinated to a central metal ion. A substantial number of sandwich type metal complexes with phthalocyaninato ligands have been synthesized (117-125). Owing to their excellent environmental stability, these complexes display unique physical, spectroscopic, electrochemical and optical properties that can be tuned by varying the central metal ion or a peripheral side-group. Bis-phthalocyanines are promising for the potential use in optical-limiting devices to protect sensors and eyes from intense light pulses [126-127].

Lanthanide phthalocyanine (Pc) sandwich compounds with the formula  $\text{Ln}(\text{Pc})_2$  have been known for over twenty-five years [128]. Much attention has been paid to bis(phthalocyaninato) lanthanide complexes, especially the lutetium (III) derivative.  $\text{Lu}(\text{Pc})_2$ ,

where Pc represents the dianion of phthalocyanine, has been shown to undergo up to seven redox processes, five of them having been characterized with respect to the color changes, like  $[\text{Lu}(\text{Pc})_2]^+$  orange,  $\text{Lu}(\text{Pc})_2$  green,  $[\text{Lu}(\text{Pc})_2]^-$  light blue,  $[\text{Lu}(\text{Pc})_2]^{2-}$  dark blue, and  $[\text{Lu}(\text{Pc})_2]^{3-}$  violet [129]. For  $\text{Lu}(\text{Pc})_2$ , the lanthanide ion has a formal oxidation state of +3, with one of the phthalocyanine ligands having a charge of -2, and the second phthalocyanine ligand being considered to be a singly oxidized radical with a charge of -1. So far, it is not clear whether the unpaired spin present in this complex is localized on one phthalocyanine ring or delocalized over both rings. However, the intrinsic semiconducting properties found recently for the  $\text{Lu}(\text{Pc})_2$  derivative are probably more in favor of a delocalized system (130). Other lanthanide sandwich compounds have essentially the same structure in which the two phthalocyaninato rings are rotated approximately  $45^\circ$  with respect to one another [131-134].

## **References**

- [1] Prasad, P. N., Reinhardt, B. A., Chem. Mater., 1990, 2, 660.
- [2] Boyd, R. W., Nonlinear Optics: Academic Press, New York 1992.
- [3] Shen, Y. R., The Principles of Nonlinear Optics: Wiley, New York, 1984.
- [4] Bloembergen, N., Nonlinear Optics: W. A. Benjamin, New York, 1965.
- [5] Zyss, J., J. Mol. Electron., 1985, 1, 25.
- [6] Kelderman, E., "Molecules for second order non-linear optics", Ph.D thesis, Utrecht (NL), 1993.
- [7] Terhune, P. R., Maker, W. D., and Savage, C. M., Physical Review Letters, 1965, 14 (17), 681-684.
- [8] Pizzi, R. A., Michael Faraday, Chemist, Chemistry chronicles, 2004, 39-42.
- [9] Garetz, B. A., "The Kerr effect," Optics News 12 (10), 28-31, 1986.
- [10] Gross, E., Nature, 1930, 126 (201), 400.
- [11] Raman, C. V., "A Classical Derivation of the Compton Effect," Indian Journal of Physics 3 (1928), 357-369.
- [12] Woodbury, E. J., and Ng, W. K., Proc. Institute of Radio Engineers (IRE), 1962, 50, 2367.
- [13] Eckhardt, G., Hellwarth, R. W., McClung, F. J., Schwarz, S. E., Weiner, D., and Woodbury, E. J., Physical Review Letters, 1962, 9 (11), 455.
- [14] Bloembergen, N., American Journal of Physics, 1967, 35, 11, 989.
- [15] Kaiser, W., and Maier, M., 1972, In: Arecchi, F.T., Schulz-DuBois, (Eds)., Laser Handbook, North-Holland.
- [16] Penzkofer, A., Laubereau, A., Kaiser, W., Prog. Quantum Electron, 1979, 6, 55.
- [17] Raymer, M.G., Walmsley, I. A., 1990, In: Wolf, E.(Ed.), Progress in Optics, 28, North-Holland, Amsterdam.
- [18] Chiao, R. Y., Townes, C. H., and Stoicheff, B. P., Physics Review Letters, 1964, 12 (21), 592-595.
- [19] Bloembergen N., and Lallemand, P., Physical Review Letters, 1966, 16 (3), 81-84.
- [20] Chao R. Y., and Godine, J., Physical Review, 1966, 185, 430.

- [21] Cho, C. W., Foltz, N. D., Rank, D. H., and Wiggins, T. A., *Physical Review Letters*, 1967, 18, 107.
- [22] Akhmanov, S. A., Khokhlov R. V., *Problems of Nonlinear Optics* (VINITI, Moscow 1964) Engl. transl. New York, Gordon & Breach, 1972.
- [23] Williams, D. J. *Angew. Chem. Int. Ed. Engl.*, 1984, 23, 690.
- [24] Yariv, A., *Quantum Electronics*: Wiley, 1975, New York, 419.
- [25] Bass, M., Franken, P. A., Ward, J. F., Weinreich G., *Phys. Rev. Lett.*, 1962, 9, 446–448.
- [26] (a) Nalwa, H. S., Miyata Seizō, “*Nonlinear Optics of Organic Molecules and Polymers*” 1997, CRC Press. (b) Auerhammer, J. M., and Eliel, E. R., 1996, *Opt. Lett.*, **21** (11), 773. (c) Colvin, V. L., Schlamp, M.C., Alivisatos, A.P., *Nature*, 1994, 370, 354 (d) Zyss, J., Chemla, D. S., and Nicoud, J. F., *J. Chem. Phys.*, 1981, 74, 4800. (e) Zyss, J., Nicoud, J. F., Coquillary, M., *J. Chem. Phys.*, 1984, 81, 4160. (f) Marder, S.R., Perry, J.W., Schaeffer, W.P., *Science*, 245, 1989. 626. (g) Becker, R. A., *MRS Bulletin* 13, 21, 1988. (h) Zemike, F., and Midwinter, J. E., *Applied Nonlinear Optics*, Wiley, New York, 1973.
- [27] Fan, Y. X., Eckhardt, R. C., Byer, R. L., Route, R. K., Fiegelson, R. S., *Appl. phys. lett.*, 1984, 45, 313.
- [28] Blau, W., *Phys. Technol.*, 1987, 18, 250.
- [29] Chemla, D. S., Zyss, J., Eds. *Nonlinear Optical Properties of Organic Molecules and Crystals*: Academic Press, New York, 1987, vols 1 and 2.
- [30] Di Bella, S., *Chemical Society Reviews*, 2001, 30 (6), 355-366.
- [31] Dehu, C., Meyers, F., Bredas, J. L., *J. Amer. Chem. Soc.*, 1993, 115, 6198.
- [32] Williams, D. J., *Thin Solid Films*, 1992, 216,117.
- [33] Carters, G., Zyss, J., Eds. *Nonlinear Optical Processes in Organic Materials* *J. Opt. Soc. Am. B*, 1987, 4.
- [34] Long, N. J., *Angew.Chem. Int. Ed. Engl.*, 1995, 34, 21.
- [35] Alain, V., Thouin, L., Blanchard-Desce, M., Gubler, U., Bosshard, C., Günter, P., Muller, J., Fort, A., Barzoukas, M., *Advanced Materials*, 1999, 11, 14, 1210-1214.
- [36] Bozec, L. H., Renouard, T., Bourgault, M., Dhenaut, C., Brasselet, S., Ledoux, I., Zyss, J., *Synthetic Metals*, 2001, 124 (1), 185-189.

- [37] Powell, C. E., Humphrey, M. G., *Coordination Chemistry Reviews*, 2004, 248, 725–756.
- [38] Oudar, J. L., and Chemla D. S., *The Journal of Chemical Physics*, 1977, 66 (6), 2664-2668.
- [39] Zyss J., *J. Chem. Phys.*, 1993, 98, 6583-6599.
- [40] Maury, O., and Bozec, H. L, *Accounts of Chemical Research*, 2005, 38 (9), 691-704.
- [41] Maury, O., Viau, L., Sénéchal, K., Corre, B., Guégan, J.-P., Renouard, T., Ledoux, I., Zyss, J., Bozec, H. L., *Chem. Eur.*, 2004, 10, 4454.
- [42] Brunel, J., I. Ledoux, Zyss, J., and Blanchard-Desce, M., *Chemical Communications*, 2001, 10, 923-924.
- [43] Thalladi, V. R., S. Brasselet, et al., *J. Am. Chem. Soc.*, 1998, 120 (11), 2563-2577.
- [44] Ledoux, I., J. Zyss, Siegel, J.S., Brienne, J., Lehn J.-M., *Chemical Physics Letters*, 1990, 172 (6), 440-444.
- [45] Ledoux, I. and Zyss J., *Comptes Rendus Physique*, 2002, 3 (4), 407-427.
- [46] Zyss, J., Van, T. C., and Ledoux, I., *Chemical Physics*, 1993, 177 (1), 281-296.
- [47] Blanchard-Desce, M., Baudin, J.-B., Jullien, Ludovic., Lorne, R., Ruel, O., Brasselet, S., and Zyss, J., *Optical Materials*, 1999, 12 (2-3), 333-338.
- [48] Cherioux, F., H. Maillotte, Audebert, P., Zyss J., *Chemical Communications-Royal Society of Chemistry*, 1999, 20, 2083-2084.
- [49] Dhenaut, C., I. Ledoux, Samuel, I.D.W., Zyss, Manuel, B., and Bozec, H. L, *Nature*, 1995, 374 (6520), 339-342.
- [50] Sastre, A., Torres, T., Díaz-García, M.A., Agulló-López, F., Dhenaut, C., Brasselet, S., Ledoux, I., and Zyss, J., *J. Am. Chem. Soc.*, 1996, 118 (11), 2746-2747.
- [51] Renouard, T., H. Le Bozec, S., Ledoux, I., and Zyss, J., *Chemical Communications*, 1999, (10), 871-872.
- [52] Zyss, J., I. Ledoux, Volkov, Sergei., Chernyak, Vladimir., Mukamel, Shaul., Bartholomew, G. P., and Bazan, G. C., *J. Am. Chem. Soc.*, 2000, 122 (48), 11956-11962.
- [53] Lu, D., Chen, G., Perry, J. W., Goddard, W. A. III, *J. Am. Chem. Soc.*, 1994, 116 (23), 10679-10685.
- [54] Oudar, J. L., Chemla, D. S., *Opt. Commun.*, 1975, 13, 164.
- [55] Zyss, J., *J. Chem. Phys.* 1979, 70, 3333

- [56] Zyss, J., *J. Chem. Phys.*, 1979, 71, 909.
- [57] Joffre, M., Yaron, D., Silbey, R., and Zyss, J., *J. Chem. Phys.*, 1992, 97, 5607-5615.
- [58] Miller, C. K., and Ward, J. F., *Phys. Rev. A*, 1977, 16, 1179.
- [59] Buckingham, A. D., Orr, B. J., *Q. Rev. Chem. Soc.*, 1967, 21, 195.
- [60] Applequist, J., *J. Chem. Phys.*, 1985, 83, 809.
- [61] Levine, B. F., and Bethea, G. C., *Appl. Phys. Lett.*, 1975, 63, 2666.
- [62] Kajzar, F., Messier, J., *Phys. Rev. A*, 1985, 32, 2352.
- [63] Oudar, J. L., *J. Chem. Phys.*, 1977, 67, 446.
- [64] Dulcic, A. and Sauteret, C., *J. Chem. Phys.*, 1978, 69, 3453.
- [65] Orr, B.J., and Ward J.F., *Molecular Physics*, 1971, 20 (3), 513-526.
- [66] Kanis, D. R., Ratner, M. A., Marks, T. J., *Chem. Rev.*, 1994, 94, 195.
- [67] Dürr, H., Bouas-Laurent, H., Elsevier, Amsterdam, 1990.
- [68] Irie, M., *Chem. Rev.*, 2000, 100, 1683.
- [69] Delaire, J.A., Nakatani, K., *Chem. Rev.*, 2000, 100, 1817.
- [70] Kawata, S., Kawata, Y., *Chem. Rev.*, 2000, 100, 1777.
- [71] Guerchais, V., Ordonneau, L., Bozec, H. L. *Coordination Chemistry Reviews*, 2010, 254, 2533–2545.
- [72] Morimoto, M., Irie, M., *Chem. Commun.*, 2005, 3895.
- [73] Kobatake, S., Takami, S., Muto, H., Ishikawa, T., Irie, M., *Nature*, 2007, 446, 778.
- [74] Tian, H., Yang, S., *Chem. Soc. Rev.*, 2004, 33, 85.
- [75] Wybourne B. G., *Spectroscopic Properties of Rare Earths*, Interscience Publishing, New York 1965.
- [76] Chen, R. T., *Optics and Laser Tech.*, 1993, 25 (6), 347-365.
- [77] Werts, M. H. V., Hofstraat, J. W., Geurts, F. A. J., Verhoeve, J. W., *Chem. Phys. Lett.*, 1997, 276,196-201.
- [78] Becquerel, J., *Phys. Z.* 1908, 8, 632.
- [79] Ermolaev, V. L., Sveshnikov, E. B., *Russ. Chem. Rev.*, 1994, 63, 905.

- [80] Bünzli, J.-C. G., and Piguet, C., *Chem. Soc. Rev.*, 2005, 34, 1048–1077.
- [81] Cotton S., *Lanthanides and Actinides chemistry*, John Wiley and Sons Ltd., West Sussex, England, 2006.
- [82] Kuriki, K., and Koike, Y., *Chem. Rev.* 2002, 102, 2347-2356
- [83] Stouwdam, J. W., Hebbink, G. A., Huskens J., and Van Veggel, F. C. J. M., *Chem. Mater.*, 2003, 15, 4604.
- [84] Koechner, W., *Solid-State Laser Engineering* 4th edition, Springer
- [85] Weber, J. K. R., Felten, J. J., Cho, B., Nordine, P. C. *Nature*, 1998, 395, 769.
- [86] Hryciw, A., Blois, C., Meldrum, A., Clement, T., DeCorby, R., Quan Li , *Optical Materials*, 2006, 28 873–878.
- [87] Stepikhova, M.V., Krasil'nikova, L.V., Krasil'nik , Z.F., Shengurov, V.G., Chalkov , V.Yu., Zhigunov, D.M., Shalygina, O.A., Timoshenko , V.Yu., *Optical Materials*, 2006, 28, 893–896.
- [88] Edwards, A., Claude, C., Sokolik, I., Chu T. Y., and Okamoto, Y., Dorsinville, R., *J. Appl. Phys.*, 1997, 82 (4), 1841-1846.
- [89] Chen, Z., Deng, Z., Shi, Y. Xu, Y., Xiao, J., Zhang, Y., Wang, R., *Journal of Luminescence*, 2007, 122–123, 671–673.
- [90] Kido, J., and Okamoto, Y., *Chem. Rev.*, 2002, 102, 2357.
- [91] Emsley, J., *The Elements*. 3rd Ed. New York, Oxford University Press, Inc., 1998.
- [92] Krane, K. S., *Introductory Nuclear Physics*, Wiley 1988.
- [93] Boni, L. D., Gaffo, L., Misoguti, L., Mendonc, C.R., *Chemical Physics Letters*, 2006, 419, 417–420.
- [94] Lupton, J.M., *Appl. Phys. Lett.*, 2002, 81, 2002, 2478.
- [95] Chang, S.C., He, G., Chen, F.C., Guo, T.F., Yang, Y., *Appl. Phys. Lett.*, 2001, 79, 2088.
- [96] Kojima, H., *J. Electrochem. Soc.*, 1997, 144, 3628.
- [97] Rittenberg, D.K., Sugiyra, K.I., Sakata, Y., Mikami, S., Epstein, A.J., Miller, J.S., *Adv. Mater.*, 2000, 12, 126.
- [98] Takahashi, K., Kuraya, N., Yamaguchi, T., Komura, T., Murata, K., *Sol. Energy Mater. Sol. Cell*, 2000, 61, 403.

- [99] Weohrle, D., Kreienhoop, L., Schnurpfeil, G., Elbe J, J., Tennigkeit, B., Hiller, S., Schlettwein, D., *J. Mater. Chem.*, 1995, 5, 1819.
- [100] Spikes, J.D., *Photochem. Photobiol.*, 1986, 43, 691.
- [101] Neto, N.M.B., Correa, D.S., Dos Santos, D.S., Misoguti, L., Oliveira, O.N., Zilio, S.C., Mendonca, C.R. ,*Mod. Phys. Lett. B*, 2003, 17, 83.
- [102] Flaherty, S.M. O, Hold, S.V., Cook, M.J., Torres, T., Chen, Y., Hanack, M., Blau, W., J., *Adv. Mater.*, 2003, 15, 19.
- [103] Dougherty, T.J., Henderson, B.W., Schwartz, S., Winkelman, J.W., Lipson, R.L., Henderson, B.W., Dougherty T.J., (Eds.), *Historical Perspective. Photodynamic Therapy, Basic Principles and Clinical Application*, New York, 1992, 1–18.
- [104] Dougherty, T.J., Kaufman, J.E., Goldfarb, A., Weishaupt, K.R., Boyle, D., Mittleman, A., *Cancer Res.*, 1978, 38, 2628.
- [105] Neto, N.M.B., Andrade, A.A., De Boni, L., Misoguti, L., Zilio, S.C., Mendonca, C.R., *Appl. Phys. B*, 2004, 79, 751.
- [106] Leznof, C. C., Lever, A. B. P., Eds. *Phthalocyanines, Properties and Applications*; VCH, Weinheim, Germany, 1996.
- [107] McKeown, N. B., *Phthalocyanine Materials: Synthesis, Structure, Function*; Cambridge University Press, Cambridge, U.K., 1998.
- [108] Simon, J., Bassoul, P., *Design of Molecular Materials: Supramolecular Engineering*; Wiley-VCH: Weinheim, Germany, 2000.
- [109] Gurek, A. G., Basova, T., Luneau, D., Lebrun, C., Kol'tsov, E., Hassan, A. K., Ahsen, V., *Inorganic Chemistry*, 2006, 45, (4), 1667.
- [110] Shirk, J.S., Lindle, J.R., Bartoli, F.J., Boyle, M.E., *J. Phys. Chem.*, 1992, 96, 1992, 5847.
- [111] Clarkson, G. J., McKeown, N. B., Treacher, K. E., *J. Chem. Soc., Perkin Trans.* 1995, 1, 1817.
- [112] Pol, V. d., Neelman, J. F., Zwikker, E., Nolte, J. W., Drenth, R. J. M., *W. Trav. Chim. Pays-Bas*, 1988, 107, 615.
- [113] Guillon, D., Skoulios, A., Piechocki, C., Simon, J., Weber, P. *Mol. Cryst. Liq. Cryst.*, 1983, 100, 275.

- [114] Piechocki, C., Simon, J., Andre', J. J., Guillon, D., Petit, P., Skoulios, A., Weber, P. *Chem. Phys. Lett.*, 1985, 122, 124.
- [115] Ohta, K., Jacquemin, L., Sirlin, C., Bosio, L., Simon, J., *New J. Chem.*, 1988, 12, 751.
- [116] Cian, A. D., Moussavi, M., Fischer, J., and Weiss, R., *Inorg. Chem.*, 1985, 24, 3162.
- [117] Guillard, R., Dormond, A., Belkalem, M., Anderson, J. E., Liu Y. H., and Kadish, K. M., *Inorg. Chem.*, 1987, 26, 1410.
- [118] Ovchinnikova, N. A., Tomilova, L. G., Seregina, N. B., Minin V. V., and Luk'yanets, E. A., *Zh. Obshch. Khim.*, 1992, 62, 1631.
- [119] Kadish, K.M., Moninot, G., Hu, Y., Dubois, D., Ibnlfassi, A., Barbe J.-M., and Guillard, R., *J. Am. Chem. Soc.*, 1993, 115, 8153,
- [120] Iwase, A., Harnood C., and Kameda, Y., *J. Alloys Compd.*, 1993, 192, 280.
- [121] Jiang, J., Xie, J., Choi, M. T. M., Yan, Y., Sun, S. and Ng, D. K. P., *J. Porphyrins. Phthalocyanines.*, 1999, 3, 322.
- [122] Merey S., and Bekaroglu, O., *J. Chem. Soc., Dalton Trans.*, 1999, 4503.
- [123] Jiang, J., Liu, W., Poon, K.-W., Du, D., Arnold D. P., and Ng, D. K. P., *Eur. J. Inorg. Chem.*, 2000, 205.
- [124] Abdurrahmanoglu, S., Ozkaya, A. R., Buluta M., and Bekaroglu, O., *Dalton Trans.*, 2004, 4022–4029
- [125] Wei, T.H., Hagan, D., Sence, J M.J., Van Stryland, E.W., Perry, J.W., Coulter, D.R., *Appl. Phys. B*, 1992, 54, 46.
- [126] Mendonc, C. R., Gaffo, L., Misoguti, L., Moreira, W.C., Oliveira Jr., O.N., and Zilio S.C., *Chemical Physics Letters*, 2000, 323, 300–304.
- [127] Moskalev, P. N., and Kirin, I. S., *Russ. J. Znorg. Chem.*, 1970, 15, 7.
- [128] Kadish, K. M., Nakanishi, T., Gürek, A., Ahsen, V., and Yilmaz I., *J. Phys. Chem. B*, 2001, 105, 9817-9821.
- [129] Moussavi, M., Cian, A. D., Fischer, J., and Weiss, R., *Inorg. Chem.* 1988, 27, 1287-1291.
- [130] Decian, A., Moussavi, M., Fischer, J. and Weiss, R., *Znorg. Chem.*, 1985, 24, 3162.
- [131] Gieren A., and Hoppe, W., *Chem. Commun.*, 1971, 413.

[132] Kasuga, K., Tsutsui, M., Petterson, R. C., Tatsumi, K., Van Opdenbosch, N., Pepe G., and Meyer, E. F. Jr., *J. Am. Chem. Soc.*, 1980, 102, 4826.

[133] Trojan, K. L., Kendall, J. L., Kepler, K. D., and Hatfield, W. E., *Inorganica Chimica Acta*, 1992, 198-200, 795-803.

[134] Gürek, A. G., Ahsen, V., Luneau, D., and Pecaut, J., *Inorg. Chem.*, 2001, 40, 4793-4797.

## Part B: Gold nanoparticles (AuNPs) for nonlinear optics

### B-1.10: Introduction

Metal nano-objects like copper, silver and gold are of great interest in the field of nanosciences and their importance for science and technology is highly increased over the past decades. Particles with dimensions on the order of a billionth of a meter are known as nanoparticles. Their diameters are range from 1 to 100 nanometers.

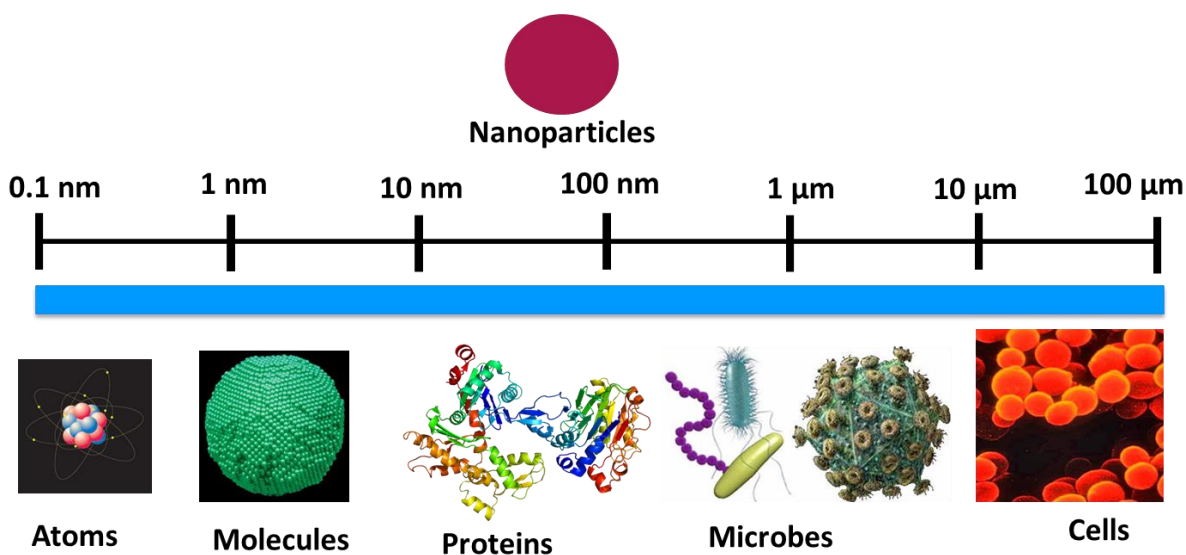


*Figure 1.11: Sizes of nanoparticles in comparison with other biological entities.*

When dealing with such small structures, the ratio between surface (interface) and inner atoms becomes significant and these particles can be and treated as an isolated group of atoms or molecules (Figure 1.11). This means that surface atoms with partial coordination strongly influence the physical and chemical behavior of the nanomaterials, their properties differing from those of molecules and bulk solids as well, and being sometimes complementary with them. The huge development of nanoparticle studies in the last years is due to the improvement of the characterization techniques and synthesis methods at the nanoscale. Metallic nanoparticles have raised a great interest in the scientific community because of their tremendous physical, chemical and attractive linear and nonlinear [1-2] optical properties arising from the collective oscillations of their conduction band electrons or surface plasmons [3]. Because of their interesting properties, these NPs have been shown

to display applications in various fields, from photonic and electronic devices to catalysis [4], medicine [5], and imaging [6-7]. Furthermore, AuNPs show high chemical stability and photostability, and are nontoxic for living organisms. Their physiochemical stability, bright colors and biocompatibility explain why indications of AuNPs utilization are dated back to the 5<sup>th</sup> century B.C. in Egypt and China.

### **B-1.11: Historical Background**

The fascinating colors of metal colloids have attracted the attention of people for a long time. Gold liquid solutions were first mentioned by Egyptians and Chinese in 5<sup>th</sup> century BC. For instance, the ancient Egyptians and Romans used metal colloids to color glass of intense shade of yellow, red, or mauve, depending on the concentration of gold [8]. Figure 1.12 shows one of the prominent examples; the “Lycurgus Cup” is dated 4<sup>th</sup> century AD and found across the Roman Empire [9]. It is made of dichroic glass which changes color when held up to the light. The opaque green cup turns to a glowing translucent red when light is shone through it. The glass contains tiny amounts of colloidal gold and silver, which are responsible for these unusual optical properties. Another example of gold was used in the ruby colored glass window in Milan Cathedral, Italy, made by Niccolo da Varallo between 1480 and 1486, illustrating the birth of St. Eligius, patron saint of goldsmiths the red color is due to colloidal gold [10].



Figure 1.12: (a) Stained glasses (b) The Lycurgus Cup, British Museum 1958 (c) Stained-glass windows in Milan Cathedral, Italy.

In the 16th century the glass-coloring process was refined by Andreus Cassius and Johann Kunchel. In 1842, John Herschel invented a photographic process called Chrysotype (from the Greek word for gold) that used colloidal gold to record images on paper. Gold colloids have also been used in medicine because of their therapeutic properties [11]. Michael Faraday was the first one who scientifically investigated their synthesis and unique optical properties (Figure 1.13).

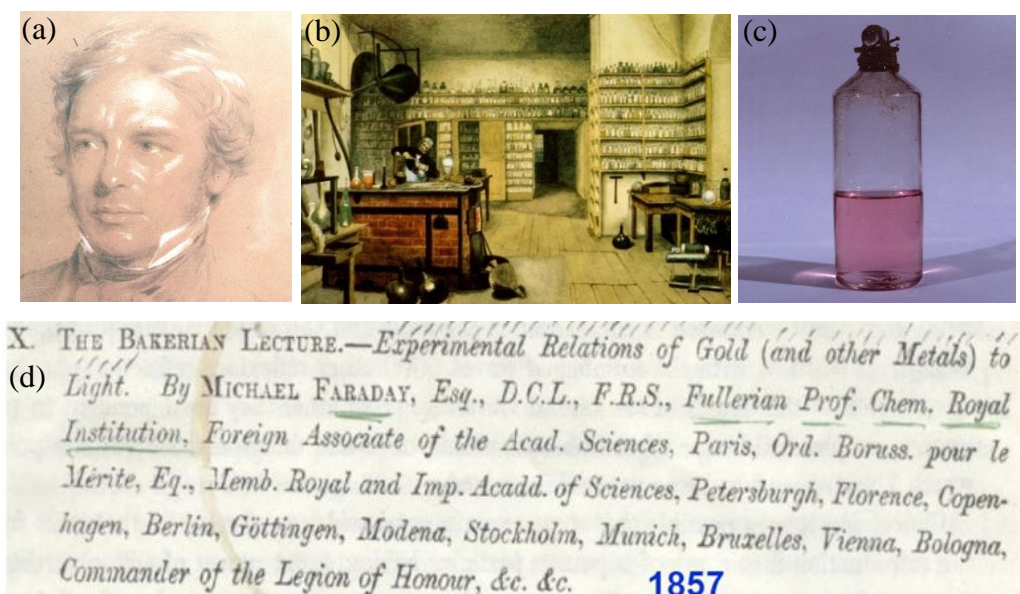


Figure 1.13 (a) Portrait of Michael Faraday. (b) Michael Faraday in his lab, by Harriet Moore (Wikipedia) (c) Reproduced by Courtesy of the Royal Institution of Great Britain Faraday's colloidal ruby gold. (d) First publication of gold Nanoparticles by reduction of gold chloride with white phosphorus

In 1857, he reported the synthesis of deep-red solutions of colloidal gold by reduction of chloroaurate ( $\text{AuCl}_4^-$ ) by phosphorus in water, which is known to have been inspired by “Paracelsus’ procedure, reported in 16th century about the preparation of “*Aurum Potabile*. Faraday also discovered that the optical properties of colloids are different from those of the corresponding bulk metal. This was probably the first reported observation of the effects of quantum size, and might be considered to be the birth of nanoscience [12]. To date, Faraday original samples are still preserved and on display at the Faraday Museum in London. Even

before the “actual” discovery by Michael Faraday, colloidal gold was commonly used to stain glass to provide a ruby-like color [13].

Around the turn of the twentieth century, the field of colloidal chemistry was undergoing tremendous growth due to the pioneering contributions from Ostwald and Mie and the Nobel Prize winners Svedberg and Zsigmondy. Other physical and chemical synthetic methods for colloidal metal nanoparticles have been developed in the early 20<sup>th</sup> century, until the fundamental work of Turkevich in 1951. He reported an easy method for AuNPs synthesis where citrate plays not only the role of reducing agent but also acts as a stabilizing agent [13-14]. Since the first publications of Haruta [15-16] on the catalytic properties of small AuNPs and the breakthroughs reported by Schmid [17-18] and Brust et al. [19-20], the number of publications related to gold nanoparticles has considerably increased.

### **B-1.12: Synthesis**

In the synthesis of metal nanoparticles, controlling the shape and size is currently one of the most important and challenging tasks. Therefore, a great attention has been paid to develop synthetic routes for producing metal NPs in tailored size and shape regimes [21-23]. Many techniques and synthetic methods have been developed from Michael Faraday until now in order to fulfill the demand of different forms of nanoparticles for various applications. The different shapes of nanoparticles such as rod, tubes, cubes, disks, wires, tubes, triangular prisms and so on strongly influence the physical, chemical, optical, electronic, and catalytic properties of the materials that can be studied and correlated with modern quantum theory [24].

### **Bottom up and bottom down method:**

Two basic strategies used to obtain NPs are “top-down” and “bottom-up” methods as represented in Figure 1.14 [22, 25-26]. The first method (“top-down”) is defined as the division of a massive solid into smaller portions. This method includes milling or attrition, to the mechanical crushing of source material using a milling process, chemical methods, and volatilization of a solid followed by condensation of the volatilized components. This method is applied to produce metallic and ceramic nanomaterials. For metallic nanoparticles, for

example, traditional source materials (such as metal oxides) are pulverized using high-energy ball mills.

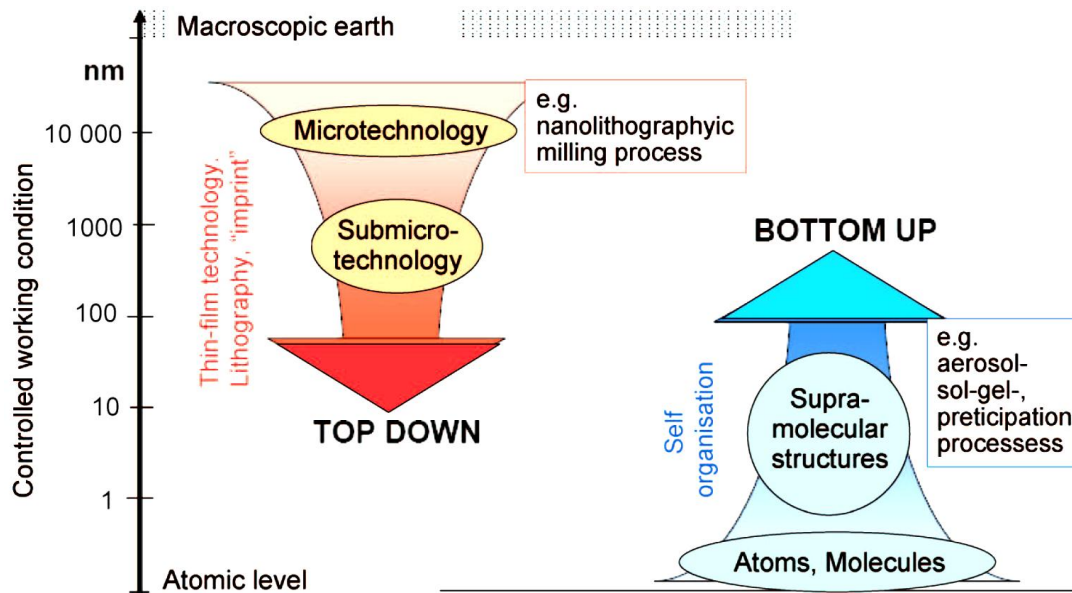


Figure 1.14: Methods of nanoparticle production: top-down and bottom-up [164].

The other common examples of top down techniques are laser ablation, grinding and lithography. Photolithography and Electron Beam Lithography (EBL) are the common examples of lithographic techniques. Photolithography is an inexpensive synthetic method to synthesize nanoparticles but its solution is limited by diffraction. Electron beam techniques have considerable potential for formation of small features as compared to photolithography techniques [24]. Much attention has been paid to this method because of its high resolution and high monodispersity but on the other hand it suffers from need to remove large amounts of material and its resolution is also limited by electron scattering phenomena [22, 27].

**B-1.13: Deposition methods: Electron scattering phenomena with material**

In deposition techniques, magnetron sputtering is a vacuum process used to deposit very thin films on substrates. It is performed by applying a high voltage across a low-pressure gas to create plasma.

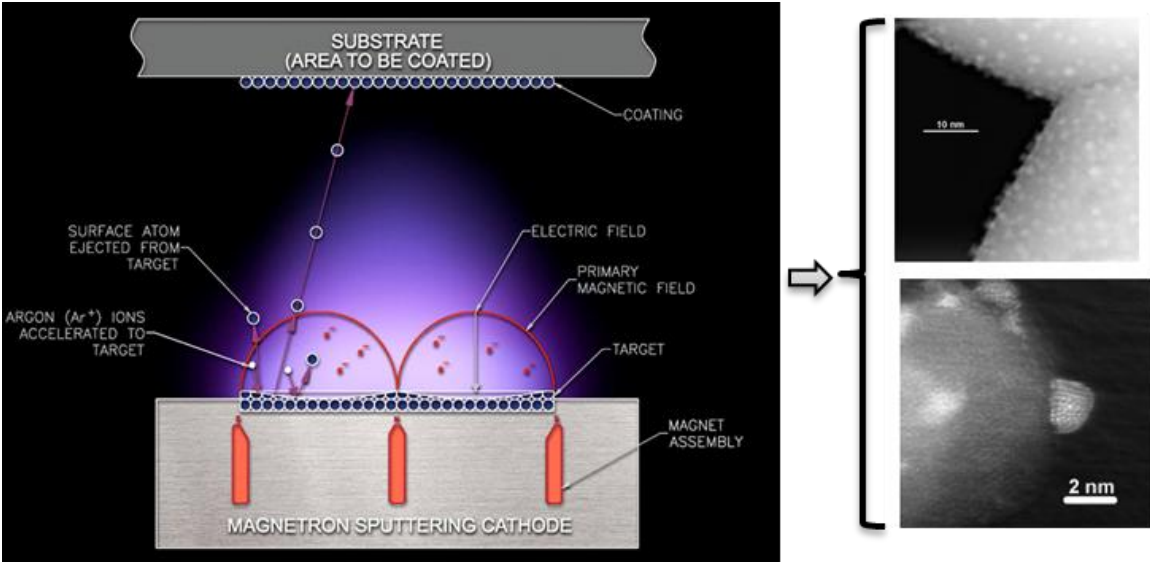


Figure 1.15: Magnetron sputtering technique [28].

During sputtering, energized plasma ions hit a ‘target’ which is composed of the desired coating material (Au of high purity). Atoms from that target are dislodged by the impact of the ion and ejected from the surface with enough energy to travel to and bond with another substrate [Figure 1.15].

In the laser vaporization method, the material is removed from a solid or liquid surface by irradiating it with a laser beam. At low laser flux, the material is heated by the absorbed laser energy and evaporates or sublimates. At high laser flux, the material is typically converted into plasma. Usually, laser ablation refers to material removal with a pulsed laser, but it is also possible to ablate material with a continuous wave laser beam if the laser intensity is high enough. A target (high purity Au) is vaporized by a laser and neutral clusters are deposited on the substrate. Laser pulses can vary over a very wide range of durations, from millisecond to femtosecond; and fluxes can be precisely controlled [Figure 1.16]. This makes laser ablation a very valuable method for both research and industrial applications.

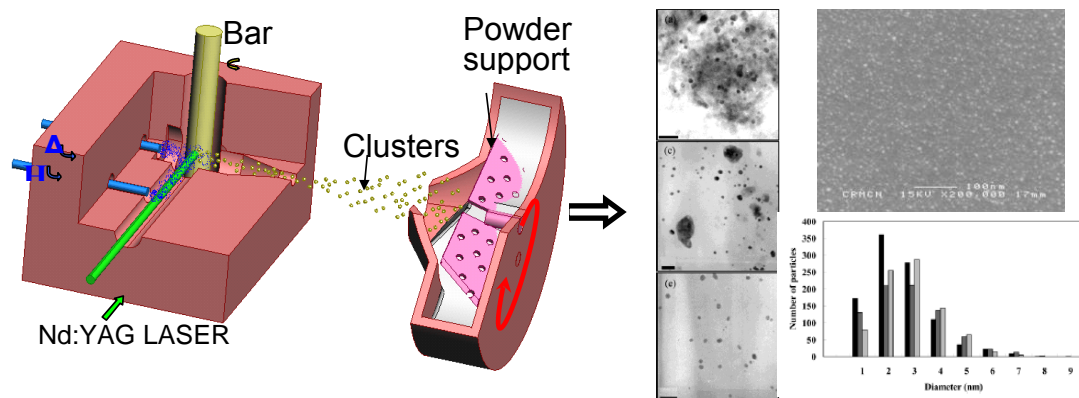


Figure 1.16: Laser vaporization technique (deposition on divided substrates and deposition on flat supports) [29]

### **B-1.14: Solution growth methods**

In “Bottom-up methods” the atoms (produced from reduction of ions) are assembled to generate nanostructures. In order to restrict the process to nanoscale objects, it usually uses an agent to stop growth of the particle at the nanoscale [30]. This method produces selected, more complex structures elaborated from atoms to molecules, with a control of size and shape. It includes aerosol processes, precipitation reactions and sol gel processes. This method is more popular in the synthesis of NPs as compared to “Top-down methods” [31]. Gas phase processes are among the most common industrial-scale technologies for producing nanomaterials in powder or film forms. Metal nanoparticles are obtained from the gas phase by producing a vapor of the product material using chemical or physical means [32-37]. The wet-chemical synthesis of nanomaterials typically takes place at lower temperatures than gas phase synthesis. The most important liquid phase processes in nanomaterial production are precipitation, sol-gel processes and hydrothermal synthesis.

The other chemical synthesis method includes templating, photochemistry, seeding, thermal, sonochemical, and electrochemistry reduction techniques [22, 24, 38-53]. Among such procedures, those involving an aqueous medium are the most convenient ones to develop because of water’s ability to solubilize a variety of ions and stabilizing molecules. On the other hand, nanoparticles prepared in organic media are interesting for applications to catalytic processes and for further surface modifications with organic functional groups to fine by tune their properties [54-57]. The formation of nanoparticles in aqueous media

involves the reduction of a metal precursor salt by a suitable reducing agent such as sodium borohydride, ascorbic acid, formaldehyde and hydrazine. The reduction of metal precursor salt can also be done by radiations such as ultraviolet, microwave, and ionizing radiations like, gamma, X-rays or electron beams [24].

#### **B-1.14.1: Turkevich Method**

It is well-known that chemical reduction of gold salts produces spherical gold nanoparticles [58-59]. Turkevich proposed a synthetic method in which spherical gold nanoparticles are synthesized through citrate reduction. Citrate plays a double role as a reducing and stabilizing agent. An aqueous solution of Au<sup>III</sup> (around 10<sup>-3</sup> M) is heated until ebullition. A citrate solution is added (1%). The mixture is stirred under heating. After a few minutes, the color becomes grey then red corresponding to the formation of AuNPs of increasing sizes.

Current research is focusing on one-dimensional NPs such as nanorods (NRs) and nanowires because their morphological anisotropy are related to very complex physical properties and self-assembly behaviors as compared to spherical NPs, and can be particularly attractive for various optoelectronic devices [60]. The methods commonly used for the synthesis of AuNRs, nanowires and nanotubes are electrochemical [44] and photochemical [41] reduction methods in aqueous surfactant media, and template methods using appropriate membranes such as porous alumina templates [61-62], polycarbonate membrane templates [63], and carbon nanotube templates [64-65]. Jana and co-workers have used a seeding growth method to make varied aspect ratio Au and Ag NRs [64-69].

#### **B-1.14.2: Electrochemical methods**

The formation of AuNRs by electrochemical method was first demonstrated by Wang et al. They reported a method for high-yield preparation of AuNRs in the presence of cationic surfactants, co-surfactants, and other additives, which were found empirically to favor NRs formation [45-46]. The synthesis is conducted within a simple two-electrode type electrochemical cell. A gold metal is used as the anode, and a platinum plate of similar dimensions as the cathode. Both electrodes are immersed in an electrolytic solution containing a cationic surfactant, cetyltrimethylammonium bromide (CTAB) and a small

amount of a much more hydrophobic cationic surfactant, tetradodecylammonium bromide (TOAB), which acts as a rod-inducing co-surfactant. The CTAB serves not only as the supporting electrolyte but also as a stabilizer for the NPs, to prevent their further aggregation. The electrolytic cell containing the mixed solution is then placed inside an ultrasonic bath at 36 °C. Before the electrolysis, appropriate amounts of acetone and cyclohexane are added into the electrolytic solution. Acetone is used for loosening the micellar framework, then facilitating the incorporation of the cylindrical-shape-inducing co-surfactant into the CTAB micelles; cyclohexane is necessary to enhance the formation of elongated rod-like CTAB micelles. They found that the small amount of silver ions addition is critical for the length of the NRs, but the complete mechanism and the exact role of the silver ions, is still unknown [70].

### **B-1.14.3: Seeding**

Various methods based on seed mediated growth have been reported for controlled synthesis of AuNRs. The reduction of Au Salt on a pre-made small seed is achieved by a weak reducing agent (ascorbic acid) in the presence of a cationic surfactant (mostly CTAB) leading to NRs of different ARs and dimensions stabilized by a bilayer of CTAB. The seeds serve as nucleation sites for the anisotropic growth. Murphy and co-worker have developed a seed-mediated growth method to synthesize Au and Ag NRs in aqueous solution, with the surfactant (CTAB) as a directing agent [42] to produce rods over spheres. According to their proposed growth mechanism, the CTAB head group would bind better to the {100} faces of gold that exist along the length of the pentahedrally twinned rods compared to the {111} gold faces that are at the ends of the rods, as a result of epitaxy [71]. It has also been reported that the length of the surfactant tail is critical for producing AuNRs; with longer chain lengths surfactant tail supports longer AuNRs [72]. The growth of citrate stabilized AuNPs using a wide range of reducing agent and condition has been studied by Jana et al. [73]. They also produced nanorods by changing the concentration of surfactant used and by adding AgNO<sub>3</sub> to the method used to synthesis nanospheres [74]. Nevertheless, this seed mediated method suffers from poor reproducibility because it is very sensitive to numerous experimental parameters such as the nature and purity of the reactants (e.g., Au salt precursors, additives, reducing agents, and surfactants) and the size and surface coating of the seeds [75-76].

#### **B-1.14.4: Photochemical methods**

AuNRs synthesis with well-controlled AR is also possible by using photochemical reduction of Au salts in the presence of CTAB and Ag ions [34]. El-Sayed et al. improved this method by using CTAB-capped seeds instead of citrate-capped ones, and they demonstrated that, as observed in the electrochemical growth technique, the control of NR anisotropy can be enhanced in the presence of Ag (I) during NR formation [77]. Esumi et al. were the first to use photochemical reduction in the presence of elongated micelles formed by the hexadecyltrimethylammonium chloride (HTAC) cationic surfactant to obtain anisotropic gold nanostructures [41]. The factors affecting the nucleation and growth of AuNRs have been investigated by Mulvaney and Liz-Marzan groups [70]. A dependence of the nanorod AR on the size of the seeds has been observed, increasing the size of the seed results in lowering  $R$  for a constant concentration of reagents [78].

One-pot synthesis of AuNRs by ultrasonic irradiation was also reported [79]. Recently, AuNRs of small AR were synthesized by radiolytic reduction of Au<sup>III</sup> in the presence of chemically induced seeds, Ag ions, and CTAB [80]. All of these methods involve synthesis at temperatures close to room temperature. Zijlstra et al. reported seedless synthesis of gold NRs at high temperatures up to 97 °C [81]. This process itself is highly promising for producing nanorods in size, and, more importantly, will be useful in resolving the growth mechanism of anisotropic metal nanoparticles due to its simplicity and the relatively slow growth rate of the nanorods.

#### **1.14.5: Radiolysis**

Radiolysis is a powerful method to synthesize NPs of different ARs, controlled size and shapes [82-83]. Solvent radiolysis induces the formation of solvated electrons and of reducing radicals that are able to reduce metal ions. The radiolytic process displays the specific advantage to induce a homogeneous reduction and nucleation in solutions. Radiolytic one-pot synthesis of AuNRs solutions is reported by Remita et al. [84]. Nanorods of controlled AR were obtained by  $\gamma$ -reduction of Au<sup>III</sup> complexes in a micellar solution formed by a mixture of surfactants cetyltrimethylammonium bromide (CTAB) and

tetraoctylammonium (TOAB) and in presence of acetone, cyclohexane and silver ions. By increasing the silver ion concentrations, aspect ratios up to 10 are obtained [84].

### **B-1.15: Physical, Chemical and optical Properties**

#### **B-1.15.1: General Physico-chemical and catalytic properties of gold**

##### **1.15.1.1: Physical**

A well-known feature of nanometric particles is their lower melting temperature as compared to the bulk. For example gold undergoes a decrease in melting temperature of about 400°C going from bulk to nanometer particles, and of 50°C from the 20 nm to 5 nm particles [85]. Thermal conductivity is enhanced for small particles due to higher surface/volume ratio, while phonons energy becomes higher for very small particles [46]. Another surface phenomenon is the plasmon polariton absorbance band due to the coherent oscillation of  $6s^1$  (Au) conduction band electrons in the presence of resonant electromagnetic waves [86].

##### **B-1.15.1.2: Chemical Properties**

Gold is a highly malleable and ductile metal; one ounce (approximately 28 grams) of gold can be extended into a 1250 miles long wire (thickness 1 micron). It is a good conductor of heat and electricity. It is generally inert and is not attacked by air and most reagents. This makes its stable in normal conditions [87]. Gold ions in solution are reduced and precipitated out as Au metal by other metals acting as reducing agents. During the reaction the added metal is oxidized and dissolved, allowing gold to be removed from the solution and to be recovered as a solid precipitate. Gold nanoparticles are resistant also to strong oxidizing or highly acid environments, though “aqua regia” or solution containing  $I^-$  or  $CN^-$  can immediately dissolve them [88]. Common oxidation states of gold include +1 (aurous compounds) and +3 (auric compounds). The general characteristics of the gold are given in the table 1.1.

Table 1.1: General characteristics of the gold

| Property             | Value  |
|----------------------|--|
| Atomic number        | 79   |
| Atomic Mass          | 196.966 g.mol <sup>-1</sup>                            |
| Electronegativity    | 2.54 (pauling scale)                                   |
| Density              | 19.30 g.cm <sup>-3</sup>                               |
| Melting Point        | 1064.18 °C   |
| Boiling Point        | 2856 °C  |
| Van der Waals radius | 166 pm   |
| Isotopes             | 5 (mass no. 195-199)                                   |
| Electronic Shell     | [Xe] 4f <sup>14</sup> 5d <sup>10</sup> 6s <sup>1</sup> |

### **B-1.15.1.3: Catalytic Properties:**

Au is usually considered as a chemically inert metal, but in 1987 Haruta *et al.* showed that nanosized (<5 nm) Au particles can be very effective catalysts [89-90] and are catalytically active for several chemical reactions [91]. It has been reported that the catalytic properties, reactivities and selectivities are greatly enhanced by NP catalysts as compared to their bulk counterparts. Therefore, nanocatalysis is developing very fast in the area of catalysis. It is now well known that Au is about 1000 times more active than Pt in the electrochemical and catalytic oxidation of CO in a basic (but not acidic) environment [92]. Haruta first reported the high catalytic activity of AuNPs supported on metal oxides for low-temperature CO oxidation and for the selective epoxidation of propene [93-95]. In the last 25 years, researchers have found that AuNPs are excellent catalysts for many other technological and environmentally important reactions such as hydrogenation of CO<sub>2</sub> and CO into methanol and decomposition of halogenated compounds [96]. Great attention has been paid to the size dependence on the activity and selectivity [93-94, 96-97] on catalytic activity. While particle size is an important consideration, many other factors such as geometry, composition, oxidation state, and chemical/physical environment can play a role in determining NP reactivity. Nanometer-sized gold particles have been proven to be highly active for several

reactions, including low-temperature oxidation of CO, partial oxidation of hydrocarbons, the water–gas shift reaction and reduction of nitrogen oxides when dispersed over certain oxides and carbides [94, 98].

## **B-1.15.2: Optical properties: Surface Plasmon Resonance**

### **B-1.15.2.1: General considerations**

First pointed out by Gustav Mie in 1908 [99], the interaction of light with metal nanoparticles results in the “**collective oscillation of the metal-free electrons with respect to the nanoparticle lattice in resonance with the light field**”, in other words AuNPs exhibit a strong absorption band in the visible region when the frequency of the electromagnetic field is resonant with the coherent electron motion; this phenomenon is known as surface plasmon resonance (SPR) [4, 6-7, 86, 100]. The surface plasmon absorption (SPA) results from the dipole oscillations of the free electrons with respect to the ionic core of a spherical nanoparticle. A net charge difference is shown on the nanoparticle surface interacting with an electric field, resulting in a polarization of the electrons with respect to the ionic core of a nanoparticle as represented in Figure 1.17.

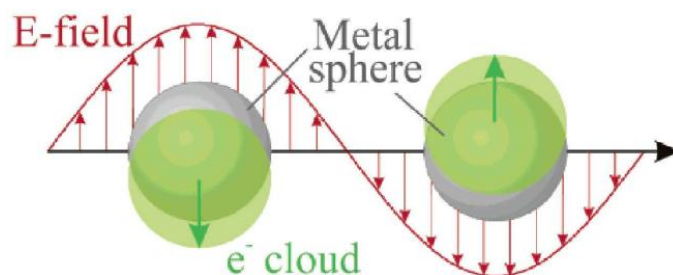


*Figure 1.17: Origin of surface plasmon resonance due to coherent interaction of the electrons in the conduction band with electromagnetic field.*

Under light irradiation, the conduction electrons in gold submitted to an AC electric field collectively oscillate. At the resonant frequency, the incident light interacts best with the nanostructure. Some of the photons will be released with the same frequency in all directions and this process is known as “scattering” (extinction cross-section  $C_{sca}$ ). At the same time, some of the photons will be converted into phonons or vibrations of the lattice and this process is referred to as “absorption” (extinction cross-section  $C_{abs}$ ). In general, the SPR

absorption peak of a solution of gold nanoparticles should include both scattering and absorption components [101]. The transmitted intensity is given by

$$I(z) = I_0 \exp(-n_0 C_{\text{ext}} z) \quad (1.1)$$

Here  $I_0$  is the intensity of the incident beam,  $I(z)$  is the intensity of the beam after travelling a path length  $z$  within the sample,  $n_0$  is the number density of particles and  $C_{\text{ext}} = C_{\text{abs}} + C_{\text{sca}}$  is the extinction cross section of a single particle,  $C_{\text{ext}}$  is the sum total of the absorption and scattering cross sections respectively.

The striking colors of the AuNPs solutions are due to the red shift of the plasmon band to the visible frequency ( $\sim 520$  nm). The red shift of the plasmon occurs due to the quantum confinement of electrons in the nanoparticle, since the mean free path of electrons is greater than nanoparticle size [102] and the origin of the red color of AuNPs is explained via the Mie theory.

Mie theory has been successfully applied to the calculation of noble metal nanoparticles extinction cross section. Mie [99] solved Maxwell's equation for an electromagnetic light wave interacting with small spheres having the same dielectric constant as the bulk metal. The solution of this electrodynamics calculation with appropriate boundary conditions for a spherical object leads to a series of multipole oscillations for the extinction cross-section of the nanoparticles [86]. The Mie model expressions of the extinction cross-section  $\sigma_{\text{ext}}$ , absorption cross-section  $\sigma_{\text{abs}}$  and scattering cross-section  $\sigma_{\text{sca}}$  [86] for a single sphere of radius ( $R$ ) are:

$$\sigma_{\text{ext}} = \frac{2\pi}{|k|^2} \sum_{L=1}^{\infty} (2L+1) \text{Re}(a_L + b_L) \quad (1.2)$$

$$\sigma_{\text{sca}} = \frac{2\pi}{|k|^2} \sum_{L=1}^{\infty} (2L+1) (|a_L|^2 + |b_L|^2) \quad (1.3)$$

With  $\sigma_{\text{abs}} = \sigma_{\text{ext}} - \sigma_{\text{sca}}$  and

$$a_L = \frac{m\psi_L(mx)\psi'_L(x) - \psi'_L(mx)\psi_L(x)}{m\psi_L(mx)\eta'_L(x) - \psi'_L(mx)\eta_L(x)} \quad b_L = \frac{m\psi_L(mx)\psi'_L(x) - \psi'_L(mx)\psi_L(x)}{m\psi_L(mx)\eta'_L(x) - \psi'_L(mx)\eta_L(x)} \quad (1.4)$$

$$m = \frac{n}{n_m} \quad x = |\vec{k}|R$$

where  $k$  is the incident photon wavevector,  $n$  is the complex refractive index of the spherical particle  $n_m$  is the real refraction index of the non-absorbing surrounding medium and  $\psi_L$  and  $\eta_L$  are the spherical Ricatti- Bessel functions. The resulting electric and magnetic fields inside the sphere are expressed as a multipolar series of spherical harmonics with different symmetris, identified by the multipolar order  $L$ .  $L= 1$  corresponds to the dipolar oscillation while  $L= 2$  is associated with the quadrupole oscillation and so on. In metal sphere the excitation due to the optical electric fields are plasmons polaritons, while those due to the optical magnetic fields are electric currents.

The  $x$  parameter determines whether the sphere is in quasistatic (dipolar:  $R \ll \lambda$  then  $|x| \ll 1$ ) or in dynamic regime (multipolar:  $R \sim \lambda$ ). This type of size dependence is called extrinsic size effect in contrast to the intrinsic size effect due to the metal dielectric constant dependence on the size. In the quasistatic case, scattering contributions, which are proportional to  $|x|^6$ , and absorption contribution for  $L > 1$ , which that are proportional to  $|x|^i$  with  $i > 4$ , can be neglected to obtain a simplified expression for  $\sigma_{\text{ext}}$ .

For nanoparticles much smaller than the wavelength ( $< 20\text{nm}$ ), only the dipole oscillation contributes significantly to the extinction cross section and thus Mie's theory reduces to the following equation [86]:

$$\sigma_{\text{ext}} = 9 \frac{\omega}{c} \varepsilon_m^{\frac{3}{2}} V \frac{\varepsilon_2(\omega, R)}{[\varepsilon_1(\omega, R) + 2\varepsilon_2]^2 + \varepsilon_2(\omega, R)^2} \quad (1.5 \text{ a})$$

$$\varepsilon(\omega, R) = \varepsilon_1(\omega, R) + i\varepsilon_2(\omega, R) \quad (1.5 \text{ b})$$

Where  $V$  is the sphere volume,  $\varepsilon(\omega, R)$  is the sphere complex dielectric constant,  $c$  is the speed of light,  $\varepsilon_m$  is the dielectric constant of the surrounding medium  $\varepsilon(\omega, R) = \varepsilon_1(\omega, R) + i\varepsilon_2(\omega, R)$  are the medium real dielectric and imaginary parts of  $\varepsilon$ ,

respectively. The resonance condition is fulfilled when  $\epsilon_1(\omega) = -2\epsilon_m$  if  $\epsilon_2$  is small or weakly dependent on  $\omega$ . Equation (1.5 a) points out that the  $\sigma_{\text{ext}}$  is directly proportional to the sphere volume. Besides, the dielectric constant is dependent on R as well as on the photo frequency  $\omega$ , due to intrinsic size effects. But for larger nanoparticles, light cannot polarize the nanoparticles homogeneously and retardation effects lead to the excitation of higher-order modes [103].

From equation (1.5a), it can be seen that the peak intensity and position of the SPA band is dependent on the size and shape of the metal nanoparticles, the dielectric constant of the metals as well as that of the medium surrounding the particles [6]. As size increases, the absorption maximum is slightly red shifted [104] and bandwidth changes also occur. Link and El-Sayed [4] have shown that the bandwidth decreases with the increase of the nanoparticles size when nanoparticle diameters are less than 20 nm, and that the bandwidth increases with the increase of the nanoparticle size when nanoparticle diameters are larger than 20 nm. He also found that the absorption coefficient is linearly dependent on the volume of the nanoparticles, which is in agreement with the Mie theory [99].

#### B-1.15.2.2: Shape-dependent properties: the Gans theory

When the shape of the nanoparticles changes from NSs to NRs, the SPA spectrum also changes. AuNRs exhibit optical properties that are different from their spherical counterparts. SPA of AuNRs have two bands: a strong long wavelength band in the red and near infrared regions due to the longitudinal oscillation of electrons, and a weak band shorter wavelength band in the visible region around 520 nm due to the transverse electronic oscillation. Using an extension of the Mie theory it is attempted here to explore theoretically the relationship between the aspect ratio of the AuNRs and the position of this absorption maximum. According to Gans, [105-107] the extinction cross-section  $\sigma_{\text{ext}}$  of randomly oriented particles in the dipole approximation is given by the following equation:

$$\sigma_{\text{ext}} = \frac{2\pi V \epsilon_m^{3/2}}{3\lambda} \sum_j \frac{1/P_j^2 \epsilon_2(\omega, R)}{\left( \epsilon_1(\omega, R) + \frac{1-P_j}{P_j} \epsilon_m \right)^2 + \epsilon_2(\omega, R)^2} \quad (1.6)$$

where  $N$  is the number of particles per unit volume,  $V$  is the volume of each particle,  $\epsilon_m$  the dielectric constant of the surrounding medium,  $\lambda$  the wavelength of the interacting light, and  $\epsilon_1$  and  $\epsilon_2$  are the real and complex part of the material dielectric constant. The latter one is frequency dependent, while  $\epsilon_m$  is assumed to be a constant.  $P_j$  are the depolarization factors for the three axes  $A, B, C$  of the rod with  $A > B = C$ . They are defined as

$$P_A = \frac{1 - e^2}{e^2} \left[ \frac{1}{2e} \ln \left( \frac{1 + e}{1 - e} \right) - 1 \right]$$

$$P_B = P_C = \frac{1 - P_A}{2} \quad (1.7)$$

where

$$e = \sqrt{1 - \left(\frac{B}{A}\right)^2} = \sqrt{1 - \left(\frac{1}{R}\right)^2} \quad (1.8)$$

The ratio  $A/B$  is the aspect ratio  $R$  [4].

The absorption spectrum of AuNRs is very sensitive to the AR (length/width) and calculation or measurements can be done on the basis of the dielectric function of gold using the above equations. When AR increases, the absorption maximum of the longitudinal band is greatly red shifted [108]. Nanoparticles have large surface to volume ratio. The absorption difference of the longitudinal band is responsible for the color difference of the nanorod solution.

The SPR frequency depends not only on the metal, but also on the size and shape of the nanoparticle [6, 99], on the dielectric properties of the surrounding medium [109], and on inter-nanoparticle coupling interactions [86, 110], Therefore, the optical properties desired for a specific application can be tuned by generating nanoparticles of definite size and shape in the preferred media in order to develop new effective nanomaterials and nanodevices.

### **B-1.16: Nanoparticles and quadratic second order nonlinear Optics**

The main applications of nonlinear optical phenomena are optical limiting, optical Kerr effect and second or third harmonic generation. AuNPs possess a huge number of easily

polarizable electrons allowing strong light matter interaction and therefore high non-linear optical properties. To observe third order NLO effects with negligible contribution from bare thermal effects or particles degradation, it is important to use fast spectroscopies based on femtosecond or at least picosecond laser sources. The strong nonlinear properties of nanoparticles are usually attributed to local field enhancement effects due to plasmon oscillation [111]. SPR enhancement can be obtained at the harmonic frequencies yielding more versatility, whereas SPR enhancement at the fundamental frequency is usually avoided in order to preserve the sample solution from degradation. The nonlinear polarization displays a quadratic or cubic dependence with respect to the fundamental electric field. The concentration of electromagnetic energy into small volumes can enhance these processes by orders of magnitude. Nonlinear optical susceptibility ( $\chi$ ) is measured on nanostructures are much larger than in bulk metals (up to  $10^5$  times larger) [112]. The HLS technique has already been used in the past for the determination of the large first hyperpolarizabilities ( $\beta$ )  $10^5$ - $10^6 \times 10^{-30}$  esu) for CuNPs [113], and other noble metal NPs [114-116]. There also exist several reports of HLS from silver nanoparticles, possibly the earliest reports of HLS from any nanoparticle [114-115, 117]. Johnson et al. [114] suggested that high  $\beta$ -values of noble metal NPs are due to SPR enhancement of the second harmonic (SH) scattering signal. HLS from nanocrystalline gold nanoparticle suspensions [118-119] and from highly concentrated gold nanoparticle samples has been observed [120-121]. Various experimental studies have been reported on the exaltation of quadratic NLO properties of molecular units by gold nanostructures. The exaltation of SHG from ultrathin dye layers deposited on fractal gold surfaces has been reported [122]. A SHG signal of individual molecules in the presence of very small gold NPs (1nm) has been evidenced in the context of biological membrane imaging [123].

Metals exhibit simple cubic lattice structures. Au shows a face-centered cubic structure [124], and displays an inversion center; therefore SHG is forbidden in these bulk metals. SHG appears in centrosymmetric particles due to surface effects especially when NPs size smaller than the excitation wavelength [125-126]. Generally, SHG is observed in metal nanoparticles aggregates and non-spherical particles such as rods and L – shaped structures. It is important to study the origin and role of multipole effects in SHG response of AuNPs. There are two different types of multipole effects. The first type arises from the light matter interaction

Hamiltonian and corresponds to microscopic multipole moments at the atomic and molecular levels. Such multipoles can enable second order nonlinear effects from centrosymmetric materials [127] which are forbidden within the electric dipole approximation of the light matter interaction. The second type of multipoles arises from the Mie scattering theory [110]. The standard Mie theory is based on a dipolar microscopic interaction and effective multipoles arises from size and retardation effects. Electric dipolar optical response arises from the particles smaller than the wavelength [86] whereas dipolar effects may no longer provide a complete description when the size of the particle is closer to the wavelength, thus higher multipoles play an important role that should also be considered. On another hand a few nanometer AuNPs are submitted to dipolar plasma oscillation modes only and as the particle size increase, new higher order plasma oscillation modes such as quadrupole modes start to emerge, resulting in new bands in the extinction spectrum of NPs [128-129].

The contribution of multipoles to the linear optical response of metal NPs has been discussed in the literature (109, 129-131). For example, metallic nanoshells can be driven selectively into dipolar and quadrupolar oscillation patterns [128]. Size dependence of multipolar plasmon resonance from elongated AgNPs has also been studied [129], and prediction of the multipolar character of charge density distribution in triangular nanoprisms has been published; multipolar plasmon resonances have been observed with scanning near-field microscope [132].

Multipole effects play an important role in the nonlinear response of metal NPs, including SERS [133], HLS [134-136], and SHG [137]. Multipole effect is interesting especially for HLS which corresponds to incoherent scattering of SHG. Such scattering can arise even from centrosymmetric particles due to retardation effects [138]. On the other hand, dipolar effects can provide direct evidence of symmetry breaking of individual particles even though the macroscopic sample is centrosymmetric. To find out the exact origin of the second-order nonlinearity in metal NPs, experiments on Au and Ag particles of smaller dimensions (<100 nm) have been done using femtosecond laser pulses at 800 nm [138-139] By carrying out wavelength-dependent HLS and “slit experiments” with 32 nm Ag NPs, Hao et al. [137] have shown that the SH response contains both dipolar and quadrupolar contributions. Recently,

Nappa et al. [138] have done polarization-resolved HLS experiments with Au and Ag NPs and have shown that the origin of SH emission from these particles is purely dipolar in nature. Therefore, the origin of the SH in metallic nanospheres is currently under discussion.

### **B-1.17: Applications of Gold nanoparticles**

Most well-known application of AuNPs is to stain glass, a technique used since a long time and that is still used today (“Ruby glass”). AuNPs in electronics and optics is used in nanoscale electronics, sub-wavelength optical devices [140-143], for nonlinear optics [144-146], and for optical data storage [147-148]. AuNPs is widely used in chemistry as a catalyst, chemical sensors, biosensors, polymer additives and poly reagent etc. [15-16, 149]. Depollution can be done by AuNPs especially with small AuNPs (< 5 nm) that can transform carbon monoxide (CO), which is very toxic, into carbon dioxide (CO<sub>2</sub>) at room temperature [figure 1.18]. The potential applications of AuNPs for depollution are tunnels, catalytic converters, fireman masks etc.

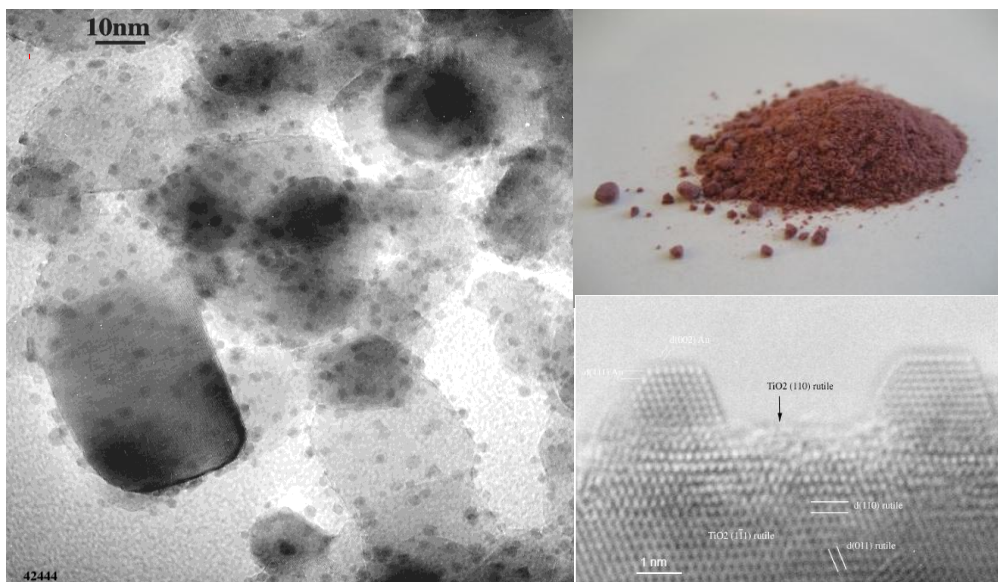


*Figure 1.18: Application of AuNPs in depollution [150-151].*

The most important applications of AuNPs are in biological science. They are used to label organic substances or biological material primarily for electron microscopy. This is because gold has a very high contrast compared to organic substances due to its high electron density, and is therefore easily distinguished in electron microscopy. Because of its inert nature, it is

possible to specifically bind gold colloids to a desired target without altering its structure [152]. Recently this gold labeling technique has also been applied to detect specific biological substances (DNA) with light microscopy. In this application, no use of plasmon resonance is required. The strong electromagnetic field around the particles, which can be much higher than the exciting light field at the particle plasmon frequency, is used to enhance nonlinear optical effects such as surface enhanced Raman scattering (SERS) [153-157]. Sokolov et al. [158] had earlier employed Au nanoparticles for cancer imaging using laser confocal microscopy, whereas the dark-field imaging technique was shown by El-Sayed et al. [159]. AuNPs are promising radiosensitiser agents for radiotherapy because of their biocompatibility and excellent absorber of X-rays. In this context, AuNPs are currently being investigated to enhance the biological effect of radiation treatment at the tumor site. The nanometer size and high Z properties of AuNPs provide potential advantages in enhancing radiation dose to the tumor while preserving the surrounding normal tissue which is the ultimate goal in radiotherapy [160]. It has been shown that this radiobiological enhancement widely varies with irradiation energy and the size and concentration of the AuNPs. Recent research has been done on the radiosensitization properties of AuNPs in a size range from 14 to 74 nm. The highest radiosensitization enhancement factor (REF) is for 50 nm diameter AuNPs [161]. This technology is currently being evaluated in Canada where they used AuNPs (thousand times smaller than a cancer cell) to attached them to molecules like antibodies that are directed against cancer cells. After being injected into the patient, these molecules bind to the cancer cell and are absorbed inside, delivering the AuNPs into their target. When the organ is treated with radiation, the nanoparticles capture and concentrate the radiation around them, which in turn increases the specific killing of cancer cells [162].

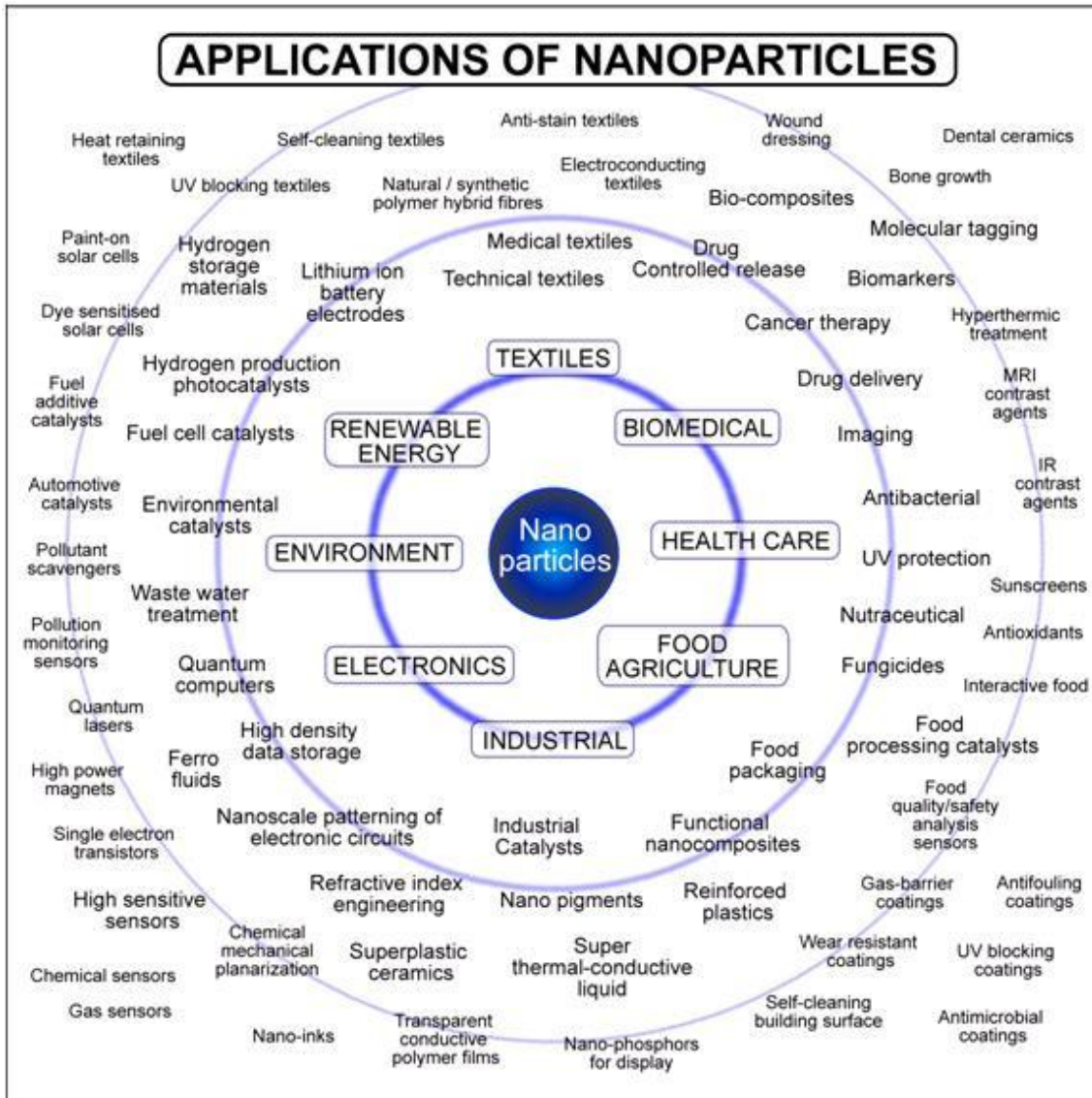


Figure 1.19: Applications of AuNPs [163].

## **References**

- [1] Vance, F. W., Lemon, B. I., Hupp, J. T., *J. Phys. Chem. B*, 1998, 102, 10091-10093.
- [2] Ganeev, R. A., Ryasnyansky, A. I., Kamalov, S. R., Kodirov, M. K., Usmanov, T., *J. Phys. D* 2001, 34, 1602-1611.
- [3] Feldheim, D. L., Foss, C. A., Jr. *Metal nanoparticles: synthesis, characterization, and applications*; Marcel Dekker, Inc.: New York, 2002.
- [4] Link S., El-Sayed M.A., *J Phys Chem B*, 1999, 103, 8410.
- [5] Ghosh SK, Nath S, Kundu S, Esumi K, Pal T (2004) *J Phys Chem B* 108:13963
- [6] Link S, El-Sayed, M. A., *Int Rev Phys Chem.*, 2000, 19, 409.
- [7] Link S, El-Sayed, M. A., *Annu Rev Phys Chem.*, 2003, 54, 331.
- [8] Thomas, K. G., Ipe, B. I., and Sudeep P. K., *Pure Appl. Chem*, 2002, 74 (9),1731–1738.
- [9] Freestone, I., Meeks, N., Sax, M., and Catherine, H., *Gold bulletin*, 2007, 40 (4), 270-277.
- [10] Murphy, C. J., *Science*, 2002, 298, 2139–2141.
- [11] Antonii, F., *Panacea Aurea-Auro Patabile*; Bibliopolio Frobeniano: Hamburg 1618.
- [12] (a) Thompson, D., *Gold bulletin*, 2007, 40 (4), 267-269 (b) Faraday, M., *Philos Trans.*, 1857, 147, 145-181.
- [13] Turkevich. J, Stevenson. P. C., Hillier, J., *Discuss Faraday Soc.*, 1951, 11, 55-75.
- [14] Enüstün, B. V., Turkevich J., *J Am Chem Soc* 1963, 85, 3317-3328.
- [15] Haruta, M, Kobayashi, T, Sano H, Yamada N., *Chem Lett.*, 1987, 405-408.
- [16] Haruta, M., Yamada, N., Kobayashi T., Ijima S., *J Catal.*, 1989, 115, 301-309.
- [17] Schmid, G., *Chem Rev* 1992, 92, 1709-1727.
- [18] Schmid, G., Chi, L. F., *Adv Mater.*, 1998, 10, 515-26.
- [19] Bethell, D., Brust, M., Shiffrin, D. J., Kiely, C., *J Electroanalyt Chem* 1996, 409, 137-43.
- [20] Brust, M., Kiely, C., *Colloid. Surf A: Physicochem Eng Asp* 2002, 202, 175-86.
- [21] Nikoobakht, B. and El-Sayed, M. A., *Chem. Mater.*, 2003, 15, 1957-1962.
- [22] Eustis, S. and El-Sayed, M. A., *Chem. Soc. Rev.*, 2006, 35, 209–217.
- [23] Tao, A. R., Habas, S., Yang, P., *Small*, 2008, 4, 310.
- [24] Perez-Juste, J., Pastoriza-Santos, I., Liz-Marzan, L. M., Mulvaney, P., *Coordination Chemistry Reviews*, 2005, 249 1870–1901.

- [25] Raab, C., Simkó, M., Fiedeler, U., Nentwich, M., Gazsó, A., NanoTrust-Dossier No. 006en, February 2011, ISSN: 1998-7293, <http://epub.oeaw.ac.at/ita/nanotrust-dossiers/dossier006en.pdf>
- [26] Shenhar R., and Rotello, V. M., *Acc. Chem. Res.*, 2003, 36, 549–561.
- [27] Haes, A. J., Hall, W. P., Chang, L., Klein W. L., and Van Duyne, R. P., *Nano Lett.*, 2004, 4, 1029–1034.
- [28] Veith, G. M., Lupini, A. R., Pennycook, S. J., Ownby, G. W., Dudney, N. J., *Journal of Catalysis*, 2005, 231, 151–158.
- [29] Arrii, S., Morfin, F, Renouprez, A. J., Rousset, J. L., *J. Am. Chem. Soc.*, 2004, 126 (4), 1199-1205.
- [30] Kamat, P. V., *J. Phys. Chem. B*, 2002, 106, 7729–7744.
- [31] Gopalakrishnan, J., *Chem. Mater.*, 1995, 7, 1265.
- [32] Remita, H. and Remita S., *Metal clusters and nanomaterials: contribution of radiation chemistry.*
- [33] Liang H-P., Wan L-J., Bai C-L., and Jiang L., *J. Phys. Chem. B*, 2005, 109, 7795-7800.
- [34] Renaud, G., Lazzari, R., Revenant, C., Barbier, A., Noblet, M., Ulrich, O., Leroy, F., Jupille, Borensztein, J. Y., Henry, C. R., Deville, J.-P., Scheurer, F., Mane-Mane, J., Fruchart, O., *Science*, 300, 1416, 2003.
- [35] Belloni, J. Mostafavi, M. Remita, H. Marignier, J.L. and Delcourt, M. O., *New J. Chem.*, 1998, 1239-1255.
- [36] Anderson, M., Pedersen, J.S., Palmqvist, A. E. C. *Langmuir*, 2005, 21, 11387.
- [37] Wang, W., Chen, X., Efrima, S., *J. Phys. Chem. B*, 1999, 103, 7238.
- [38] Kim, F., Song, J. H., and Yang, P., *J. Am. Chem. Soc.* 2002, 124, 14316-14317.
- [39] Böhmer, M. R., Fokkink, L. G. J., Schoonenberger, C., van der Zande, B. M. I., *J. Phys. Chem. B* 1997, 101, 852.
- [40] Nicewarner-Pena, S. R., Freeman, R. G., Reiss, B. D., He, L., Pena, D. J., Walton, I. D., Cromer, R., Keating, C. D., Natan, M. J., *Science* 2001, 294, 137.
- [41] Esumi, K., Matsuhisa, K., Torigoe, K., *Langmuir* 1995, 11, 3285.
- [42] Murphy C. J., Jana N. R., *Adv. Mater.*, 2002, 14, 80.

- [43] Sun Y. G., Xia Y. N., *Adv. Mater.*, 2002, 14, 833.
- [44] Yu, Y. Y., Chang, S. S., Lee, C. L., Wang, C. R. C., *J. Phys. Chem. B*, 1997, 101, 6661.
- [45] Chang, S. S., Shih, C. W., Chen, C. D., Lai, W. C., Wang, C. R. C., *Langmuir* 1999, 15, 701.
- [46] Daniel M.-C., and Astruc, D., *Chem. Rev.*, 2004, 104, 293–346.
- [47] Jin, R. C., Cao, Y. W., Mirkin, C. A., Kelly, K. L., Schatz, G. C., and Zheng, J. G., *Science*, 2001, 294, 1901–1903.
- [48] Murphy, C. J., Sau, T. K., Gole, A. M., Orendorff, C. J. G., Gou, J. L., Hunyadi, S. E., and Li, T., *J. Phys. Chem. B*, 2005, 109, 13857–13870.
- [49] Pileni, M. P., *Langmuir*, 1997, 13, 3266–3276.
- [50] Van der Zande, B. M. I., Bohmer, M. R., Fokkink, L. G. J., Schonenberger, C., *J. Phys. Chem. B*, 1997, 101, 852.
- [51] Jana N. R., *Small*, 2005, 1, 875.
- [52] Zhu, Y.-J., Hu, X.-L., *Chem. Lett.*, 2003, 32, 1140.
- [53] Niidome, Y., Nishioka, K., Kawasaki, H., Yamada, S., *Eng. Asp.*, 2005, 257-258, 161.
- [54] Aiken, J. D., III; Finke, R. G. *J. Mol. Catal. A* 1999, 145, 1-44.
- [55] Kumar, A., Mandal, S.; Mathew, S. P., Selvakannan, P. R., Mandale, A. B., Chaudhari, R. V., Sastry, M., *Langmuir* 2002, 18, 6478-6483.
- [56] Shipway, A. N., Willner, I., *Chem. Commun.* 2001, 2035-2045.
- [57] Yamada, M., Kuzume, A., Kurihara, M., Kubo, K., Nishihara, H., *Chem. Commun.* 2001, 2476-2477.
- [58] Frens, G., *Nature* 1973, 241, 20.
- [59] Leff, D. V., Ohara, P. C., Heath, J. R., Gelbart, W. M., *J. Phys. Chem.* 1995, 99, 7036.
- [60] Hu, J. T., Odom, T. W., Lieber, C. M., *Acc. Chem. Res.* 1999, 32, 435.
- [61] Martin, B. R., Dermody, D. J., Reiss, B. D., Fang, M. M., Lyon, L. A., Natan, M. J., Mallouk, T. E., *Adv. Mater.*, 1999, 11, 1021.
- [62] Van der Zande, B. M. I., Bohmer, M. R., Fokkink, L. G. J., Schonenberger, C., *Langmuir*, 2000, 16, 451.
- [63] Cepak, V. M., Martin, C. R., *J. Phys. Chem. B*, 1998, 102, 9985.
- [64] Govindaraj, A., Satishkumar, B. C., Nath, M., Rao, C. N. R., *Chem. Mater.*, 2000, 12, 202.

- [65] Fullam, S., Cottell, D., Rensmo, H., Fitzmaurice, D., *Adv. Mater.*, 2000, 12, 1430.
- [66] Foss Jr., C.A., Hornyak, G.L., Stockert, J.A., Martin, C.R., *J. Phys.Chem.*, 1992, 96, 7497.
- [67] Martin, C.R., *Science*, 1994, 266, 1961.
- [68] Jana, N. R, Gearheart, L., and Murphy, C. J., *J. Phys. Chem. B*, 2001, 105, 4065-4067.
- [69] Jana, N. R, Gearheart, L., and Murphy, C. J., *Adv. Mater.*, 2001, 13, 1389-1393.
- [70] Perez-Juste, J., Liz-Marzan, L. M., Carnie, S., Chan, D. Y. C., Chan, D. Y. C., Mulvaney, P., *Adv. Funct. Mater.*, 2004, 14, 571.
- [71] Johnson, C. J.; Dujardin, E.; Davis, S. A.; Murphy, C. J.; Mann, S. J. *Mater. Chem.*, 2002, 12, 1765.
- [72] Gao, J., Bender, C. M., and Murphy C. J., *Langmuir* 2003, 19, 9065-9070.
- [73] Jana, N.R., Gearheart, L., Murphy, C.J., *Chem. Mater.*, 2001, 13, 2313.
- [74] Brown, K.R., Walter, D.G., Natan, M.J., *Chemistry of Materials*, 2000, 12, 306–313.
- [75] Jiang, X. C., Brioude, A., Pileni, M. P., *Colloids Surf. A*, 2006, 277, 201.
- [76] Jiang, X. C., Pileni, M. P., *Colloids Surf. A*, 2007, 295, 228.
- [77] El-Sayed, M. A., Nikkobakht, B., *Chem. Mater.*, 2003, 15, 1957.
- [78] Gole, A., Murphy, C., *Chem. Mater.*, 2004, 16, 3633.
- [79] Okitsu, K., Sharyo, K., Nishimura, R., *Langmuir*, 2009, 25, 7786.
- [80] Biswal, J., Ramnani, S. P., Tewari, R., Dey, G. K., Sabharwal, S., *Radiat. Phys. Chem.*, 2010, 79, 441.
- [81] Zijlstra, P., Bullen, C., Chon, J. W. M., Gu, M., *J. Phys. Chem. B*, 2006, 110, 19315.
- [82] Krishnaswamy, R., Remita, H., Imperor-Clerc, M., Even, C., Davidson, P., Pansu, B., *Chem. Phys. Chem.*, 2006, 7, 1510.
- [83] Ksar, F., Surendran, G., Ramos, L., Keita, B., Nadjo, L., Prouzet, E., Beaunier, P., Hagege, A., Audonnet, F., Remita, H., *Chem. Mater.*, 2009, 21, 1612.
- [84] Abidi, W., Selvakanan, P. R., Guillet, Y., Lampre, I., Beaunier, P., Pansu, B., Palpant B., and Remita, H., *J. Phys. Chem. C*, 2010, 114, 14794.
- [85] Burda C., Chen X., Narayanan R., and El-Sayed M. A., *Chem. Rev.*, 2005, 105 (4), 1025–1102.

- [86] Kreibig, U., Vollmer, M., *Optical properties of metal clusters*". Springer Verlag: Berlin, 1995.
- [87] Maeda, H., Wu, J., Sawa, T., Matsumura, Y., Hori, K., *Journal of Controlled Release*, 2000, 65 (1-2), 271-284.
- [88] Ferrari, M., *Nature Reviews*, 2005, 5, 161-171.
- [89] Haruta, M., Kobayashi, T., Sano, H., Yamada, N., *Chem. Lett.* , 1987, 405.
- [90] Hvolbæk, B., Janssens, T. V. W., Clausen, B. S., Falsig, H., Christensen, C. H., and Nørskov, J. K., *Nanotoday*, 2007, 2 (4), 14-18.
- [91]. Zhu, Y., Jin, R., and Sun, Y., *Catalysts* 2011, 1, 3-17, doi: 10.3390/catal1010003
- [92] Haruta, M., *J. New. Mat. Electrochem. Systems*, 2004, 7, 163-172.
- [93] Haruta, M. *Cattech* 2002, 6, 102-115.
- [94] Cuenya, B. R., Baeck, S.-H., Jaramillo, T. F., and McFarland, E. W., *J. AM. CHEM. SOC.* 2003, 125, 12928-12934.
- [95] Haruta, M., Yamada, N., Kobayashi, T., Iijima, S. *J. Catal.*, 1989, 115,301.
- [96] Haruta, M. *Catal. Today*, 1997, 36, 153-166.
- [97] Valden, M., Goodman, D. W. *Isr., J. Chem.*, 1998, 38, 285-292.
- [98] Cuenya, B. R., *Thin Solid Films*, 2010, 518, 3127–3150.
- [99] Mie, G., *Ann. Phys.*, 1908, 25, 377.
- [100] El-Sayed, M. A., *Acc. Chem. Res.*, 2001, 34, 257.
- [101] Shalaev, V. M., Sarychev, A. K., *Phys. Rev. B.*, 1998, 57, 13265–13288.
- [102] Pincon, N., Palpant, B., Prot, D., Charron, E., and Debrus, S., *Eur. Phys. J. D* 19, 2002, 395–402.
- [103] Kerker, M. J., *J Colloid Interface Sci.*, 1985, 105, 297.
- [104] Berciaud, S., Cognet, L., Tamarat, P., and Lounis, B., *Nano Letters*, 2005, 5 (3), 515.
- [105] Gans, R., *Ann. Phys.*, 1915, 47, 270.
- [106] Papavassiliou, G. C., *Prog Solid State Chem.*, 1980, 12, 185.
- [107] Link, S., Mohamed, M. B., and El-Sayed, M. A., *Phys. Chem. B*, 1999, 103, 3073-3077.
- [108] Eustis, S., and El-Sayed M., *J. Phys. Chem. B*, 2005, 109 (34), 16350–16356.

- [109] Kelly, K. L., Coronado, E., Zhao, L. L., and Schatz, G. C., *J. Phys. Chem. B*, 2003, 107 (3), 668–677.
- [110] Bohren, C. F., and Huffman D. R., *Absorption and Scattering of Light by Small Particles*, John Wiley and Sons, Inc., 1983.
- [111] Rechberger, W., Hohenau, A., Leitner, A., Krenn, J. R., Lamprecht, B., Aussenegg, F. R., *Opt. Commun.*, 2003, 220, 137.
- [112] Li, K., Stockman, M. I., and Bergman, D. J., *Phys. Rev. Lett.*, 2003, 91, 227402.
- [113] Chandra, M., Indi, S. S., and Das P. K., *J. Phys. Chem. C*, 2007, 111 (28), 10652–10656.
- [114] Johnson, C.K., Soper, J.A., *J. Phys. Chem.*, 1989, 93, 7281.
- [115] Johnson, R. C., Li, J., Hupp, J. T., Schatz, G. C., *Chem. Phys. Lett.*, 2002, 356, 534-540.
- [116] Chandra, M., Indi, S. S., Das, P. K., *Chem. Phys. Lett.*, 2006, 422, 262-266.
- [117] Baranov, A.V., Bobovich, Ya.S., Petrov, V.I., *Opt. Spectrosc.*, 1986, 61, 1986, 315.
- [118] Galletto, P., Brevet, P.F., Girault, H.H., Antoine, R., Broyer, M., *J. Phys. Chem. B*, 1999, 103, 1999, 8706.
- [119] Galletto, P., Brevet, P.F., Girault, H.H., Antoine, R., Broyer, M., *Chem. Commun.*, 1999, 581.
- [120] Antoine, R., Pellarin, M., Palpant, B., Broyer, M., Prevel, B., Galletto, P., Brevet, P.F., Girault, H.H., *J. Appl. Phys.*, 1998, 84, 1998, 4532.
- [121] Antoine, R., Brevet, P.F., Girault, H.H., Bethell, D., Schiffrin, D.J., *Chem. Commun.*, 1997, 1901.
- [122] Anceau, C., Brasselet, S., Zyss J., Gadenne, and P., *Opt. Lett.*, 2003, 28, (9), 713-715.
- [123] Peleg, G., Lewis, A., Linial, M., and Loew, L. M., *Proc. Natl. Acad. Sci., USA*, 1999, 96, 6700–6704.
- [124] Ashcroft, N. W., Mermin, N. D., *Solid State Physics*, Saunders college publishing, 1976.
- [125] McMahon, M. D., Lopez, R., Haglund, R. F., Ray, E. A. and Bunton, P. H., *Physical review B*, 73, 2006, 041401,
- [126] Bozhevolnyi, S. I., Beermann, J., Coello V., *Phys. Rev. Lett.*, 2003, 90, 197403.
- [127] Guyot-Sionnest, P., Chen, W., and Shen Y. R., *Phys. Rev. B*, 1986, 33, 8254–8263.
- [128] Oldenburg S. J., Hale G. D., Jackson J. B., Halas N. J., *Appl. Phys. Lett.*, 1999, 75, 1063.

- [129] Krenn, J. R., Schider, Rechberger, G. W., Lamprecht, B., Leitner, A., Aussenegg, F. R., and Weeber, J. C., *Appl. Phys. Lett.*, 2000, 77, 3379.
- [130] Taminiou, T. H., Stefani, F. D., Segerink F. B., and Hulst, N. F. V., *Nature Photonics*, 2008, 2, 234 – 237.
- [131] Félidj, N., Grand, J., Laurent G., Aubard, J., Lévi, G., Hohenau A., Galler, N., Aussenegg, F. R., and Krenn, J. R., *J. Chem. Phys.*, 2008, 128, 094702.
- [132] Esteban, R., Vogelgesang, R., Dorfmueller, J., Dmitriev, A., Rockstuhl, C., Etrich, C., and Kern, K., *Nano Lett.*, 2008, 8 (10), 3155–3159.
- [133] Laurent, G., Félidj, N., Aubard, J., Lévi, G., Krenn, J. R., Hohenau, A., Schider, G., Leitner, A. and Aussenegg F. R., *Phys. Rev. B.*, 2005, 71, 045430.
- [134] Dadap, J. I., Shan, J., and Heinz, Tony F., *JOSA B*, 2004, 21 (7), 1328-1347.
- [135] Nappa, J., Revillod, G., Russier-Antoine, I., Benichou, E., Jonin, C., Brevet, P. F., *Phys. Rev. B*, 2005, 71, 165407.
- [136] Nappa, J., Russier-Antoine, I., Benichou, E., Jonin, Ch., and Brevet, P. F., *J. Chem. Phys.*, 2006, 125, 184712.
- [137] Russier-Antoine, I., Benichou, E., Bachelier, G., Jonin, C., and Brevet, P. F., *J. Phys. Chem. C*, 2007, 111 (26), 9044–9048.
- [138] Nappa, J.; Revillod, G.; Russier-Antoine, I.; Benichou, E.; Jonin, C.; Brevet, P. F. *Chem. Phys. Lett.* 2005, 415, 246-250.
- [139] Hao, E. C.; Schatz, G. C.; Johnson, R. C.; Hupp, J. T. *J. Chem. Phys.* 2002, 117, 5963.
- [140] Salerno, M., Krenn, J. R., Lamprecht, B., Schider, G., Ditlbacher, H., Felidj, N., Leitner, A., and Aussenegg, F. R., *Opto- Electron. Rev.*, 2002, 10 (3), 217–224.
- [141] Krenn, J. R., *Nat. Mater.*, 2003, 2 (4), 210–211.
- [142] Maier, S. A., Kik, P. G., Atwater, H. A., Meltzer, S., Harel, E., Koel, B. E., and Requicha, A. A. G., *Nat. Mater.*, 2003, 2 (4), 229–232.
- [143] Barnes, W. L., Dereux, A., and Ebbesen, T. W., *Nature*, 2003, 424 (6950), 824–830.
- [144] Liau, Y. H., Unterreiner, A. N., Chang, Q., and Scherer, N. F., *J. Phys. Chem. B*, 2001, 105 (11), 2135–2142.

- [145] Yelin, D., Oron, D., Thiberge, S., Moses, E., and Silberberg, Y., *Optics Express*, 2003, 11(12), 1385–1391.
- [146] Nappa, J., Revillod, G., Russier-Antoine, I., E. Benichou, Jonin, C., and Brevet, P. F., *Phys. Rev. B*, 2005, 71(16), 165, 407.
- [147] Ditlbacher, H., Krenn, J. R., Lamprecht, B., Leitner, A., and Aussenegg, F. R., *Opt. Lett.*, 2000, 25 (8), 563–565.
- [148] Chon, J. W. M., Bullen, C., Zijlstra, P., and Gu, M., *Adv. Funct. Mater.*, 2007, 17 (6), 875.
- [149] Galvagno, S., Parravano, G., *J. Catal.*, 1978, 55, 178-190.
- [150] Zanella, R., Giorgio, S., Henry, C.R., Louis, C., *J. Phys. Chem. B*, 2002, 106, 7634.
- [151] Zanella, R., Delannoy, L., Louis, C., *Appl. Catal. A*, 2005, 291, 62.
- [152] Hayat, M., *Colloidal Gold: Principles, Methods, and Applications*, 1989, volume 1-3. Academic Press, London, 1st edition.
- [153] Taton, T. A., *Science*, 2000, 289, 1757.
- [154] Moskovits, M., *Rev. Mod. Phys.*, 1985, 57, 783.
- [155] Kneipp, K., Wang, Y., Kneipp, H., Itzkan, I., Dasari, R. R., and Feld, M. S., *Phys. Rev. Lett.*, 1996, 76, 2444.
- [156] Nie, S. and Emory, S. R., *Science*, 1997, 275, 1102.
- [157] Kneipp, K., Kneipp, H., Itzkan, I., Dasari, R. R., and Feld, M. S., *J. Phys.-Condes. Matter*, 2002, 14 (18), R597–624.
- [158] Sokolov K, Follen M, Aaron J, Pavlova I, Malpica A, Lotan R, Richards-Kortum R (2003) *Cancer Res* 63:1999
- [159] El-Sayed, I. H., Huang, X., El-Sayed, M. A., *Nano Lett.*, 2005, 5, 829.
- [160] Weibo Cai, G. T., Hong, H., Sun, J., *Applications of gold nanoparticles in cancer nanotechnology*, *Nanotechnology, Science and Application*, 2008, 1, 17-32.
- [161] Chithrani, D. B., Jelveh, S., Jalali, F., van Prooijen, M., Allen, C., Bristow, R. G., Hill, R. P., Jaffray, D. A., *Radiat Res.*, 2010, 173, (6), 719-728.
- [162] <http://www.nanomedicine.dtu.dk/Research/Gold.aspx>
- [163] <http://networksandservers.blogspot.fr/2011/01/nanotechnology.html>

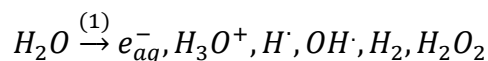
## Part C: Experimental Investigation tool

### C-1.18: Radiolysis

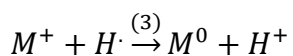
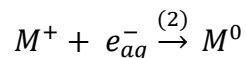
Radiolysis of aqueous solutions of metal ions is well known to lead to reduced metal sols. Ionizing radiations are known since their discovery, X-rays by Roentgen in 1895 and gamma rays by Becquerel in 1896, who found that uranium was fogging the photographic plates, by reducing silver ions into atoms, and finally into tiny metal clusters in the emulsion.

#### C-1.18.1: Principles: Radiolytic reducing species

The interaction of high-energy radiation such as gamma rays with a solution of metals ions induces ionization and excitation of the solvent, and leads to the formation of radiolytic molecular and radical species throughout the solution. For example, in aqueous solutions (1)



H<sup>·</sup> atoms [(H<sup>+</sup>/H<sup>·</sup>) = -1.88 eV at pH 7] and solvated electrons e<sub>aq</sub><sup>-</sup> [(H<sub>2</sub>O/e<sub>aq</sub><sup>-</sup>) = -2.87 eV] [1-2] are strongly reducing agents capable to reduce metal ions to lower valences and finally to metal atoms. For instance, from monovalent cations, metal atoms are formed according to



where M<sup>+</sup> is the symbol for monovalent metal ions, possibly complexed by a ligand. Similarly, multivalent ions are reduced by multistep reactions including intermediate valencies.

Such reduction reactions have been observed directly by pulse radiolysis for many metal ions. Most of their rate constants are known and the reactions are often diffusion-controlled. In contrast, OH<sup>·</sup> radicals (E<sup>0</sup> (HO<sup>·</sup>/H<sub>2</sub>O) = 2.34 eV at pH = 7) [3] are able to oxidize ions or atoms into higher oxidation states and thus to counterbalance the reduction reactions (2) and (3). For this reason, the solution is generally added with an OH<sup>·</sup> radical scavenger. Among

various possible molecules, the preferred choice is to use solutes whose oxidation by  $\text{OH}^\bullet$  creates radicals that are unable to oxidize metal ions but that, in contrast, exhibit themselves a strong reducing power, such as radicals of secondary alcohols or formate anions. The mechanism of gold nanorods formation by radiolysis in CTAB-micellar solutions has already been reported [4] as shown in Figure 1.20.

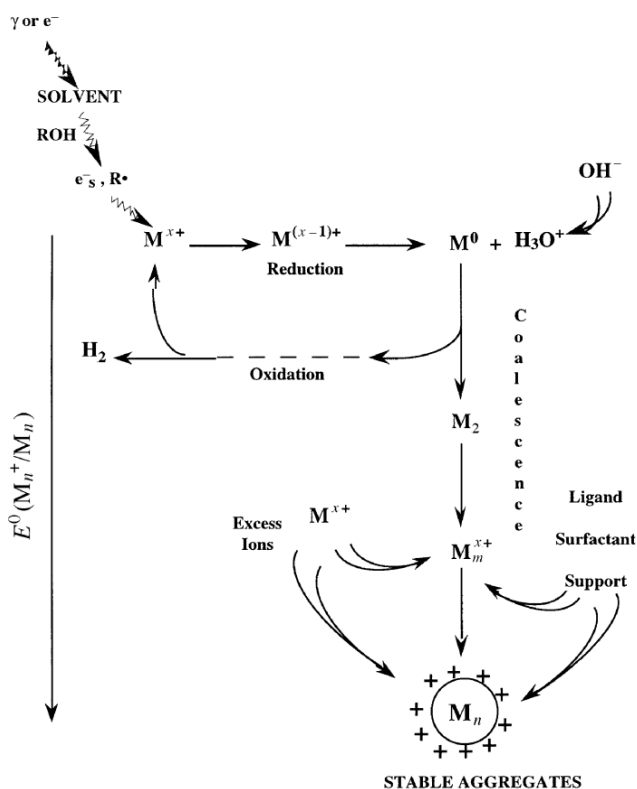


Figure 1.20: Scheme of metal ion reduction in solution by ionizing radiation. The isolated atoms formed coalesce into clusters. They are stabilized by ligands, polymers or supports. The redox potential increases with the nuclearity. The smallest oligomers may undergo reverse corrosion [5].

### **C-1.18.2: Irradiation facilities**

The gamma- irradiation source used in the present work was a  $^{60}\text{Co}$   $\gamma$ -facility of 7000 Curies with a dose rate of  $1.75 \text{ Gys}^{-1}$  ( $6300 \text{ Gyh}^{-1}$ ) at Laboratoire de Chimie Physique (LCP), Orsay. In order to control the size of the metal nanoparticles and to avoid cluster coalescence into large colloids, which eventually precipitate, stabilizing agents must be added to the medium prior to irradiation. Stabilizing agents like, polymers (poly vinyl alcohol PVA, polyacrylate PA) or surfactants (SDS, CTAB) are widely used. In such conditions, small metal clusters

from a few atoms to a few nanometers (less than 2 nm) were successfully stabilized depending on the irradiation conditions.

### **C-1.19: General characterization methods: UV-Vis-NIR Spectroscopy, Transmission Electron Microscopy (TEM) and Dynamic Light Scattering (DLS).**

Characterization is necessary to control nanoparticle synthesis and applications. It is done by using a wide range of techniques, mainly derived from materials science.

#### **C-1.19.1: UV-Vis-NIR Spectroscopy:**

The word ‘spectroscopy’ is used as a generic term for all the analytical techniques based on the interaction of waves and matter. An Ultraviolet- visible -near infrared spectrophotometer is used for optical absorbance and reflectance measurements in the wavelength range (175-2000 nm). In this wavelength range the absorption of the electromagnetic radiation is caused by the excitation (i.e. transition to a higher energy level) of the bonding and non-bonding electrons of the ions or molecules.

The monochromatic light beam is sent on a split mirror which divides the light beam into two separate beams; one of them is used as sample light beam (Intensity  $I$ ) and another is a reference light beam (Intensity  $I_0$ ). The sample light beam is passed through a target sample and the reference light beam is passed through a reference solvent. Photodetectors measure the intensity transmitted from the sample and reference. Spectrophotometry is used for both qualitative and quantitative investigations of samples. The wavelength at the maximum of the absorption band will give information about the structure of the molecule or ion, and the area of the absorption band is proportional to the amount of the absorbing species. The maximum absorption wavelength ( $\lambda_{max}$ ) depends on the presence of particular chromophores (light-absorbing groups) in a molecule. Quantitative measurements are based on Beer’s Law (also known as “Lambert-Beer Law”). In this model, the intensity of the reference beam, which should have little or no light absorption, is defined as  $I_0$ , and the intensity of the sample beam is defined as  $I_1$ . In addition, absorption can be presented either in terms of transmittance ( $T = I_1/I_0$ ) or absorbance ( $A = \log_{10} I_0/I_1$ ). If no absorption occurs,  $T = 1.0$  and  $A = 0$ . The ratio between the incident light intensity and the transmitted light intensity (for a specific

wavelength) is exponentially dependent on the concentration (C) of absorbing molecules (at that specific wavelength) and of the thickness of the sample crossed by the light. Beer-Lambert law is written as:

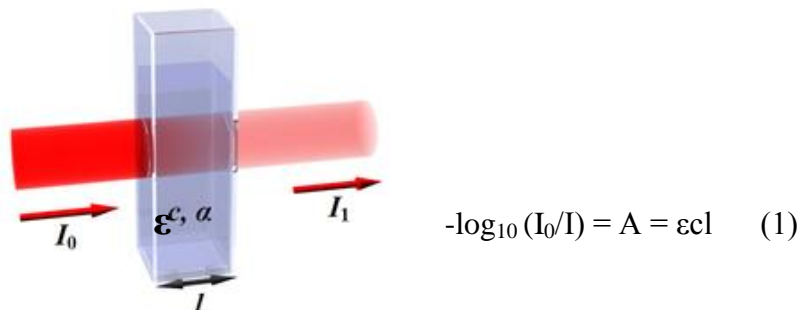


Figure 1.21: Illustration of Beer-Lambert law

Where,

A = absorbance [no units, because it is calculated as  $A = \log_{10} (I_0/I)$ ,  $I_0$  is the incident light's intensity and I is the light intensity after it passes through the sample].

$\epsilon$  = molar absorbance or absorption coefficient [ $\text{dm}^3 \text{mol}^{-1} \text{cm}^{-1}$ ];

c = concentration (molarity) of the compound in the solution [ $\text{mol dm}^{-3}$ ];

l = path length of light in the sample [cm].

(Figure 1.21)

The absorption coefficient  $\epsilon$  is wavelength-dependent, and its variation versus the wavelength describes the absorption spectrum of a material. However, the decreased intensity of the transmitted light can also be due to other effects such as surface reflectance and light scattering. The Beer-Lambert Law tends to break down at very high concentrations, as molecule cannot be considered as non-interacting species. It is also no more valid if the sample scatters light. When light is intense, non-linear optical process can also modify the absorption behavior. The limits of the linear relation in Beer-Lambert Law may be caused by, deviations in absorptivity coefficients at high concentrations ( $>0.01\text{M}$ ) due to electrostatic interactions between molecules in close distance, strong scattering of light in the sample, fluorescence of the sample, and nonlinear effects.

### C-1.19.2: Transmission Electron Microscopy (TEM)

TEM is a microscopy technique which operates on the same basic principles as the optical microscope but uses electrons instead of light. TEM uses electromagnetic lenses to focus the electrons to form a thin beam. The electron beam then travels through an ultra-thin specimen that we want to study. Depending on the density of the material investigated, some of the electrons are scattered and disappear from the beam. At the bottom of the microscope the unscattered electrons hit a fluorescent screen; an image is formed from the interaction of the electrons transmitted through the specimen and the screen. The image is magnified and focused onto an imaging device, such as a fluorescent screen, or a layer of photographic film, or is detected by a sensor such as a CCD camera. TEM is an imaging technique in all areas of biological and biomedical research because of its ability to view the finest structures. The resolution of the TEM can reach 0.2 nm and the magnification can be up to  $6 \times 10^5$ . However, in TEM, the transmission of electron beam is highly dependent on the properties of material to be examined. Such properties include density, composition, etc. For example, porous materials will allow more electrons to pass through, while dense material will allow less. As a result, a specimen with a non-uniform density can be examined by this technique. Figure 1.22 shows a schematic outline of a TEM. A TEM contains four parts: electron source, electromagnetic lens system, sample holder, and imaging system.

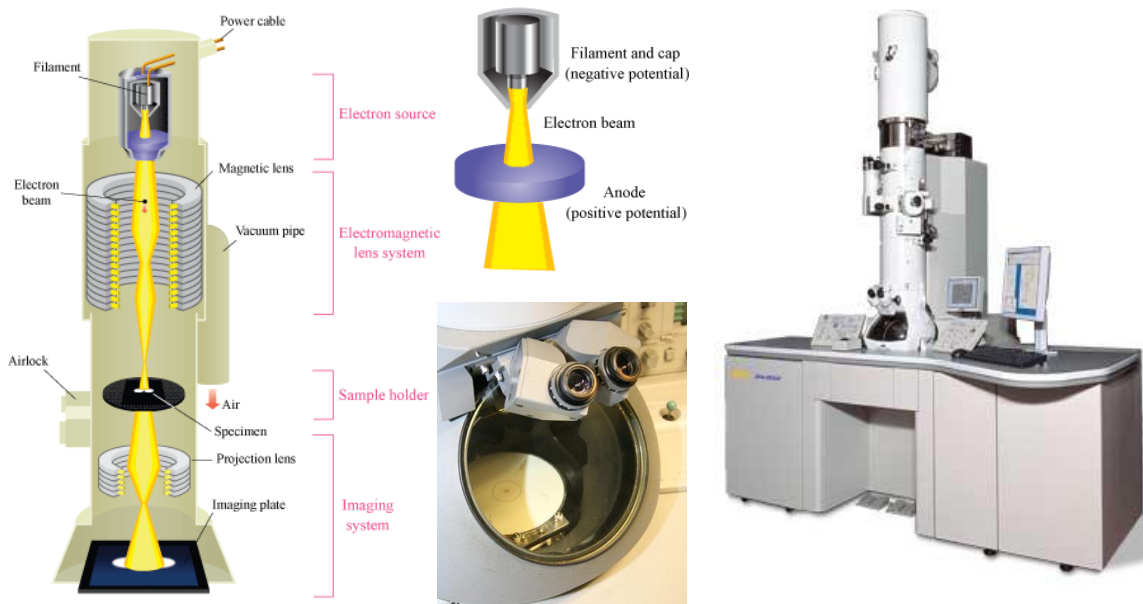


Figure 1.22: (a) Schematic outline of a TEM (b) Electron source of a TEM (c) The imaging system of a TEM (d) Photograph of TEM [6].

**C-1.19.3: Dynamic Light Scattering (DLS)** sometimes also referred to as **Photon Correlation Spectroscopy (PCS)** or **Quasi-Elastic Light Scattering (QELS)**.

DLS is the most versatile, non-invasive, well-established and relevant analytical technique used routinely for measuring in situ sizes, size distributions, and (in some cases) shapes of nanoparticles in liquids. It offers insight concerning the nature of the interactions between particles and their environments, typically in the submicron region. With the latest technology, particles with size lower than 1 nanometer can be investigated [7-12].

Particles, emulsions and molecules in suspension undergo Brownian motion. If the particles or molecules are illuminated with a laser, the intensity of the scattered light fluctuates at a rate depending on the particle size; smaller particles are “kicked” further by solvent molecules and move more rapidly. Analysis of these intensity fluctuations yields the velocity of the Brownian motion and hence the particle size using the Stokes-Einstein relationship (Kuebler).

$$D = k_B T / 6\pi\eta r \quad (2)$$

where  $r$  is the particle radius,  $k_B$  is the Boltzmann constant ( $k = 1.38 \times 10^{-23} / \text{JK}^{-1}$ ),  $T$  is the temperature and  $\eta$  is the viscosity of the solvent.

The DLS software displays the particle population for different diameters. If the system is monodisperse, there should only be one population with one unique diameter value, whereas a polydisperse system would show particle populations with different diameters. The diameter measured in DLS is called the hydrodynamic diameter and refers to how a particle diffuses within a fluid. The diameter obtained by this technique is that of a sphere that has the same translational diffusion coefficient as the particle being measured. The translational diffusion coefficient will depend not only on the size of the particle “core”, but also on any surface structure, as well as the concentration and type of ions present in the medium. This means that the size can be larger than that measured by electron microscopy.

### Advantages of Dynamic Light Scattering technology

- Relatively cheap technique
- Accurate, reliable and repeatable particle size analysis in one or two minutes
- Mean size only requires knowledge of the viscosity of the liquid
- Simple or no sample preparation, high concentration, turbid samples can be measured directly
- Size measurement of sizes  $< 1\text{nm}$
- Low volume requirement (as little as  $12\mu\text{L}$ )

### **C-1.20: Instrumentation: NLO techniques for molecular engineering**

The two most commonly used powerful tools to characterize molecular first-order hyperpolarizability of different chromophores and nanoparticles in solutions are Harmonic Light Scattering (HLS) [13-15] and Electric Field Induced Second Harmonic Generation (EFISH) [16-18]. EFISH measures the scalar product of dipole moment ( $\mu$ ) and the vector part of the hyperpolarizability tensor ( $\beta$ ), while HLS measures an orientational spatial average of the  $\beta$ . The great advantage of HLS as compare to EFISH is the absence of an orienting electric field used to reduce the intrinsic symmetry of an isotropic solution [19]. Therefore, non-dipolar or ionic species can be investigated. The HLS technique allows the determination of  $\beta$  for different types of chromophores such as ionic species, dipolar, and octupolar [20–22]. In contrast, EFISH may only be applied to dipolar and neutral chromophores but typically displays better signal-to-noise ratios due to the fact that the harmonic emitted light is coherent. Moreover, the sign of  $\beta$  can be determined [23-24]. Several publications report on second harmonic scattering in macroscopically isotropic media along with a theoretical description of the phenomenon [25-28]. Many researchers, starting with Maker [14] employed this HLS scattering method for determining the first-order hyperpolarizability of organic molecules in liquid solution [15, 29].

#### **1.20.1: Electric Field-Induced Second-Harmonic Generation (EFISH) at $1.907\ \mu\text{m}$**

The Electric-Field-Induced Second Harmonic Generation (EFISH) technique has been widely used to measure the quadratic hyperpolarizability of NLO polar molecules [30] and

has been considered as the most suitable technique for the screening and development of molecular systems with NLO properties since the early 1970s. In EFISH experiments, hyperpolarizability is evaluated by measuring  $I^{2\omega}$  generated from a chromophore solution under the influence of a strong static electric field  $E^0$ . When the solution is under the combined influence of an optical laser field  $E^\omega$  and of a static  $E^0$ , the solution becomes noncentrosymmetric and a laser beam interacting with the solution produces a coherent second-harmonic (SH) signal. The macroscopic polarization at the SH frequency is defined by

$$P_i^{2\omega} = \beta_{ijk} E_j^\omega E_k^\omega + \gamma_{ijkl} E_j^\omega E_k^\omega E_l^0 \quad (3)$$

Where  $i, j, k, l$  refer to molecular axes ( $x, y, z$ ),  $\beta_{ijk}$  and  $\gamma_{ijkl}$  being respectively the second – and third-order hyperpolarizability tensor components of the molecule.

EFISH experiments have been performed at 1.907  $\mu\text{m}$ , using a commercial (SAGA from Thales Laser) Q-switched  $\text{Nd}^{3+}$ : YAG nanosecond laser operating at  $\lambda = 1.064 \mu\text{m}$ , 10 Hz repetition rate. The pulse duration is 9 ns. The 1.064  $\mu\text{m}$  laser beam is then focused into a 50 cm long hydrogen Raman cell of high hydrogen pressure ( $\text{H}_2 = 55 \text{ bar}$ ) which shifts the fundamental beam to  $\lambda = 1.907 \mu\text{m}$  by stimulated Raman scattering. Only the back scattered 1.907  $\mu\text{m}$  Raman emission was collected by use of a dichroic mirror in order to eliminate most of the residual 1.064  $\mu\text{m}$  pump photons. A Schott RG 1000 filter is used to filter out any remaining visible light from the laser flash lamp and antistokes emission. Suitable attenuators are used to control the power of the incident beam which is focused into the EFISH cell with a 20 cm focal length lens. The input polarization is controlled by a half-wave plate and a Glan polarizer.

The measurements are carried out into a wedged shaped cell, constituted by two thick fused quartz windows assembled on a stainless steel holder. The inter-electrode distance is 2 mm, giving a pulsed electric field (5 KV) synchronized with laser pulse. The EFISH cell follows the classic design of Levine and Bethea who performed the first experiments with a wedge cell to determine the SHG in solution in 1975 [31]. The whole cell is translated perpendicular to the incident beam to produce a periodic second harmonic generation signal (Maker

fringes). The schematic diagram of the EFISH experimental setup is shown in Figure 1.23 (a), together with the sketch of the EFISH measurement cell (1.23 b) and an example of a SHG signal plotted as a function of the cell displacement (1.23 c). The windows are the most delicate part of the system, in fact, if the laser beam is not perfectly focused in the center of the cell, they can be damaged by the laser impact. For this reason the main radiation is, at first, attenuated with filters and then focused on the right position after preliminary alignment using a He-Ne laser.

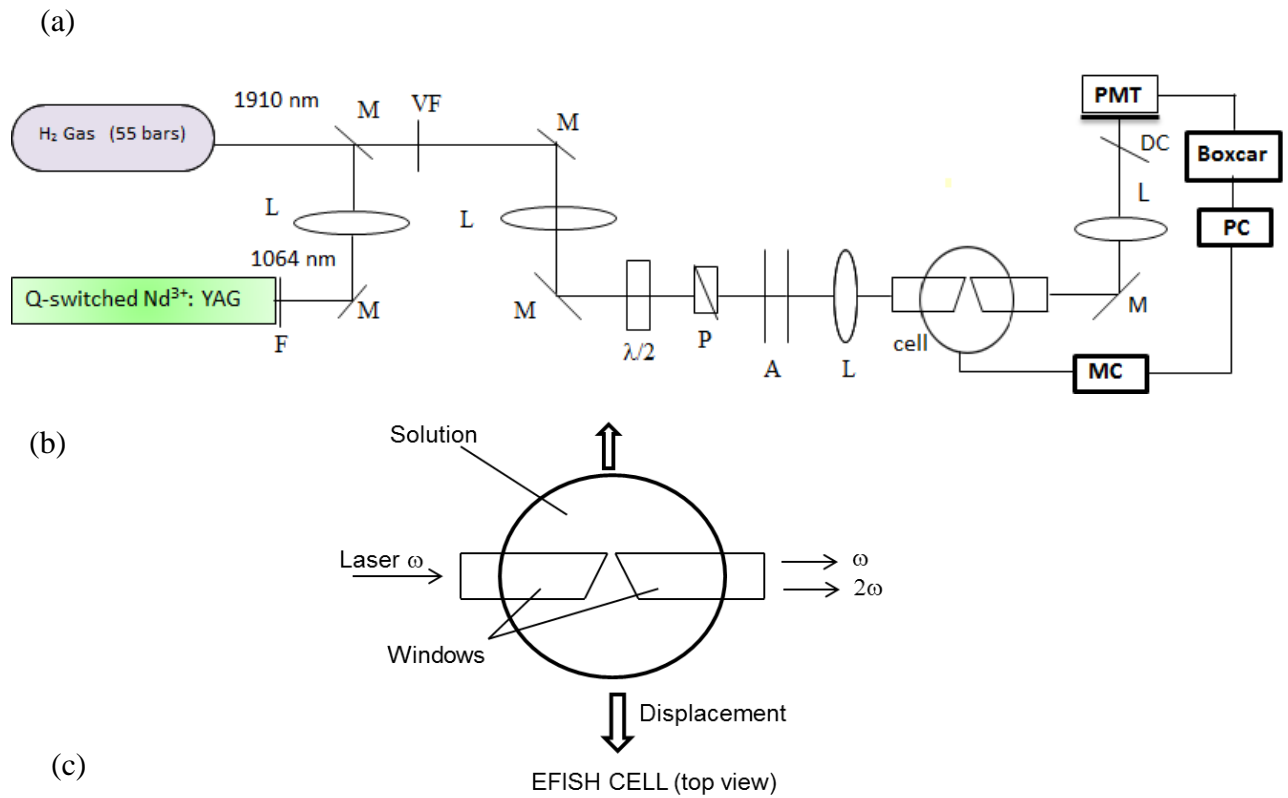


*Figure 1.23: (a) EFISH Experimental Set-up at 1.907  $\mu\text{m}$ . [F: Filter; M: Mirrors; L: Lens;  $\lambda/2$ : Half wave plate; P: Polarizer; A: Attenuator; PMT: Photomultiplier tube; DC: dichroic mirror; MC: Micro controller; PC: personal computer]. (b) EFISH measurement cell (c) Excel plot of the SHG signal from dichloromethane solvent as a function of cell displacement.*

In this technique, molecules are aligned by the pulsed high voltage (5 kV, pulse width 200  $\mu\text{s}$ ) synchronized with the laser beam pulse to the cell. This “poling” field is applied to break the statistical centrosymmetry of the solution by dipolar orientation of solvent and of chromophore molecules. Two output radiations are observed, the fundamental beam ( $\omega$ ) and a second harmonic ( $2\omega$ ) generated by the interaction between the laser and the sample. The fundamental radiation is removed by filters, and only the second harmonic radiation is detected by a photomultiplier, connected to a high-speed boxcar integrator card and processed by a home-made computer program to calculate the interfringe distance and the fringe amplitude. These data are then used to calculate the  $\vec{\mu} \cdot \vec{\beta}_{vec}$  value of the sample. The intensity of this harmonic radiation depends on the nonlinear first-order hyperpolarizability  $\beta$  of the sample molecules.

In EFISH experiments, the fundamental beam is polarized along the direction of the applied field. Therefore the generated second harmonic will also be polarized along this direction, because of the symmetry properties of a  $C_\infty$  symmetry medium. The resulting quadratic susceptibility takes the following form  $\chi^{(2)} = NF\gamma E^o$  where

$$\gamma = \gamma_e + \frac{\mu \cdot \beta}{5kT} \quad (4)$$

where  $N$  is the number of molecules per volume unit,  $F$  is the local field factor,  $\mu$  the ground state dipole moment of the molecule,  $\gamma$  is the global EFISH hyperpolarizability, i.e. the sum of a purely electronic cubic contribution  $\gamma_e$  and a quadratic, orientational one  $\mu \cdot \beta / 5kT$ . The  $\mu\beta$  value of the investigated chromophore can then be inferred from the amplitude and period of the resulting so-called ‘Maker Fringes’, as the cubic contribution  $\gamma_e$  can be usually neglected. The necessity to use a wedged shape cell and to measure the intensity of harmonic radiation  $2\omega$  as a function of the cell displacement is related to the phase shift between the fundamental

and harmonic waves into the medium. Upon cell translation, the intensity of the second harmonic radiation is modulated as interference fringes, known as Maker fringes.

The width and the periodicity of the fringes are correlated to the macroscopic susceptibility  $\Gamma(x)$  of the solution that depends on  $I^{2\omega}$  and on the coherence length  $l_c(x)$ , according to this relation

$$\Gamma(x) = \frac{1}{l_c(x)} \cdot \left[ A \cdot \frac{\sqrt{I^{2\omega}(x)}}{I^{2\omega}(0)} \cdot \frac{E(0)}{E(x)} + B \right] \cdot 10^{-12} \text{ esu} \quad (5)$$

Where  $I^{2\omega}(x)$  is the intensity of the harmonic at the concentration (0 is the solvent),  $E(x)$  is the intensity of the electric field, A and B are constants depending on the solvent and the windows. The microscopic  $\gamma_{\text{EFISH}}$  value can be inferred from macroscopic susceptibilities of the solvent  $\Gamma(0)$  and of the solute  $\Gamma(x)$ , according to:

Since as,

$$\gamma_{\text{EFISH}} = \frac{M}{\rho N_A f x} \cdot [(1+x)\Gamma(x) - \Gamma(0)] \quad (6)$$

Where  $N_A$  is the Avogadro's number ( $6.02 \times 10^{23}$ ), M the molecular weight of the compound,  $\rho$  the density of the solvent, x the molar fraction of the compound and f a local field correction factor. It is then possible to obtain the  $\beta$  value from  $\gamma_{\text{EFISH}}$  and Eq (4). Since the contribution of the third order hyperpolarizability  $\gamma_e$  at  $2\omega$  is usually lower than the contribution of the second order, generally  $\gamma_e$  can be ignored. In this way the  $\mu_0\beta_{\text{vec}}$  value can be inferred directly from the  $\gamma_{\text{EFISH}}$  value.

EFISH then provides the value of the scalar product  $\mu\beta$ , where  $\mu$  represents the ground state molecular dipole moment and  $\beta$  is the projection of the vectorial component of the tensor of the quadratic hyperpolarizability along the dipole moment axis. The ground state dipole moment can be measured independently and so  $\beta$  can be calculated by EFISH measurement. It is important to work in a non-absorbing, or at least weakly absorbing medium, for this reason we work systematically at a fundamental wavelength of 1.907  $\mu\text{m}$ , so that the values of second harmonic radiations  $2\omega$  (0.950  $\mu\text{m}$ ) are remote from the absorption bands ( $\pi \rightarrow \pi^*$ ,

CT, MLCT and/or LLCT) of the studied organic or organometallic molecules (generally these bands are not beyond 0.6-0.8  $\mu\text{m}$ ). The most common solvents used for  $\beta$  measurements at 1.907  $\mu\text{m}$  reported in the literature are dichloromethane or chloroform. The compounds were dissolved in chloroform or dichloromethane at various concentrations (up to  $\sim 10^{-2}$  mol L<sup>-1</sup>). The measurement cell has a volume of 4 millilitres. The measurements are carried out in CH<sub>2</sub>Cl<sub>2</sub> or CHCl<sub>3</sub> solution (but sometimes in acetonitrile). First, a scan for the pure solvent is performed, and then the compound solution is measured. Each measurement is processed to calculate the interfringe and the fringe amplitude. The measurements of solvent and sample solution were repeated five times, resulting in average amplitude values used to calculate the  $\mu\beta$  value. In this way possible errors due to the decrease of the energy of the incident radiation during the measurement are minimized. After each scan the cell is carefully washed (it is possible to use any solvent, but it is necessary to rinse the cell with CH<sub>2</sub>Cl<sub>2</sub> before the new measurement) and dried with compress air.

HLS and EFISH both exhibit complications that contribute to significant uncertainties in measurement of  $\beta$  values [32-34]. For example absorption by the sample at the fundamental or second harmonic wavelengths (often referred to as self-absorption) can attenuate the amount of the HLS or EFISH signal produced, thus leading to an underestimation of  $\beta$  value. Using Beer-Lambert correction factors, one can minimize this problem as far as the concentration is not too high [35]. More complicated issues include the presence of resonant effects such as two-photon absorption and emission. Two photon induced fluorescence (TPF) often mix-up with second harmonic wavelength for HLS measurements. It appears as an experimental “noise,” and this can lead to serious experimental error, then it limiting the applicability of the technique [15, 29]. Several methods have been used to address the problems of Stokes fluorescence and TPF, including spectrally resolving the scattered light, using a picosecond or femtosecond laser to separate the fluorescence in the time domain, or using a high repetition rate femtosecond laser to suppress the fluorescence [35]. A number of approaches to avoid and to separate TPF from SH signal have been developed and reported, including spectroscopic correction using emission spectra [33], fluorescence quenching using a fluorescence quencher [36], and to avoid fluorescence using long excitation wavelength [37]. In this work we used this latter method. The determination of Zero-frequency

hyperpolarizability,  $\beta_{ijk}(0)$ , is important in order to perform molecular comparisons, to compare to theoretical models, and to relate hyperpolarizabilities derived from SHG-based experiments (HLS and EFISH) to values relevant to the electro optic effect. The simple two-state dispersion model (TSM) derived by Oudar and Chemla for  $\beta$  is widely used to deduce  $\beta_{ijk}(0)$  from experimental values [38].

### **C-1.20.2: Third Harmonic Generation (THG)**

One step beyond SHG is third-harmonic generation (THG), in which three photons at  $\omega$  frequency form a new photon at  $3\omega$ . In non-centrosymmetric media, THG can use two successive second order nonlinear steps. This indirect conversion process requires lower input laser intensity and can result in higher conversion efficiencies as compared to direct conversion which utilizes the third order nonlinearity of the medium. The generated SH field ( $2\omega$ ) in the first step will couple with the unconverted fundamental beam ( $\omega$ ) and generates a new frequency component at  $3\omega$  as shown in Figure 1.24. The conversion efficiency varies with the different frequency processes, the nonlinear material and high power laser sources.

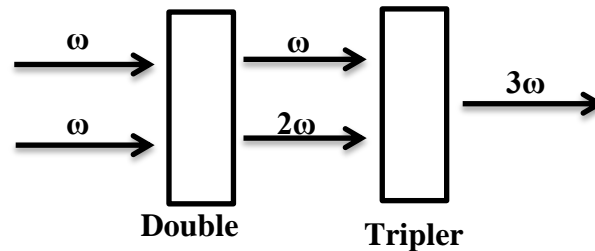


*Figure 1.24: Geometry of Third harmonic generation*

In the present work, we have investigated the real third-order molecular hyperpolarizabilities  $\gamma_e$ , by direct THG. Therefore, the medium must remain centrosymmetric.

The experimental set-up for THG is same as used for EFISH, the only difference is that here we do not apply any static field  $E_Z^0$ . In addition, we must replace the filter used in front of the PMT so that we can collect only the third harmonic response.

The coupling of three components of the incident field  $E_Z^\omega$  in the centrosymmetric solution leads to the formation of polarization at  $3\omega$  by a third order process

$$P_Z^{(3)}(3\omega) = \epsilon_0 \chi_{ZZZZ}^{(3)}(-3\omega; \omega, \omega, \omega) (E_Z^\omega)^3 \quad (7)$$

For a homogenous medium, the susceptibility and hyperpolarizability are linked by

$$\chi_{THG}^3 = \chi_{ZZZZ}^3(-3\omega; \omega, \omega, \omega) = N^* (f^\omega)^3 Y_{THG} \quad (8)$$

Where

$$Y_{THG} = \langle Y_{ZZZZ}(-3\omega; \omega, \omega, \omega) \rangle \quad (9)$$

For an isotropic medium, the orientational distribution function adapted is given by

$$\gamma_{THG} = \frac{1}{5} (\gamma_{xxxx} + \gamma_{yyyy} + \gamma_{zzzz} + 2\gamma_{xxyy} + 2\gamma_{xxzz} + 2\gamma_{yyzz}) \quad (10)$$

Note that the hyperpolarizability  $\gamma_{THG}(-3\omega; \omega, \omega, \omega)$  as measured by THG and the electronic contribution  $\gamma_e(-2\omega; \omega, \omega, 0)$  obtained by EFISH may be of the same order of the magnitude.

As shown in the intensity expression (11), the third harmonic signal at the output of the cell has a periodicity equal to  $2L_c$

$$I^{3\omega} = I_0 \sin\left(\frac{\pi L}{2L_c}\right) \quad \text{Where,} \quad L_c = \frac{\lambda}{6(n_\omega^2 - n_{3\omega}^2)} \quad (11)$$

Similarly to the results obtained from the EFISH experiment,

$$\chi_{THG,s}^3(x) = \chi_{THG,q}^3 + \sqrt{\frac{I_0^{3\omega}(x) L_c(0)}{I_0^{3\omega}(x0) L_c(x)}} \left( \chi_{THG,s}^{(3)}(0) - \chi_{THG,q}^{(3)} \right) \quad (12)$$

and

$$Y_{THG,solute} = \frac{M_{solute}}{(f^{3\omega})(f^\omega)^3 N_{A\rho}} \left( (1+x) \chi_{THG,s}^{(3)}(x) - \chi_{THG,s}^{(3)}(0) \right) \quad (13)$$

Usually, organic systems have limited transparency towards the UV spectral range therefore; the selection of the wavelength should first be made so that the third harmonic signal does

not fall in the UV-visible region of high absorption. For this reason, we can use fundamental wavelength at 1.9  $\mu\text{m}$  in order to avoid strong absorption in the UV blue region.

### **C-1.20.2: Harmonic Light Scattering at 1.907 $\mu\text{m}$**

If a solution containing acentric molecules or nanoparticles of interest is illuminated with photons of frequency  $\omega$  and intensity  $I^\omega$ , an incoherent second harmonic signal is emitted, corresponding to HLS or nonlinear light scattering. The observed  $I^{2\omega}$  is directly related to the orientationally averaged hyperpolarizability,  $\beta_{HLS}(-2\omega; \omega, \omega)$ . HLS in solution is the only technique capable of providing experimental data on the NLO properties of octupolar or ionic molecules.

A schematic diagram of the experimental apparatus for the HLS measurement at 1.907  $\mu\text{m}$  is shown in Figure 1.25. The 1.064  $\mu\text{m}$  laser beam is emitted by a Q-switched  $\text{Nd}^{3+}$ :YAG nanosecond laser (SAGA from Thales Laser) at 10 Hz repetition rate. The typical energy per pulse at 1.907  $\mu\text{m}$  is 7 mJ peak powers. A Schott RG 1000 filter is used to filter out any remaining visible light from the laser flash lamps and from antistokes emission.

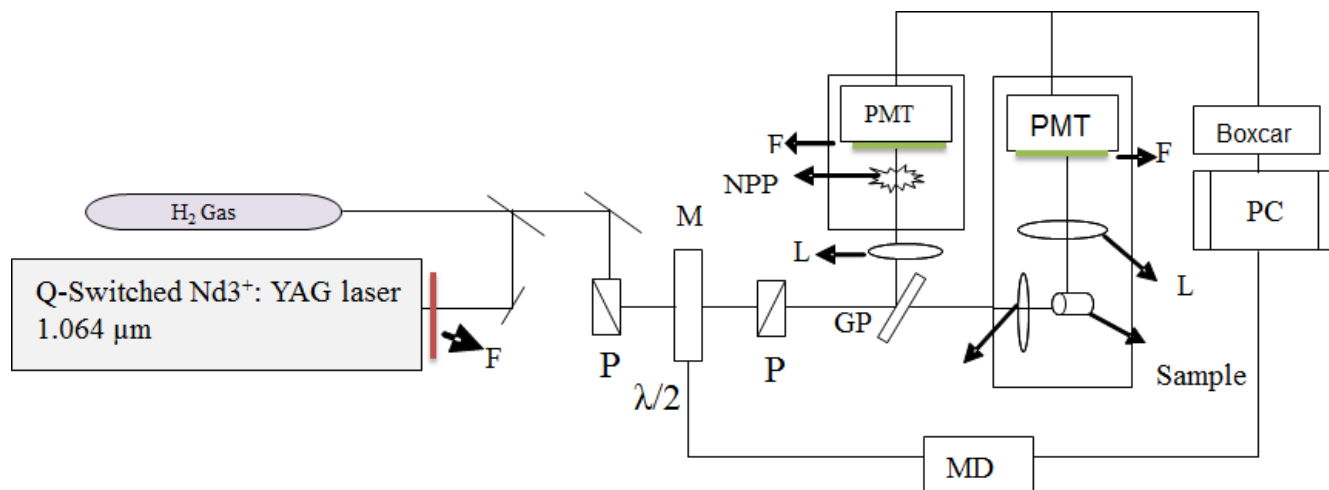


*Figure 1.25: Schematic representation of HLS at 1.907  $\mu\text{m}$ . F: Filter; M: Mirrors; L: Lens;  $\lambda/2$ : Half wave plate; P: Polarizer; A: Attenuator; PMT: Photomultiplier tube; MD: Motor Driver; PC: personal computer and NPP: Reference material.*

The intensity of the incoming fundamental beam is varied using a half-wave plate rotated between two crossed polarizers. HLS photons at 954 nm, collected at 90° of the sample cell

are focused onto a photomultiplier using two collecting lenses. The detected signal is then sampled and averaged using a Stanford research system boxcar integrator and processed by a computer. A low intensity reference beam is extracted from the main beam at a 45° incidence angle by a glass plate and focused onto a highly nonlinear NPP (N-4-nitrophenyl-prolinol) powder used as a frequency doubler. The variation of the second harmonic intensity scattered from the solution is recorded on the computer as a function of the reference second harmonic signal provided by the NPP powder, both signals scaling as the square of the incoming fundamental intensity. Figure 1.26 shows the second harmonic intensity observed from a reference Ethyl violet (ETV) solution plotted with respect to the SH intensity collected from the NPP powder (frequency doubler) at a 1907 nm fundamental wavelength.

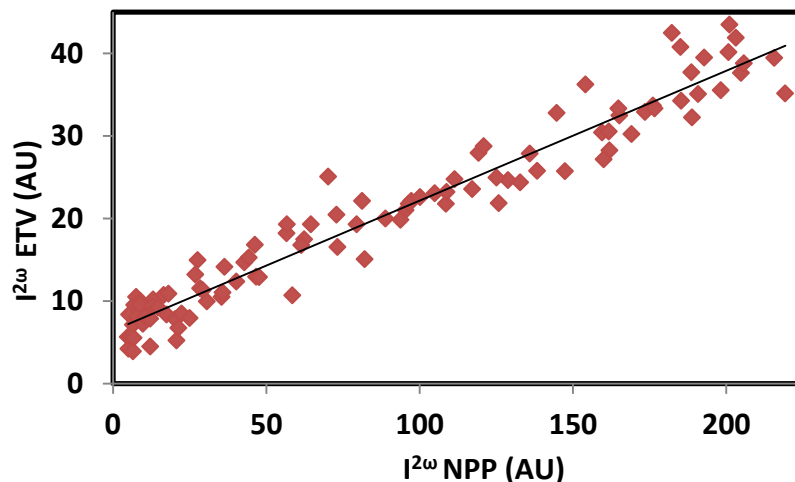


*Figure 1.26: Second harmonic intensity recorded from ETV is plotted with respect to the SH intensity collected from the NPP powder (frequency doubler) at 1907 nm fundamental wavelength.*

The intensity of the second-harmonic ( $I^{2\omega}$ ) light is proportional to the number of scattering centers ( $N$ ), the square of the first hyperpolarizability ( $\beta^2$ ) and the square of the intensity of harmonic light ( $I_\omega^2$ ). For a solvent (s) and analyte (a) combination the following relation has been derived:

$$I^{2\omega} = g(N_s \langle \beta_s^2 \rangle + N_a \langle \beta_a^2 \rangle) I_\omega^2 \quad (14)$$

where  $g$  is a geometry factor,  $N_s$  and  $N_a$  are the number of solvent ( or reference solution) and analyte molecules per unit volume, respectively;  $\beta_s$  and  $\beta_a$  are the molecular hyperpolarizability of the solvent (or the reference molecule) and analyte molecule, respectively. The slopes  $P$  of the lines obtained from the variation of  $I^{2\omega}$  as a function of  $I_{NPP}^{2\omega}$  are given by

$$p(\text{solute}) = \frac{I_s^{2\omega}}{(I^\omega)^2} \propto N_s \langle \beta^2 \rangle_s \quad (15)$$

However, at 1.907  $\mu\text{m}$ , the signal generated by the solvent is generally not detectable. It is necessary to use as a reference a solution of highly NLO molecule whose  $\beta$  is known. Ethyl violet (ETV) is chosen as this reference molecule. The slope of this ETV molecule is given by

$$p(\text{ETV}) = \frac{I_{\text{ETV}}^{2\omega}}{(I^\omega)^2} \propto N_{\text{ETV}} \langle \beta^2 \rangle_{\text{ETV}} \quad (16)$$

We measure successively the signal emitted by the ethyl violet and the molecule we want to characterize the solute. By neglecting the quadratic hyperpolarizability of the solvent with respect to that of the solute, the obtained ratio between the slope of the unknown solution and that of ETV solution is given by

$$\frac{p(\text{solution})}{p(\text{ETV})} = \frac{N^*(\text{solute})}{N^*(\text{ETV})} \times \frac{\beta_{\text{HLS}}^2(\text{solute})}{\beta_{\text{HLS}}^2(\text{ETV})} \quad (17)$$

Finally,  $\beta$  solution is given by

$$\beta(\text{solution}) = \beta_{\text{HLS}}(\text{ETV}) \sqrt{\left(\frac{N^*(\text{ETV})}{N^*(\text{solute})}\right) \left(\frac{p(\text{solution})}{p(\text{ETV})}\right)} \quad (18)$$

Solvents like chloroform, dichloromethane, dimethylformamide have been used to dissolve the different compounds at various concentrations (up to  $\sim 2 \times 10^{-2}$  mol L<sup>-1</sup>). The sample solutions to be measured were first filtered with 0.2/0.45  $\mu\text{m}$  filters to eliminate small dust

particles which can be burned by the laser beam and induce parasitic optical signals. Afterwards, about 3.5 ml of the solution were poured into a 1 cm long quartz cuvette, which is placed at the focus of the incoming fundamental beam. Our reference sample is ethyl violet, whose  $\beta$  value at 1.907  $\mu\text{m}$  has been measured with respect to the know  $\beta$  value of  $[\text{Ru}(\text{bpy})_3]^{2+}$  ( $\beta_{[\text{Ru}(\text{bpy})_3]^{2+}} = 320 \times 10^{-30}$  [39]). The observed  $\beta$  value of ethyl violet is  $\beta_{\text{ETV}} = 170 \times 10^{-30}$  esu. The concentration used range from  $3 \times 10^{-3}$  to  $10^{-2}$   $\text{molL}^{-1}$ . It must be noted that most classical organic solvents are not transparent at 1.91  $\mu\text{m}$ ; only chlorinated solvents are an exception. Hence most of the experiments have been done by the use of dichloromethane or chloroform for the HLS measurements.

#### **C-1.20.4: HLS at 1.064 $\mu\text{m}$**

The measurement of SHG from AuNPs is done at 1.064  $\mu\text{m}$ . Here we do not need to use Raman cell to increase the wavelength, hence the beam coming from the laser is directly sent onto the half wave plate placed between the two crossed polarizers. An interference filter is used to collect only second harmonic at 532 nm. The second harmonic intensity collected from the solvent by the photomultiplier can be written as

$$I^{2\omega}(\text{solvent}) = G(\text{solvent})N^*(\text{solvent}) \beta_{\text{HLS}}^2(\text{solvent})(I^\omega)^2 \quad (19)$$

Similarly, the second harmonic signal collected from the reference material (NPP powder) is

$$I^{2\omega}(\text{NPP}) = K(\text{NPP})(I^\omega)^2 \quad (20)$$

The acquisition program system provides the ratio of the slopes obtained by  $I^{2\omega}$  as a function of  $I^\omega$

$$p(\text{solvent}) = G(\text{solvent})N^*(\text{solvent}) \frac{\beta_{\text{HLS}}^2(\text{solvent})}{K(\text{NPP})} \quad (21)$$

In the second step, we change the solvent cell with the cell containing the solution of the molecule to be investigated. By considering that the molecules of solute are completely dissolved in the solvent and that the emission of the scattered second harmonic intensity by the solution is described by an additive model, we have

$$I^{2\omega}(\text{solution}) = G(\text{solution})[N^*(\text{solvent})\beta_{\text{HLS}}^2(\text{solvent}) + N^*(\text{solute})\beta_{\text{HLS}}^2(\text{solute})](I^\omega)^2 \quad (22)$$

The slope of the solution is then given by

$$p(\text{solution}) = G(\text{solution}) \frac{[N^*(\text{solvent})\beta_{\text{HLS}}^2(\text{solvent}) + N^*(\text{solute})\beta_{\text{HLS}}^2(\text{solute})]}{K(\text{NPP})} \quad (23)$$

In the hypothesis, where  $G(\text{solvent}) \approx G(\text{solution})$  (assuming a small difference between the local field of solution and of the pure solvent), the ratio of the two slopes can be obtained

$$\frac{p(\text{solution})}{p(\text{solvent})} = \frac{[N^*(\text{solvent})\beta_{\text{HLS}}^2(\text{solvent}) + N^*(\text{solute})\beta_{\text{HLS}}^2(\text{solute})]}{N^*(\text{solvent})\beta_{\text{HLS}}^2} \quad (24)$$

Therefore,

$$\beta_{\text{HLS}}(\text{solute}) = \beta_{\text{HLS}}(\text{solvent}) \sqrt{\frac{N^*(\text{solvent})}{N^*(\text{solute})} \left[ \frac{p(\text{solution})}{p(\text{solvent})} - 1 \right]} \quad (25)$$

Knowing the  $\beta$  value of the solvent, we deduce the  $\beta$  value of the solute.

Figure 1.27 shows the SH intensity observed from water is plotted with respect to the SH intensity collected from the NPP powder (frequency doubler) at 1064 nm fundamental wavelength.

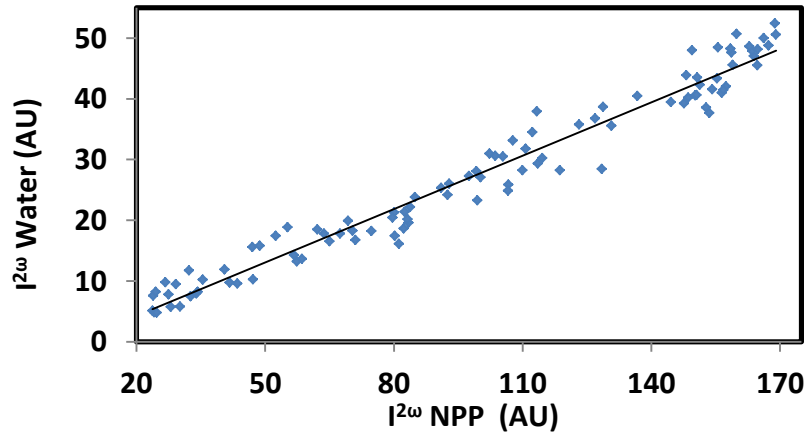


Figure 1.27: Second harmonic intensity recorded from water is plotted with respect to the SH intensity collected from the NPP powder (frequency doubler) at 1064 nm fundamental wavelength.

### **C-1.21: Variable incident polarization in HLS experiments at 1.064 $\mu\text{m}$**

Variable incident polarization has been implemented to provide a direct measurement of the nonlinear anisotropy from a simple analysis of the harmonic scattering depolarization ratio. The HLS experiment has been adapted to allow for polarization dependent measurements as shown in Figure 1.28.

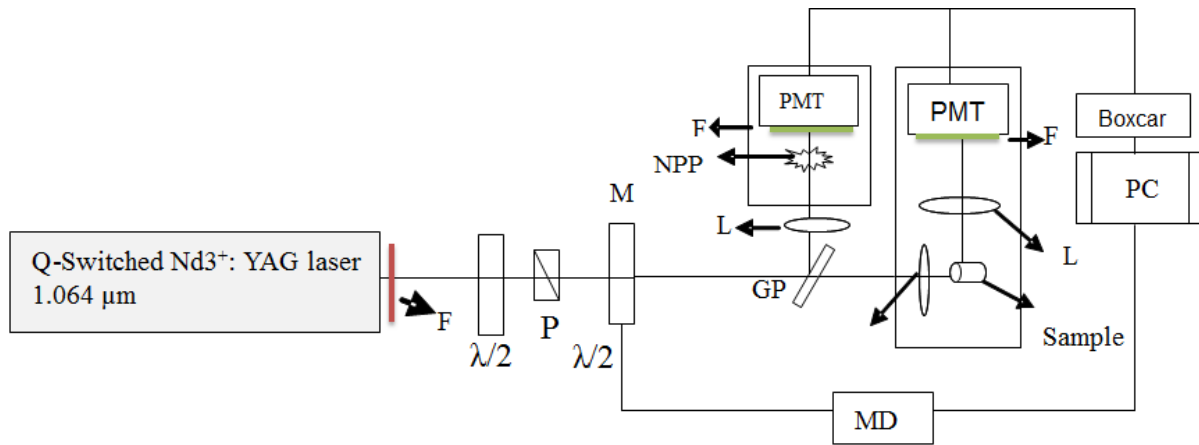


Figure 1.28: Schematic representation of Variable incident polarization in HLS (VIP-HLS) at 1.064  $\mu\text{m}$ . F: Filter; M: Mirrors; L: Lens;  $\lambda/2$ : Half wave plate; P: Polarizer; A: Attenuator; PMT: Photomultiplier tube; MD: Motor Driver; PC: personal computer and NPP: Reference material.

The constant incident intensity is monitored by a half-wave plate and a Glan polarizer, and the fundamental polarization is controlled by the rotation of a second half wave plate. The second harmonic signal emitted by a NPP powder and detected by a photomultiplier serves as a reference so as to level off short and long term fluctuations. The fundamental beam is focused into a cell which contains the filtered solutions, and the scattered harmonic signal is collected and focused on a second photomultiplier by two symmetrically set identical converging lenses. Different polarization configurations as shown in Figure 1.29 are being used to evaluate the  $\langle \beta^2 \rangle_{IJKLMN}$  macroscopic components which subsequently permit to retrieve the nonlinear anisotropy. For all configurations with perpendicular incident and scattered polarizations, the resulting scattered harmonic intensity is proportional to the same

$\langle \beta_{ZXX}^2 \rangle$  averaged square tensor coefficient. A variable incident polarization VIP-HLS experiment without analyzer is therefore sufficient to infer the two independent coefficients  $\langle \beta_{XXX}^2 \rangle$  and  $\langle \beta_{ZXX}^2 \rangle$  from the measurement of the overall scattered harmonic intensity.

$$I_X^{2\omega} + I_Z^{2\omega} = (\langle \beta_{XXX}^2 \rangle + \langle \beta_{ZXX}^2 \rangle) \cos^2 \phi + 2 \langle \beta_{ZXX}^2 \rangle \sin^2 \phi \quad (26)$$

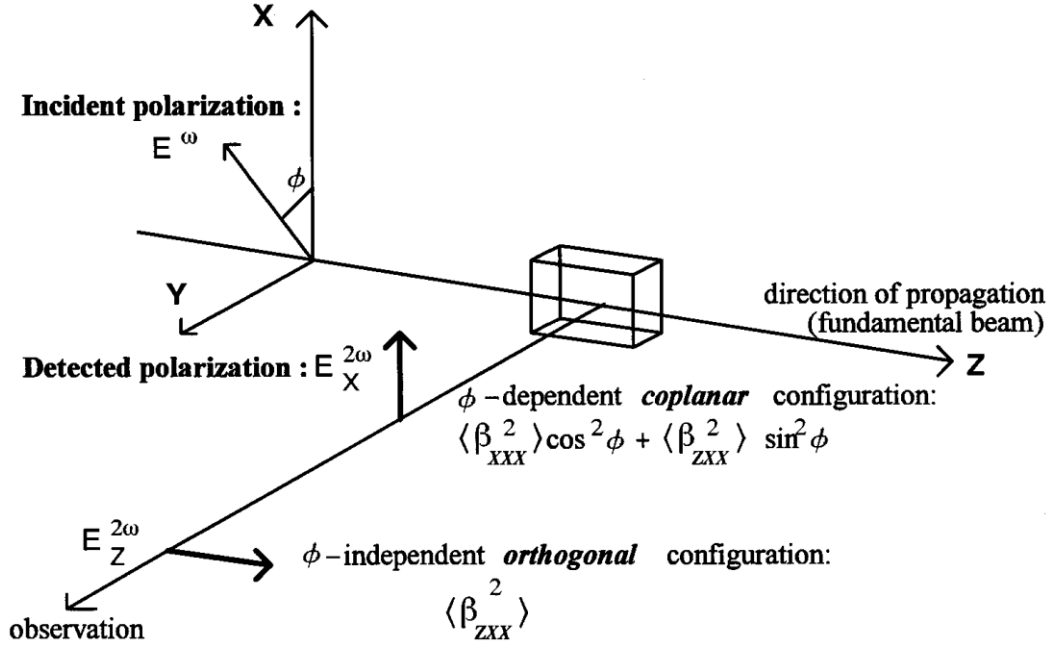


Figure 1.29: Fundamental incoming beam propagating along Z and polarized in the (X, Y) plane. The observation direction is along Y, and polarization state of SH along X or Z plane.

We may choose to measure individual components or  $I_X^{2\omega}$  or  $I_Z^{2\omega}$  scattering intensities by just adding a polarizer before the half waveplate in the corresponding direction. We then have access to the depolarization ratio (D) defined by,

$$D = \frac{I_{2\omega}(\varphi=90^\circ)}{I_{2\omega}(\varphi=0^\circ)} = \frac{\langle \beta_{ZXX}^2 \rangle}{\langle \beta_{XXX}^2 \rangle} \quad (27)$$

Moreover, the two independent Cartesian components  $\beta_{ZXX}$  and  $\beta_{XXX}$  are related to the norms of the octupolar  $\beta_{J=3}$  and dipolar  $\beta_{J=1}$  components by

$$\langle \beta_{ZXX}^2 \rangle = \frac{1}{45} \left( \|\beta_{J=1}\|^2 + \frac{12}{7} \|\beta_{J=3}\|^2 \right) \quad (28)$$

$$\langle \beta_{XXX}^2 \rangle = \frac{1}{35} \left( 7\|\beta_{J=1}\|^2 + 2\|\beta_{J=3}\|^2 \right) \quad (29)$$

Thus, the extend of depolarization factor gives access to the molecular anisotropy

$\rho^2 = \frac{\|\beta_{J=3}\|^2}{\|\beta_{J=1}\|^2}$  or  $\rho = \frac{\|\beta_{J=3}\|}{\|\beta_{J=1}\|}$  both factors being linked by

$$D = \frac{1}{97} + \frac{12\rho^2}{7} + 2\rho^2 \quad (30)$$

In the normal HLS regime with constant incident polarization and variable  $I^\omega$  intensity the second harmonic detected signal corresponds to

$$I^{2\omega} = I_X^{2\omega} + I_Z^{2\omega} = GN^* \langle \beta_{HLS}^2 \rangle (I^\omega)^2 \quad (31)$$

where

$$\langle \beta_{HLS}^2 \rangle = \langle \beta_{XXX}^2 \rangle + \langle \beta_{ZXX}^2 \rangle = \frac{2}{9} \|\beta_{J=1}\|^2 + \frac{2}{21} \|\beta_{J=3}\|^2 \quad (32)$$

From equation (27) and (31) it is possible to infer  $\|\beta_{J=1}\|$  and  $\|\beta_{J=3}\|$  values from polarization dependent HLS experiments.

It must be pointed-out, that unlike the EFISH experiment, the HLS experiment provides access to the octupolar component of the quadratic hyperpolarizability. These two experiments are complementary. Indeed, with the EFISH experiment, we have shown that for molecules of  $C_{\infty v}$  symmetry, we could access the dipolar component  $\|\beta_{J=1}\|$ . Knowing this value, as shown in the above formulae, results given by the HLS experiment allow inferring the  $\|\beta_{J=3}\|$  octupolar component. The norm of the quadratic hyperpolarizability is then calculated simply by

$$|\beta^2| = \|\beta_{J=1}\|^2 + \|\beta_{J=3}\|^2 \quad (33)$$

### **C-1.22: Improved Version of HLS and EFISH Experimental Set-up**

In the beginning of this year we faced some problems from the electronic parts of the experimental set-up. This problem was serious because the motors used to rotate the half wave plate in the HLS technique and to translate cell in EFISH is controlled by a specific model of microcontroller, i.e. ITL 09 which was out of order.

The improved version of experimental set-up has been developed by Colin Lopez, who is working as research engineer in the physics department and at LPQM. It took almost 3 months to get ready with the new system. The new system shows considerable improvements as compared to the old system. They are,

- 1) Less volume of electronics: In the new system there is no boxcar. The role of the boxcar is controlled by the acquisition card.
- 2) In the new system we use the oscilloscope through which we can observe the SH signal produce by the reference (NPP) or from the different molecules. This help us to easily and quickly compare the SH signals from different molecules and get an idea about the best molecule among them.
- 3) In the old system the noise was large, leading to significant uncertainties in the determination of the slopes in HLS measurements at 1.9  $\mu\text{m}$ . To partially overcome this problem, it was necessary to do several measurements to get an average slope value for a given signal. Sometimes we needed to repeat the measurements to check the repeatability of experimental results. In the new system, the noise is much lower allowing one measurement only, due to a much better repeatability of collected data.
- 4) In old version there was only one option to average the signal on several pulses, i.e. 32 whereas in new version we have several options to choose, i.e. average are 8, 16, 32, 64, and 128 pulses. The quality of the slope can be improved by choosing the highest average, i.e. 128. This takes longer time but choosing 32 and 64 also provide good slopes.

- 5) Amplifier: In the improved version we can control the amplification according to the response of the molecules.
- 6) The most important point we adapted in new system as compared to old system is to measure one point before the signal at **A** and one point after the signal at **B**, then allow to deduct A from B. As a consequence, the recorded signal is almost independent on the fluctuations of the baseline.

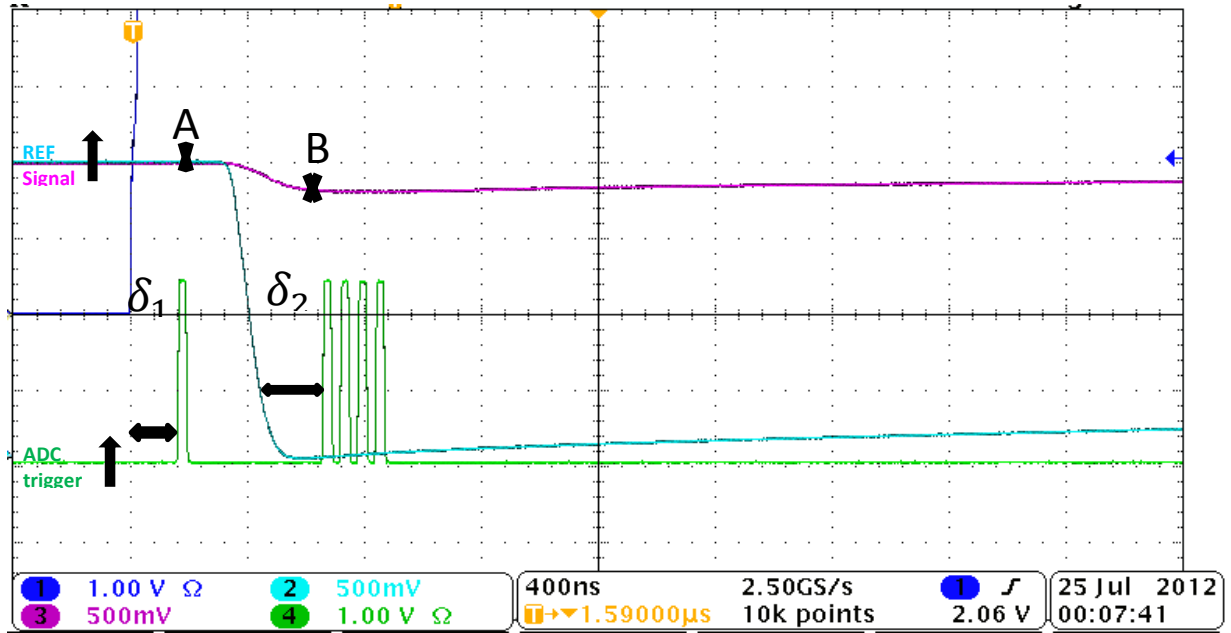


Figure 1.30: New version of Experimental set-up.

For example at Time ( $t_1$ )

$$V_{A1} = \text{offset}_{A1} + v_{a1} \quad (34)$$

$$V_{B1} = \text{offset}_{B1} + v_{b1} \quad (35)$$

$$\Delta V_1 = V_{B1} - V_{A1} = (\text{offset}_{B1} + v_{b1}) - (\text{offset}_{A1} + v_{a1}) \quad (36)$$

As A1 and B1 have the same offset,

$$\Delta V_1 = V_{B1} - V_{A1} = v_{b1} - v_{a1} \quad (37)$$

In the previous version collected data corresponded to Eq. 35. This included the offset and its fluctuations.

About Analog to digital converter (ADC): The resolution is 10 bit and frequency is 20 Hz. Step for ADC trigger is 7.5 ns.

### **C-1.22.1: Comparison between the graphs acquired from the old system and the new system from EFISH at 1.907 $\mu\text{m}$ and from HLS at 1.064 and 1.907 $\mu\text{m}$**

#### **C-1.22.1.1: EFISH at 1.907 $\mu\text{m}$**

Figure 1.31 shows the graph of dichloromethane observed from the old version of the experimental set-up. It is difficult to get perfect fringes from the old system because of the noise. The graph clearly shows the occurrence of the noise during the measurements.

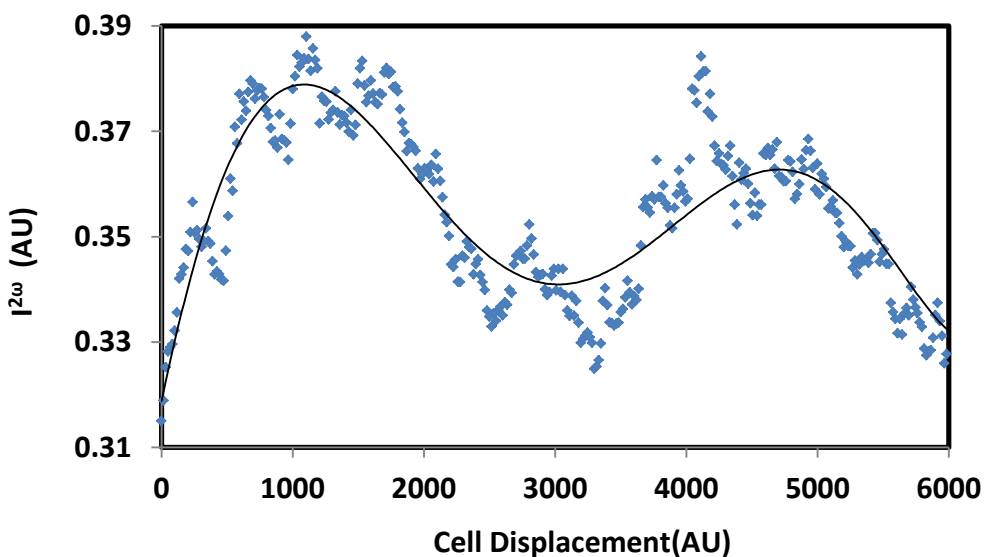


*Figure 1.31: Plot of the SHG signal from the DCM solvent as a function of cell displacement observed from the old system of the experimental set-up.*

In Figure 1.32 (a) shows the graph of dichloromethane observed from the new version of the experimental set-up. This graph is far better than the one we observed in Figure 1.31. This graph has been performed by choosing 16 averages at a point. Therefore, there is a possibility to improve the graph by choosing average between 32, 64 and 128 at a point. Figure 1.32 (b) is the plot of the SH signals from the DCM with the help of the new system and shows two perfect fringes without any noise.

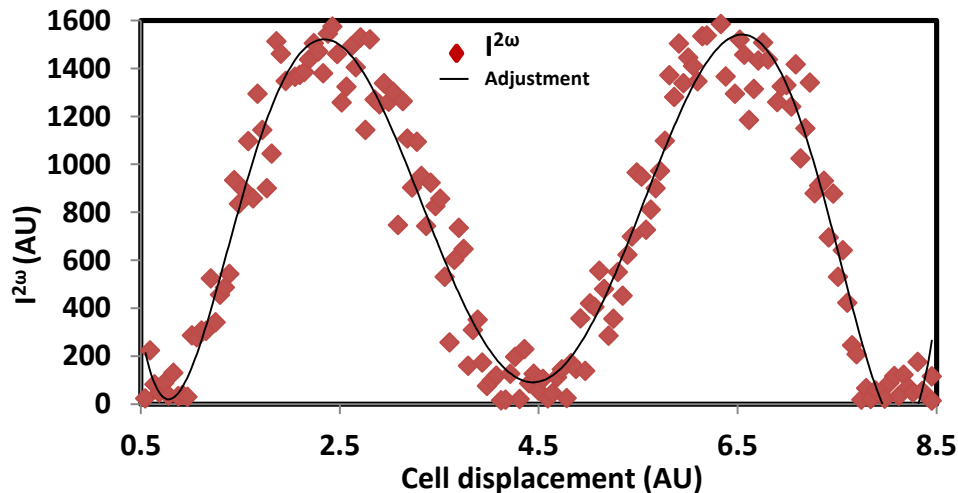
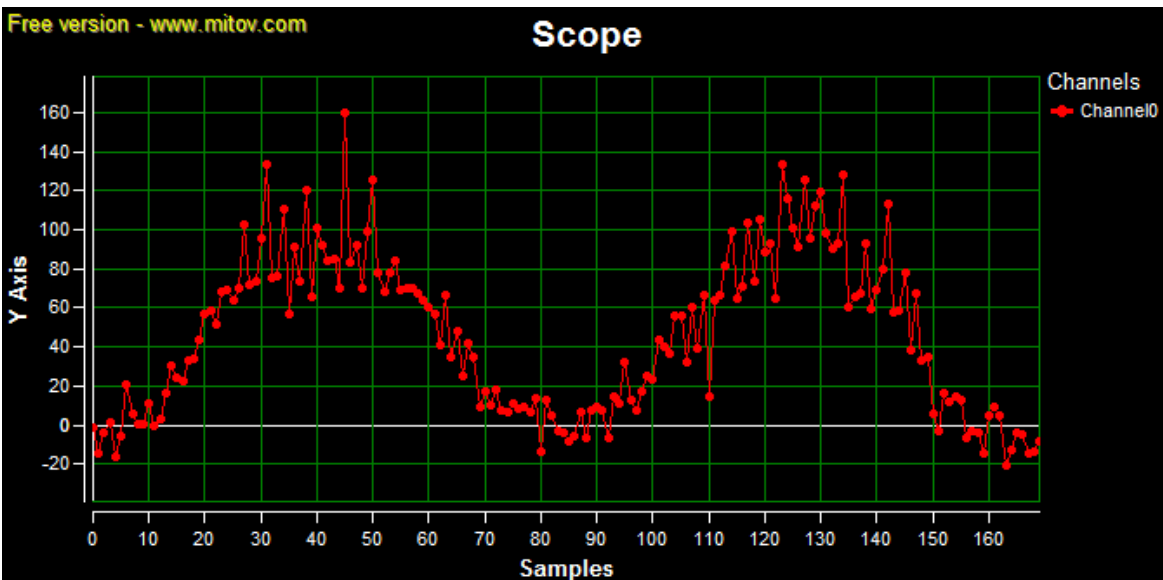
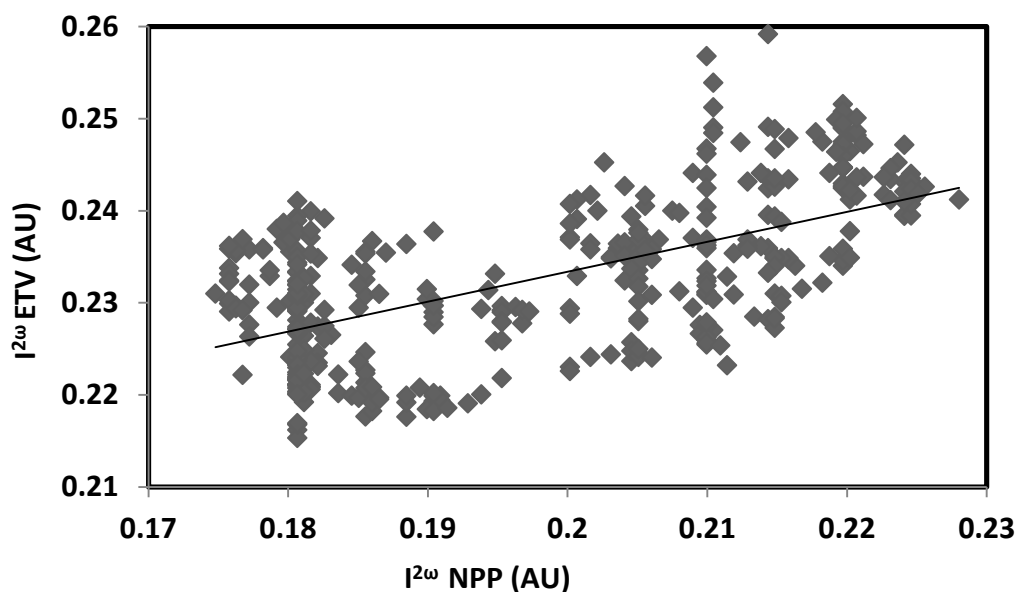


Figure 1.32: (a) SHG signal from the DCM solvent as a function of cell displacement observed from the new system of the experimental set-up. (b) Excel plot of the SHG signal from the DCM solvent as a function of cell displacement observed from the old system of the experimental set-up.

### **C-1.22.1.2: HLS at 1.907 $\mu\text{m}$**

Figure 1.33 shows the graph of an ETV solution observed from the old version of the experimental set-up. It is difficult to get a reproducible slope from the older version because of the noise. It is clear from the graph that the scattered points suffered from the occurrence of the noise during the measurements. Moreover, offset fluctuations caused sometimes a large uncertainty in the slope values. Therefore, some of them becoming negative due to which we needed to repeat measurements several times.



*Figure 1.33: Second harmonic intensity recorded from an ETV solution in DCM is plotted with respect to the SH intensity collected from the NPP powder (frequency doubler) at 1.907  $\mu\text{m}$  fundamental wavelength (old version of HLS).*

Figure 1.34 (a) shows the SH intensity recorded from an ETV solution (in red) and from NPP powder (in green) recorded at 1.907  $\mu\text{m}$  using the new version of the experimental set-up. The graph clearly shows that as the intensity of the fundamental wavelength increases the SH signal from ETV and NPP increases linearly with very low noise. This measurement has been performed by averaging 64 data. Therefore, there is a possibility to improve the graph by choosing an average up to 128 data. Figure 1.34 (b) is the excel plot of the SH signals from the ETV using the new system.

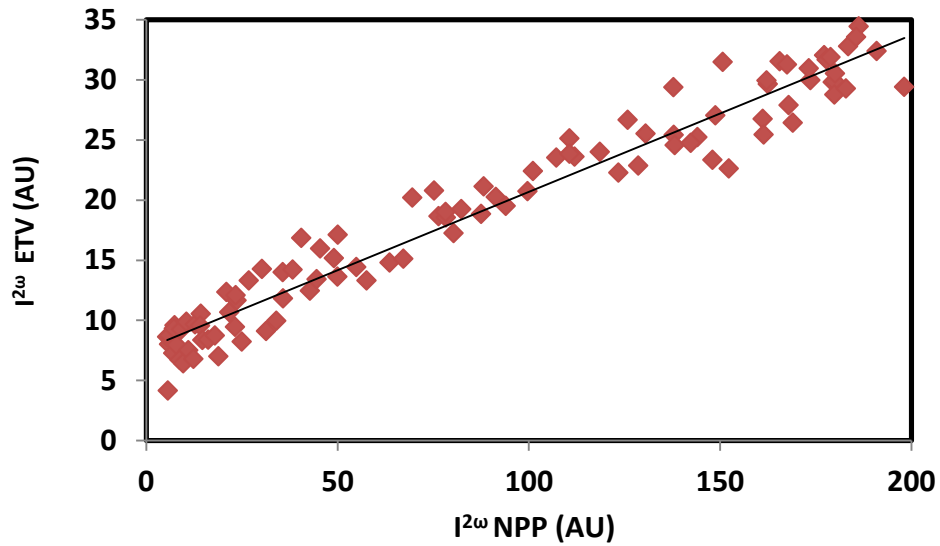
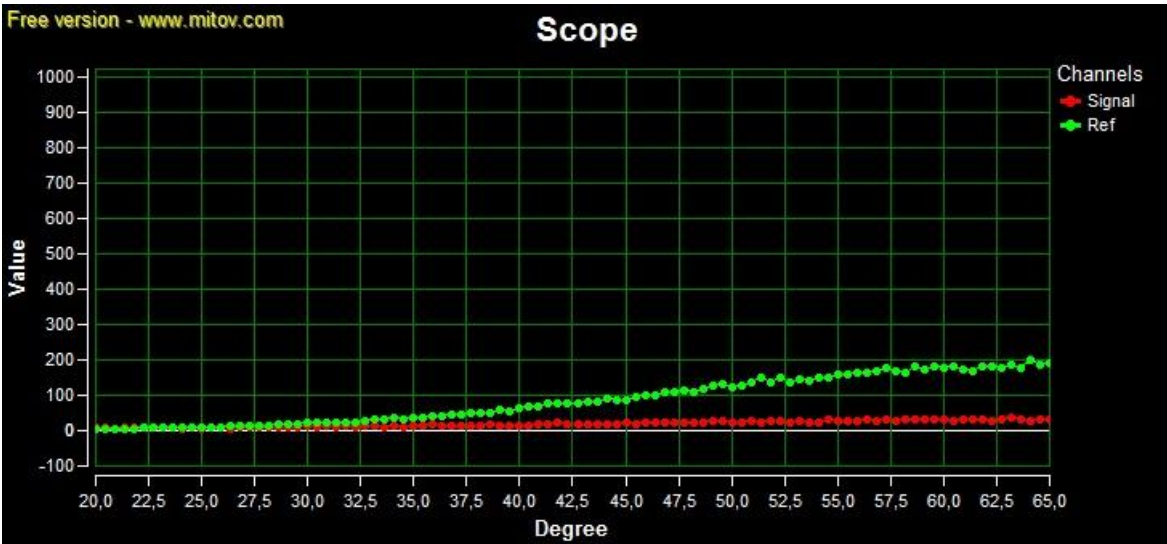
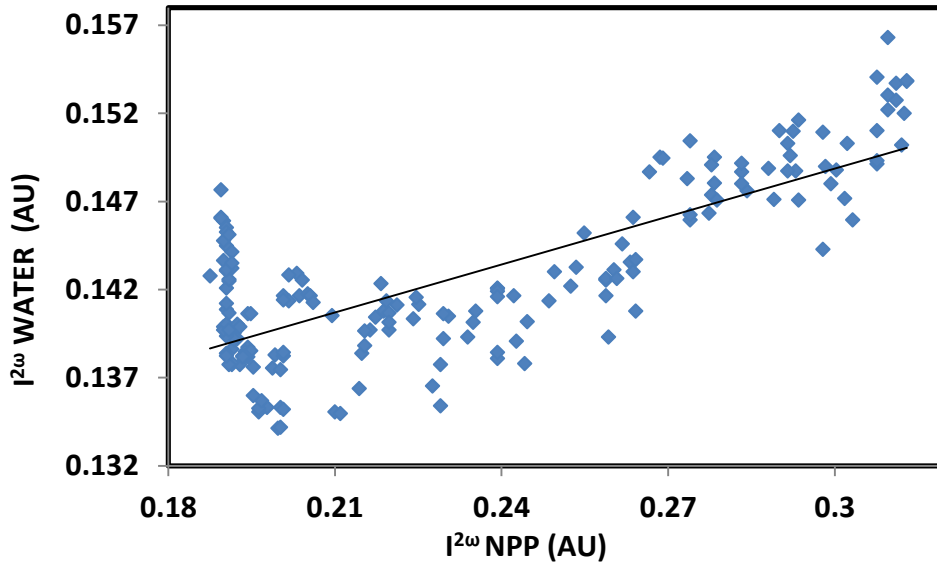


Figure 1.34: (a) SH intensity recorded from an ETV and NPP powder is shown in red and green colors respectively at  $1.907 \mu\text{m}$  using the new version. (b) Excel plot of the SH intensity recorded from an ETV with respect to the SH intensity collected from the NPP powder at  $1.907 \mu\text{m}$  using the new version.

**C-1.22.1.3: HLS at  $1.064 \mu\text{m}$**

Figure 1.35 shows the graph of water observed from the old version of the experimental set-up at  $1064 \text{ nm}$  fundamental wavelength. This graph also shows a strong noise but with less variations as compare to the signal observed in Figure 1.33.



*Figure 1.35: Second harmonic intensity recorded from water is plotted with respect to the SH intensity collected from the NPP powder (frequency doubler) at 1064 nm fundamental wavelength the (old version).*

Figure 1.36 (a) shows the SH intensity recorded from water (in red) and from NPP powder (in green) at 1.064  $\mu\text{m}$  from the new version of the experimental set-up. The graph clearly shows that as the intensity of the fundamental wavelength increases the SH signal from water and NPP linearly increases without any noise. This measurement has been performed by choosing 64 averages at a point. Therefore, there is a possibility to improve the graph by choosing average 128 at a point.

Figure 1.36 (b) is the plot of the SH signals recorded from water with respect to the SH intensity observed from the NPP powder at 1064 nm fundamental wavelength from the new version of the experimental set-up and shows a linear slope with very low noise level.

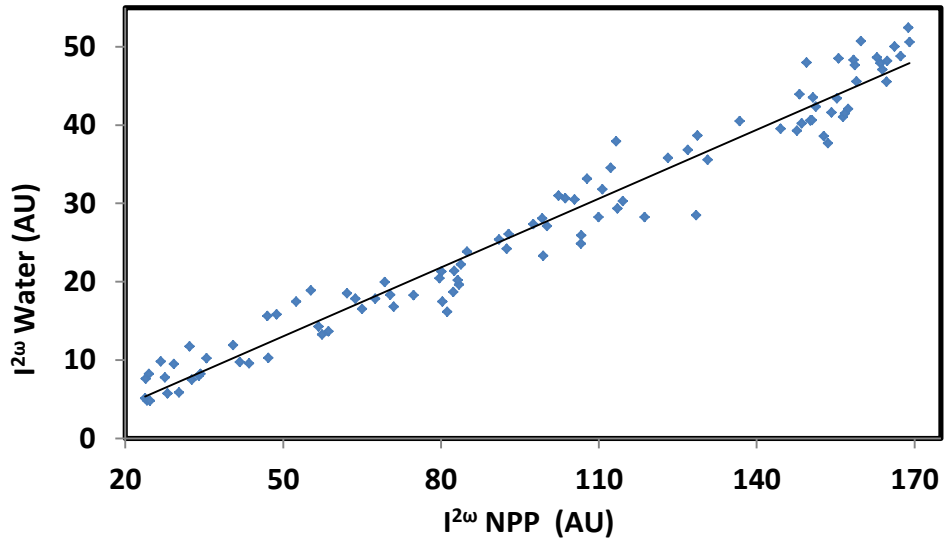


*Figure 1.36: Plot of the SH intensity recorded from water plotted with respect to the SH intensity collected from the NPP powder at 1064 nm fundamental wavelength (new version).*

Finally the improved version of the experimental set-up is far better than the old version. We checked that results obtained from the “old” and “new” version are similar. The  $\beta$  value obtained from NR4 by new system is similar as that obtained by old version, with a much faster acquisition process.

## References

- [1] Abidi W., and Remita, H., Recent Patent on Engineering, Special Issue: Light-driven reactions and materials in the environmental technology, 2010, 4, 170.
- [2] Abidi, W., Selvakanan, P. R., Guillet, Y., Lampre, I., Beaunier, P., Pansu, B., Palpant B., and Remita, H., J. Phys. Chem. C, 2010, 114, 14794.
- [3] Schwarz, H. A., Dodson R.W., J Phys. Chem., 1989, 93, 409-414.
- [4] Smith, D. k., Korgel, B. A. Langmuir, 2008, 24, 644.
- [5] Belloni, J., Mostafavi, M., Remita, H., Marignier, J.-L., Delcourt, M.-O., New J. Chem., 1998, 22, 1239-1255.
- [6] [http://www.hk.phy.org/atomic\\_world/tem/tem02\\_e.html](http://www.hk.phy.org/atomic_world/tem/tem02_e.html)
- [7] Berne, B.J., and Pecora, R., Dynamic Light Scattering, Dover Publications, New York, 2000.
- [8] Chu, B., and Liu, T., J. Nanopart. Res., 2000, 2, 29.
- [9] Brown, W., Ed., 1993, Dynamic Light Scattering: The Method and Some Applications. Clarendon Press, Oxford
- [10] Pecora R., Ed., 1985. Dynamic Light Scattering: Applications of Photon Correlation Spectroscopy. Plenum., New York.
- [11] Schmitz K.S., 1990, An Introduction to Dynamic Light Scattering by Macromolecules. Academic Press, San Diego.
- [12] Kuebler, Sigrid (15 November 2007). "Characterizing Stable Protein formulations" Genetic Engineering & Biotechnology News 27 (20).
- [13] Terhune, R. W., Maker, P. D., and Savage, C. M., Physical Review Letters, 1965, 14 (17), 681-684.
- [14] Maker, P. D., Phys. Rev. A, 1970, 1, 923.
- [15] Clays, K., Persoons, A., Phys. Rev. Lett., 1991, 66, 2980.
- [16] Oudar, J. I., J. Chem. Phys., 1977, 66, 2664.
- [17] Levine. B.F., Chem. Phys., 1975, 63, 115.
- [18] Kajzar, F., Ledoux, I., Zyss, J., J. Phys. Rev. A, 1987, 36, 2210.
- [19] Giordmaine, J.A., Phys. Rev. A, 1965, 138 1599.

- [20] Coe, B.J., Chamberlain, M.C., Essex-Lopresti, J.P., Gaines, S., Jeffery, J.C., Houbrechts, S., Persoons, A., *Inorg. Chem.*, 1997, 36, 3284.
- [21] Vance, F.W., Hupp, J.T., *J. Am. Chem. Soc.*, 1999, 121, 4047.
- [22] Dhenault, C., Ledoux, I., Samuel, I.F.W., Zyss, J., Bourgault, M., Bozec, H. Le, *Nature*, 1995, 374, 339.
- [23] Dalton, L. R., Sullivan P. A., and Bale, D. H., *Chem. Rev.*, 2010, 110 (1), pp 25–55.
- [24] Choa, M. J., Choia, D. H., Sullivanb, P. A., Akelaitis, A. J. P., Dalton, L. R., *Progress in Polymer Science* 33 (2008) 1013–1058.
- [25] Giordmaine, J. A., *Phys. Rev. Lett.*, 1965, 138, 1599.
- [26] Cyvin, S. J., Rauch, J. E., and Decius J. C., 1965, *J. Chem. Phys.* 43, 4083.
- [27] Bersohn. R., Pao, Y.- H., and Frisch, H. L., 1966, *J. Chem. Phys.* 45, 3184.
- [28] Buckingham, A. D., Orr, B. J., *Q. Rev. Chem. Soc.*, 1967, 21, 195-212.
- [29] Clays, K., Persoons, A. *REV. Sci. Instrum.*, 1992, 63, 3285.
- [30] Oudar, J. L., *Journal of Chemical Physics*, 1977, 67 (2), 446-457.
- [31] Levine, B. F., and Bethea, C. G., *Journal of Chemical Physics*, 1975, 63 (6), 2666-2682.
- [32] Flipse, M. C., Jonge, R. de, Woudenberg, R. H., Marsman, A. W., Walree, C. A. van, Jenneskens, L. W., *Chemical Physics Letters*, 1995, 245 (2-3), 297-303.
- [33] Song, N. W., Kang, T.-I., Jeoung, S. C., Jeon, S.,-J., Cho' B. R., Kim, D., *Chemical Physics Letters*, 1996, 261 (3), 307-312.
- [34] Noordman, O. F. J., Van Hulst, N.F., *Chem. Phys. Lett.*, 1996, 253, 145.
- [35] Wang, C. H., Lin, Y. C., Tai, O. Y., Jen, A. K. Y., *J. Chem. Phys.*, 2003, 119, 6237.
- [36] Schmalzlin, E., Bitterer, U., Langhals, H., Brauchle, C., and Meerholz, K., *Chemical Physics*, 1999, 245 (1-3), 73-78.
- [37] Pauley M. A., and Wang, C. H., *Chemical Physics Letters*, 1997, 280 (5-6), 544-550.
- [38] Singer, K. D., Kuzyk, M. G., and Sohn, J. E., *J. Opt. Soc. Am. B*, 1987, 4.
- [39] Le Bouder, T., Maury, O., Bondon, A., Costuas, K., Amouyal, E., Ledoux, I., Zyss, J., and Le Bozec, H., *J. AM. Chem. Soc.*, 2003, 125, 12284-12299.

## Chapter 2: New developments in molecular engineering for quadratic NLO

### Part A: Novel metal complexed Pt and Ir complexes

#### A-2.1: Platinum complexes

In the first chapter we pointed-out that organometallic, coordination complexes and photochromic materials are highly desirable for their potential applications in the field of photonic devices. They show luminescent and second-order NLO properties, and may display higher nonlinearities than purely organic materials. Their properties can be tuned by introducing charge-transfer transitions between the metal and the ligands and their influence can be controlled according to the nature, oxidation state and coordination sphere of the metal centre [1]. Recently numerous experiments have been done by EFISH and HLS technique in order to determine the hyperpolarizability of cationic cyclometallated Ir (III) complexes containing a substituted 1, 10 phenanthroline [2-3] or 2, 2'-bipyridine ligand [4];  $\beta$ -diketonate Ir (III) and Pt (II) complexes with a cyclometallated 2-phenylpyridine ligand [5]; terpyridine and cyclometallated dipyritylbenzene platinum (II) complexes, with the tridentate ligand carrying a strong electron acceptor group [6] etc. NLO properties mainly originated from MLCT (metal-to-ligand charge-transfer) and ILCT (intra-ligand charge-transfer). Apart from these complexes, various 4,4'-stilbenoid-substituted  $N^C^N$  platinum(II) complexes show significant quadratic hyperpolarizabilities, higher than those typical of purely organic 4,4'-disubstituted stilbenes, probably due to the polarization along the C-Pt bond [7].

These results encouraged us to extend the research and studies of their NLO properties. Hence, we investigated Pt (II) complexes via a collaboration by Dominique Roberto and her group, working in Dipartimento di Chimica dell'Università degli Studi di Milano, Milan, Italy where they synthesised new complexes to determine the second-order NLO properties of cyclometallated 1,3-di (2-pyridyl)benzene platinum(II) complexes. EFISH measurement carried out at the Dipartimento di Chimica of the Università degli Studi di Milano, working in DMF solutions at a concentration of  $1 \times 10^{-4}$  M, with a non-resonant incident wavelength of 1.907  $\mu\text{m}$ , obtained by Raman-shifting the fundamental 1.064  $\mu\text{m}$  wavelength produced by

a Q-switched, mode-locked Nd<sup>3+</sup>:YAG laser manufactured by Atalaser. The  $\mu\beta_{\text{EFISH}}$  values reported are the mean values of 16 successive measurements performed on the same sample. The sign of  $\mu\beta$  is determined by comparison with the reference solvent (DMF). HLS measurements are performed at LPQM, ENS Cachan in DMF as a solvent, with concentrations from 1 to 2 x 10<sup>-3</sup> M, working with a low-energy non-resonant incident radiation of 1.907  $\mu\text{m}$ . This class of materials is interesting because of their remarkable luminescent properties [8-10].

Phosphorescent organometallic complexes have drawn attention to the importance of heavy-metal-enhanced singlet  $\rightarrow$  triplet (S-T) intersystem crossing and phosphorescence in the development of advanced optoelectronic materials [11].

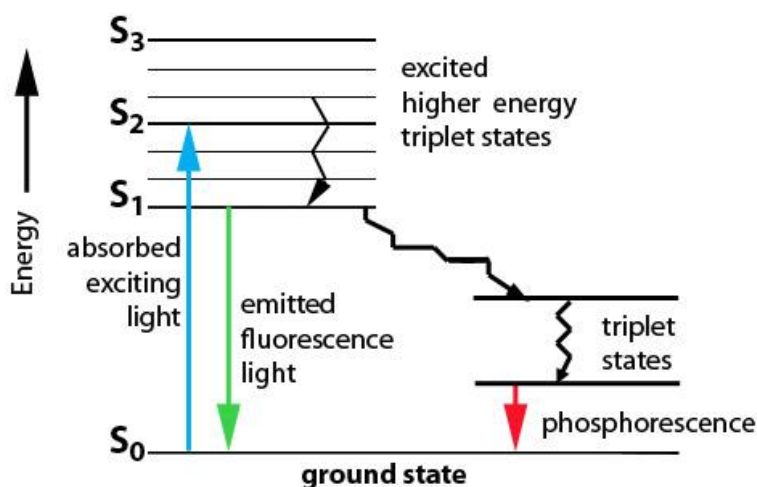
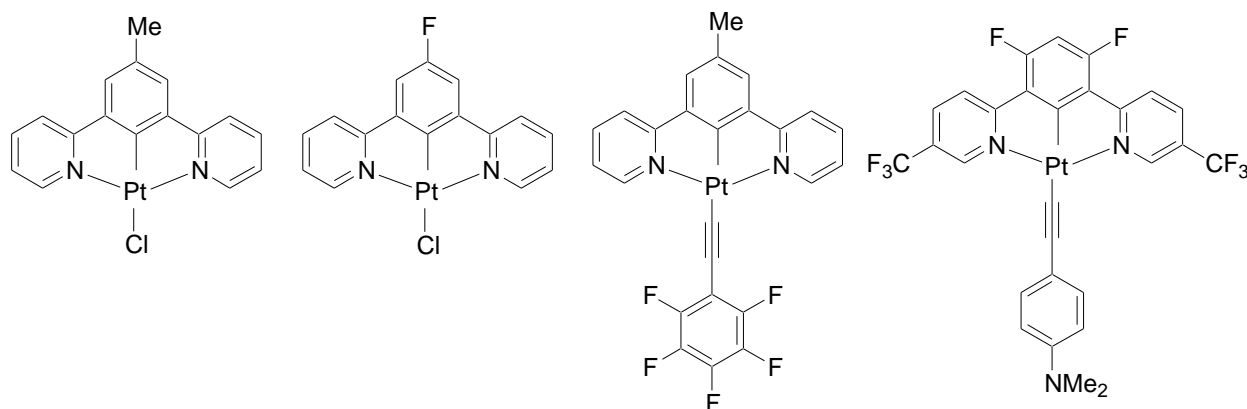


Figure 2.1: The Jablonski diagram describes the energy levels and different transitions between states.

Triplet states are difficult to study as they are usually non-emissive. Emission from a triplet excited state to the singlet ground state requires a spin flip. Phosphorescence can be measured when the triplet emission becomes partially allowed by spin-orbit coupling. The amount of spin-orbit coupling in a molecule can be greatly increased by introducing heavy atoms such as Pt and Ir into the chemical structure [12], which feature high phosphorescence yields and relatively long emission lifetimes. These properties are particularly useful in LEDs [13-14].

The effect of the nature of the substituents on the cyclometallated 1, 3-di (2-pyridyl) benzene ligand and of the monodentate ancillary ligand (chloride or various substituted phenylacetylides) on the quadratic hyperpolarizability has been investigated. The complexes studied are shown in scheme 2.1.



*Scheme 2.1: Structures of the Pt (II) complexes investigated by HLS and EFISH.*

Meanwhile, the dipolar and octupolar contributions to the quadratic hyperpolarizability [15-16] of these platinum (II) complexes have been determined experimentally by a combination of EFISH and HLS [17-19] techniques, working with a non-resonant incident wavelength of 1.907  $\mu\text{m}$ , whose second harmonic  $2\omega$  and third harmonic  $3\omega$  lie at 953 and 636 nm respectively, in a transparent region of the absorption spectra of all the Pt (II) complexes investigated.

#### **A-2.1.1: Characterization of Platinum (II) complexes**

All platinum (II) complexes are fully characterized by IR, NMR and UV-visible spectroscopies. The absorption band maxima are presented in Table 2.1. All complexes show intense bands in the region 260–320 nm, which can be assigned to intraligand  $^1\pi-\pi^*$  transitions of the cyclometallated 1, 3-di (2-pyridyl) benzene [20] and of the ancillary acetylide [21] ligands. The less intense absorption bands at 330–450 nm were reported to correspond to transitions with a mixed charge-transfer/ligand-centered character [22]. Although the substitution of the chloride ligand by various phenylacetylide ligands does not change the spectral profile substantially, the individual bands in the region 330-450 nm

become rather less well-resolved, with evidence of a tail to longer wavelengths. This tail might tentatively be attributed to a  $\pi_{C\equiv C} \rightarrow \pi^*_{N\wedge C\wedge N}$  ligand-to-ligand charge-transfer (LLCT) transition, by analogy with other Pt (II) acetylide complexes [21, 23-29].

*Table 2.1: Experimental electronic spectra HLS  $\beta$  values, related dipolar and octupolar contributions and modulus of the quadratic hyperpolarizability for some of the investigated Pt (II) complexes determined at 1.907  $\mu\text{m}$  in DMF solution.*

| Complexes | $\lambda_{\text{max}} / \text{nm}$ | $\mu\beta_{\text{EFISH}}$<br>( $\times 10^{-48}$ )<br>esu | $\mu_{\text{tot}}$<br>D | $\beta_{\text{EFISH}}$<br>[30] | $\beta_{\text{HLS}}$<br>( $\times 10^{-30}$ )<br>esu) | $\ \bar{\beta}^{J=1}\ $<br>( $\times 10^{-30}$ )<br>esu) | $\ \bar{\beta}^{J=3}\ $<br>( $\times 10^{-30}$ )<br>esu) | $\ \bar{\beta}\ $<br>( $\times 10^{-30}$ )<br>esu) |
|-----------|------------------------------------|---|-------------------------|--------------------------------|---|--|--|--|
| <b>1</b>  | <b>355, 381,<br/>412, 460, 495</b> | <b>-480</b>   | <b>10.19</b>            | <b>-47</b>                     | <b>285</b>  | <b>36</b>  | <b>922</b>   | <b>923</b>   |
| <b>2</b>  | <b>322, 377,<br/>422, 486,</b>     | <b>-1060</b>  | <b>6.01</b>             | <b>-176</b>                    | <b>432</b>  | <b>136</b>   | <b>1384</b>  | <b>1391</b>  |
| <b>3</b>  | <b>330, 355, 380,<br/>408</b>      | <b>-2290</b>  | <b>12.72</b>            | <b>-180</b>                    | <b>345</b>  | <b>139</b>   | <b>1098</b>  | <b>1107</b>  |
| <b>4</b>  | <b>326, 344,<br/>385, 493</b>      | <b>-2020</b>  | <b>4.31</b>             | <b>-469</b>                    | <b>278</b>  | <b>363</b>   | <b>710</b>   | <b>797</b>   |

### **A-2.1.2: NLO properties of Platinum (II) complexes**

The second-order NLO properties of the Pt (II) complexes are investigated by the EFISH and HLS technique (see Table 1). All the compounds have  $C_{2v}$  symmetry. All complexes are characterized by a negative value of  $\mu\beta_{\text{EFISH}}$ , due to the negative value of  $\Delta\mu_{\text{eg}}$  upon excitation, which reflects a decrease of the dipole moment upon excitation as suggested by the above reported negative solvatochromic behaviour of the low energy MLCT transitions [30]. Second-order dipolar NLO response is probably dominated by the charge transfer from platinum to the cyclometallated ligand. In accordance, when taking into consideration the Pt (II) chloride complexes (**1 and 2**, Table 2.1), the substitution of a methyl group (complex **1**) by a fluorine atom (complex **2**) on the metallated benzene ring causes an increase of the absolute value of  $\mu\beta_{\text{EFISH}}$  and a decrease of the dipole moment, therefore leading to a large increase (by a factor of 3.7) of  $\beta_{\text{EFISH}}$ , as expected for a stronger charge transfer process. A large  $\mu\beta_{\text{EFISH}}$  value ( $-2290 \times 10^{-48}$  esu) is also reached upon substitution of the chloride ancillary ligand of complex **1** by a pentafluorophenylacetylide ligand (complex **3**) probably caused by an increased charge transfer from the Pt- pentafluorophenylacetylide moiety. The

absolute value of  $\beta_{EFISH}$  remains similar to complex **2** by a relevant increase of the dipole moment. In the case of complex **4** having a phenylacetylide ligand with a strong donor dimethylamino in the *para* position of the phenyl ring, the LUMO level is completely centered on the cyclometallated 1, 3-di (2-pyridyl) benzene chelated ligand and the HOMO on the phenylacetylide ligand. It follows a strong HOMO-LUMO electron transfer and producing one of the largest values of  $\beta_{EFISH}$  ( $-469 \times 10^{-30}$  esu) amongst the Pt (II) complexes investigated (Table 2.1).

In order to have a complete understanding of the various components of the second order NLO properties of these platinum (II) complexes, and in particular to evaluate not only the dipolar but also the octupolar contribution to the quadratic hyperpolarizability, we carried out an HLS experiments. The dipolar ( $J = 1$ ) and octupolar ( $J = 3$ ) contributions and the modulus of the quadratic hyperpolarizability ( $\|\bar{\beta}\|$ ) have been calculated using the following equations, [15-16, 31].

$$\|\bar{\beta}\|^2 = \|\bar{\beta}^{J=1}\|^2 + \|\bar{\beta}^{J=3}\|^2 \quad (1)$$

$$\|\bar{\beta}^{J=1}\| = \sqrt{\frac{3}{5}} |\beta_{EFISH}| \quad (2)$$

$$\langle \beta_{HLS}^2 \rangle = \langle |\beta_{xxx}|^2 \rangle + \langle |\beta_{zzx}|^2 \rangle = \frac{2}{9} \|\bar{\beta}^{J=1}\|^2 + \frac{2}{21} \|\bar{\beta}^{J=3}\|^2 \quad (3)$$

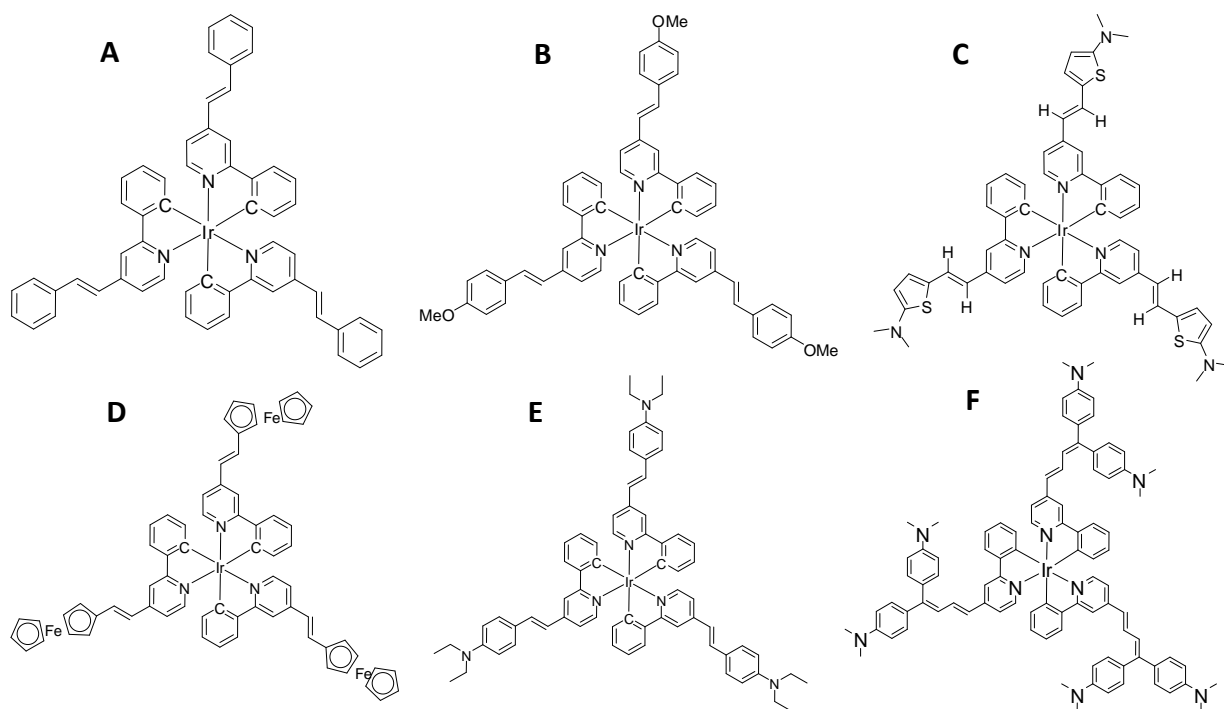
The resulting values of  $\|\bar{\beta}^{J=3}\|$  reported in Table 1 show that the dipolar contribution is much lower than the octupolar one, in accordance with previous evidence which has suggested that even the quadratic hyperpolarizability of a dipolar second-order NLO chromophore can be largely dominated by the octupolar component, as for instance in the case of cyclometallated neutral Ln (III) [31] and cationic Ir (III) [2-3] complexes. In particular, complexes **1**, **2** and **3** are characterized by a remarkably high value of the quadratic hyperpolarizability  $\|\bar{\beta}\|$  due to an important contribution of the octupolar component, the dipolar component being less than 13% of the octupolar one. As expected, the dipolar contribution to the quadratic hyperpolarizability  $\|\bar{\beta}^{J=1}\|$  of complex **4** is relatively high (51%), due to a particularly strong

charge transfer from the ancillary NMe<sub>2</sub>-phenylacetylide to the cyclometallated 1, 3-di (2-pyridyl) benzene ligand. In agreement with this suggestion, by enhancing the acceptor properties of the cyclometallated chelated ligand the increase of the quadratic hyperpolarizability is more relevant for the dipolar contribution than for the octupolar one (enhancement factor of 3.8 and 1.5, respectively, on-going from **1** to **2**).

In conclusion, the Pt (II) complexes investigated are a new family of organometallic second-order NLO chromophores with a response easily tuneable by a rational approach, where the Pt atom plays the role of a central bridge of the transfer process from the donor to the acceptor moieties of the molecular structure.

### **A-2.2: Cyclometalated Iridium (III) Complexes**

A special attention has also been focused on the synthesis and photophysical characterization of octahedral 4d<sup>6</sup> and 5d<sup>6</sup> metal complexes [32]. As far platinum derivatives the attraction of these d<sup>6</sup> complexes for such applications comes from their long excited-state lifetimes and high luminescent efficiencies. Therefore, cyclometalated iridium (III) complexes have been



*Scheme 2.2: Newly synthesized Cyclometalated Ir (III) complexes with different donor group.*

used for the preparation of OLEDs, due to their high phosphorescence efficiencies and multicolor emission [33]. In addition, these complexes display strong charge transfer transition (MLCT and ILCT) properties and they are expected to be interesting chromophores for second order NLO. In this context, Le Bozec et al. synthesized tris-cyclometallated Ir complexes incorporating various  $\pi$ -donor conjugated groups in order to introduce strong charge transfers [34]. In addition, these complexes, possessing  $D_3$  symmetry, represent a new class of neutral octupolar NLO phores [35]. In this contribution, they designed and synthesised a new family of Ir[C<sup>N</sup>-ppy- (CH=CH) n-Ar-D]<sub>3</sub> complexes as shown in scheme 2.2. As expected, these complexes an exhibit strong second-order NL activity measured by HLS at 1.907  $\mu\text{m}$ , which are controlled by the  $\pi$ -conjugated linker group or the end donor group.

#### **A-2.2.1: NLO properties:**

The UV-Vis absorption spectra of A to F compounds are recorded in  $\text{CH}_2\text{Cl}_2$  and presented in Table 2.2 along with measured  $\beta_{\text{HLS}}$  value.

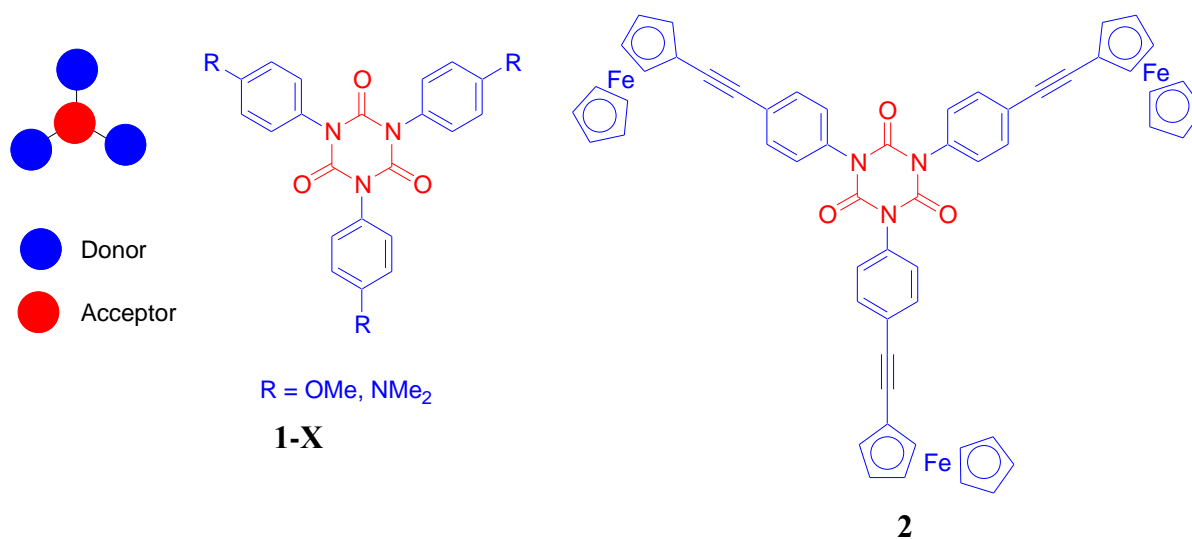
*Table 2.2: UV–Vis absorption spectra for Cyclometalated Ir (III) complexes with HLS  $\beta$  values determined at 1.907  $\mu\text{m}$  incident wavelength in  $\text{CH}_2\text{Cl}_2$ .*

| Compound  | $\lambda_{\text{max}} / \text{nm}$ | $\beta_{\text{HLS}} ( \times 10^{-30} \text{ esu} )$ |
|---|------------------------------------|--|
| <b>A</b> -C=CH-C <sub>6</sub> H <sub>5</sub>  | <b>315, 402, 499</b>               | <b>252</b>   |
| <b>B</b> -C=CH-C <sub>6</sub> H <sub>4</sub> -OMe   | <b>348, 375, 483</b>               | <b>299</b>   |
| <b>C</b> -C=CH-C <sub>4</sub> H <sub>2</sub> S- NMe <sub>2</sub>  | <b>455, 503</b>                    | <b>332</b>   |
| <b>D</b> -C=CH-C <sub>5</sub> H <sub>4</sub> Fe (C <sub>5</sub> H <sub>5</sub> )                            | <b>318, 398, 493</b>               | <b>334</b>   |
| <b>E</b> -C=CH-C <sub>6</sub> H <sub>4</sub> -NEt <sub>2</sub>  | <b>412</b>                         | <b>397</b>   |
| <b>F</b> -(C=CH) <sub>2</sub> -(C <sub>6</sub> H <sub>4</sub> -NMe <sub>2</sub> ) <sub>2</sub> <sub>3</sub> | <b>377, 454, 525</b>               | <b>464</b>   |

The color of Ir (II) complexes is orange; their spectra show intense bands in the ultraviolet part of the spectrum between 315 to 400 nm and in the blue edge of the visible range. The second-order NLO responses of the newly synthesized cyclometalated iridium (III) complexes are measured in  $\text{CH}_2\text{Cl}_2$  and concentration about  $10^{-3}$  M by the HLS technique, working at incident wavelength of 1.907  $\mu\text{m}$ . The experimental errors recorded for  $\beta$  value are 10 percent. The donor group plays an important role on the  $\beta$  values.

### A-2.3: New Organometallic Octupolar Chromophores: Donor-substituted triaryl-1, 3, 5-triazinanes-2, 4, 6-triones

The hyperpolarizability of various kinds of  $D_3$  or  $D_{3h}$  symmetry molecules has been studied [36-39] for a long time. Special attention has also been paid to triazinane-2, 4, 6-triones, more commonly known as isocyanurates. Frederic Paul and his group working in Universite de Rennes 1 extended the NLO study of triaryl-1, 3, 5-triazinanes-2, 4, 6-triones. They functionalized the central octupolar backbone with electron releasing groups at the periphery, such as methoxy and dimethylamine in complexes **1-X** and extended analogues as presented in Scheme 2.3 [40]. The NLO properties of these compounds have been investigated by HLS at 1.907  $\mu\text{m}$  at LPQM, ENS Cachan.

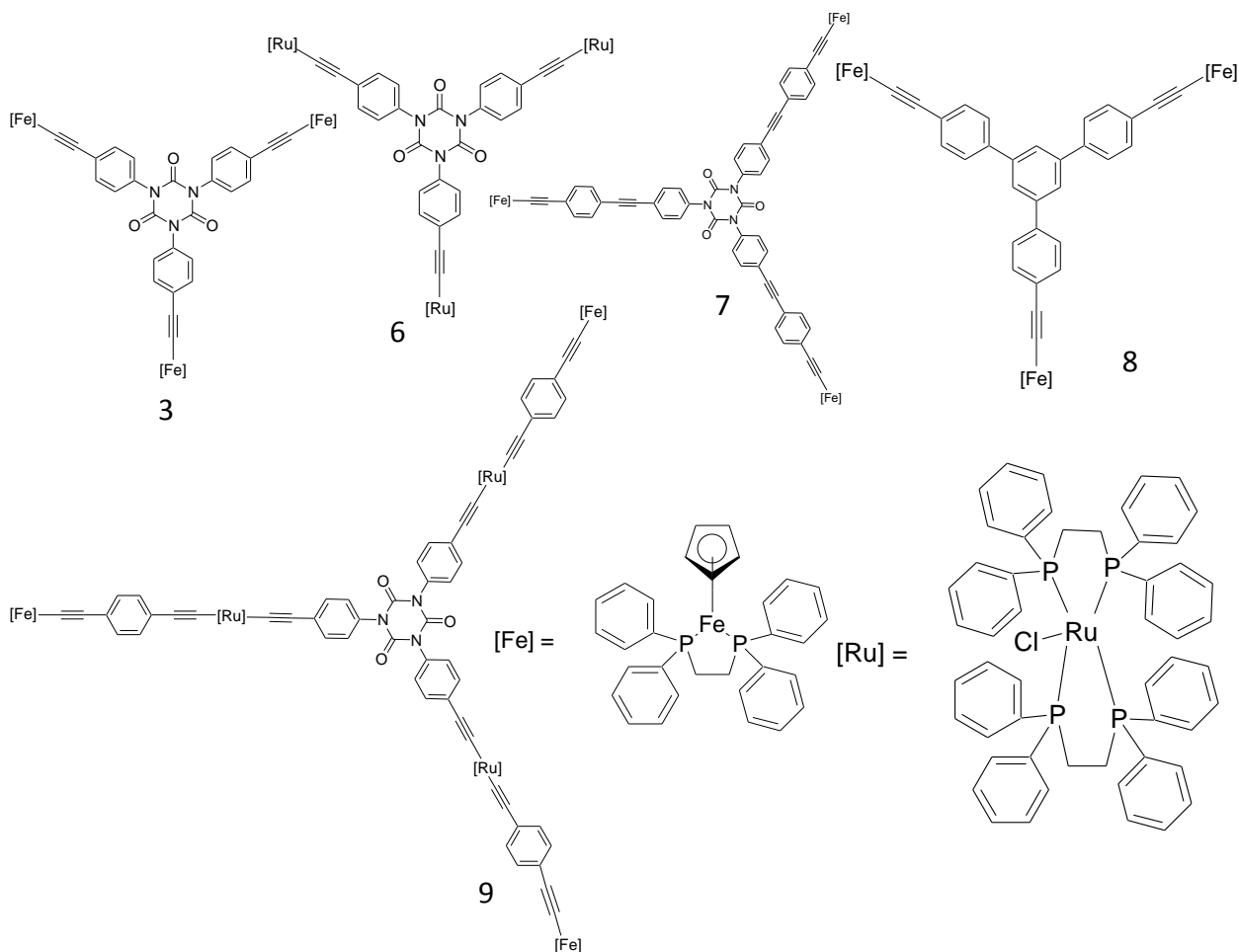


*Scheme 2.3: Compounds 1-X and 2*

Using a strong organometallic electron releasing end group like ethynylferrocene, the resulting molecule displays a larger hyperpolarizability **2** as compared to the purely organic analogues substituents [40]. Thus, polarizable  $d^6$  transition metal centers acting as donor groups in these NLO-active structures are very valuable to optimize their second-order NLO-activities.

All these observations inspired the chemists from Rennes University to design the molecules by directly connecting metal centers to the peripheral aryl rings via  $\sigma$ -bonds rather than via  $\pi$ -bonds and to infer their hyperpolarizability value. Hence, a new organometallic derivative **3** has been synthesized in Rennes 1 and its hyperpolarizability has been measured by HLS in

LPQM at ENS Cachan [41]. As expected, **3** is a more active octupolar molecule as compared to **2**. To exactly find out the role played by the peripheral metal centers and by the central spacer on the properties of such compounds, other similar kinds of molecules are synthesized. These are a ruthenium analogue **6**, as well as the extended analogue **7** and the 1, 3, 5-phenylene analogue **8** of **3** whereas **9** includes ruthenium in the conjugated arms, and [Fe] as the end group. The newly synthesized analogues of **3** are displayed in Scheme 2.4.



Scheme 2.4: Compounds **3**, **6**, **7**, **8** and **9** ( $[Fe] = (\eta^2\text{-dppe})(\eta^5\text{-C}_5\text{Me}_5)\text{Fe}$  and  $[Ru] = \text{trans-}(\eta^2\text{-dppe})_2\text{Ru}$ ).

### **A-2.3.1: Characterization of Octupolar molecules**

The UV-Vis absorption spectra of **3**, **6**, **7**, **8** and **9** compounds are recorded in  $\text{CH}_2\text{Cl}_2$  and presented in Table 1. The complexes of Fe (II) **3**, **7**, **8** and **9** are orange in color whereas Ru (II) **6** is yellow and absorbs at the blue edge of the visible range, their lowest-lying

absorptions being ascribed to  $d \rightarrow \pi^*$  MLCT transitions [42]. As expected, when going from **3** to **7** and **9**, the extension of the  $\pi$ -conjugated arms leads to a bathochromic shift of this transition. Similarly, the red shift of this transition when comparing **8** with **3** suggests that a better delocalization of  $\pi$ -electrons takes place within the three branches through the 1,3,5-arylene core compared to the isocyanurate one.

### **A-2.3.2: NLO properties of Octupolar molecules**

The hyperpolarizability and static hyperpolarizability ( $\beta_0$ ) values of compounds **3**, **6**, **7**, **8** and **9** are measured by HLS at 1.907  $\mu\text{m}$  in the same ( $\text{CH}_2\text{Cl}_2$ ) solvent and their concentration is about 1 to  $2 \times 10^{-3}$  M. Their  $\beta$  values are shown in Table 2.3. The corresponding static hyperpolarizability ( $\beta_0$ ) value is also calculated from UV data [43]. The measurement of sample 2 is performed in chloroform at 1.064  $\mu\text{m}$  [40]. The experimental error recorded for  $\beta$  is about 15 percent. According to results mentioned in Table 2.3, **9** displays the best NLO performances among the new derivatives presently synthesized. Replacing Fe (II) by Ru (II) end groups has apparently only a minor influence on  $\beta_{\text{HLS}}(0)$  values. On the other hand, increasing the length of the arms of the cyclotrimer results only in a small enhancement of  $\beta_{\text{HLS}}(0)$  (around 10%) for **7** comparative to **3**, but reduces the transparency range of **7** (approximately 40 nm loss as compared to **3**). Comparison between **3** and **8** reveals that changing the triphenyl isocyanurate linker for a 1, 3, 5-triphenylbenzene one has also very little effect on the  $\beta_{\text{HLS}}(0)$  value, or on the NLO-activity of the compound, except to decrease the transparency range of the resulting chromophore about 40 nm. Finally, compound **9**, which contains longer arms, containing both Ru (II) and Fe (II) in the conjugation end groups shows best NLO active molecules among them. The static hyperpolarizabilities of **3**, **6**, **7**, **8** and **9** are all significantly larger than that previously found for **2**, in line with the importance of  $\sigma$ -coordination (via the alkynyl bridge) vs.  $\pi$ -coordination (via the cyclopentadiene ring) of the metallic center to the central core. The present  $\beta_{\text{HLS}}(0)$  values are also larger than previously found for the most active organic derivatives such as 1-NMe<sub>2</sub> [5].

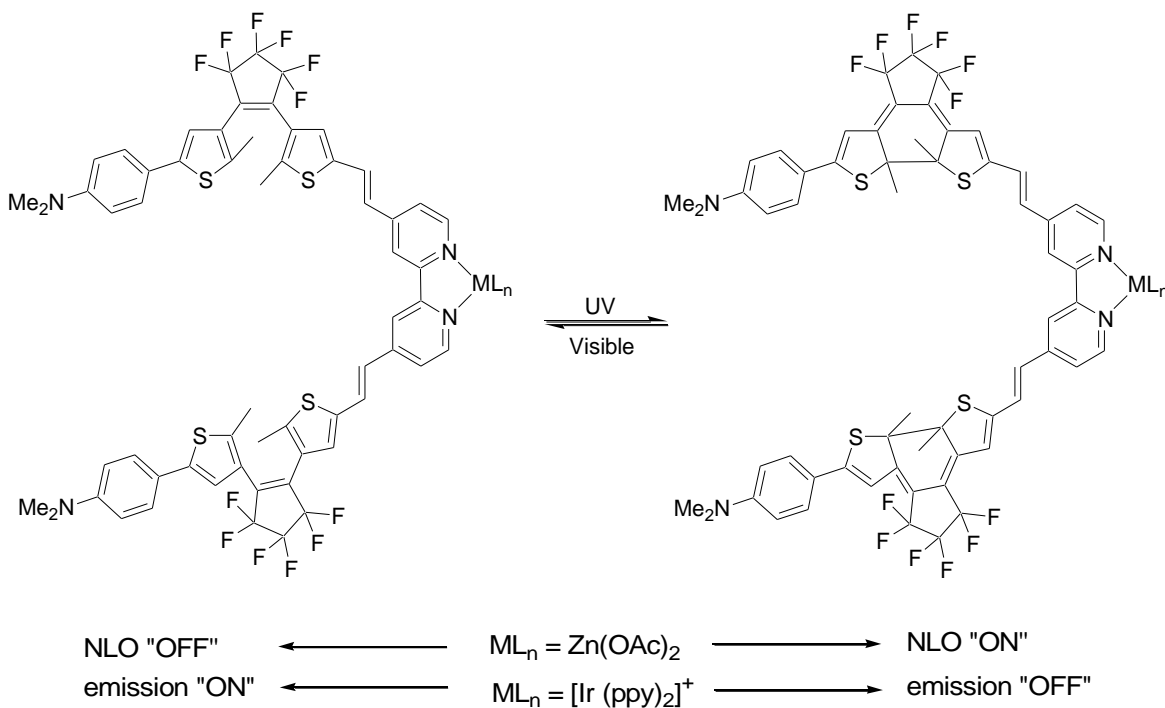
*Table 2.3: HLS  $\beta$  values determined at 1.907  $\mu\text{m}$  incident wavelength for selected octupoles in  $\text{CH}_2\text{Cl}_2$  [<sup>a</sup> Measurement performed in chloroform at 1064 nm]*

| Compound           | $\lambda_{\max}$ / nm | $\beta_{\text{HLS}} (\times 10^{-30} \text{ esu})$ | $\beta_0 (\times 10^{-30} \text{ esu})$ |
|--------------------|-----------------------|--|---|
| 1-NMe <sub>2</sub> | 270                   | 55   | 50                                      |
| 2                  | 342                   | 49 <sup>a</sup>                                    | 26 <sup>a</sup>                         |
| 3                  | 400                   | 322  | 254                                     |
| 6                  | 342                   | 288  | 243                                     |
| 7                  | 446                   | 374  | 276                                     |
| 8                  | 442                   | 312  | 232                                     |
| 9                  | 496                   | 858  | 583                                     |

According to the respective electron-donor characters as inferred from Hammett electronic substituent parameters (ESPs) [44-45] of Fe(II) and Ru(II) end groups larger as compare to the amino group, therefore their NLO response are expected to be larger. The significantly higher  $\beta$  values of Fe(II) and Ru(II) derivatives show that the interest of  $d^6$  organometallic centers does not only originate from their electron-releasing power (as derived from their Hammett ESPs), but also from their more “polarizable” nature as compared to purely organic substituents. More generally, the trinuclear compounds presently studied exhibit hyperpolarizabilities which rival those obtained for very active inorganic or organometallic NLO-phores [46]. Actually, when compared to data reported for trinuclear organometallics featuring similar end groups, the value found for 8 is clearly larger than that previously obtained for a smaller trinuclear Fe(II) derivative featuring a 1,3,5-triethynylarylene bridge [47]. Also, the  $\beta_{\text{HLS}}(0)$  value found for 6 exceeds those derived for related trinuclear Ru (II) acetylide assemblies [48]. In spite of the fact that a comparison between hyperpolarizabilities measured by HLS should be made with caution when different wavelengths, references and corrections are used for their derivation, a clear advantage of 6 over those Ru(II) derivatives nevertheless resides in its improved transparency–activity trade-off ( $\lambda_{\max} = 400$ ).

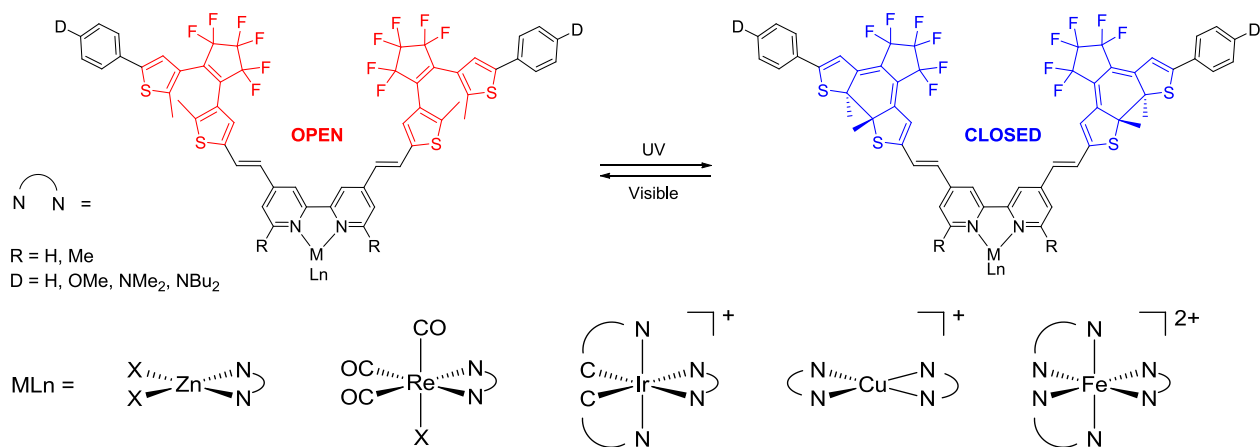
## Part B: Photochromic molecules: Metal complexes with bipyridine dithienylethenes ligands for nonlinear optics

Various diarylethene-containing polyimine ligands and their transition-metal complexes have been synthesized [49-58] and their photochromic behavior has been widely used for the photomodulation of luminescence and electronic properties. Le Bozec et al. are involved for several years in the use of 4, 4' - disubstituted-2, 2' -bipyridines as precursors to dipolar and octupolar metal complexes for second-order nonlinear properties [59-67]. In order to carry out the photoswitching of the NLO properties, they recently prepared a new type of 4,4' -bis(ethenyl)-2,2'-bipyridine ligand functionalized by a 4-(dimethylamino)phenyldithienylethene (DTE) group and the corresponding zinc bis (acetate) dipolar complex (Scheme 2.5) [68]. The quadratic hyperpolarizability of the open and closed forms of this compound is measured by the EFISH and HLS technique at 1.907  $\mu\text{m}$  available in our laboratory, LPQM, ENS Cachan. The excellent photochromic property of this complex was exploited to design the first example of metal-containing photochromic ligands allowing an efficient switching of the quadratic NLO properties.



Scheme 2.5: DTE-based bipyridines with  $\text{ML}_n$  dipolar complexes

In contrast, by complexation of the same photochromic bipyridine ligand to the luminescent bis-cyclometalated Ir (III) centre, an efficient photoregulation of the emission was found, whereas no significant modification of the quadratic NLO response related to photocyclization [69] could be observed, due to the weaker contribution of the Intraligand charge transfer (ILCT) vs Metal-ligand charge transfer (MLCT) transitions to the quadratic hyperpolarizability. These new observations and promising applications motivated us to extend the study to another series of chromophores in which DTE-based bipyridines combine with different donor groups (D) such as H, OMe, NMe<sub>2</sub>, and NBU<sub>2</sub>, with different metallic fragments, namely the stronger Lewis acid ZnCl<sub>2</sub> as well as the Ru (bipy)<sub>2</sub><sup>2+</sup>, Re(CO)<sub>3</sub>Br, Cu, and Fe moieties as shown in scheme 2.6. In this chapter we will describe their optical properties, photochromic behaviors, luminescence properties of these complexes, together with the quadratic hyperpolarizability of the open and photocyclized forms, measured by the EFISH and HLS techniques. In particular, the role of the metal center on the photochromic and NLO activity is shown to be very important.



*Scheme 2.6: Newly synthesized DTE-based bipyridines with different metal complexes and donor group.*

#### **B-2.4: Characterization of Photoswitching molecules**

Optical studies have been performed for all the newly synthesized photochromic molecules. All open forms show a strong absorption band between 338 to 386 nm and all closed forms between 620-729 nm. All samples are soluble in CH<sub>2</sub>Cl<sub>2</sub> or CHCl<sub>3</sub>; therefore samples are prepared in these solvent and characterized by means of UV-Visible spectroscopy and <sup>1</sup>H and

$^{13}\text{C}$  NMR in lower concentration. The synthesis and characterization by UV-visible spectroscopy and NMR are done by Lucie Ordroneau from Université de Rennes 1. Irradiation of the open form with UV light at 350 nm results in the colour change from transparent or pale yellow to deep blue or green and the appearance of a new broad band after 600 nm in the electronic absorption spectrum (depending upon the molecules), corresponding to the closed form as shown in Figure 2.2.

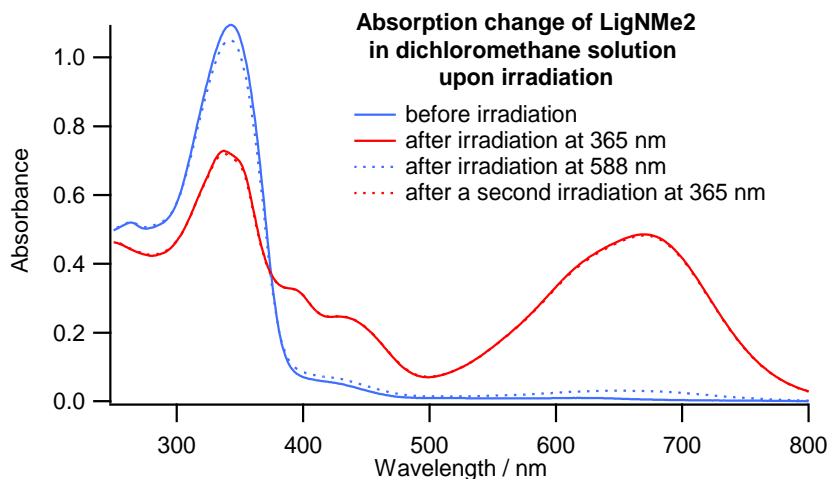


Figure 2.2: UV-Visible absorption change of Lig NMe<sub>2</sub>

$^1\text{H}$  NMR spectroscopy can be used to estimate the proportion of open and closed forms in the photostationary state (PSS). For both ligands, the photocyclization process was confirmed by  $^1\text{H}$  NMR spectroscopy experiments. The chemical conversion from the open form to the closed one in dipolar system varies for different photochromic complexes, i.e. 80 to 95% whereas other complexes specially the octupolar ones show 50 to 65% conversion only to the ring-closed isomers.

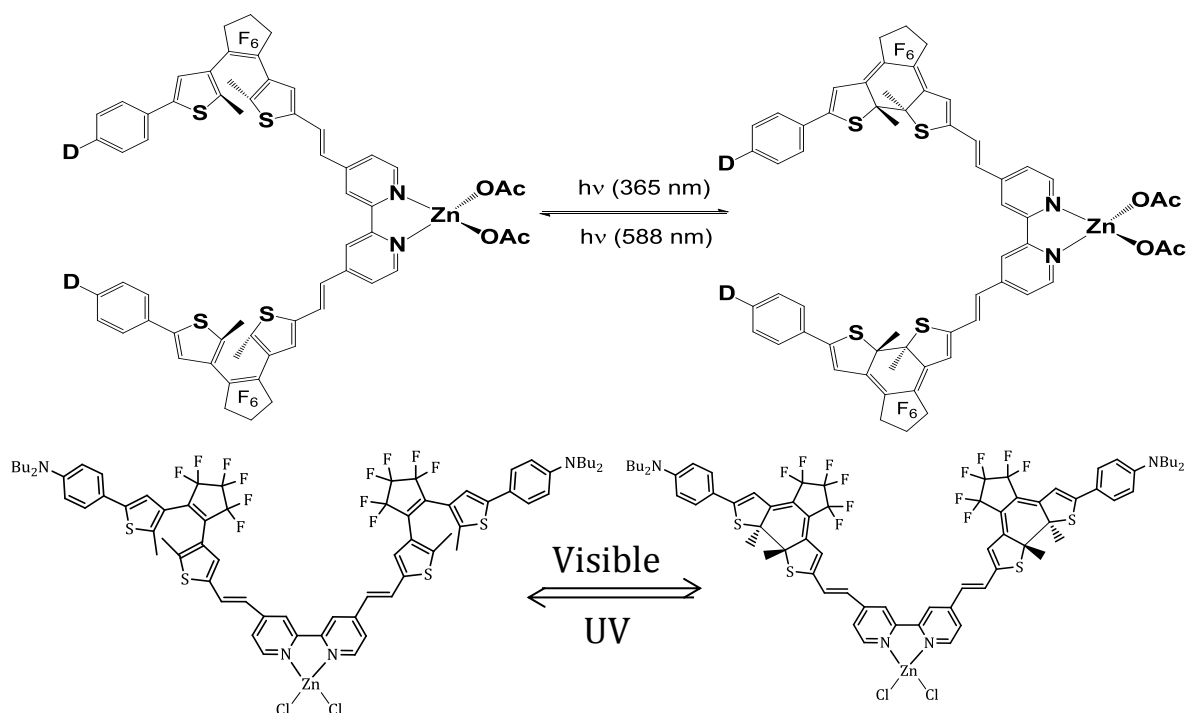
### **B-2.5: Experimental procedure**

The second-order NLO responses of the newly synthesized photochromic dipolar, tetrahedral and octupolar molecules are measured in  $\text{CH}_2\text{Cl}_2$  and concentrations about  $10^{-3}$  M by the EFISH and HLS technique, working with a nonresonant incident wavelength of 1.907  $\mu\text{m}$ . Using this wavelength ensures that any contribution to the signal from two-photon fluorescence becomes negligible, as its harmonic at 955 nm lies far from the fluorescence domain. The static  $\mu\beta_0$  values are also calculated at zero frequency by using the two-level

model [70]. The experimental error recorded for  $\mu\beta$  and  $\mu\beta_0$  of the open form is 20 percent and 5 percent for the closed form.

### **B-2.6: Photochromic properties and characterization of newly synthesized dipolar molecules**

The photocyclization process for each ligand and complex was monitored by  $^1\text{H}$  NMR and UV–Visible spectroscopy in dichloromethane. The photochromic behavior of ligand and its  $\text{Zn}(\text{OAc})_2$  complex has already been described. Upon illumination at 350 nm, new absorption bands at 629 nm and 687 nm appear [68], originating from the formation of the closed isomers as shown in Table 2.4. Complexation to  $\text{Zn}(\text{OAc})_2$  results in a typical bathochromic shift ( $\Delta\lambda = 6\text{--}18$  nm) of the intra-ligand charge transfer (ILCT) bands, as has been observed for related bis (acetato) zinc(II) complexes [71]. Similarly, upon irradiation at 350 nm, the yellow solutions of the open form of  $\text{ZnCl}_2$  turn green, with the emergence of a new low-energy broad band at 714 nm which can be attributed to the intraligand (IL)  $S_0 \rightarrow S_1$  transition of the closed DTE form [72].



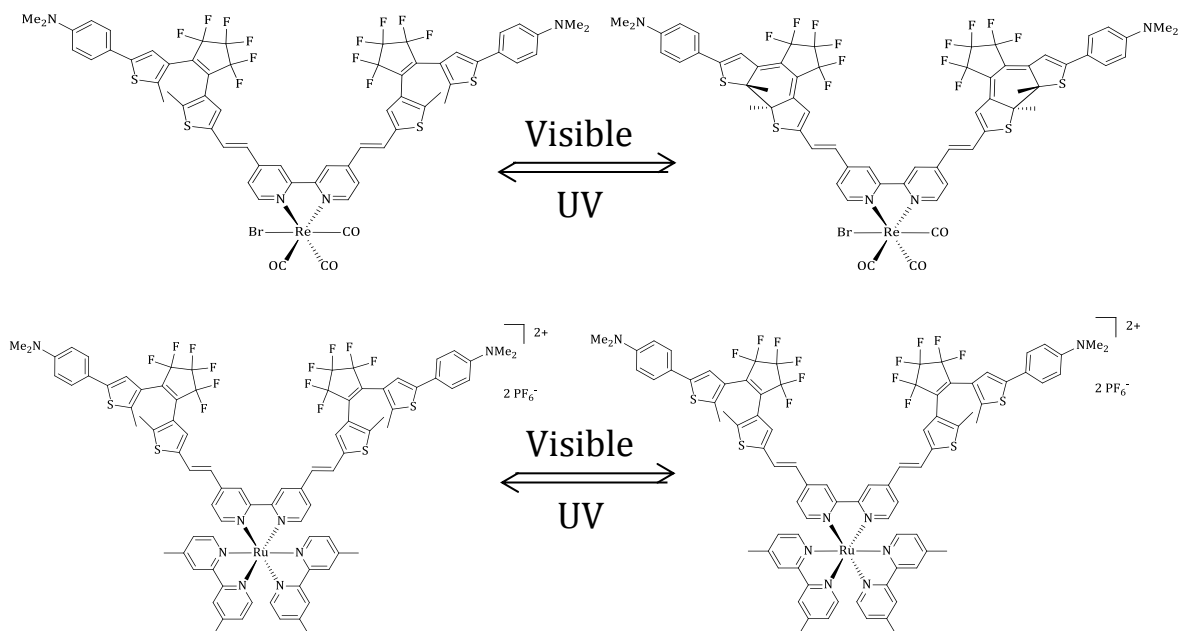


Figure 2.3: Chemical structure of photochromic bipyridine Zn (II), Re (I), and Ru (II) complexes.

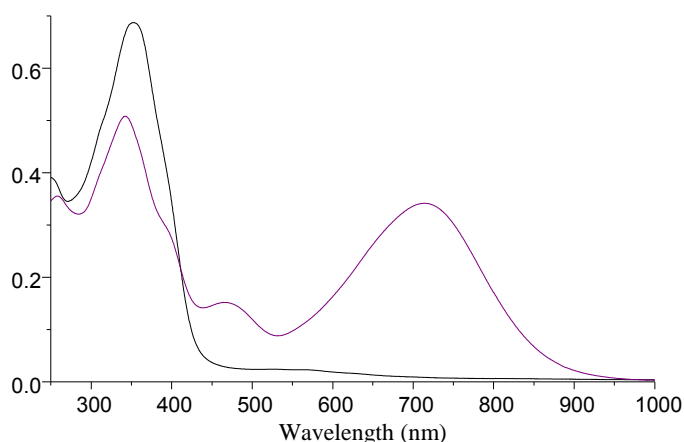


Figure 2.4: UV/Vis absorption change of  $ZnCl_2$  ( $D = NBU_2$ ) in  $CH_2Cl_2$  ( $1.5 \times 10^{-5} M$ ) upon irradiation. Open form shows in black and photostationary state in purple.

Their  $^1H$  NMR spectra show the characteristic downfield shift of the methyl signals and an upfield shift of the two thiophene protons. According to  $^1H$  NMR analysis, integration of the methyl groups indicates a photocyclization yield of 85% for the  $ZnCl_2$  ( $D = NBU_2$ ) open form and 90% for the  $Zn(OAc)_2$  ( $D = NMe_2$ ) open form. The conversion rate for the zinc complex (the irradiation time under the experimental conditions) to achieve the PSS is 1500 s for  $Zn(OAc)_2$  ( $D = NMe_2$ ), and 2500 s for  $ZnCl_2$  ( $D = NBU_2$ ) [72]. The absorption maxima of the closed-ring forms are dependent on the nature of the donor groups and metallic fragments.

Excitation at 588 nm, in the absorption band of the closed forms, led to the quantitative regeneration of the open isomers. Replacement of the NMe<sub>2</sub> group with the more strongly donating NBU<sub>2</sub> end group induces a small red shift ( $\Delta\lambda = 10$  nm) of the IL band, and complexation to ZnCl<sub>2</sub> induces a much larger bathochromic shift ( $\Delta\lambda = 35$  nm) than for Zn(OAc)<sub>2</sub>, in agreement with the higher Lewis acidity of ZnCl<sub>2</sub> vs Zn(OAc)<sub>2</sub>. The electronic absorption spectra of both rhenium and ruthenium complexes also show intense IL absorptions near 340 and 380 nm (shoulders). In addition, the ruthenium complex displays another broad band in the visible at 490 nm corresponding to MLCT  $d\pi(\text{Ru}) \rightarrow \pi^*(\text{bipy})$  transitions, whereas the rhenium complex shows a moderately intense absorption shoulder at 410 nm which can be assigned as the  $d\pi(\text{Re}) \rightarrow \pi^*(\text{bipy})$  transition.

*Table 2.4: UV-Vis absorption spectra for complexes in the open and closed (PSS) forms, emission data in the open form and percentage conversion at photostationary state [68, 72]*

| <b>Compound</b>  | <b><math>\lambda_{\text{max}}</math> / nm/Open</b> | <b><math>\lambda_{\text{max}}</math> /nm/Closed</b> | <b><math>\lambda_{\text{emission}}</math><br/>/nm open</b> | <b>Ring<br/>closing %</b> |
|--|--|---|--|---------------------------|
| <b>Ligand (1b)<sup>[ref. 68]</sup></b>   | <b>348</b>   | <b>347,395,438,669</b>                              |  | <b>95</b>                 |
| <b>Ligand (L<sup>a</sup>)<sup>[ref. 72]</sup></b>                                  | <b>346</b>   | <b>339,400,441,679</b>                              |  | <b>95</b>                 |
| <b>Zn (OAc)<sub>2</sub>, [D= NMe<sub>2</sub>]</b>                                  | <b>360</b>   | <b>343, 394. 450, 687</b>                           |  | <b>90</b>                 |
| <b>ZnCl<sub>2</sub> [D= NBU<sub>2</sub>]</b>                                       | <b>351</b>   | <b>342, 390, 463, 714</b>                           |  | <b>85</b>                 |
| <b>Re (CO)<sub>3</sub> Br [D=<br/>NMe<sub>2</sub>]</b>                             | <b>340, 380, 410</b>                               | <b>336, 387, 443, 705</b>                           | <b>652, 725</b>  | <b>65</b>                 |
| <b>(dmbipy)<sub>2</sub>Ru(PF<sub>6</sub>)<sub>2</sub> [D=<br/>NMe<sub>2</sub>]</b> | <b>338, 377, 491</b>                               | <b>336, 387, 443, 716</b>                           | <b>680, 753</b>  | <b>62</b>                 |

Photocyclizations of Re(CO)<sub>3</sub>Br and (dmbipy)<sub>2</sub>Ru](PF<sub>6</sub>)<sub>2</sub> [D = NMe<sub>2</sub>] open forms are also performed by irradiation with UV light at 350 nm, giving rise to lower-energy absorption bands at 705 and 716 nm, respectively, corresponding to the ring-closed isomers (Figure 2.5). Thus, a substantial bathochromic shift of the IL band ( $\Delta\lambda = 36\text{--}47$  nm) is also observed upon complexation of ligand to the Re (I) and Ru (II) organometallic fragments. The ratio of the

methyl signals between the closed and open DTE units (ring closing) in the photostationary states (PSS) is lower (60–65%) than those found for the zinc (II) complexes according to  $^1\text{H}$  NMR [72]. Finally, for all ligands and complexes, excitation at 650 nm, in the absorption band of the closed forms, leads to the quantitative regeneration of the open isomers, indicating a fully reversible closed-to-open photoisomerization.

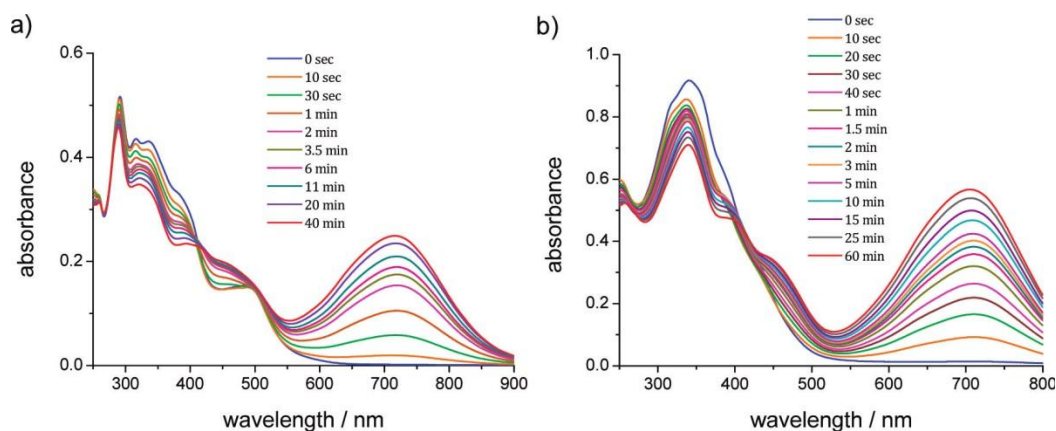


Figure 2.5: UV–Vis absorption spectra changes of (a)  $(\text{dmbipy})_2\text{Ru}(\text{PF}_6)_2$  [ $D = \text{NMe}_2$ ] and (b)  $\text{Re}(\text{CO})_3\text{Br}$  [ $D = \text{NMe}_2$ ] in dichloromethane upon excitation at 350 nm [72].

### **B-2.6.1: Luminescent Properties**

None of the ligands and complexes displays detectable luminescence in solution at room temperature when excited in the UV or visible bands. It is likely that the luminescence is inhibited by the competitive photocyclization pathway of the DTE unit. At 77 K (EPA), only rhenium and ruthenium complexes emit, displaying structured luminescence spectra with vibronic progressions of  $1400\text{--}1500\text{ cm}^{-1}$ , typical of aromatic and/or C=C bond vibrations. The emission characteristics are summarized in Table 2.4, and the emission spectra of  $\text{Re}(\text{CO})_3\text{Br}$  and  $(\text{dmbipy})_2\text{Ru}(\text{PF}_6)_2$  open and their PSS are shown in Figure 2.6.

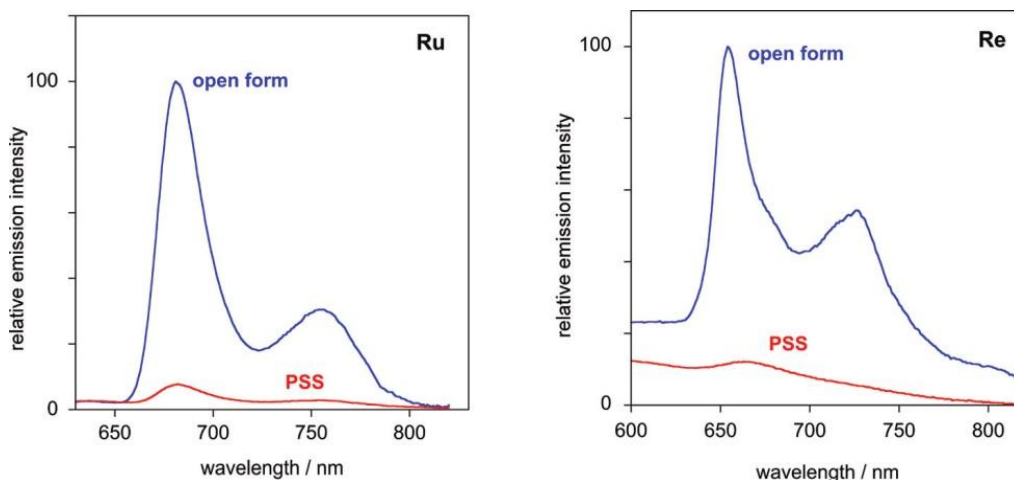


Figure 2.6: (Left) Emission spectrum of  $(dmbipy)_2 Ru(PF_6)_2$  at 77 K (blue line) upon excitation into the lowest energy absorption band (490 nm) and the corresponding spectrum recorded for the photostationary state (red line). (Right) Corresponding spectra of  $Re(CO)_3 Br$  open and its PSS.

### **B-2.6.2: NLO properties**

The SH intensity as observed from the open and closed forms of  $ZnCl_2 [D= NBu_2]$  in  $CHCl_2$  by the EFISH technique is plotted in Figure 2.7. The figure clearly shows a strong SH signal from the closed form as compare to the solvent (dichloromethane) and open form. The  $\mu\beta$

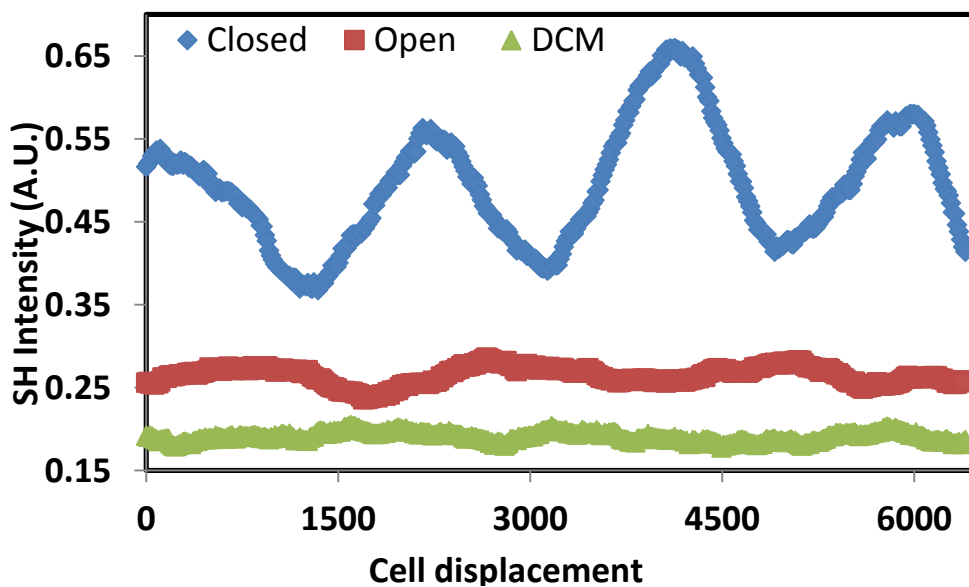


Figure 2.7: Comparison between the SH intensity collected from open and closed form of  $ZnCl_2 [D= NBu_2]$  and  $CHCl_2$ .

EFISH values of the newly synthesized photochromic dipolar zinc and rhenium complexes before and after UV irradiation are reported in Table 2.5, along with the values previously reported for Zn(OAc)<sub>2</sub> [68]. As expected, we have noticed weak  $\mu\beta$  value from open form of ZnCl<sub>2</sub> and Re(CO)<sub>3</sub>Br which are quite similar to the  $\mu\beta$  value obtained from the open form of Zn(OAc)<sub>2</sub>, in the absence of conjugation between the amino donor group and the bipyridyl metal acceptor moieties.

An intense increase of the second-order NLO activity is observed after UV irradiation and subsequent accumulation of ring-closed isomers: in the case of ZnCl<sub>2</sub> [D= NBU<sub>2</sub>] the second-order NLO response is increased almost 14-fold after only 35% of ring closing, while a 21-fold enhancement is observed after 65% of ring closing which consists mainly of a mixture of open-closed and closed-closed isomers approximately in 2:1 ratio.

Table 2.5: EFISH  $\mu\beta$  values determined at 1.910  $\mu\text{m}$  incident wavelength of Zn (II) and Re (I) complexes.

| Compound                                      | EFISH open form<br>$\times 10^{-48}$ esu |              | EFISH after UV irr.<br>$\times 10^{-48}$ esu |              | Ring closing<br>% | Enhance<br>ment<br>Factor |
|---|--|--------------|--|--------------|-------------------|---------------------------|
|   | $\mu\beta$                               | $\mu\beta_0$ | $\mu\beta$                                   | $\mu\beta_0$ |                   |                           |
| Zn(OAc) <sub>2</sub> , [D= NMe <sub>2</sub> ] | 200                                      | 160          | 4220   | 1800         | 90                | 11                        |
| ZnCl <sub>2</sub> [D= NBU <sub>2</sub> ]      | 113                                      | 105          | 3850   | 1460         | 35                | 14                        |
|   |  |              | 5650   | 2143         | 65                | 21                        |
| Re(CO) <sub>3</sub> Br [D= NMe <sub>2</sub> ] | 240                                      | 187          | 2920   | 1148         | 65                | 6                         |

Furthermore, it is also interesting to note that this latter EFISH  $\mu\beta_0$  value is even higher than that previously reported for Zn(OAc)<sub>2</sub> [D= NMe<sub>2</sub>] in the PSS (90% of ring closing), as expected from the higher Lewis acidity of ZnCl<sub>2</sub> vs Zn(OAc)<sub>2</sub>. A similar, but somewhat less dramatic, behavior is observed for the rhenium(I) complex, with an increase of  $\mu\beta_0$  from  $187 \times 10^{-48}$  to  $1148 \times 10^{-48}$  esu in the PSS (65% of ring closing). The lower efficiency of the Re(I) complex in comparison with that of the corresponding Zn(II) complexes has already been shown in dipolar donor-substituted styryl bipyridine metal chromophores [73-74] and could be explained by the presence of two vectorially opposed charge-transfer transitions

(MLCT and ILCT), which contribute to a lowering of the total NLO response. The large enhancement of  $\mu\beta_0$  after ring closure clearly reflects the delocalization of the  $\pi$ -electron system in the closed forms, and as expected, the largest NLO enhancement is observed with the complex featuring the harder  $\text{ZnCl}_2$  Lewis acid associated with the better  $\text{NBu}_2$  donor group, in agreement with the higher red shift of the intraligand (IL) transition which dominates the second-order NLO response. This efficient on/off switching markedly contrasts with the absence of switching of the NLO response observed for the cyclometalated phenylpyridine Ir (III) complex featuring the same photochromic bipyridyl ligand, in which the EFISH response was found to be mainly controlled by a MLCT/ ILCT process from the cyclometalated phenylpyridine Ir (III) moiety to the  $\pi^*$  orbitals of the bipyridine, and not by an intraligand transition [69].

The HLS technique is also used for the molecular first-hyperpolarizability  $\beta$  measurements of the dicationic ruthenium complex and for comparison with the neutral Re complex. The closed forms of Ru and Re complexes show an additional MLCT maximum to high energy of the main IL (DTE) band, therefore the  $\beta_0$  value is calculated [70] taking the major  $\lambda_{\text{max}}$  values. The inferred  $\beta$  and  $\beta_0$  values are given in Table 2.6.

| Compound   | HLS open form<br>( $\times 10^{-30}$ esu) |           | HLS after UV irr.<br>( $\times 10^{-30}$ esu) |           | Ring closing<br>% | Enhance<br>ment<br>Factor<br>for $\beta_0$ |
|--|---|-----------|---|-----------|-------------------|--|
|  | $\beta$                                   | $\beta_0$ | $\beta$                                       | $\beta_0$ |                   |  |
| Re (CO) <sub>3</sub> Br [D= NMe <sub>2</sub> ]                                 | 229                                       | 178       | 965   | 380       | 65                | 2  |
| (dmbipy) <sub>2</sub> Ru (PF <sub>6</sub> ) <sub>2</sub> [D=NMe <sub>2</sub> ] | 325                                       | 223       | 1113  | 419       | 62                | 2  |

Table 2.6: HLS  $\beta$  values determined at 1.907  $\mu\text{m}$  incident wavelength of Re (I) and Ru (II) complexes.

Much attention has been paid to the large  $\beta$  responses of bipyridine ruthenium chromophores, such as octupolar D<sub>3</sub> tris-chelate ruthenium complexes, which are dominated by low-lying ILCT or MLCT excitations, depending on the electron-donating or -accepting nature of the substituents on the bipyridyl ligands [61-65]. It turned out that (dmbipy)<sub>2</sub>Ru](PF<sub>6</sub>)<sub>2</sub> [D=

NMe<sub>2</sub>] in its open form also shows a fairly large  $\langle\beta\rangle$  value, larger than that of the rhenium complex, which can be reasonably attributed to low-energy MLCT  $d\pi(\text{Ru})\rightarrow\pi^*(\text{bipy})$  transitions. Upon photocyclization of the DTE,  $\langle\beta_0\rangle$  is found to increase by a factor of ca. 2, a result which is consistent with an NLO response mainly controlled by the red shifted IL transition.

### **B-2.7: Photochromic properties and characterization of tetrahedral Copper metal complexes with bipyridine DTE ligands**

In previous section we have shown an efficient photochromic NLO enhancement of dipolar metal complexes featuring a bis-DTE bipyridine ligand [68, 72]. In the first chapter we discussed about the non-dipolar (octupolar) molecules which emerged as an important and promising class of NLO chromophores, giving rise to two- and three-dimensional architectures [75]. In this respect metal ions are versatile templates to build up tetrahedral ( $T_d$ ,  $D_{2d}$ ) and octahedral ( $D_3$ ) octupolar arrangements [60, 62, 76]. It has been already shown that the association of  $d^{10}$  Cu(I), Ag(I) and Zn(II) ions with tetrasubstituted 6,6',4,4'-bipyridyl ligands gives rise to pseudo-tetrahedral metal complexes with fairly large quadratic hyperpolarizabilities [64, 77-78].

A new bis-bipyridine Cu (I) complex featuring four DTE units was designed by Le Bozec et al. It is important to point-out that a very few single molecules containing four or more DTE

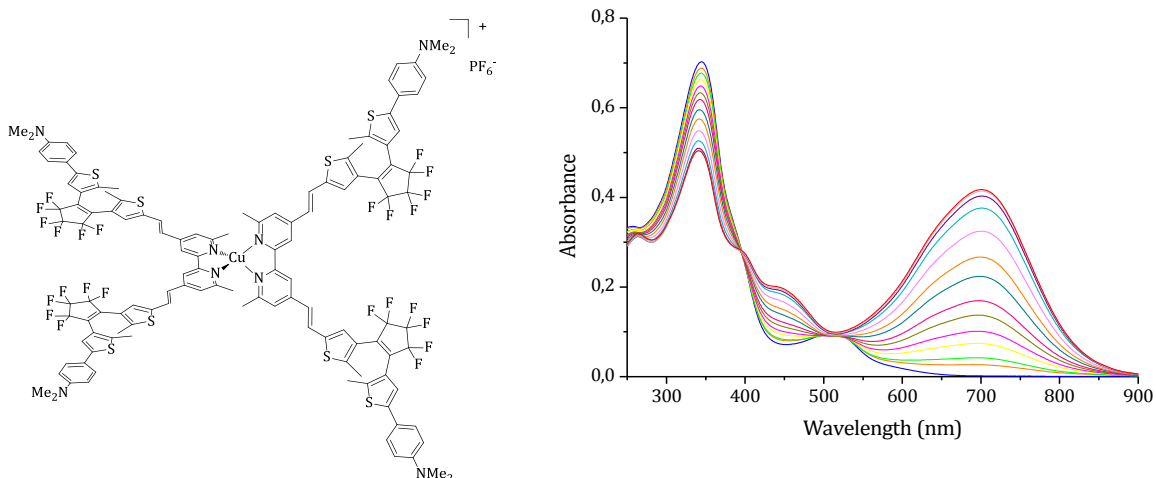


Figure 2.8: (Left) Chemical structure of  $[\text{Cu}(\text{L}_{o,o})_2]\text{PF}_6$ . (Right) Experimental UV-vis absorption spectral change of  $[\text{Cu}(\text{L}_{o,o})_2]\text{PF}_6$  in  $\text{CH}_2\text{Cl}_2$  upon excitation at 350 nm.

have been synthesised so far [79], and in the majority of them two vicinal DTE units cannot be simultaneously closed [80-82] whereas the two reported cases with full switching [79, 83] use saturated or poorly conjugated bridging units to connect the different photochromic DTE fragments. In this part, we demonstrate that the quadruple DTE copper complex is converted into its fully closed isomer upon UV irradiation, and we present for the first time the modulation of the quadratic NLO activity of an octupolar chromophore.

### **B-2.7.1: Characterization of newly synthesized Tetrahedral Cu complexes**

The UV-visible spectrum of  $[\text{Cu}(\text{L}_{o,o})_2]\text{PF}_6$  is recorded at 298 K in  $\text{CH}_2\text{Cl}_2$  and shows an intense band, similar to that of  $\text{L}_{o,o}$  around 350 nm, assigned to the (IL)  $\pi \rightarrow \pi^*$  transition of the bipyridyl moieties with some mixing of the DTE units (Table 2.7). Another, weaker band appears in the visible at 511 nm corresponding to the d  $\pi(\text{Cu}) \rightarrow \pi^*(\text{bipy})$  MLCT transition [84]. The photocyclization process for both ligand and complex is monitored by  $^1\text{H}$  NMR in  $\text{CH}_2\text{Cl}_2$ .

*Table 2.7: UV-Vis absorption spectra for Cu (L)<sub>2</sub> PF<sub>6</sub> complexes.*

| Compound  | $\lambda_{\text{max}}$ / nm/Open | $\lambda_{\text{max}}$ /nm/Closed |
|---|----------------------------------|-----------------------------------|
| <b>L</b>  | <b>340</b>                       | 340, 395, 431, <b>668</b>         |
| <b>Cu (L)<sub>2</sub> PF<sub>6</sub> [D= NMe<sub>2</sub>]</b> | <b>344, 511</b>                  | 343, 399, 450, <b>701</b>         |

Upon irradiation at 350 nm, the yellow solution of  $\text{L}_{o,o}$  and the red solution of  $[\text{Cu}(\text{L}_{o,o})_2]\text{PF}_6$  turn green, with the emergence of a new intense and broad band at 668 and 701 nm, respectively, attributed to the intraligand (IL)  $S_0 \rightarrow S_1$  transition of the closed DTE form displayed in figure 2.8. According to  $^1\text{H}$  NMR and UV-vis analyses a photocyclization yield of around 65% is observed for both ligand and complex, showing that coordination to the Cu(I) ion does not give rise to perturbation of the photochromic behavior.

### **B-2.7.2: NLO properties**

The  $T_d$  (or  $D_{2d}$ ) symmetry reduces the nonlinear microscopic coefficient to only one non-vanishing term,  $\beta_{xyz}$ , which can be easily deduced from the following relation:  $\langle \beta_{\text{HLS}}^2 \rangle = 4/7 \beta_{xyz}^2$  [75]. The experimentally inferred  $\beta$  values at 1.907  $\mu\text{m}$  and the corresponding off

diagonal  $\beta_{xyz}$  coefficients for the Cu (I) complex before and after UV irradiation are mentioned in Table 2.8.

Table 2.8: HLS  $\beta$  values and  $\beta_{xyz}$  determined at 1.907  $\mu\text{m}$  incident wavelength of  $[\text{Cu}(\text{L}_{o,o})_2]\text{PF}_6$  complexes.

| Compound   | $\beta^{(a)}$ and ( $\beta_{xyz}$ ) <sup>(b)</sup><br>( $\times 10^{-30}$ esu)<br>Before UV irradiation | $\beta^{(a)}$ and ( $\beta_{xyz}$ ) <sup>(b)</sup><br>( $\times 10^{-30}$ esu)<br>After UV irradiation | Ring closing<br>% | Enhancement<br>Factor |
|--|---|--|-------------------|-----------------------|
| $[\text{Cu}(\text{L}_{o,o})_2]\text{PF}_6$ [D=<br>NMe <sub>2</sub> ] | $\beta = 266 \pm 52^{(a)}$<br>$\beta_{xyz} = 352 \pm 70^{(b)}$  | $\beta = 1672 \pm 160^{(a)}$<br>$\beta_{xyz} = 2212 \pm 220^{(b)}$                                     | 65                | 6                     |

Before photocyclisation,  $[\text{Cu}(\text{L}_{o,o})_2]^+$  shows a fairly large  $\beta$  value which can be reasonably attributed to the low energy MLCT  $d\pi(\text{Cu}) \rightarrow \pi^*(\text{bipy})$  transition. A substantial enhancement of the second-order NLO activity is then observed after UV irradiation and subsequent accumulation of the ring-closed isomers, a result which is consistent with an NLO response mainly controlled by the red-shifted ILCT transition. The molecular first hyperpolarizability is increased almost six fold after only 65% of ring-closing, to reach an impressive  $\beta_{xyz}$  value of  $2212 \times 10^{-30}$  esu, which is to our knowledge the largest off-diagonal hyperpolarizability coefficient ever reported for octupolar chromophores having  $T_d$  or  $D_{2d}$  symmetry [85].

### **B-2.8: Photochromic properties and characterization of Octahedral Iron metal complexes with bipyridine DTE ligands**

In previous section we have shown an efficient photochromic NLO enhancement in dipolar metal complexes and tetrahedral complexes containing a bis-DTE bipyridine ligand [68, 72]. In that respect, we continue this study with octahedral ( $D_3$ ) Fe complexes. In earlier studies, the  $\beta$  has been inferred for octahedral complexes bearing different metals at the centre; huge  $\beta$  values have been reported and shown to be two to three times higher than for dipolar complexes [64].

We extend the study of photochromic molecules to the octahedral  $D_3$  symmetry, based on new octupolar Fe (II) complexes. All molecules exhibit strong absorption bands in the visible region. As we know that these bands are very sensitive to the nature of the donor group

therefore, we incorporated three different donor groups in order to explore their influence on  $\beta$  values.

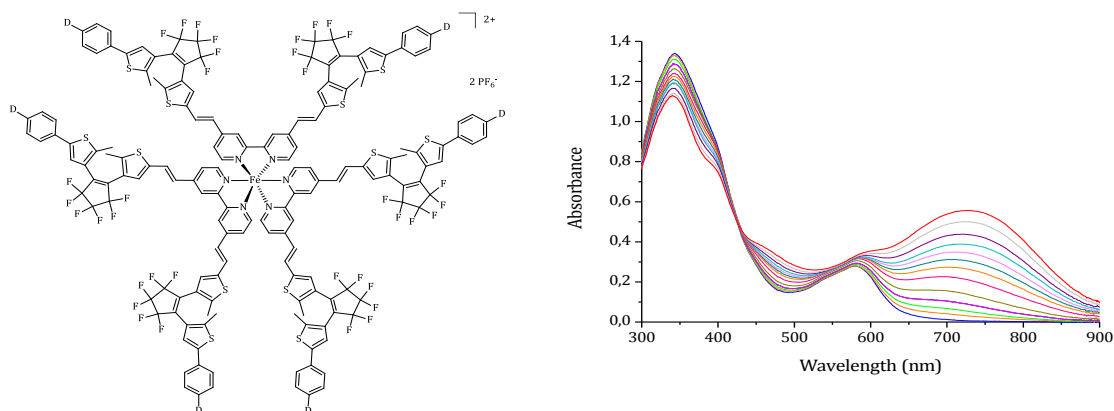


Figure 2.9: (Left) Chemical structure of photochromic bipyridine Fe (II) ( $D = H, NMe_2$  and  $NBu_2$ ) complexes (Right) UV-Vis absorption spectra changes in  $CH_2Cl_2$  upon irradiation excitation at 350 nm.

### **B-2.8.1: Characterization of the newly synthesized Octahedral Fe complexes**

The UV-visible spectrum of Fe (II) is recorded at 298 K in  $CH_2Cl_2$  and shows an intense band similar to that of the ligands around 350 nm, assigned to (IL)  $\pi \rightarrow \pi^*$  transition of the bipyridyl moieties with some mixing of the DTE units (Table 2.9). Another band appears in the visible at 580 nm corresponding to the  $d\pi(Fe) \rightarrow \pi^*(bipy)$  MLCT transition [84].

Table 2.9: Electronic absorption data for complexes in the open and closed (PSS) forms, emission data in the open form and percentage conversion at photostationary state

| Compound                  | $\lambda_{max}$ / nm/Open | $\lambda_{max}$ / nm/Closed |
|---------------------------|---------------------------|-----------------------------|
| Fe [D= H]                 | 386, 576                  | 382, 590, 630               |
| Fe [D= NMe <sub>2</sub> ] | 330, 585                  | 339, 710                    |
| Fe [D= NBu <sub>2</sub> ] | 343, 580                  | 340, 729                    |

The photocyclization process for both ligand and complex is monitored by  $^1H$  NMR in  $CH_2Cl_2$ . Upon irradiation at 350 nm, a new broad band emerges at 630, 710, and 729 nm, attributed to the intraligand (IL)  $S_0 \rightarrow S_1$  transition of the closed DTE form. According to  $^1H$

NMR and UV-vis analyses, a photocyclization yield of around 60% is observed for the complex.

Table 2.10: HLS  $\beta$  values of Fe complexes determined at 1.907  $\mu\text{m}$  incident wavelength.

| Compound                  | $\beta_{\text{HLS}}$ open form ( $\times 10^{-30}$ esu) | $\beta_{\text{HLS}}$ Closed form ( $\times 10^{-30}$ esu) | Ring closing % | Enhancement Factor |
|---------------------------|---|---|----------------|--------------------|
| Fe [D= H]                 | 225   | 1076  | 60             | 4                  |
| Fe [D= NMe <sub>2</sub> ] | 250   | 2000  | 60             | 8                  |
| Fe [D= NBu <sub>2</sub> ] | 304   | 1535  | 35             | 5                  |
|                           |   | 1900  | 60             | 6                  |

### **B-2.8.2: NLO properties**

The  $\beta$  values of the octupolar Fe (II) complexes open and closed forms are reported in Table 2.10. They increase considerably with the strength of donor group. A dramatic increase of the second-order NLO activity is observed after UV irradiation and subsequent accumulation of ring-closed isomers: in the case of Fe [D=H and NMe<sub>2</sub>] the second-order NLO response is increased almost 4-fold and 8 fold respectively after 60% of ring closing; in the case of Fe [D= NBu<sub>2</sub>] the response is increased almost 5-fold after 35% of ring closing whereas a 6 fold enhancement is observed after 60% of ring closing which consists mainly of a mixture of open-closed and closed-closed isomers approximately in a 2:1 ratio. This can be explained by the presence of two vectorially opposed charge-transfer transitions in iron (MLCT and ILCT), which contributes to a lowering of the total NLO response. The large enhancement of  $\beta$  after ring closure clearly reflects the delocalization of the  $\pi$ -electron system in the closed forms.

### **B-2.9: Role of MLCT transition with respect to NLO activity**

The MLCT band in the visible region contributes to the NLO activity. Therefore, it is important to estimate the influence of both transitions to the molecular hyperpolarizability. The ILCT and MLCT are roughly parallel but in opposite direction as displayed in Figure 2.10. Recently, Vance and Hupp used electroabsorption spectroscopy to calculate the

contributions from both MLCT and ILCT transitions to the NLO response on an octupolar complex [86].

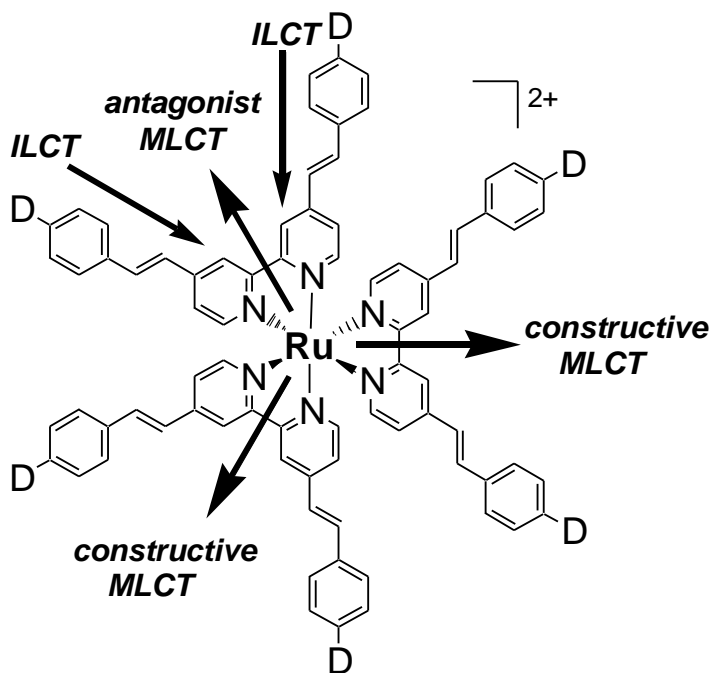


Figure 2.10: Constructive or antagonist interactions between the MLCT and ILCT transitions.

They suggested that the total hyperpolarizability ( $\beta_{\text{TOT}}$ ) results from the summation of the two contributions  $\beta_{\text{ILCT}}$  and  $\beta_{\text{MLCT}}$  which are in opposite sign and thus destructively interfere.

$$\beta_{\text{TOT}} = |\beta_{\text{ILCT}}| - |\beta_{\text{MLCT}}|$$

The proposed model based on an antagonist contribution of both ILCT and MLCT does not allow us to justify all the experimental results. But this can be a possible reason for not getting higher  $\beta$  values from  $\text{Re}(\text{CO})_3 \text{Br}$  [ $\text{D} = \text{NMe}_2$ ] as compared to  $\text{Zn}(\text{OAc})_2$ , [ $\text{D} = \text{NMe}_2$ ]. Zn shows only ILCT contribution, d electron subshell is complete, and d electrons do not tend to transfer to other orbitals, whereas Re shows contribution from MLCT as well as ILCT, as the d subshell is incomplete and d electrons may tend to transfer to empty orbitals of the ligand.

### **Part C: Lanthanide Series**

As discussed in chapter 1, the lanthanides series, porphyrins and phthalocyanines show various applications in different domain because of their outstanding properties and their uses as contrast agents for medical imaging as well as for their catalytic, magnetic, and luminescence properties [87]. The study of the NLO properties of lanthanides remains in its beginnings and becomes currently an emerging field of research. In this context, Le Bozec et al recently reported the first dipolar lanthanide terpyridyl complex family exhibiting a high hyperpolarizability coefficient  $\beta$  and evidenced so-called *f*-electrons induced second-order NLO activity enhancement along the lanthanide series [88]. To get more insight into this intriguing phenomenon, another experiment was performed with multipolar lanthanide complexes,  $\text{Na}_3[\text{Ln}(\text{dipic})_3]$ . It confirms the *f*-electrons induced NLO activity enhancement as a general property of *f*-block elements and strongly suggests a significant direct contribution of *f* electrons to the hyperpolarizability  $\langle \beta \rangle$  [89-91]. In the present work we have designed octupolar complexes using phthalocyanines and lanthanides to study the second order NLO properties. Octupolar molecules, in which symmetry constraints impose a cancellation of the dipole moment, have considerably extended the possibilities of molecular engineering of second-order nonlinear optical molecules by enlarging the dimensionality of the charge transfer.

The 3D delocalization between two cycles exists in double-decker complexes formed by phthalocyanines (Pc) with various ions, especially with lanthanide (III) ions [92], and can acts as a model template for electronic interactions along the edges of a cube. Electron spin resonance (ESR) studies of  $[\text{Pc}_2\text{Lu}]$  and theoretical calculations correlated to the observed absorption spectrum have shown that the molecule has an odd number of electrons and that the unpaired electron is completely delocalized over both rings, giving rise to a characteristic electronic transition in the near-IR region [93-94].

More interestingly, X-ray diffraction studies of  $[\text{Pc}_2\text{Nd}]$  and  $[\text{Pc}_2\text{Lu}]$  showed that the two Pc rings are rotated  $45^\circ$  with respect to each other [95-96], giving a non-centrosymmetric structure of approximately  $D_{4d}$  symmetry.

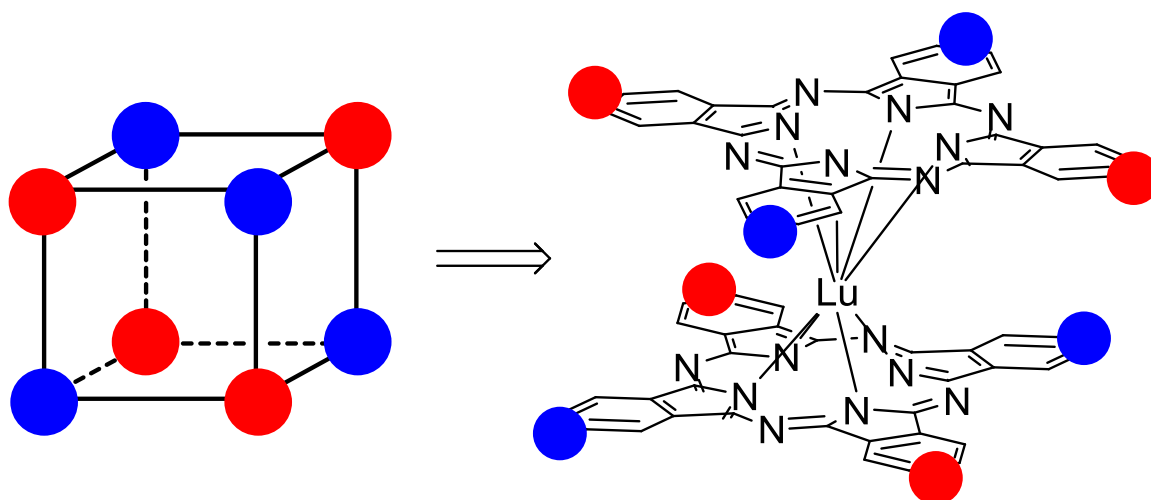
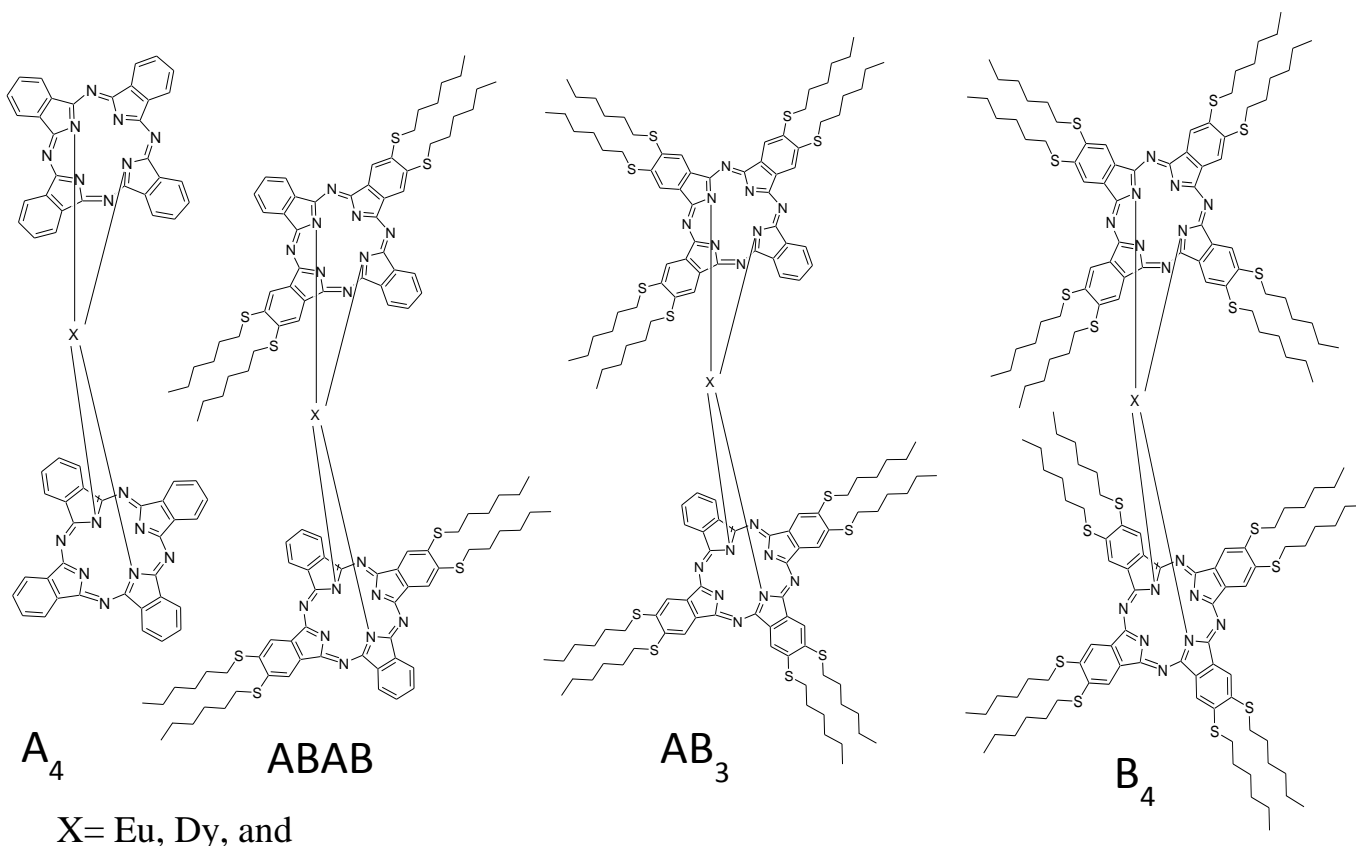


Figure 2.11: Bis (phthalocyanine) lutetium complex  $[Pc_2Lu]$  as a point-charge template for an octupole

Because of their extended  $\pi$ -electron systems, phthalocyanines and their transition-metal complexes have been used to build up interesting nonlinear compounds, including various octupolar structures [97].



Scheme 2.7: Bis (phthalocyanine) ( $Ln = Eu, Dy, \text{ and } Lu$ ) complex  $[Pc_2Eu]$   $[Pc_2Dy]$  and  $[Pc_2Lu]$  template for an octupole.

In this context, Bretonnière et al. from ENS Lyon and Ahsen et al, from Gebze Institute of Technology from Turkey reported the first step towards the construction of a true octupolar cube using lanthanide (such as Eu, Dy, and Lu) complexes with crosswise ABAB macrocycles. A bis-(phthalocyaninato) lanthanide sandwich complex with a crosswise ABAB phthalocyanine bearing electron-donor (thioalkyl) groups on two opposite rings was synthesized and its first molecular hyperpolarizability ( $\beta$ ) measured.

Although there are no real electron-acceptor groups, the required ABAB-type alternation for one face of the cube is present, as thioalkyl groups and hydrogen atoms do not display the same electronic properties. Similarly, AB<sub>3</sub> (3 electron-donor groups two opposite rings), A<sub>4</sub> (no electron donor groups on two opposite rings), and B<sub>4</sub> (4 electron-donor groups on two opposite rings) double-decker complexes are synthesized and their hyperpolarizability is measured. This is the first step towards an optimized cubic structure with alternating donor and acceptor groups with the synthesis, crystal structure determination, and measurement of the molecular first-order hyperpolarizability  $\beta$  by HLS, of original lanthanides sandwich complexes displaying the required ABAB, AB<sub>3</sub>, A<sub>4</sub> and B<sub>4</sub>-type alternation for one face of the cube. The structures are shown in scheme 2.7. They are characterized by an intense absorption in the near-IR due to an intervalence transition. Bis- (phthalocyaninato) lanthanide sandwich complexes with ABAB, AB<sub>3</sub>, A<sub>4</sub>, and B<sub>4</sub> are further oxidized [(Lu (Pc)<sub>2</sub><sup>+</sup>] and reduced [(Lu (Pc)<sub>2</sub><sup>-</sup>] and their  $\beta$  value is calculated.

### **C-2.10: Crystal structure**

The crystal structure is taken for bis (phthalocyaninato) - lutetium (III) complexes by X-ray diffraction analysis [97]. The molecular central core structures are very similar to that of the previously reported unsubstituted [96] and octasubstituted [98] bis (phthalocyaninato)-lutetium (III) complexes. Two phthalocyanine rings flank the central Lu<sup>3+</sup> ion. The Lu<sup>3+</sup> ion is octacoordinated by eight nitrogen atoms of the isoindole N2 and N6 (Niso) in a slightly distorted square antiprism geometry. As expected, there is a staggering angle ( $\alpha$ ) of 45° between the two cycles that creates a chiral noncentrosymmetric molecule. This small angle, combined with the short interplanar distance, gives hope for good electronic delocalization and good optical properties. The values of interplane distance ( $d_{N4-N4}$ ) of Eu, Dy and Lu are

2.841 Å, 2.773 Å, and 2.656 Å respectively. The interplane distance ( $d_{N4-N4}$ ) of Ln ABAB decrease from Eu to Lu following the same variations as the ionic radii of the metal cations.

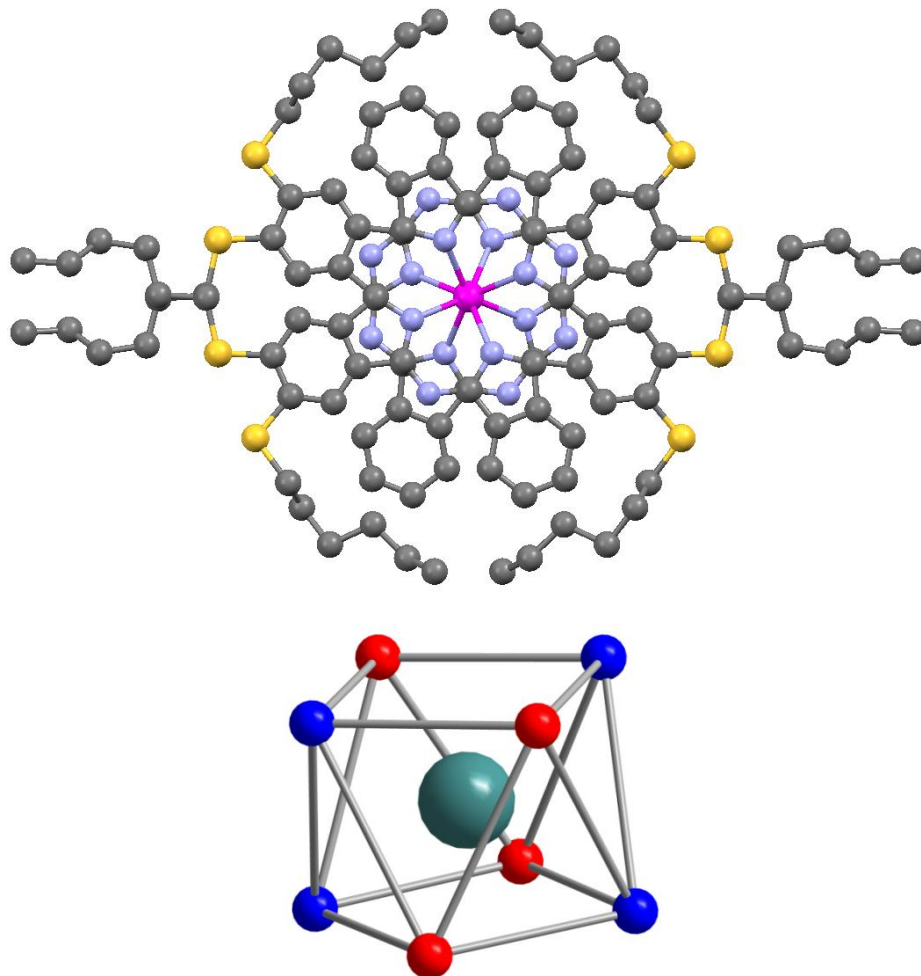
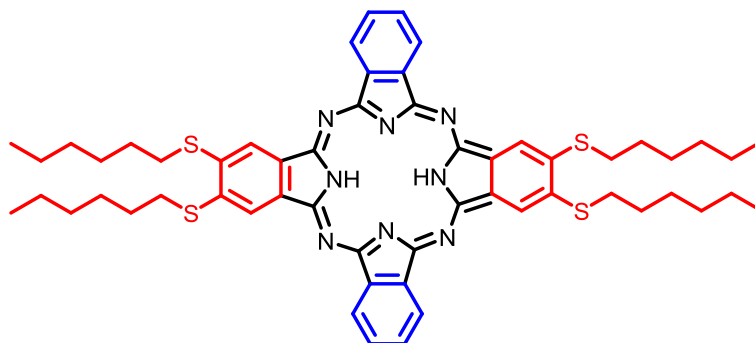


Figure 2.12: (a) X-ray crystal structure of  $M = \text{Lu}, \text{Dy}, \text{Y}$  and  $\text{Eu}$  ( $\text{H}$  atoms and the solvent molecule have been omitted for clarity) and (b) coordination polyhedron around the  $\text{La}^{3+}$  ion



Scheme 2.8: The structure of phthalocyanine ABAB

The Lu<sup>3+</sup> ion is octacoordinated by the eight nitrogen atoms of the isoindoles (N2 and N6, denoted as N<sub>iso</sub>) in slightly distorted square-antiprism geometry (Figure 2.12 b). In Figure 2.12 b, the N2 atoms in red color (the N<sub>iso</sub> atoms of the isoindole rings bearing the electron accepting groups) and the N6 atoms in blue color (which bear the electron donating groups) are pictured in different colors to show the parallel between the coordination polyhedron and the octupolar cube in Figure 2.11.

### **C-2.11: Linear properties**

The structure of phthalocyanine ABAB is shown in scheme 2.8. Figure 2.13 (a), (b), and (c) shows the absorption spectra of our newly synthesized bis (phthalocyaninato) - lanthanide (III) ABAB complexes in neutral, oxidized and reduced form in chloroform. In accordance with their electronic structure, Pcs present intense  $\pi$ - $\pi$  bands in the visible (Q band) and UV (B or Soret band) spectral regions. Graph presents the classical spectrum of a low symmetry phthalocyanine ABAB with B band at 340 nm and an intense Q band split in two with maxima at 682 and 719 nm. Several less intense components observed at the foot of the Q band are considered to be of vibronic origin. Upon complexation, small hypsochromic shifts are observed for both the B and Q bands, with disappearance of the splitting. The substitution of the Pc ring with the four electron-donating thio (hexyl) groups provokes a red shift of all maxima relative to the unsubstituted analogues [92].

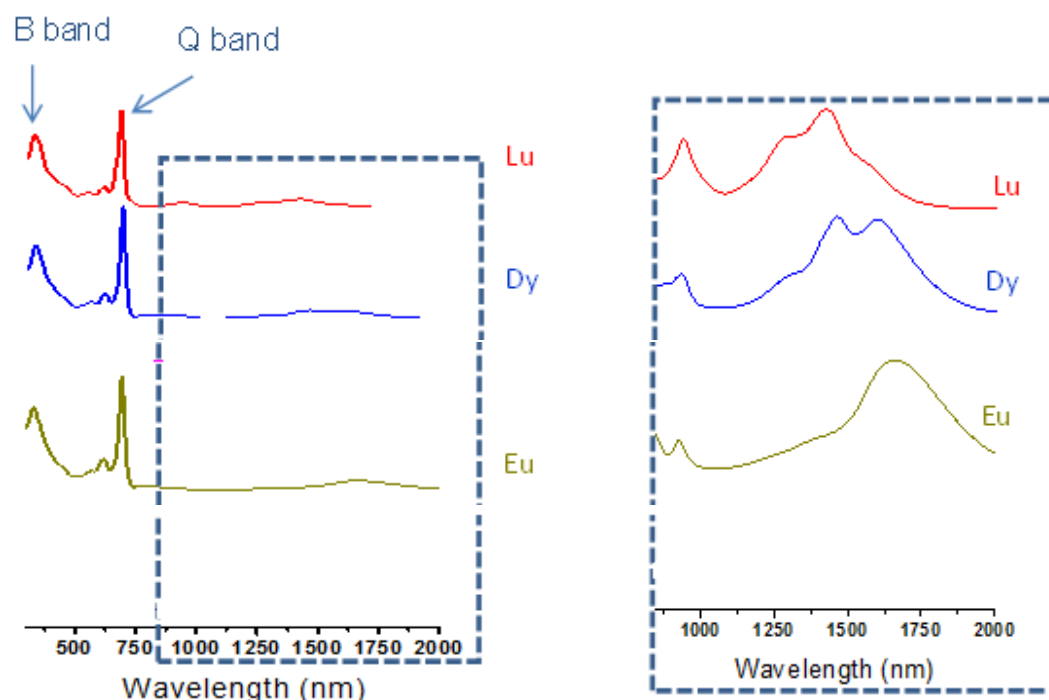


Figure 2.13: (a) Absorption spectra of newly synthesized bis (phthalocyaninato) - lanthanide (III) ABAB complexes in the neutral forms in chloroform. The inset shows the zoom NIR absorption of bis (phthalocyaninato) – lanthanide (III) complexes.

The UV-NIR spectrum of neutral Lu ABAB bis (Phthalocyanine) shows a relatively intense absorption at 682 nm with a vibronic band at 645 nm due to the phthalocyanine Q band. The broad band at 400 with a shoulder at 443 nm is attributed to the phthalocyanine Soret band. In addition, the intramolecular charge transfer (ICT) between two Pc rings of neutral Lu ABAB bis (Phthalocyanine) shows a broad and intense absorption band in the infrared region appearing between 1075 and 1705nm. The electronic absorption spectra of ABAB Eu and Dy are similar to Lu ABAB and the electronic spectral data summarized in Table 2.11.

Table 2.11: UV-Vis absorption spectra of neutral, oxidised and reduced forms of Ln (Eu, Dy, and Lu) ABAB bis-phthalocyanine in chloroform ( $1 \times 10^{-5}$  M).

| Sample<br>ABAB | Form     | $\lambda_{\max}$ (nm) |          |           |
|----------------|----------|-----------------------|----------|-----------|
|                |          | B                     | Q        | ICT       |
| Eu             | Neutral  | 322                   | 609, 686 | 1118-1911 |
| Eu             | Oxidized | 351                   | 614, 748 | -----     |
| Eu             | Reduced  | 346                   | 638, 695 | -----     |
| Dy             | Neutral  | 336                   | 680      | 1165-1865 |
| Dy             | Oxidized | 412                   | 609, 732 | -----     |
| Dy             | Reduced  | 330                   | 640, 706 | -----     |
| Lu             | Neutral  | 340                   | 621, 671 | 1075-1705 |
| Lu             | Oxidized | 417                   | 588, 726 | -----     |
| Lu             | Reduced  | 340                   | 632, 721 | -----     |

The position of the ICT band for the Ln ABAB is dependent on the size of central rare earths. These results indicate that the interaction between the two rings becomes stronger as the ring-to-ring separation decreases along with the lanthanide contraction. More accurately, the blue-shift is due to the decreased distance between the Pc rings. It can be correlated with the radius of the lanthanide (III): Eu < Dy < Lu.

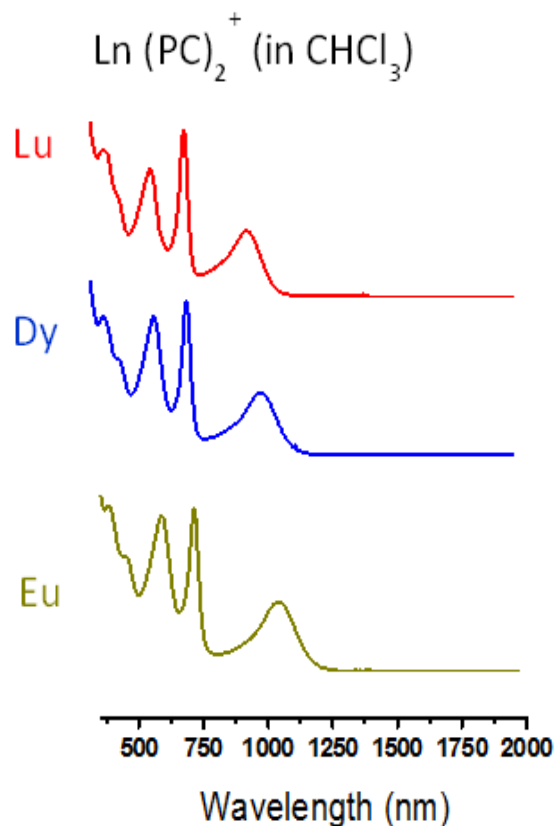


Figure 2.13: (b) Absorption spectra of newly synthesized bis (phthalocyaninato)- lanthanide (III) ABAB complexes in the oxidised forms in chloroform.

The spectral changes are due to chemical oxidation in the UV-Vis-NIR spectrum of Lu ABAB bis (Phthalocyanine). The strongest absorption Q band at 743 nm loses intensity and exhibits red shift. Significant increase has been observed from the intensity of the 588 nm and 970 nm bands corresponding to radical  $\pi-\pi^*$  transitions. In addition one electron, which causes the intermolecular transition in the neutral form, is removed in the oxidized form and all bands corresponding to those transitions disappeared. The electronic absorption spectra of oxidized Eu and Dy ABAB forms are similar to the oxidized form of Lu ABAB.

The reduced form shows two small but sharp peaks around 632 nm and 721. The intervalence transition is absent due to the addition of a second electron by reduction. Moreover the bands at 933 nm and 550 nm, which are linked to the radical part of the complex, also disappeared by reduction. The electronic absorption spectra of reduced Eu and Dy ABAB forms are similar to the reduced form of Lu ABAB.

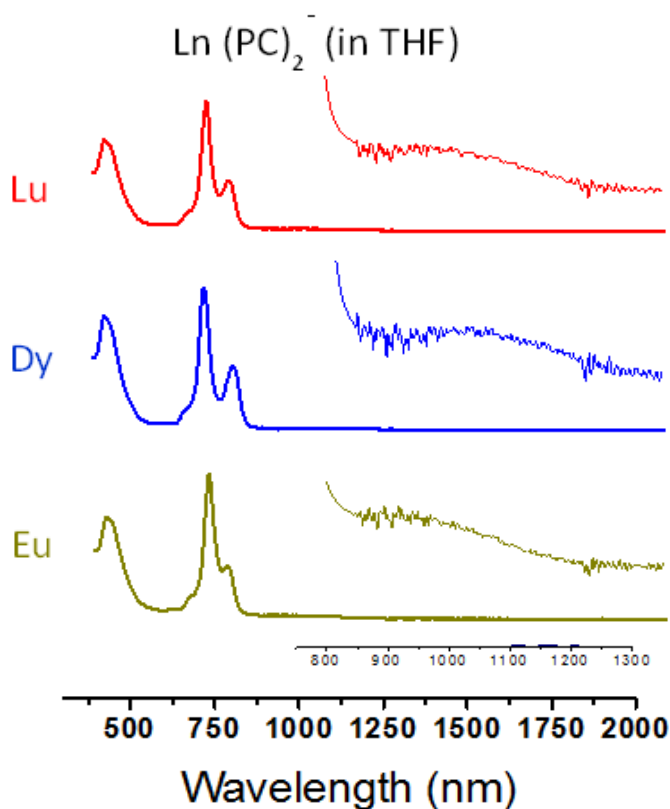


Figure 2.13: (c) Absorption spectra of newly synthesized bis (phthalocyaninato)- lanthanide (III) ABAB complexes in the reduced forms in chloroform.

### **C-2.12: NLO properties**

The second-order NLO polarizabilities  $\beta$  of the newly synthesized bis-(phthalocyaninato) lanthanide complexes are measured by HLS at 1.907  $\mu\text{m}$  in  $\text{CHCl}_3$  (neutral and oxidized form) and 5% of THF in  $\text{CHCl}_3$  (for the reduced form) solutions, using concentrations about  $10^{-5}$  M. The experimental error recorded for  $\beta$  value is about 15 percent. Figure 2.14 shows the SH intensity recorded from the bis-(phthalocyaninato) Lu ABAB (neutral form) with respect to the SH response collected from NPP powder. The observed SH response is the strongest as compare to the other complexes.

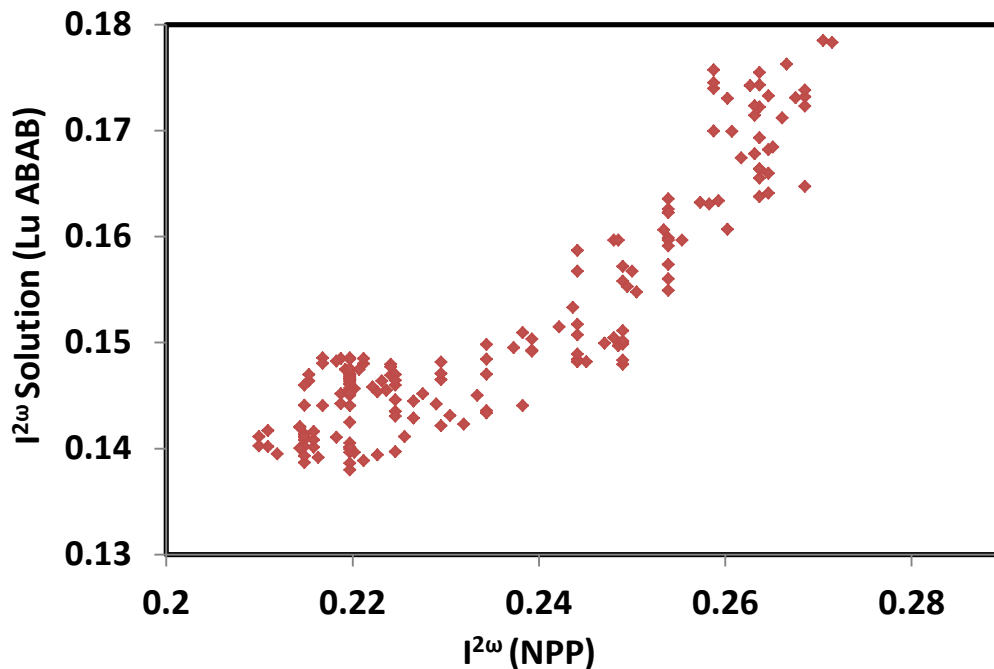


Figure 2.14: Second harmonic intensity recorded from bis-(phthalocyaninato) lutetium complexes with respect to the SH intensity from NPP.

The first hyperpolarizability obtained for these newly synthesized complexes shows exceptionally large  $\beta$  values. The highest  $\beta$  value is obtained for the bis-(phthalocyaninato Lu ABAB (neutral form), with a value of  $5800 \times 10^{-30}$  esu at  $1.907 \mu\text{m}$ . To the best of our knowledge, this is one of the highest  $\beta$  value reported for a non-dipolar compound, containing very well to the best octupolar chromophores described up to date [99] and is much higher than the value for the paracyclophane derivatives described by Bazan ( $46 \times 10^{-30}$  esu) [100]. The  $\beta$  values measured for Eu and Dy ABAB neutral complexes are slightly smaller than Lu,  $5400 \times 10^{-30}$  esu and  $5600 \times 10^{-30}$  esu respectively, then showing an influence of the number of  $f$ -electrons. Along with all these measurements we have also measured the  $\beta$  value of yttrium complex Y ABAB, in order to evidence the “ $f$ -electrons” NLO enhancement effect by comparing this  $\beta$  value with that of the dysprosium complex Dy ABAB. Yttrium presents strong chemical similarities with the lanthanides, and its ionic radius ( $1.075 \text{ \AA}$ ) is very close to that of dysprosium ( $1.083 \text{ \AA}$ ). On the other hand, yttrium is not a  $f$ -block element and therefore has a  $4f^0$  electronic configuration. Experimentally, the first hyperpolarizability value of yttrium complex is  $3010 \times 10^{-30}$  esu, a value that is

significantly lower than that of dysprosium ( $5622 \times 10^{-30}$  esu), even if these two complexes are isostructural and has roughly same ionic radii. It appears that the difference of NLO activity between Y ABAB and Dy ABAB can be better correlated to the *f* configuration rather than the ionic radius. The variation of  $\beta$  as a function of *f*-orbital filling is displayed in Figure 2.15 and there  $\beta$  values are given in Table 2.12, clearly demonstrating that the NLO activity enhancement is related with the direct contribution of *f* electrons to the hyperpolarizability.

More generally graphs for all types of complexes, i.e. ABAB, A<sub>4</sub>, B<sub>4</sub>, AB<sub>3</sub> show that  $\beta$  value increases with the filling of the *f* orbital. The  $\beta$  value of Eu, Dy and Lu for ABAB shows significantly higher  $\beta$  values as compare to the A<sub>4</sub>, B<sub>4</sub>, AB<sub>3</sub> types and all these three types are very close to each other. However, the different NLO activities between the octupolar lanthanide bis-(phthalocyanines) cannot be fully accounted for by the *f* electrons contribution only. The lanthanide contraction is also an important variable and must be taken into account. Here, it is a clear indication that crosswise ABAB compounds, bearing donor groups on two opposite rings, display higher hyperpolarizabilities than as other types of Pc derivatives (A<sub>4</sub>, B<sub>4</sub>, and AB<sub>3</sub>)

Table 2.12: The  $\beta$  values of the neutral forms of ABAB, A<sub>4</sub>, B<sub>4</sub> and AB<sub>3</sub>

| Sample | F electrons | ABAB | A <sub>4</sub> | B <sub>4</sub> | AB <sub>3</sub> |
|--------|-------------|------|----------------|----------------|-----------------|
| Eu     | 6           | 5400 | 3800           | 3900           | 3600            |
| Dy     | 9           | 5600 | 3900           | 4000           | 4000            |
| Lu     | 14          | 5800 | 4100           | 4700           | 4600            |

The position of the intramolecular charge transfer (ICT) band between 1300-1900 nm is highly dependent on the size of central rare earth metal, shifting to higher energy along with lanthanide contraction [101]. These observations show that the interaction between the two rings becomes stronger as the ring-to-ring separation decreases along with the lanthanide contraction. The short interplanar distance causes better electronic delocalization, which contributes to the hyperpolarizability. These results clearly indicate that the second-order NLO responses are not only driven by *f* electrons NLO-enhancement but also by geometrical

parameters, i.e. the lanthanide contraction [90].

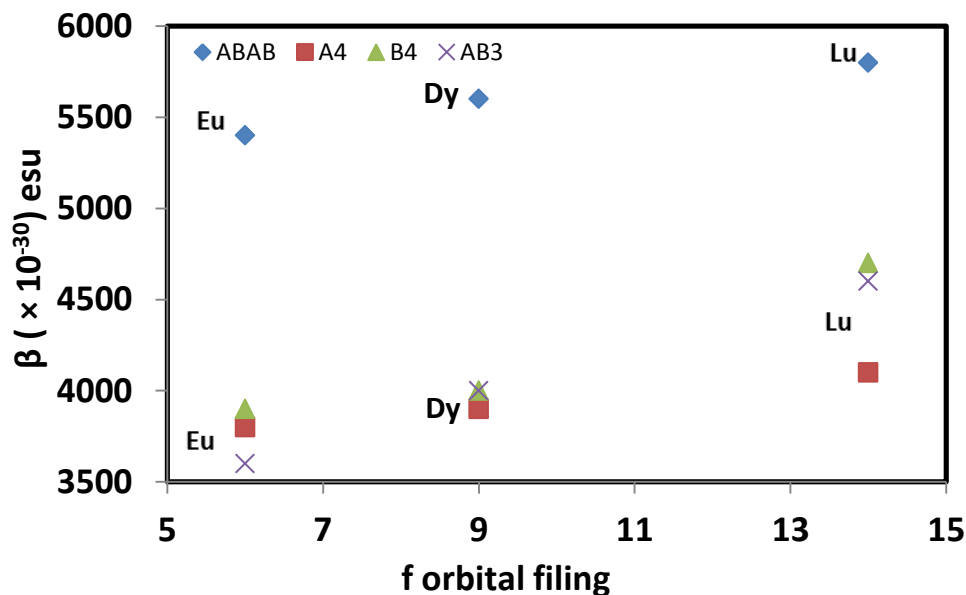


Figure 2.15: Plot of the hyperpolarizability coefficient  $\beta$  vs  $f$  orbital filling for neutral forms.

It is worth to compare the  $\beta$  value observed for neutral, oxidised and reduced forms of ABAB,  $A_4$ , and  $B_4$  type. In this context the graph is plotted, and compare the  $\beta$  values obtained from Eu, Dy, and Lu in neutral, oxidised and reduced forms for the ABAB type as shown in Figure 2.16,  $A_4$  in Figure 2.17 and  $B_4$  in Figure 2.1. Their corresponding  $\beta$  values are displayed in Table 2.13, 2.14 and 2.15 respectively.

ABAB type shows larger  $\beta$  values for the neutral form where the unpaired electron is completely delocalized over both the rings, resulting in a highly nonlinear molecule as compared to the oxidized and reduced forms.

In the oxidized and reduced forms the contribution of the intermolecular charge transfer to the hyperpolarizability vanishes causing lower NLO activity as compare to the neutral form.

While this band disappears in the oxidized form, the intensity of the bands at 588 and 970 nm, which correspond to the radical  $\pi$ - $\pi^*$  transition, significantly increase with cost of optical transparency.

Although, the reduced forms of Ln ABAB have lower NLO activity than the neutral and oxidized forms, it clearly shows a much better transparency. This transparency of reduced form of Ln ABAB provides a unique solution to suppress potential problems associated with the electronic transition at the second harmonic wavelength including the linear absorption of the generated  $2\omega$  light. Simply, the reduced Ln ABAB allows us to minimize all these problems.

Table 2.13: The  $\beta$  values of ABAB complexes in the neutral, oxidized and reduced forms

| Sample   | Eu   | Dy   | Lu   |
|----------|------|------|------|
| Neutral  | 5400 | 5600 | 5800 |
| Oxidised | 4500 | 4700 | 4700 |
| Reduced  | 3700 | 4200 | 4600 |

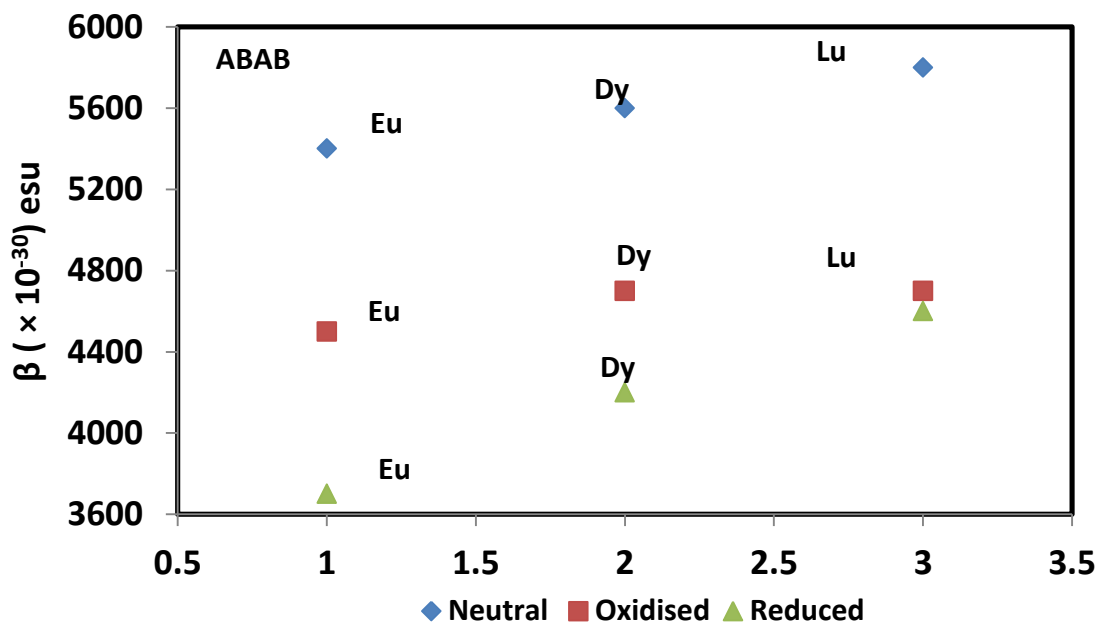


Figure 2.16: Plot of the hyperpolarizability coefficient  $\beta$  from neutral, oxidized, and reduced forms of ABAB type.

$A_4$  type shows a higher  $\beta$  value for the oxidized form as compared to the neutral and reduced form, a behaviour which is different from ABAB type but similar to  $B_4$ .

Table 2.14: The  $\beta$  values of  $A_4$  complexes in the neutral, oxidized and reduced forms

| Sample   | Eu   | Dy   | Lu   |
|----------|------|------|------|
| Neutral  | 3800 | 3900 | 4100 |
| Oxidised | 5100 | 5200 | 5300 |
| Reduced  | 3700 | 3900 | 3900 |

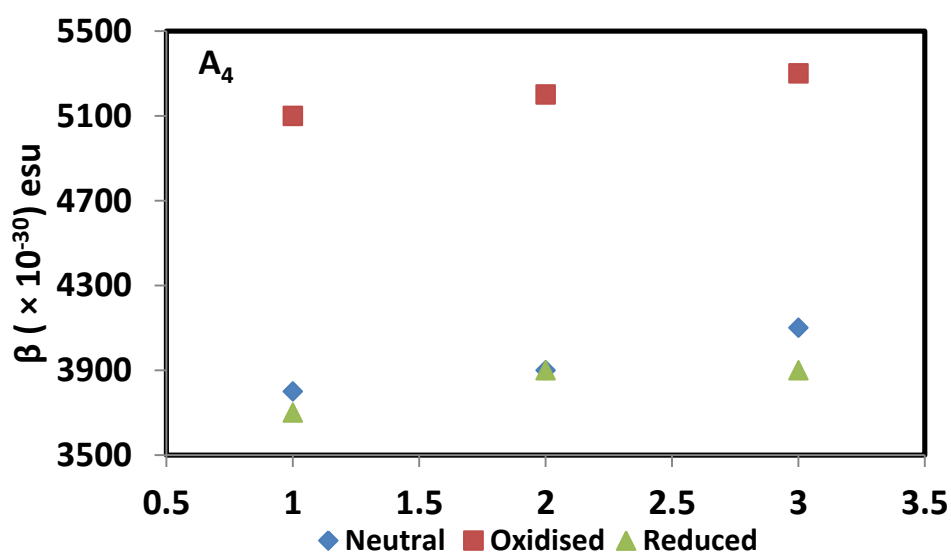


Figure 2.17: Plot of the hyperpolarizability coefficient  $\beta$  from neutral, oxidized, and reduced forms of  $A_4$  type.

Table 2.15: The  $\beta$  values of  $B_4$  complexes in the neutral, oxidized and reduced forms

| Sample   | Eu   | Dy   | Lu   |
|----------|------|------|------|
| Neutral  | 3900 | 4200 | 4700 |
| Oxidised | 4200 | 4200 | 4700 |
| Reduced  | 3300 | 3300 | 3400 |

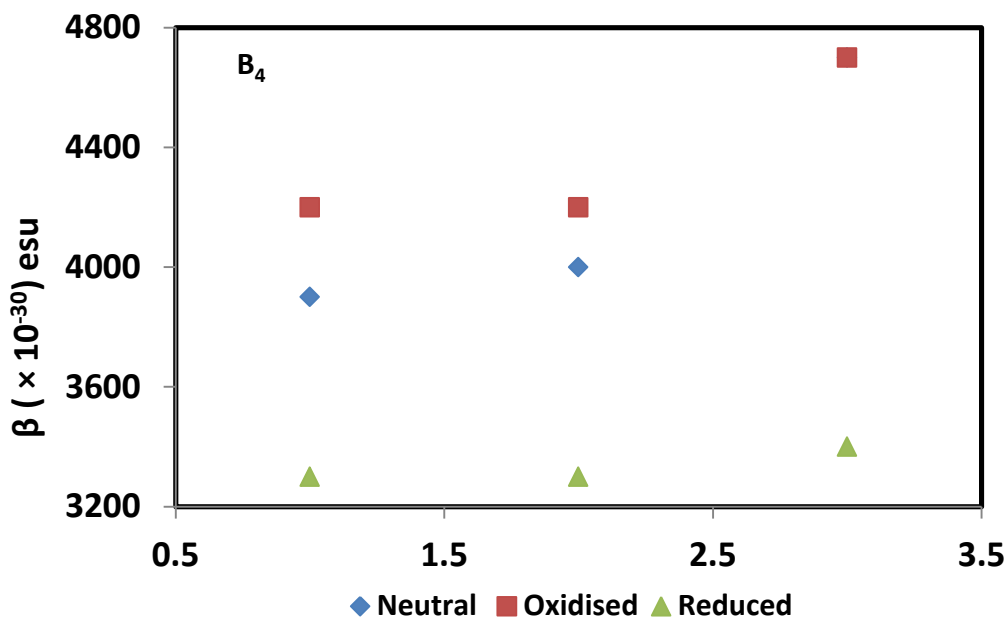


Figure 2.18: Plot of the hyperpolarizability coefficient  $\beta$  from neutral, oxidized, and reduced forms of  $B_4$  type.

The origin of the large second-order nonlinear response has not yet been investigated. At that wavelength, multilevel resonance enhancement cannot be ruled out [102-103].

In conclusion the  $\beta$  values are strongly influenced by the nature of the lanthanide ions. For each series, the NLO activity regularly increases from Eu to Lu evidence the “*f*-electrons” NLO enhancement. Moreover, the Lu(Pc)<sub>2</sub> complexes exhibits the highest hyperpolarizability over the lanthanide series. However, in the case of the reduced form of Ln(Pc)<sub>2</sub>, we observed that the NLO activity of Ln(Pc)<sub>2</sub> is intensely influenced not only by the nature of the lanthanide ion but also by the ICT. In this case, the contribution of the ICT to the hyperpolarizability vanishes and cause lower NLO activity than in the neutral form.

## References

- [1] Zyss, J., *Molecular Nonlinear Optics: Materials, Physics and Devices*, Academic Press, Boston, 1994.
- [2] Dragonetti, C., Righetto, S., Roberto, D., Ugo, R., Valore, A., Fantacci, S., Sgamellotti, A., De Angelis, F., *Chem. Comm.*, 2007, 4116-4118.
- [3] Valore, A., Cariati, E., Dragonetti, C., Righetto, S., Roberto, D., Ugo, R., De Angelis, F., Fantacci, S., Sgamellotti, A., Macchioni, A., Zuccaccia, D., *Chem. Eur. J.*, 2010, 16, 4814-4825.
- [4] Aubert, V., Ordroneau, L., Escadeillas, M., Williams, J.A.G., Boucekkine, A., Coulaud, E., Dragonetti, C., Righetto, S., Roberto, D., Ugo, R., Valore, A., Singh, A., Zyss, J., Ledoux-Rak, I., Le Bozec, H., Guerchais, V. *Inorg. Chem.*, 2011, 50, 5027-5038.
- [5] Valore, A., Colombo, A., Dragonetti, C., Righetto, S., Roberto, D., Ugo, R., De Angelis, F., Fantacci, S., *Chem. Commun.*, 2010, 46, 2414-2416.
- [6] Scarpaci, A., Monnereau, C., Hergué, N., Blart, E., Legoupy, S., Odobel, F., Gorfo, A., Pérez-Moreno, J., Clays, K., Asselberghs, I. *Dalton Trans.*, 2009, 4538-4546.
- [7] Batema, G. D., Lutz, M., Spek, A.L., van Walree, C.A., de Mello Donegà, C., Meijerink, A., Havenith, R.W.A., Pérez-Moreno, J., Clays, K., Büchel, M., van Dijken, A., Bryce, D.L., van Klink, G.P.M, van, Koten, G., *Organometallics*, 2008, 27, 1690-1701.
- [8] Williams, J.A.G., *Chem. Soc. Rev.*, 2009, 38, 1783-1801.
- [9] Murphy L., Williams, J.A.G., *Top. Organomet. Chem.*, 2010, 28, 75-111.
- [10] Kalinowski, J., Fattori, V., Cocchi, M., Williams, J.A.G., *Coord. Chem. Rev.*, 2011, 255, 2401-2425.
- [11] Glusac, K., Köse, M. E., Jiang, H., and Schanze, K. S., *J. Phys. Chem. B*, 2007, 111, 929-940.
- [12] Köhler, A., Wilson, J. S., and Friend, R. H., Al-Suti, M. K., and Khan, M. S., Gerhard, A., and Bäessler, H., *J. J. Chem. Phys.*, 2002, 116, (21), 9457-9463.
- [13] Silverman, E. E., Cardolaccia, T., Zhao, X., Kim, K-Y, Ksenija, H-G, Schanze, K. S., *Coordination Chemistry Reviews*, 2005, 249, 1491–1500.
- [14] Wilson, J. S., Köhler, A., Friend, R. H., Al-Suti, M. K., M. R. A. Al-Mandhary et al. *J. Chem. Phys.*, 2000, 113, 7627.

- [15] Zyss, J., Chem. Phys., 1993, 98, 6583-6599.
- [16] Brasselet, S., Zyss, J., J. Opt. Soc. Am. B, 1998, 15, 257-288.
- [17] Maker, P.D., Phys. Rev. A, 1970, 1, 923-951.
- [18] Clays, K., Persoons, A., Phys. Rev. Lett., 1991, 66, 2980-2983.
- [19] Zyss, J., Ledoux, I., Chem. Rev, 1994, 94, 77-105.
- [20] Farley, S.J., Rochester, D.L., Thompson, A.L., Howard, J.A.K., Williams, J.A.G., Inorg. Chem., 2005, 44, 9690-9703.
- [21] Baik, C., Han, W.-S., Kang, Y., Kang, S.O., Ko, J. J., Organomet. Chem., 2006, 691, 5900-5910.
- [22] Rochester, D. L., Develay, S., Zálíš S., Williams, J. A. G., Dalton Trans., 2009, 1728-1741.
- [23] Chan, C. W., Cheng L. K., Che, C. M., Coord. Chem. Rev., 1994, 132, 87-97.
- [24] Yam, V. W.-W., Tang, R. P.-L., Wong, K. M.-C., Cheung, K.-K., Organometallics, 2001, 20, 4476-4482.
- [25] Yang, Q.-Z., Wu, L.-Z., Wu, Z.-X., Zhang, L.-P., Tung, C.-H., Inorg. Chem., 2002, 41, 5653-5655.
- [26] Wadas, T. J., Lachicotte, R. J., Eisenberg, R., Inorg. Chem., 2003, 42, 3772-3778.
- [27] Chakraborty, S., Wadas, T. J., Hester, H., Flaschenreim, C., Schmehl, R., Eisenberg, R., Inorg. Chem., 2005, 44, 6284-6293.
- [28] Guerschais V., Fillaut, J. L., Coord. Chem. Rev., 2011, 255, 2448-2457.
- [29] Rossi, E., Colombo, A., Dragonetti, C., Roberto, D., Ugo, R., Valore, A., Falcicola, L., Brulatti, P., Cocchi, M., Williams, J.A.G., J. Mater. Chem., 2012, 22, 10650-10655.
- [30] Rossi, E., Colombo, A., Dragonetti, C., Righetto, S., Roberto, D., Ugo, R., Valore, A., Williams, J. A. G., Lobello, M. G., Angelis, D, F., Fantacci, S., Ledoux-Rak, I., Singh, A., and Zyss J., "Tuning the dipolar second-order non-linear optical properties of cyclometallated platinum(II) complexes with tridentate N<sup>C</sup>N-binding ligands", Accepted for JACS.
- [31] Valore, A., Cariati, E., Righetto, S., Roberto, D., Tessore, F., Ugo, R., Fragalà, I.L., Fragalà, M.E., Malandrino, G., De Angelis, F., Belpassi, L., Ledoux-Rak, I., Thi, K.H., Zyss, J., J. Am. Chem. Soc., 2010, 132, 4966-4970.

- [32] Tamayo, A. B., Alleyne, B. D., Djurovich, P. I., Lamansky, S., Tsyba, I., Ho, N. N., Bau, R., and Thompson M. E., *J. Am. Chem. Soc.* 2003, 125, 7377-7387.
- [33] Grushin, V. V., Herron, N., Lecloux, D. D., Marshall, W. J., Petrov, A., Wang Y., *Chem. Commun.*, 2001, 1494.
- [34] Lepeltier, M., Le Bozec, H., Guerchais, V., Lee, T. K. M., Lo, K. K. W., *Organometallics*, 2005, 24, 6069-6072.
- [35] Maury, O., Viau, L., Sénéchal, K., Corre, B., Guégan, J.-P., Renouard, T., Ledoux, I., Zyss, J., Le Bozec, H., *Chem. Eur. J.*, 2004, 10, 4454.
- [36] Lee, S.-H., Park, J.-R., Jeong, M.-Y., Kim, H. M., Li, S., Song, J., Ham, S., Jeon, S.-J., and Cho, B. R., *ChemPhysChem*, 2006, 7, 206–212.
- [37] Traber, B., Wolff, J. J., Rominger, F., Oeser, T., Gleiter, R., Goebel M., and Wortmann, R., *Chem.–Eur. J.*, 2004, 10, 1227–1238.
- [38] Brunel, J., Mongin, O., Jutand, A., Ledoux, I., Zyss J., and Blanchard-Desce M., *Chem. Mater.*, 2003, 15, 4139–4148.
- [39] Wolff, J. J., Siegler, F., Matschiner R., and Wortmann, R., *Angew. Chem., Int. Ed.*, 2000, 39, 1436–1439.
- [40] Argouarch, G., Veillard, R., Roisnel, T., Amar, A., Boucekkine, A., Singh, A., Ledoux I., and Paul, F., *New J. Chem.*, 2011, 35, 2409–2411.
- [41] Trujillo A., Veillard R., Argouarch G., Roisnel T., Singh A., Ledoux I., Paul F., 2012, *Dalton Transactions*.
- [42] Costuas, K., Paul, F., Toupet, L., Halet J.-F., and Lapinte, C., *Organometallics*, 2004, 23, 2053–2068.
- [43] Zyss, J., and Ledoux, I., *Chem. Rev.*, 1994, 94, 77–105.
- [44] Gauthier, N., Olivier, C., Rigaut, S., Touchard, D., Roisnel, T., Humphrey M. G., and Paul, F., *Organometallics*, 2008, 27, 1063–1072.
- [45] Courmarcel, J., Gland, G. Le, Toupet, L., Paul F., and Lapinte, C., *J. Organomet. Chem.*, 2003, 670, 108–122.
- [46] Maury O., and Le Bozec, H., *Acc. Chem. Res.*, 2005, 38, 691–703.

- [47] Weyland, T., Ledoux, I., Brasselet, S., Zyss, J. and Lapinte, C., *Organometallics*, 2000, 19, 5235–5237.
- [48] Hu, Q. Y., Lu, W. X., Tang, H. D., Sung, H. H. Y., Wen, T. B., Williams, I. D., Wong, G. K. L., Lin, Z., and Jia, G., *Organometallics*, 2005, 24, 3966–3973.
- [49] Fraysse, S., Coudret, C., Launay, J.-P., *Eur. J. Inorg. Chem.*, 2000, 1581-1590.
- [50] Jukes, R.T. F., Adamo, V., Hartl, F., Belser, P., De Cola, L., *Coord. Chem. Rev.*, 2005, 249, 1327-1335.
- [51] Lee, J. K. W., Ko, C. C., Wong, K. M. C., Zhu, N., Yam, V. W.-W., *Organometallics*, 2007, 26, 12-15.
- [52] Wong, H.-L., Tao, C.-H., Zhu, N., Yam, V. W.-W., *Inorg. Chem.*, 2011, 50, 471-481.
- [53] Roberts, M. N., Carling, C.-J., Nagle, J. K., Branda, N. R., Wolf, M. O., *J. Am. Chem. Soc.*, 2009, 131, 16644-16645.
- [54] Roberts, M. N., Nagle, J. K., Majewski, M. B., Finden, J. G., Branda, N. R., Wolf, M. O., *Inorg. Chem.*, 2011, 50, 4956-4966.
- [55] Zhong, Y. W., Vila, N., Henderson, J. C., Flores-Torres, S., Abruna, H. D., *Inorg. Chem.*, 2007, 46, 104470-10472.
- [56] Zhong, Y.- W., Vila, N., Henderson, J. C., Abruna, H. D., *Inorg. Chem.*, 2009, 48, 991-999.
- [57] Indelli, M. T., Carli, S., Ghirotti, M., Chiorboli, C., Ravaglia, M., Garavelli, M., Scandola, F., *J. Am. Chem. Soc.*, 2008, 130, 7286-7299.
- [58] Brayshaw, S. K., Schiffers, S., Stevenson, A. J., Teat, S. J., Warren, M. R., Bennett, R. D., Sazanovich, I. V., Buckley, A. R., Weinstein, J. A., Raithby, P. R., *Chem. Eur. J.*, 2011, 17, 4385-4395.
- [59] Renouard, T., Le Bozec, H., *Eur. J. Inorg. Chem.*, 2000, 229- 239.
- [60] Maury, O., Le Bozec, H., *Acc. Chem. Res.*, 2005, 38, 691-704.
- [61] Le Boudier, T., Maury, O., Le Bozec, H., Ledoux, I., Zyss, J., *Chem. Commun.*, 2001, 2430-2431.
- [62] Sénéchal, K., Maury, O., Le Bozec, H., Ledoux, I., Zyss, J., *J. Am. Chem. Soc.*, 2002, 124, 4561-4562.

- [63] Le Bouder, T., Maury, O., Le Bozec, H., Bondon, A., Costuas, K., Amouyal, E., Zyss, J., Ledoux, I., *J. Am. Chem. Soc.*, 2003, 125, 12884-12899.
- [64] Maury, O., Viau, L., Sénéchal, K., Corre, B., Guegan, J.-P., Renouard, T., Ledoux, I., Zyss, J., Le Bozec, H., *Chem. Eur. J.*, 2004, 10, 4454-4466.
- [65] Viau, L., Bidault, S., Maury, O., Brasselet, S., Ledoux, I., Zyss, J., Ishow, E., Nakatani, K., Le Bozec, H., *J. Am. Chem. Soc.*, 2004, 126, 8386-8387.
- [66] Bourgault, M., Baum, K., Le Bozec, H., Pucetti, G., Ledoux, I., Zyss, J., *New J. Chem.*, 1998, 22, 517.
- [67] Maury, O., GuMgan, J.-P., Renouard, T., Hilton, A., Dupau, P., Sandon, N., Toupet, L., Le Bozec, H., *New J. Chem.*, 2001, 25, 1553.
- [68] Aubert, V., Guerchais, V., Ishow, E., Hoang-Thi, K., Ledoux, I., Nakatani, K., Le Bozec, H., *Angew. Chem. Int. Ed.*, 2008, 47, 577-580.
- [69] Aubert, V., Ordronneau, L., Escadeillas, M., Williams, J. A. G., Boucekkine, A., Coulaud, E., Dragonetti, C., Righetto, S., Roberto, D., Ugo, R., Valore, A., Singh, A., Ledoux-Rak, I., Zyss, J., Le Bozec, H., Guerchais, V., *Inorg. Chem.*, 2011, 50, 5027-5038.
- [70] Oudar, J. L., *J. Chem. Phys.*, 1977, 67, 446-457.
- [71] Tessore, F., Roberto, D., Ugo, R., Mussini, P., Quici, S., Ledoux-Rak, I., Zyss, J., *Angew. Chem.*, 2003, 115, 472.
- [72] Ordronneau, L., Nitadori, H., Ledoux, I., Singh, A., Williams, J. A. G., Akita, M., Guerchais, V., and Le Bozec, H., *Inorg. Chem.*, 2012, 51 (10), 5627-5636.
- [73] Bourgault, M., Mountassir, C., Le Bozec, H., Ledoux, I., Pucetti, G., Zyss, J., *J. Chem. Soc., Chem. Commun.*, 1993, 1623-1624.
- [74] Bourgault, M., Baum, K., Le Bozec, H., Pucetti, G., Ledoux, I., Zyss, J., *New J. Chem.*, 1998, 517-522.
- [75] Zyss, J., and Ledoux, I., *Chem. Rev.*, 1994, 94, 77.
- [76] Bella, S. Di., Dragonetti, C., Pizzotti, M., Roberto, D., Tessore, F., Ugo, R., *Top. Organomet. Chem.*, 2010, 28, 1.
- [77] Renouard, T., Le Bozec, H., Brasselet, S., Ledoux I., and Zyss, J., *Chem. Commun.*, 1999, 871.

- [78] Akdas-Kilig, H., Malval, J.-P., Morlet-Savary, F., Singh, A., Toupet, L., Ledoux-Rak, I., Zyss J., and Le Bozec, H., *Dyes & Pigments*, 2012, 92, 681.
- [79] Tian, H., Chen, B., and Liu, P. H., *Chem. Lett.*, 2001, 990.
- [80] Kaieda, T., Kobatake, S., Miyasaka, H., Murakami, M., Iwai, N., Nagata, Y., Itaya A. and Irie, M., *J. Am. Chem. Soc.*, 2002, 124, 2015.
- [81] Luo, Q., Chen, B., Wang M., and Tian, H., *Adv. Func. Mater.*, 2003, 13, 233.
- [82] Jung, I., Choi, H., Kim, E., Lee, C. H., Kang S. O., and Ko, J., *Tetrahedron*, 2005, 61, 12256.
- [83] Areephong, J., Logtenberg, H., Browne, W. R., and Feringa, B. L., *Org. Lett.*, 2010, 12, 2132.
- [84] Parker, W. L., and Crosby, G. A., *J. Phys. Chem.*, 1989, 93, 5692.
- [85] Ishizuka, T., Sinks, L. E., Song, K., Hung, S.-T., Nayak, A., Clays K., and Therien, M., *J. Am. Chem. Soc.*, 2011, 133, 2884.
- [86] Vance, F. W., and Hupp, J. T., *J. Am. Chem. Soc.*, 1999, 121, 4047-4053.
- [87] *Frontiers in Lanthanide Chemistry. Chem. Rev.* 2002, 102, 1807-2476.
- [88] Sénéchal, K., Toupet, L., Zyss, J., Ledoux, I., Le Bozec, H., Maury, O., *Chem. Commun.*, 2004, 2180-2181.
- [89] Tancrez, N., Feuvrie, C., Ledoux, I., Zyss, J., Toupet, L., Le Bozec, H., and Maury, O., *J. Am. Chem. Soc.*, 2005, 127, 13474–13475.
- [90] Sénéchal-David, K., Hemeryck, A., Tancrez, N., Toupet, L., Williams, J.A.G., Ledoux, I., Zyss, J., Boucekkine, A., Guégan, J.-P., Le Bozec H., and Maury, O., *J. Am. Chem. Soc.*, 2006, 128, 12243-12255.
- [91] Furet, E., Costuas, K., Rabiller, P., and Maury, O., *J. Am. Chem. Soc.* 2008, 130, 2180-2183.
- [92] Weiss, R., Fischer, J., *Lanthanide Phthalocyanine Complexes. In The Porphyrin Handbook*; Kadish, K. M., Smith, K. M., Guillard, R., Eds.; Elsevier: Amsterdam, 1999; Vol. 16, p 171.
- [93] Corker, G. A., Grant, B., Clecak, N. J., *J. Electrochem. Soc.*, 1979, 126, 1339.
- [94] Orti, E., Brédas, J. L., Clarisse, C. *J. Chem. Phys.*, 1990, 92, 1228.

- [95] La Mar, G. N., de Ropp, J. S., Smith, K. M., Langry, K. C., *J. Am. Chem. Soc.*, 1980, 102, 4835.
- [96] De Cian, A., Moussavi, M., Fisher, J., Weiss, R., *Inorg. Chem.*, 1985, 24, 3162.
- [97] Ayhan M. M., Singh A., Hirel, C. Gürek A. G., Ahsen V., Jeanneau E., Ledoux I., Zyss J., Andraud C. and Bretonnière Y., *J. Am. Chem. Soc.*, 2012, 134 (8), 3655–3658.
- [98] Gürek, A. G., Ahsen, V., Luneau, D., Pécaut, J. *Inorg. Chem.*, 2001, 40, 4793.
- [99] Ishizuka, T., Sinks, L. E., Song, K., Hung, S.-T., Nayak, A., Clays, K., Therien, M. J., *J. Am. Chem. Soc.*, 2011, 133, 2884.
- [100] Bartholomew, G. P., Ledoux, I., Mukamel, S., Bazan, G. C., Zyss, J., *J. Am. Chem. Soc.*, 2002, 124, 13480.
- [101] J. S. Shirk, J. R. Lindle, F. J. Bartoli, M. E. Boyle, *J. Phys. Chem.*, 1992, 96, 5847-5852.
- [102] Drobizhev, M., Stepanenko, Y., Dzenis, Y., Karotki, A., Rebane, A., Taylor, P. N., Anderson, H. L., *J. Am. Chem. Soc.*, 2004, 126, 15352.
- [103] Drobizhev, M., Makarov, N. S., Rebane, A., de la Torre, G., Torres, T., *J. Phys. Chem. C*, 2008, 112, 848.

## Chapter 3: Second harmonic generation from Gold Nanoparticles

### 3.1: Introduction

The investigation of the NLO properties of metallic nanoparticles has been motivated by the high nonlinear response at the nanoscale expected from surface plasmon resonance (see chapter 1). During the last decade, very high  $\beta$  values have been reported for gold and silver nanoparticles. A similar kind of work has also been done in our laboratory where gold nanoparticles (AuNPs) have been functionalized with stilbazolium derivatives. Their hyperpolarizability values at 1.64  $\mu\text{m}$  have been measured. In spite of the fact that the plasmon resonance wavelength of AuNPs lies far from that of the SH signal at 820 nm, Hoang-Thi et al. [1] evidence a 3 times enhancement of the  $\beta$  value of stilbazolium derivatives when they were grafted to AuNPs. As gold nanoscale particles contain a huge number of highly polarizable electrons, and in spite of their quasi-spherical symmetry, they show very high  $\beta$  values inferred from HLS measurements, which are orders of magnitude higher than those of best available molecular chromophores [2]. The  $\beta$  values of the best organic dyes do not exceed  $10^{-27}$  esu, whereas  $\beta$  of gold NPs may reach  $10^{-25}$  esu. However, we must point-out that most of these AuNPs  $\beta$  values are measured in a spectrally resonant regime (1.06  $\mu\text{m}$ ).

Our current research work is represents a significant step to contribute the work in this area. Initially, we wanted to work at 1.9  $\mu\text{m}$  fundamental wavelengths in order to investigate the NLO behavior of gold NP's far from resonance, but solution measurements at 1.9  $\mu\text{m}$  must be done in chloroform or dichloromethane. We were not able to synthesize the Au nanorods in an organic phase and then we synthesized gold nanospheres (AuNSs) and different aspect ratio (AR) of gold nanorods (AuNRs) in water. Water absorbs after 1.2  $\mu\text{m}$ . Hence, we performed HLS experiments at 1.064  $\mu\text{m}$  where water does not absorb. The hyperpolarizability ( $\beta$ ) measured by second harmonic generation (SHG) at 1.064  $\mu\text{m}$  are then characterized in a resonant regime, the SPR resonance wavelength being not far from the harmonic (532 nm) one.

### **3.2: Materials**

All reagents were of high-purity grade and used without further purification; they are purchased from Sigma-Aldrich, ACROS Organics and from CLAL. Cetyl trimethyl ammonium bromide (CTAB) (purity 98%), Chloroauric acid ( $\text{HAuCl}_4 \cdot 3\text{H}_2\text{O}$ ), Acetone, Dichloromethane, Chloroform, Cyclohexane, 2-Propanol, Octadecanethiol, and Octadecylamine were purchased from Sigma-Aldrich. Tetraoctyl ammonium bromide (TOAB) was purchased from ACROS Organics and Silver nitrate ( $\text{AgNO}_3$ ) (purity 98%) from CLAL. The solutions were prepared using ultra-pure water from a Millipore system ( $18\text{M}\Omega\text{ cm}^{-1}$ ) throughout the experiment. The solutions were thoroughly deaerated by flushing with  $\text{N}_2$  gas (purity  $> 99.995\%$  and purchased from Air Liquide) before irradiation. All aqueous samples are at natural pH. All glassware and cells were cleaned by aqua regia and rinsed with ultrapure water prior to the experiments.

### **3.3: Synthesis of Gold Nanorods**

AuNRs were synthesized by gamma Radiolysis [3]. Radiolysis has proven to be a very efficient technique for the synthesis of metal nanoparticles of controlled size, composition, structure and morphology in solution [3-6]. In brief, the micellar solution was prepared by dissolving 590 mg of CTAB in 20 mL of Mille-Q  $\text{H}_2\text{O}$  and stirring it at  $50^\circ\text{C}$ . The concentration of CTAB in the solution is above the critical micellar concentration ( $\text{CMC} = 0.082\text{ M}$ ). Within 5 minutes of stirring the solution became transparent and then 8.2 mg of TOAB was added to the solution. Afterwards, 1.6 ml of  $\text{HAuCl}_4$  (0.025M) was added and stirred at  $50^\circ\text{C}$  for one hour. As the metal ions are photosensitive, the solutions are protected from light (an aluminium film covers the vials). After one hour, 430  $\mu\text{L}$  of acetone and 330  $\mu\text{L}$  of cyclohexane are added and the solution is stirred again for 15 minutes. Later on, different volumes (34  $\mu\text{L}$ , 68  $\mu\text{L}$ , 102  $\mu\text{L}$ , 136  $\mu\text{L}$ , and 170  $\mu\text{L}$  from a 0.01M stock solution) of silver nitrate ( $\text{AgNO}_3$ ) are successively added in the solution. The final solutions contains 0.082 M CTAB,  $7.5 \times 10^{-4}\text{ M}$  TOAB,  $2 \times 10^{-3}\text{ M}$   $\text{HAuCl}_4$ , 0.139 M cyclohexane, 0.266 M acetone and different concentrations of silver nitrate ( $1 \times 10^{-5}$ ,  $2 \times 10^{-5}$ ,  $10^{-4}$ ,  $3 \times 10^{-5}$ ,  $4 \times 10^{-5}$  and  $5 \times 10^{-5}\text{ M}$ ). The prepared solutions were then flushed with nitrogen and irradiated by a  $^{60}\text{Co}$  panoramic  $\gamma$ -source (dose rate =  $2.3\text{ kGy h}^{-1}$ ) at LCP, Université Paris-Sud 11, Orsay. Au ions were reduced by the radicals induced by solvent radiolysis, 14 hours exposure time (32.2

kGy) was necessary to reduce all gold ions. The energy deposited into the irradiated medium is expressed in Grays,  $1 \text{ Gy} = 1 \text{ J kg}^{-1}$  (for aqueous solutions  $1 \text{ Gy}$  corresponds to  $1 \text{ J L}^{-1}$ ). The nanorods synthesized with increasing concentration of silver were denoted NR1, NR2, NR3, NR4 and NR5. The purity of CTAB is very important in the synthesis of AuNRs by radiolysis [7-8]. The existence of impurities, mainly  $\Gamma$ , has been reported to affect the aspect ratios and the yield of the NRs using the seed-mediated method [8-10] and by radiolysis [11].

### **3.3.1: Synthesis of Au spherical particles**

AuNSs were also synthesized by gamma Radiolysis. In brief, the micelle solution was prepared by dissolving 5mL of Polyacrylic acid (PAA) solution from a 0.5 M stock solution, 76.4  $\mu\text{L}$  of 2-propanol directly from the bottle and 2 ml of a  $\text{Au}^{\text{III}}$  solution from 5 M of a stock solution of  $\text{HAuCl}_4$ . The irradiated solution contained 0.25 M PAA, 0.1 M 2-propanol and 1 M  $\text{Au}^{\text{III}}$  solution in total 10 ml of solution. 1.4 kGy/h is exposed to the by gamma source. Therefore, 4.8 kGy (3hours 25 minutes) are needed to reduce all the  $\text{Au}^{\text{III}}$  ions. The size of the nanospheres varies by changing the concentration of Au solution, PAA, the  $[\text{Au}^{\text{III}}]/[\text{PAA}]$  ratio and the dose rate. The dose rate parameter is not used for current experiment.

### **3.3.2.: Nanoparticles in thin polymeric films**

- 1) PVA solutions are prepared by adding 2.2 gram of PVA in 50 mL of MQ  $\text{H}_2\text{O}$ . To dissolve the PVA, the solution is boiled and stirred for a few hours.
- 2) 200  $\mu\text{L}$  of AuNRs are mixed with 200 $\mu\text{L}$  of PVA solution.

The prepared solution is then spin-coated on cleaned glass coverslips (3000 rpm, 1000 acc., 40 s) and kept at room temperature for few hours. The result is a thin film of a homogenous pink-violet colour where nanoparticles are homogeneously dispersed. The thin film is also prepared by just pouring it on the flat glass and leaving it for few hours at  $60^\circ$  for slow evaporation.

## **3.4: Principles**

The solutions are quite stable before irradiation. No band is detected except that of  $\text{Au}^{\text{III}}\text{Cl}_4^-$  around 200-300 nm. In the presence of CTAB,  $\text{Au}^{\text{III}}$  is complexed and the complex  $\text{Au}^{\text{III}}\text{-CTAB}$  absorbs at 400 nm [11]. High energy radiation such as  $\gamma$ -rays, X-rays or electron

beams induces excitation of the solvent. The primary effect of the interaction of high-energy  $\gamma$  rays with a solution of metals ions is the ionization and excitation of the solvent [12], leading to the formation of solvated electrons and reducing radicals throughout the solution. A schematic representation of synthesis of gold nanoparticles is displayed in Figure 3.1.

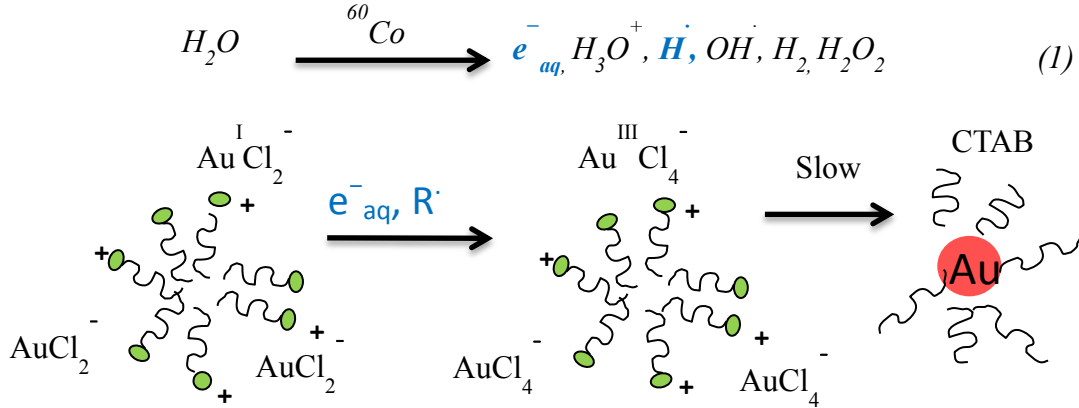


Figure 3.1: Schematic representation of synthesis of gold nanoparticles.

For example, in case of water, the radicals generated by irradiation are solvated electrons ( $e^-_{aq}$ ), hydroxy radicals ( $OH^\bullet$ ), and hydrogen atoms ( $H^\bullet$ ) [3-6, 13-17].

During the irradiation of deoxygenated water, hydroxyl radicals ( $HO^\bullet$ ), which are very strong oxidative species ( $E^0 (HO^\bullet/H_2O) = 2.34 \text{ eV}$  at pH 7) [18], are also formed. To avoid competitive oxidation reactions which may limit or even prevent metal reduction, hydroxyl scavengers are added in solution prior to irradiation. Among these scavengers, primary or secondary alcohols (such as 2-propanol) molecules or formate ions, which also react with hydrogen atoms, are generally used [3 and 19]:



Solvated electrons  $e^-_{aq}$  [ $(H_2O/e^-_{aq}) = -2.87 \text{ eV}$ ] and  $H^\bullet$  atoms [ $(H/H^\bullet) -1.88 \text{ eV}$  at pH 7] [11, 21] are strong reducing agents which are able to reduce very homogeneously metal ions to lower valences and finally to metal atoms, leading to a homogeneous nucleation and

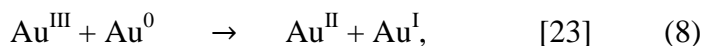
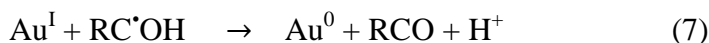
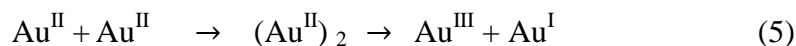
relatively monodisperse nanoparticles [22]. In the presence of CTAB and silver, radiolytic reduction of Au<sup>III</sup> leads to the formation of homogenous NRs of homogenous size.

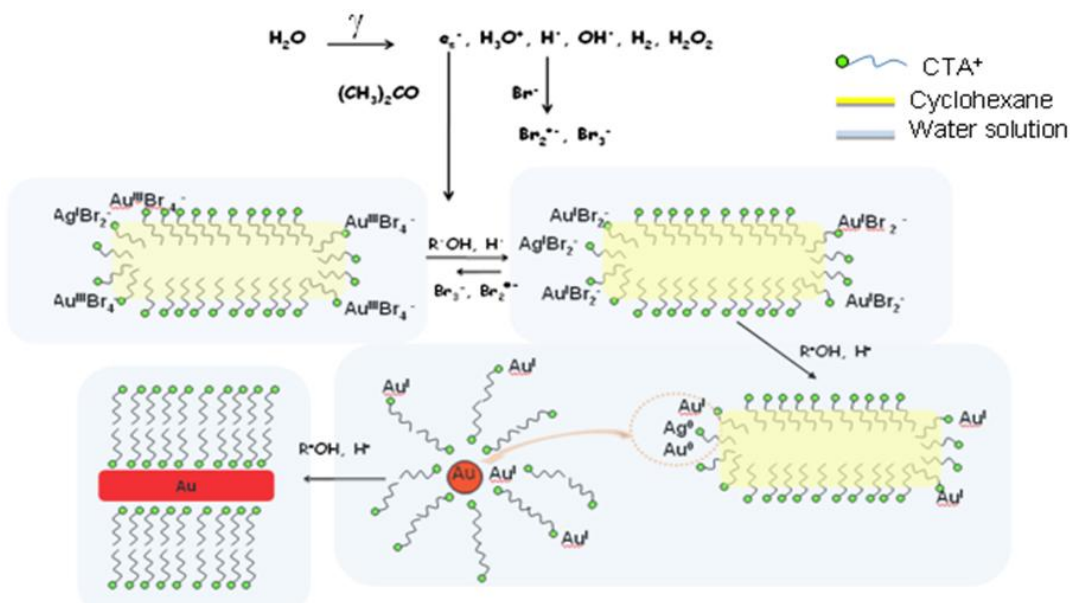
### **3.5: Mechanism of reduction and formation of AuNRs**

Different reagents play different roles in order to elongate the micelles used to induce formation of NRs. Micelles are swollen by cyclohexane, as this solvent swells the aliphatic part of the micelles and promotes their elongation. CTAB helps to limit the size and promotes the elongation of gold NPs [14]. TOAB, having the same polar head as CTAB but with a larger aliphatic part, acts as a co-surfactant, promotes elongation and due to its molecular shape, it is probably located at the cylindrical part of the micelles. Silver nitrate promotes the elongation of the NPs and allows a good control of their aspect ratios.

In the presence of a significant concentration of CTAB, the main Au<sup>III</sup> precursors, the Au<sup>III</sup>X<sub>4</sub>CTA complexes (X= Cl or Br), are reduced by alcohol radicals and H• atoms into less oxidised Au complexes. The reduction proceeds in two successive steps: first, the reduction of Au<sup>III</sup> into the unstable bivalent state Au<sup>II</sup> (reaction 3 and 4), which dimerizes to form (Au<sup>II</sup>)<sub>2</sub>, [23] and disproportionates into Au<sup>III</sup> and Au<sup>I</sup> (reaction 5), and then the reduction of Au<sup>I</sup> into atoms and clusters (reactions 6 and 7) [22-25]. The intermediate Au<sup>I</sup> and Au<sup>0</sup> atoms, which are complexed by CTA<sup>+</sup>, can diffuse along the bilayer surface and subsequently associate to form metal clusters confined in the water domain.

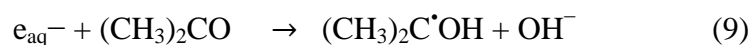
The different reduction reactions of Au<sup>III</sup> leading to Au<sup>0</sup> are then the following:





Scheme 3.1: Summarizing the reduction and growth mechanism leading to the formation of AuNRs by Radiolysis [25].

The mechanism of formation of gold nanorods by radiolysis in CTAB-micellar solutions has already been reported [25] and summarized in scheme 3.1. In the absence of acetone, only spherical gold nanoparticles were obtained, and it has been shown that the presence of acetone is necessary to synthesize gold nanorods in this one-pot radiolytic method. Acetone reacts with solvated electrons to yield the reducing alcohol radical:

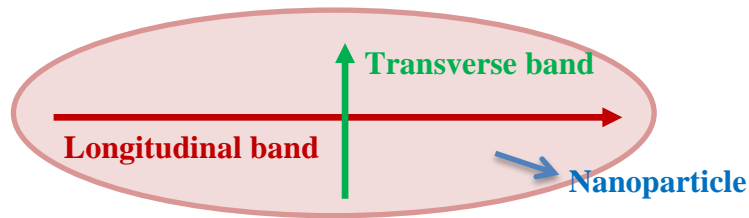


In this case, the only reducing species of the gold complexes are the alcohol radicals. The effect of acetone is to scavenge the solvated electrons (which are very strong reducing species) and to slow down the reduction kinetics leading to, in presence of CTAB and silver, the formation of gold nanorods [11]. The dose necessary to reduce the gold complexes is high because the radiolytic reduction yield is low. This is due to back oxidation of gold ( $\text{Au}^{\text{I}}$  or gold atoms) by the oxidative radicals  $\text{Br}_2^{\cdot-}$  and  $\text{Br}_3^-/\text{Br}_2^-$  [ $(\text{Br}_2^{\cdot-}/2\text{Br}^-) = 1.7 \text{ eV}$  ( $\text{Br}_2/\text{Br}_2^{\cdot-}) = 0.43 \text{ eV}$ ] formed under our radiolytic conditions [11, 25]. ( $\text{Br}^-$ ,  $\text{CTA}^+$ ) and ( $\text{AgBr}_2^-$ ,  $\text{CTA}^+$ ) complexes play the role of growth directing agents because of their efficient adsorption on preferential facets [26-27].

### **3.6: Aspect Ratio**

The aspect ratio (AR) is the length of the long axis (length) divided by the length of the short axis (width) of a cylindrical or rod-shaped particle. Increasing the aspect ratio increases the energy separation between the resonance frequencies of the long and short bands [28].

$$\text{Aspect Ratio} = \frac{\text{Length of major axis}}{\text{Width of rod diameter}}$$



The absorption band around 520 nm corresponds to the oscillation of the electrons perpendicular ( $\perp$ ) to the major (long) rod axis, and is referred to as the transverse plasmon absorption ( $SP_{\text{trans}}$ , at a shorter wavelength). The transverse absorption band is relatively insensitive to the NRs AR, but is sensitive to the surrounding medium and refractive index change in that medium.

The longitudinal absorption band occurs at longer wavelengths around 610 nm - 800 nm. This is caused by the oscillation of the electrons in parallel ( $\parallel$ ) to the major (long) rod axis, and is known as the longitudinal surface plasmon absorption ( $SP_{\text{long}}$ , at a longer wavelength). This absorption band is dependent on size of the particle and is very sensitive to aspect ratio which leads to a shift towards the infrared spectrum. The  $SP_{\text{trans}}$  does not change a lot due to increase in size, but  $SP_{\text{long}}$  change is more pronounced due to increase in major axis length of the nanorods.

### **3.7: Characterization**

#### **3.7.1: UV-Visible absorption spectroscopy**

UV-visible-NIR absorption spectroscopy is used to study the optical properties of the AuNPs and to obtain preliminary information about their size, structure, and shape in a fast and inexpensive way. Transmission Electron Microscopy (TEM) is the reference technique for

metal nanoparticles investigation. This technique allows accurate measurements of particles average size, size distribution and morphology, but due to high prize of this experiment, their access is limited.

UV-Visible absorption spectra of all samples were recorded just after irradiation dose of 32.3 kGy using with a Lambda 950 Perkin Elmer and a HP diode array HP8453 spectrophotometers, using a quartz cell of 1 cm path length. The vials containing the NPs in solution and UV-Vis spectra are displayed in Figure 3.2 and 3.3.

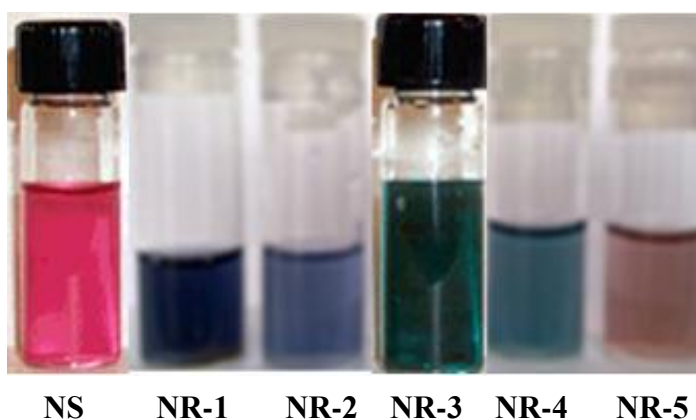


*Figure 3.2: Image of the vials containing the solutions with the synthesized AuNSs and different aspect ratios of AuNRs.*

Typical absorption spectra of gold NRs with two SPR absorption bands (TrSPR at around 510-520 nm and LgSPR at  $\lambda > 540$  nm) are obtained. By increasing silver concentration, the LgSPR band is red shifted, and its intensity increases. Consequently, increasing  $\text{Ag}^+$  amount leads to a change of the NRs size, and to an enhancement of their aspect ratio (AR), as confirmed by TEM studies. The increase in the aspect ratio is also accompanied by a decrease in the mean diameter ( $d$ ) when the concentration of  $\text{AgNO}_3$  is increased (Table 3.1), whereas no NR band was detected in the absence of silver ions.

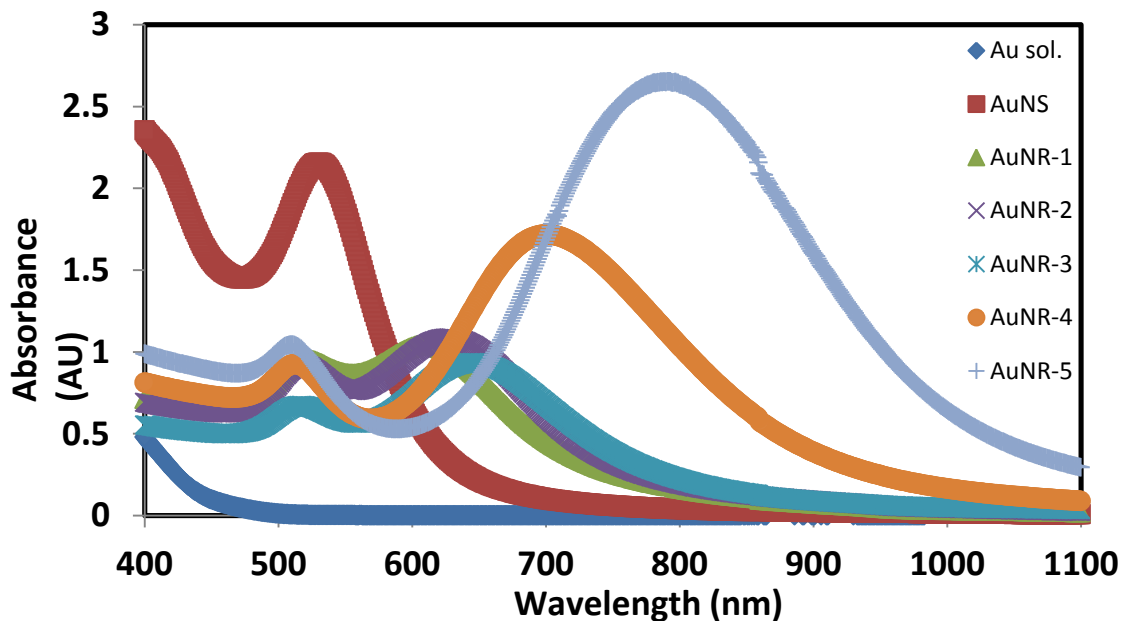


Figure 3.3: UV-Visible absorption spectra of  $Au^{III}$  solution, Au Nanospheres (without  $AgNO_3$  precursor) and Au Nanorods containing different amounts of  $AgNO_3$  precursor ( $1 \times 10^{-5} M$ ;  $2 \times 10^{-5} M$ ;  $3 \times 10^{-5} M$ ;  $4 \times 10^{-5} M$ ;  $5 \times 10^{-5} M$ ) revealing the formation of AuNRs (NR1-NR5) with different average aspect ratio after irradiation with a dose of 32.2 kGy.

Table 3.1: Parameters of the AuNRs synthesized after total reduction of the gold ions by radiolysis as a function of silver concentration.

| Sample | $[Ag^+] (10^{-5}) M$ | $\lambda$ (TrSPR, LgSPR) nm | Aspect ratios | Size Dia. (nm) |
|--------|----------------------|-----------------------------|---------------|----------------|
| NSs    | 0                    | 530                         | 1             | 6.3            |
| NR 1   | 1                    | 522,611                     | 1.7           | 15             |
| NR 2   | 2                    | 519,628                     | 1.9           | 13.5           |
| NR 3   | 3                    | 517,645                     | 2.25          | 12.6           |
| NR 4   | 4                    | 512,700                     | 2.5           | 12             |
| NR 5   | 5                    | 511,788                     | 3.2           | 11             |

$[Ag^+]$  is the initial concentration of  $AgNO_3$ ,  $\lambda(TrSPR)$  and  $\lambda(LgSPR)$  are the positions of the transversal and longitudinal SPR absorption band maxima, respectively; the last column gives the average diameter of NRs as evaluated from TEM images.

### **3.7.2: Transmission Electron Microscopy**

Transmission electron microscopy (TEM) observations were performed with a JEOL JEM 100CX II transmission electron microscope operating at 100 kV. The images have been taken at Laboratoire de Réactivité des Surfaces (Université Paris VI) in collaboration with Patricia Beaunier. The samples for TEM imaging were prepared by putting a few drops of the solution containing the NPs onto a carbon-coated copper grid and blowing it under N<sub>2</sub> gas. For the determination of the histogram, and in order to determine the average size of the nanoparticles, 200-300 particles at least were counted and measured per grid. Figure 3.4 shows TEM images of NRs. No specific aggregation phenomena were observed whatever the samples were. Pictures were digitized using a CCD camera.

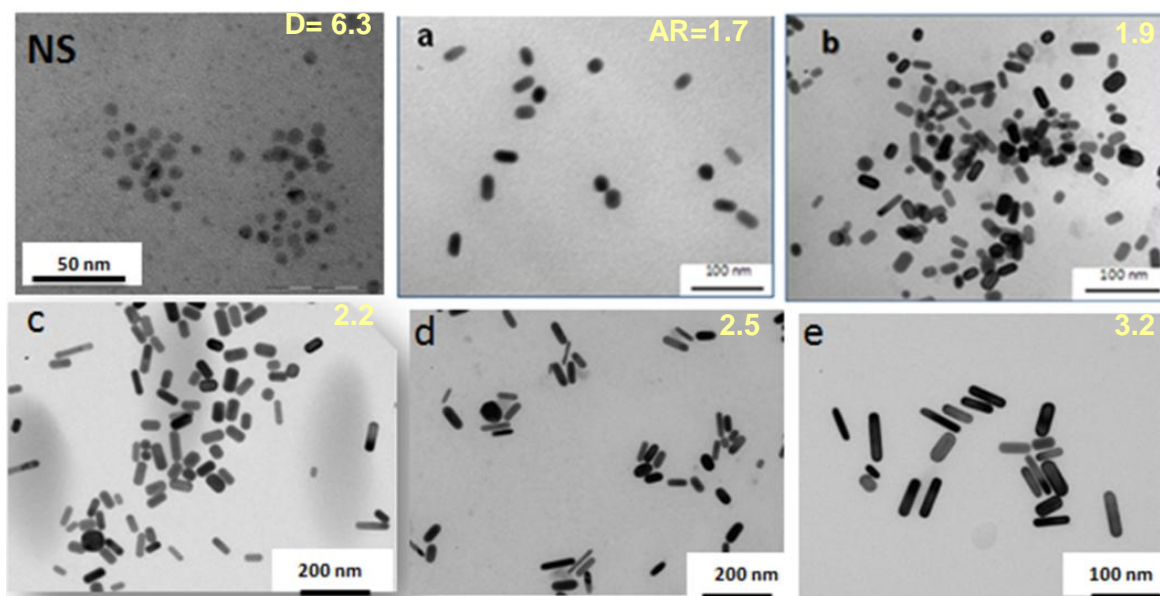


*Figure 3.4: TEM images of the Au NS and Au NRs of different aspect ratios synthesized with different amounts of silver ions (same conditions as in figure 1): (A) NR1, (B) NR2, (C) NR3, (D) NR4, and (E) NR5.*

### **3.8: NLO properties of AuNRs and AuNSs**

Freshly prepared solutions of Au precursor (HAuCl<sub>4</sub>), AuNSs and AuNRs were characterized by HLS at 1.064 μm for the determination of first order hyperpolarizability, on the basis of a known β value of the water. The β value of water is first measured by HLS using chloroform provide β<sub>CHCl<sub>3</sub></sub> = 0.19 ± 0.02 × 10<sup>-30</sup> at 1.06 μm as reference. We then

inferred a  $\beta$  value which is  $\beta_{\text{H}_2\text{O}} = 0.05 \times 10^{-30}$  esu. Our  $\beta$  value of water is different from the  $\beta$  value of water mentioned by Hupp et al. [2] and Brevet et al. [29-31] where they reported  $\beta_{\text{H}_2\text{O}} = 0.56 \times 10^{-30}$  esu and the  $\beta$  value of their particles were calculated by using this values. We preferred to choose  $\beta_{\text{H}_2\text{O}} = 0.05 \times 10^{-30}$  esu as a reference value, because it has been experimentally determined using chloroform as a reference, this latter solvent having been widely used in previous HLS studies by S. Brasselet et al for hyperpolarizability measurements of standard dyes;  $\beta$  values of these dyes have been found to be quite consistent with those of the literature, then validating the  $\beta_{\text{HLS}}$  value of the chloroform reference solvent.

In order to measure  $\beta_{\text{H}_2\text{O}}$ , the external reference method is employed and checked beforehand for the measurement [32] of the  $\beta$  values of the AuNSs and NRs. With the known value of  $\beta_{\text{CCl}_4} = 0.265 \times 10^{-30}$  esu, an absolute value of  $\beta_{\text{CHCl}_3} = 0.19 \pm 0.02 \times 10^{-30}$  esu and  $\beta_{\text{H}_2\text{O}}$  chosen between 0.06 and  $0.05 \times 10^{-30}$  esu is extracted previously [33]. Our next step is to optimize the proper concentration of the AuNSs and AuNRs for HLS measurements. The absorption spectra of our samples show strong absorbance values both at fundamental and SH wavelength because of the SP bands. Therefore, we prepared several samples with different concentrations and recorded their absorption spectra, in order to check their compatibility with HLS measurements.

In order to avoid huge absorption correction factors, we decided to perform HLS at  $1.06 \mu\text{m}$  only on samples displaying absorbance values  $A^\omega < 0.3$  at the fundamental and  $A^{2\omega} < 0.6$  at the harmonic wavelengths. The propagation length before (resp. after) the focal point in the measurement cell is 0.5 cm for the fundamental (resp. harmonic) beam. Then, the correction factor to be applied to the harmonic (resp. fundamental) HLS intensity cannot exceed that applied to the  $I^{2\omega} (I^\omega)^2$  product, i.e.  $10^{0.3} \times (10^{0.5})^2 = 4$ . In order not to exceed this correction limit, we decided to use AuNPs concentrations ranging from 1 to  $5 \times 10^{-4}$  M for  $\beta$  measurements. Absorption is corrected by the factor  $10^{\left(\frac{A2\omega+2A\omega}{2}\right)}$  in order to account for losses due to linear absorption at  $\omega$  and  $2\omega$ .

The second harmonic intensity recorded from the AuNSs and AuNRs is larger than that of water, as predicted. SH intensity increases as the shape of the particles change from sphere to NRs and the SH intensity keeps on increasing from NR1 to NR5. Figure 3.5 compares the output signal intensities at 532 nm from water and a NR4 solution.

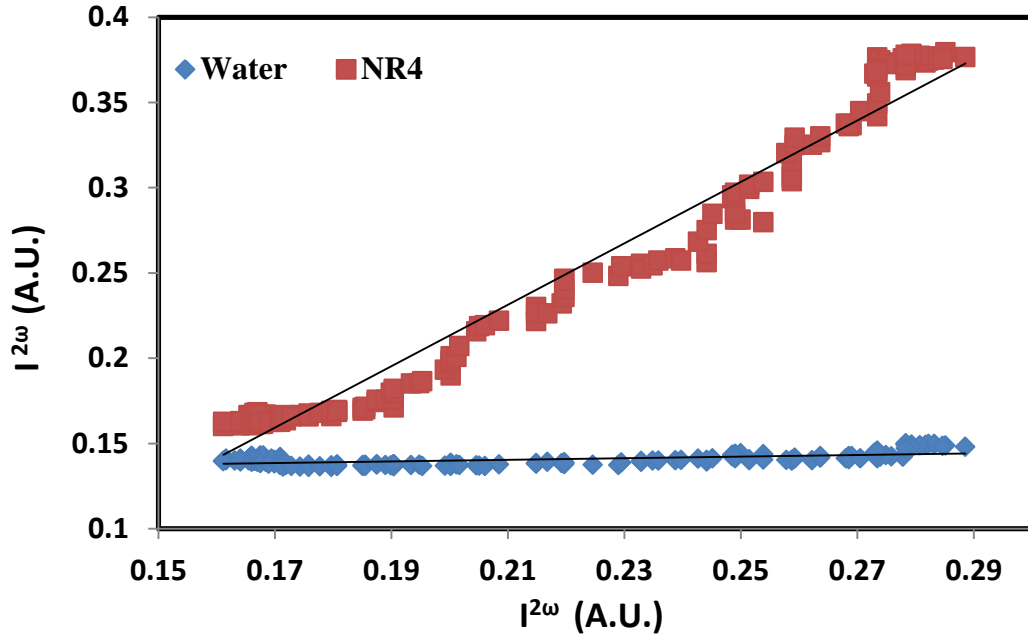


Figure 3.5: Comparison between the second harmonic intensity recorded from pure water and NR4 water solution.

It may be interesting to infer, from the  $\beta$  values of nanoparticles, the  $\beta$  values per gold atom, as proposed by other authors [29-31]. For this purpose, the volume of the AuNSs and AuNRs must be calculated. The concentration of the particles is calculated from the known concentration of initial gold solutions, and from the average volume and atom number of nanoparticles. The  $\beta$  per particle is calculated by using equations 10 and 11.

$$\beta^2 = N_{nanoparticles} \langle \beta_{nanoparticles}^2 \rangle + N_{H_2O} \langle \beta_{H_2O}^2 \rangle \quad (10)$$

$$\frac{P}{P_w} = \frac{[N_{nanoparticles} \langle \beta_{nanoparticles}^2 \rangle + N_{H_2O} \langle \beta_{H_2O}^2 \rangle]}{N_{H_2O} \langle \beta_{H_2O}^2 \rangle} \quad (11)$$

Where  $N_{nanoparticles}$ ,  $\beta_{nanoparticles}$  and  $P$  are respectively the concentration of the nanoparticles, the first hyperpolarizability and the slope of the HLS intensity of nanoparticle recorded from the solutions,  $N_{H_2O}$ ,  $\beta_{H_2O}$  and  $P_w$  are respectively the concentration of the water, the first hyperpolarizability and the slope of the HLS intensity recorded from the pure water. All calculated values are presented in Table 3.2. In HLS, a strong resonance enhancement is expected when an electronic transition is near either the incident ( $\omega$ ) or harmonic ( $2\omega$ ) frequencies [34]. With this respect, the work published by Schatz et al. [35] reported that substantial HLS responses are observed from Ag and Cu particles whereas no detectable HLS responses are observed from Pt particles. This response is attributed to enhancement due to resonance of the nonlinearly scattered light with the Ag and Cu surface plasmon absorption band whereas Pt particles, which lack visible-region plasmon absorption band, do not display detectable HLS signals. This experiment was done at 820 nm fundamental wavelength, and maximum absorption wavelength for Ag and Cu were 410 and 564 respectively.

Table 3.2: First hyperpolarizability ( $\beta$ ) of Au per atom and per particle for nanospheres (NSs) and nanorods (NRs)

| Sample            | Volume (nm <sup>3</sup> ) | N <sub>Au</sub> per particle | Particle Conc. | $\beta$ per particle (10 <sup>-26</sup> ) esu | $\beta$ per Au atom (10 <sup>-30</sup> ) esu |
|-------------------|---------------------------|------------------------------|----------------|---|--|
| Au <sup>III</sup> |                           |                              |                |   | 8  |
| AuNS              | 131                       | 7746                         | 3.7E-08        | 0.35  | 40   |
| NR 1              | 4504                      | 486860                       | 1.37E-09       | 2.57  | 50   |
| NR 2              | 3670                      | 217220                       | 3.1E-09        | 3.2   | 68   |
| NR 3              | 3533                      | 209140                       | 1.9E-09        | 3.54  | 77   |
| NR 4              | 3391                      | 200740                       | 3.3E-09        | 4   | 90   |
| NR 5              | 3343                      | 197910                       | 5E-10          | 4.60  | 103  |

In our case, the harmonic wavelength is located within the resonance range, and enhanced  $\beta$  values are observed as expected. Alternatively, parasitic signals at  $2\omega$  may arise from two-photon fluorescence, resulting in a broad emission band which may partially contribute to the harmonic signal. This problem can be avoided by doing the experiments at longer wavelength. In our case, we have analyzed the spectral composition of the HLS signal around  $2\omega$  from a solution of gold nanorods, but no two-photon fluorescence could be detected. Along with NSs and NRs we also calculated the  $\beta$  value of the Au complex precursor, (used to synthesize the NSs and NRs) which is  $\beta_{Au^{III}} = 8 \times 10^{-30}$  esu. The  $\beta$  value is very low as compare to NSs and NRs, according to the expectations because the absence of SPR band. The number of Au atom per particle is decreasing when increasing the aspect ratio of AuNRs. In earlier studies, HLS measurements of AuNPs have been done at different wavelengths, particle sizes and different  $\beta$  values of the water reference solvent. Therefore, a comparison between the  $\beta$  values measured by HLS should be made with caution. We tried to compare AuNSs sample with previously reported values of AuNPs as shown in Table 3.3. Here, we recalculated the  $\beta$  value of our AuNSs sample by using the  $\beta$  value of water used by other authors [29-31] and found that they are the same order of magnitude. The difference can be due to the different diameter of nanospheres, and to the use of different laser sources.

*Table 3.3: Comparison between the previously observed  $\beta$  values of Au per particle and our AuNSs sample.*

| Sample                      | Laser                  | Diameter | $\lambda_{max}/nm$ | $\beta_{H_2O}$ (esu)   | $\beta$ per particle<br>( $\times 10^{-25}$ ) esu |
|-----------------------------|------------------------|----------|--------------------|------------------------|---|
| AuNSs (Our sample)          | 1064 nm; 9ns; 10 Hz    | 6.3      | 530                | $0.56 \times 10^{-30}$ | 0.4   |
| Au [ref. 29] Nanospheres    | 1064 nm; 5ns; 10 Hz    | 4.9      | 508                | $0.56 \times 10^{-30}$ | $0.60 \pm 0.09$                                   |
|                             |                        | 8.6      | 518                |                        | $2.0 \pm 0.3$                                     |
| Au [ref. 30-31] Nanospheres | 800 nm; 150 fs; 76 MHz | 10       |                    | $0.56 \times 10^{-30}$ | 0.5   |

We have been able to observe the HLS intensity from NRs because very homogenous solutions are prepared and relatively high signals are produced by these particles. This is the first time that  $\beta$  values of AuNRs are measured and presented, as in Table 3.2. It is observed that  $\beta$  per Au atom increases from sphere to the rod shape and continuously increases with the increase in the aspect ratio of the NRs, as shown in Figure 3.6, even when the number of gold atoms per particle remains almost the same as for NR3, NR4, and NR5. In an earlier work, it has been stated that the HLS intensity collected from the solution of a mixture of Au NRs and NSs essentially arises from the NRs [36]. For NR3, NR4, and NR5,  $\beta$  value increases even if the transverse diameter decreases. This behavior is quite similar to that observed in reference 29 where smaller  $\beta$  values are reported from the biggest diameter AuNPs and the origin of such a behavior may stem from the saturation of the collective effect contribution to the nonlinear optical activity in bigger nano-objects. So, there is a possibility that we will also see such kind of behavior from higher aspect ratio NRs. These results clearly evidence the strong influence of LgSPR on the  $\beta$  value of NRs.

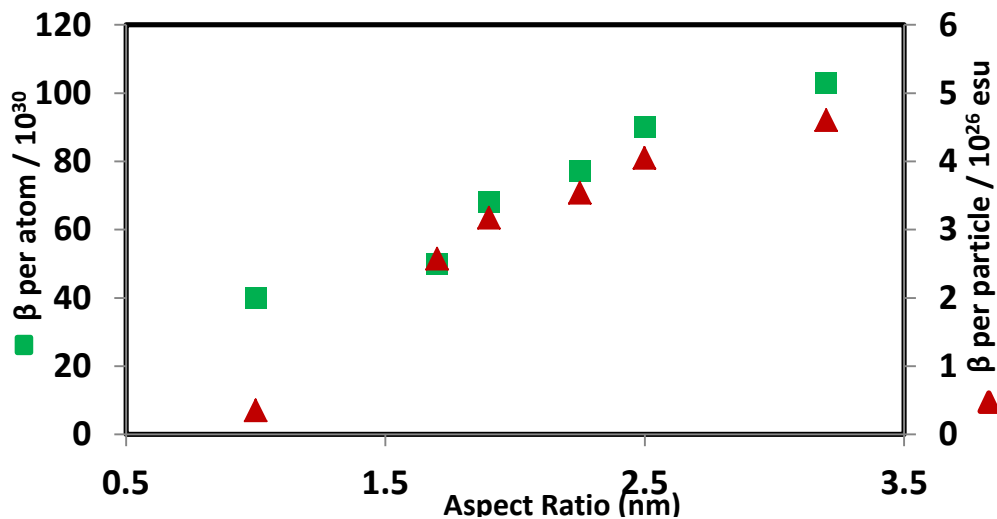


Figure 3.6: Absolute value of the first hyperpolarizability ( $\beta$ ) calculated per Au atom and per Au particle in the solution versus the aspect ratio of AuNPs.

We performed variable incident polarization experiment using HLS in order to determine the nonlinear anisotropy of the particles. The experimental set-up and details are discussed in Chapter 1. This experiment is very delicate but we could observe the expected periodic behavior of  $I^{2\omega}$  because of the relatively high signal from AuNSs and AuNRs (figure 3.7).

The figure clearly shows a much higher signal from AuNRs, with a better contrast as compared to AuNSs. The depolarization (D) ratio is inferred and shown in Table 3.4.

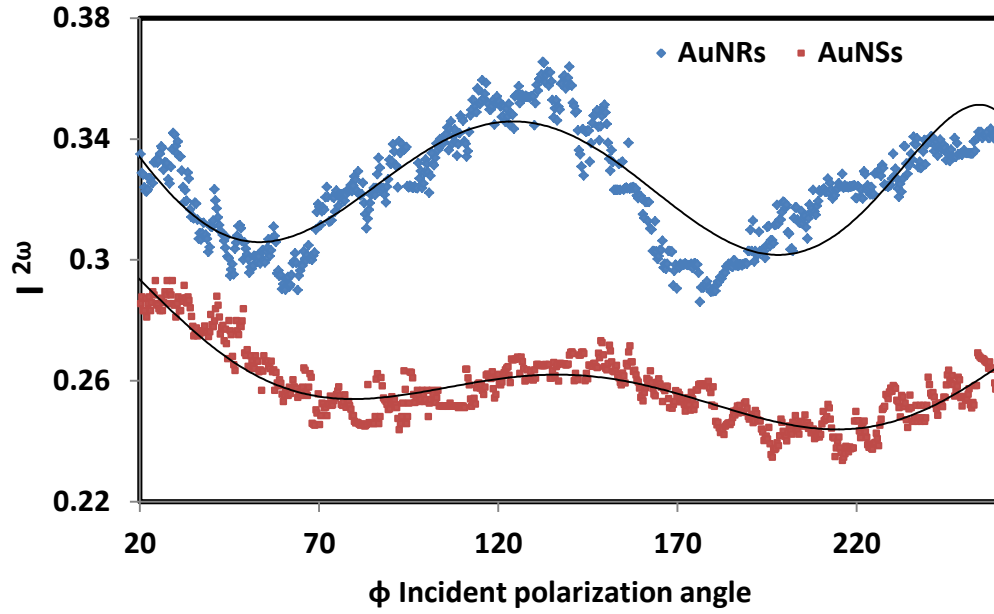


Figure 3.7: Experimental harmonic scattered intensities  $I^{2\omega}$  for Nanospheres and Nanorods solution in water, as a function of the incident polarization angle  $\phi$ .

Table 3.4: Depolarization ratio (D), norms of the dipolar and octupolar tensor components of hyperpolarizabilities, along with their squared nonlinear anisotropy  $\rho^2$

| Sample | Depolarization Ratio | $\ \beta_{J=1}\ ^2$ | $\ \beta_{J=3}\ ^2$ | $\rho^2 = \frac{\ \beta_{J=3}\ ^2}{\ \beta_{J=1}\ ^2}$ |
|--------|----------------------|---------------------|---------------------|--|
| AuNS   | 0.44                 | 0.17                | 0.89                | 5.1  |
| NR 1   | 0.33                 | 15                  | 34                  | 2.28   |
| NR 2   | 0.3                  | 26                  | 46                  | 1.8  |
| NR 3   | 0.28                 | 34                  | 52                  | 1.53   |
| NR 4   | 0.25                 | 49                  | 57                  | 1.2  |
| NR 5   | 0.22                 | 70                  | 59                  | 0.84   |

The D ratio is plotted as a function of the aspect ratio of the AuNPs (Figure 3.8). It decreases with the increase the AR. In other words, as the length of the NRs increases the D ratio decreases which clearly evidence an increase of the anisotropic behavior. Earlier a depolarization ratio has been reported  $D = 0.47 \pm 0.03$  for 20 nm AuNPs. The authors concluded that the HLS signal was of dipolar origin [31]. Our D value for 6.3 nm AuNSs is  $D = 0.44$ , then confirming this dipolar contribution to  $\beta$  even for nanospheres. However, even for relatively low D values, an octupolar contribution to the  $\beta$  tensor must be taken into account, as shown by Brasselet and Zyss [37]. In the following, we shall see that this octupolar contribution is still dominant in NSs and decreases in NRs of increasing aspect ratio. From Table 4 we observe that D significantly decreases when the aspect ratio increases, showing that the relative dipolar contribution to the  $\beta$  tensor strongly increases with the aspect ratio. Figures 3.9 and 3.10 illustrate this trend.

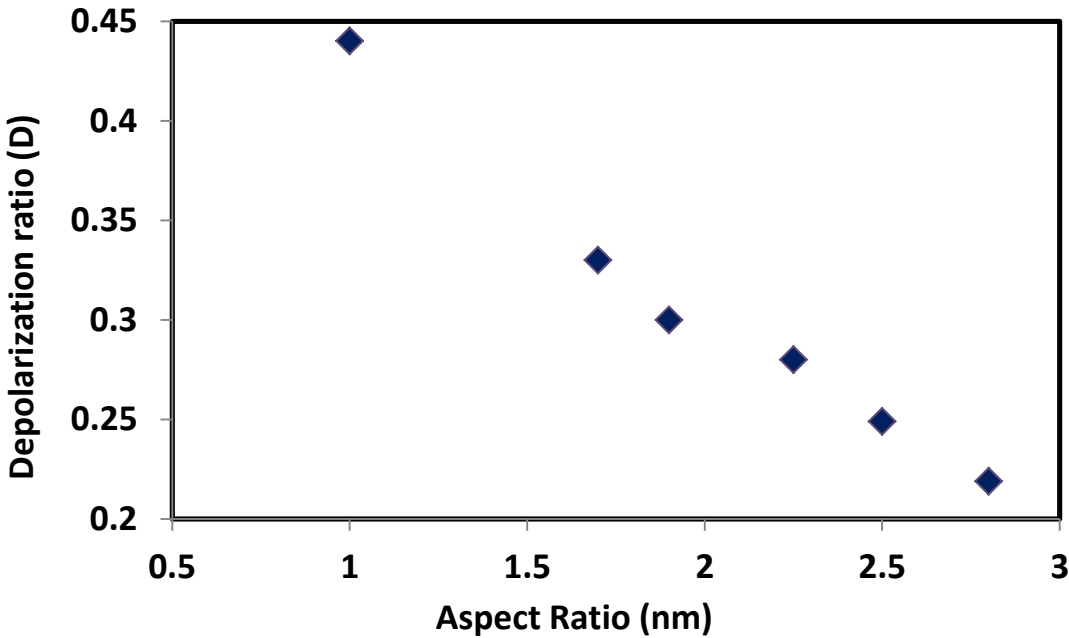


Figure 3.8: Plot of depolarization ratio (D) against the aspect ratio (AR) of the AuNPs.

The simple expression of D in terms of  $\rho$  is expressed as:

$$D = \frac{\langle \beta_{ZZXX}^2 \rangle}{\langle \beta_{XXXX}^2 \rangle} = \frac{1}{9} \frac{7+2\rho^2}{7+12\rho^2} \quad (12)$$

We may infer from D measurement the nonlinear anisotropy  $\rho$  and the intrinsic  $\|\beta_{j=1}\|$  and  $\|\beta_{j=3}\|$  components with no symmetry restrictions. The maximum depolarization for pure octupoles ( $\rho = \infty$ ) is  $D_{max} = 2/3$  and the minimal depolarization for dipoles ( $\rho = 0$ ) is  $D_{min} = 4/27 = 0.148$ . The dipolar ( $\|\beta_{j=1}\|^2$ ) and octupolar ( $\|\beta_{j=3}\|^2$ ) norms of the dipolar and octupolar  $\beta$  tensor components and their ratio ( $\rho$ ) are calculated and plotted in Figure 10. Both dipolar and octupolar responses increase with the aspect ratio, and their ratio decreases as displayed in Figure 11. It is not surprising to observe such an enhancement of the dipolar contribution with respect to the octupolar one when increasing the anisotropy of the nanoparticle. In spite of the fact that NRs are geometrically centrosymmetric, fluctuations of electronic distributions resulting in second harmonic emission. In rod-like structures, the electron distribution is less isotropic than in a sphere, and NRs may behave like dipolar-like instantaneous “plasmonic molecules”. It must be pointed-out that the depolarization ratio becomes rather weak for NRs, and displays the same value as for the standard dipolar reference DR1 NLO molecule (Bresselet-Zyss). Nanorods seems to behave like giant dipolar nonlinear molecules, at least when their  $\beta$  tensor is measured using the HLS technique, which takes into account SH contributions from electronics fluctuations in nanoparticles.

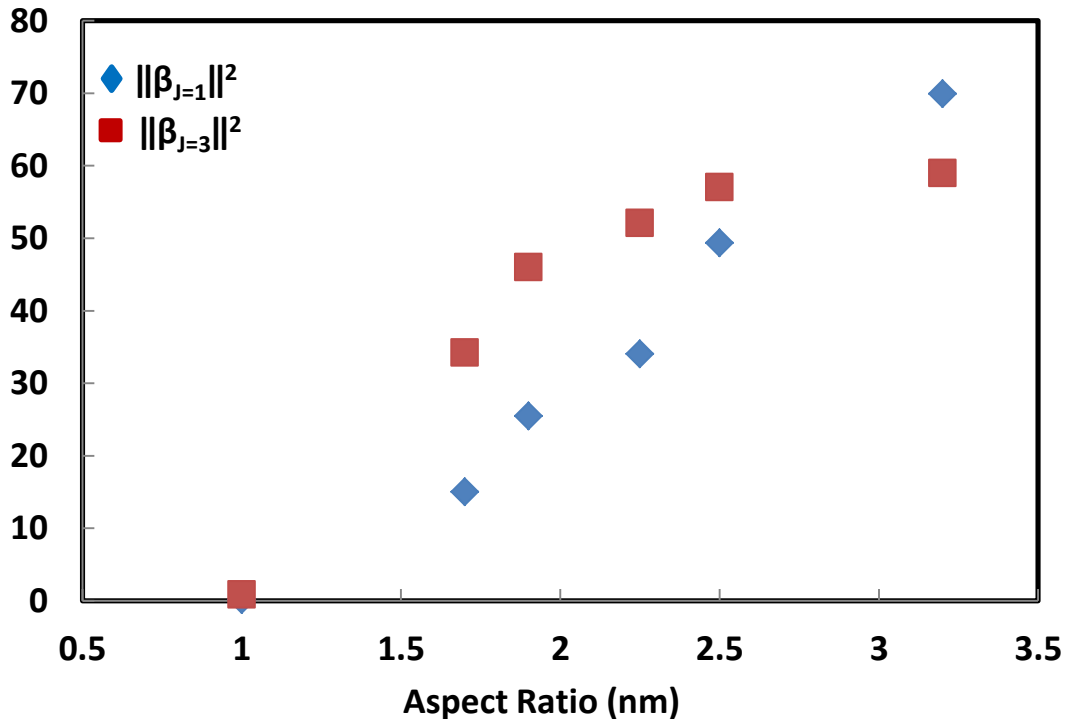


Figure 3.9: Plot of dipolar and octupolar values with respect to aspect ratios of the AuNPs.

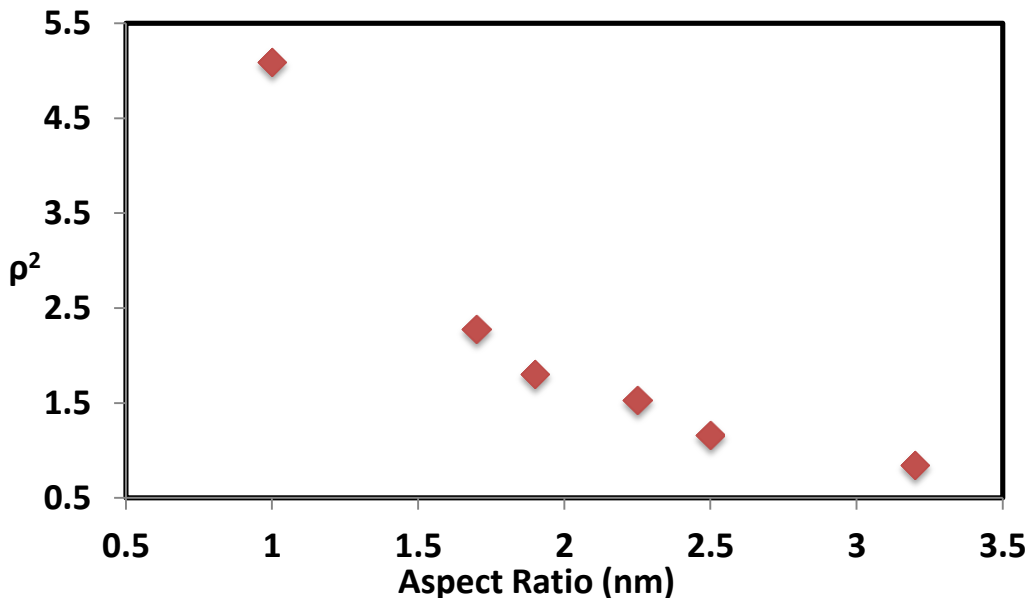


Figure 3.10: Plot of ( $\rho^2$ ) ratio against the aspect ratio of the AR.

### **3.9: Nonlinear Microscopy**

HLS provides a non-coherent averaged response over the size, shape, and orientation distributions, which prevents one from getting a deeper understanding on the origin of the nonlinear optical properties of metal nanoparticles [38]. Such information can only be revealed by the exploration of individual objects, which requires nonlinear microscopy imaging techniques with high spatial resolution. In that respect, second harmonic generation (SHG) microscopy has been widely used for the investigation of noble metal particles and received a considerable interest for its ability to probe non-centrosymmetry at the nanometric scale [39]. Nevertheless, only a few studies have been devoted to gold single particle analyses [38, 40-41]. This is mainly due to the very weak signals expected for second order nonlinear optical processes like SH generation from centrosymmetric objects.

#### **3.9.1: Nonlinear scanning microscopy**

The nonlinear properties of NRs are investigated using the nonlinear microscopy techniques described in reference [42]. The SHG images were obtained with a Nikon Eclipse TE2000-U inverted confocal microscope using a Nikon  $\times 100$  PA IR, NA=1.4, oil immersion objective. Nanoparticles were excited with a Spectra-Physics Mai Tai HP Ti: Sapphire tunable laser

that emitted 100 fs pulses at 80 MHz repetition rate. The infrared light reflected in the epidirection was blocked by a dichroic mirror (cutoff wavelength 700 nm) and a set of BG38-39 bandpass filters. The SHG signal was split into Ps and Pp polarization planes and collected by two Perkin–Elmer SPCM-AQR-14 APDs working in the photon-counting regime. The emission spectrum is obtained with an Oriel Multispec 77400 spectrometer (with 150-nm slot) equipped with an Andor DV420A OE CCD camera.

### **3.9.2: Results**

We prepared thin films of NR2 in a polymer matrix. The details about the sample preparation are discussed in the beginning of this chapter. We took advantage of the wide tunability of our excitation laser system and we tried to detect SHG from single nanoparticles with different excitation wavelengths. The excitation wavelength was varied in the 800-990 nm range when utilizing the direct Mai Tai output beam and in the 1150-1300 nm range after frequency conversion with a Spectra-Physics Opal Femtosecond Optical Parametric Oscillator (OPO). We were able to observe only a faint SH signal from NR2 at 1280 nm excitation wavelength. A typical zoom scan of the sample, which shows well-isolated diffraction-limited spots corresponding to the visible emission of single nanoparticles, is plotted in Figure 3.11.

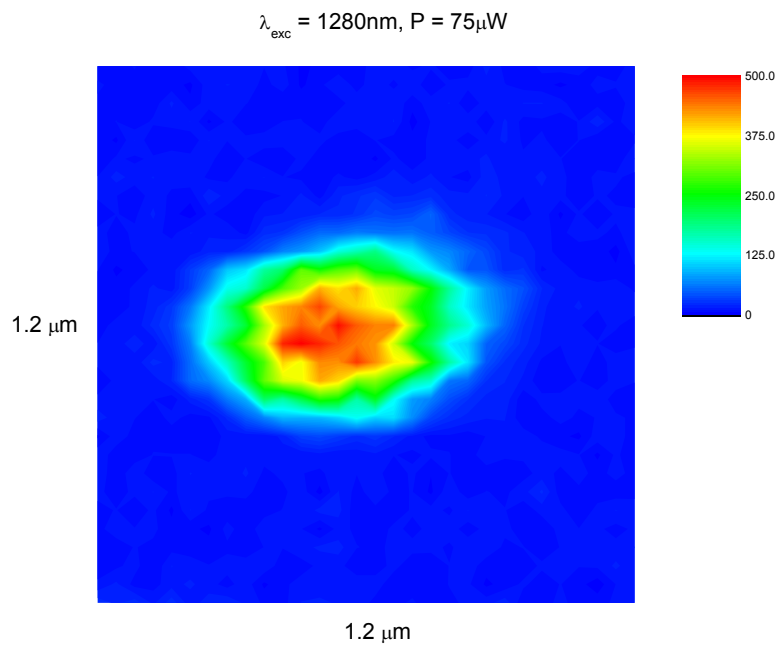


Figure 3.11: Zoom of the SHG detected during a typical scan of the NR2 dispersed on a glass coverslip.

The average incident power is  $75\mu\text{W}$ . The quadratic dependence of the harmonic signal with respect to the fundamental intensity was verified and the emitted spectrum measured. Figure 3.12 shows a relatively high degree of photo-stability of the SH emission.

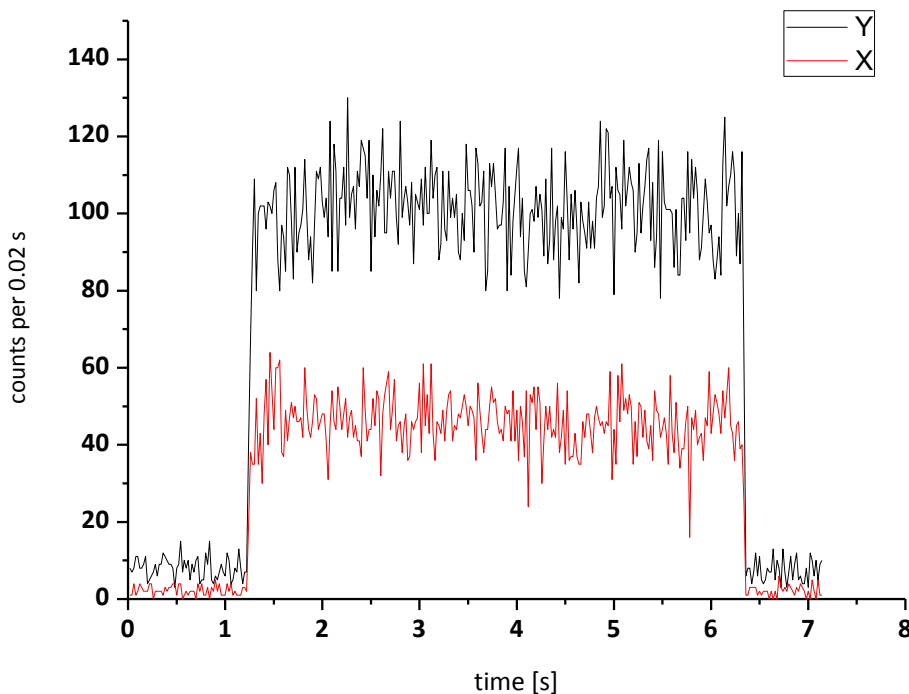


Figure 3.12: Photostability of the SHG signal scattering from a single NR2, recorded as two polarization components along x (red trace) and y (black trace), respectively.

To analyze the spectral dependence of SHG, we collected the SH photons emitted from a single NR2 particle using a spectrometer. A small peak at half the incident wavelength is detected, as shown in Figure 3.13. Therefore, polarization analyses reported below are probably performed on a signal containing SHG and luminescent components. Optimization of the excitation conditions was performed by tuning the excitation wavelength as well as by varying the incident power. Unfortunately, we did not succeed to see a more intense SH signal in the measured spectra.

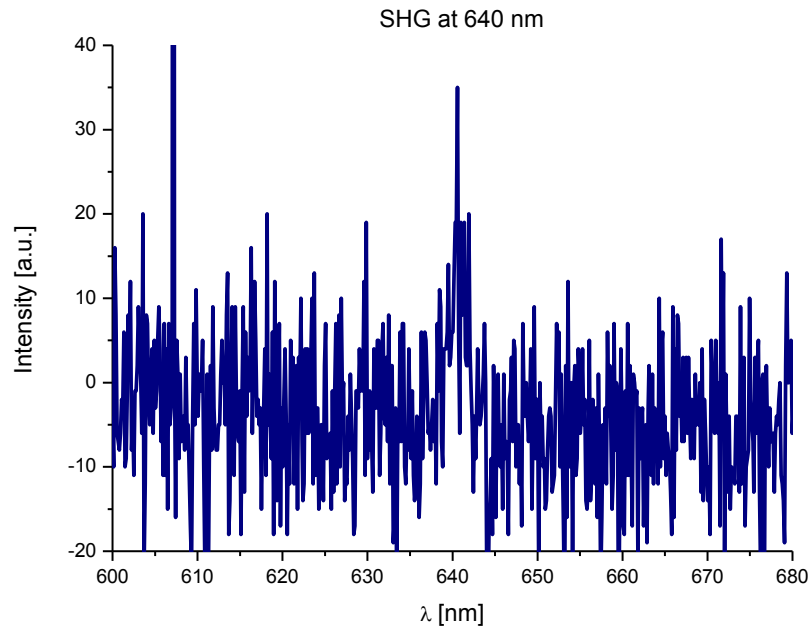


Figure 3.13: Spectral dependence of the SHG process. Typical spectrum emitted by the SHG NR2 excitation wavelengths at 1280 nm.

The x and y polarization components of the signal emitted by a single nanorod are analyzed as a function of the rotation of the incident excitation-beam polarization (Figure 3.14).

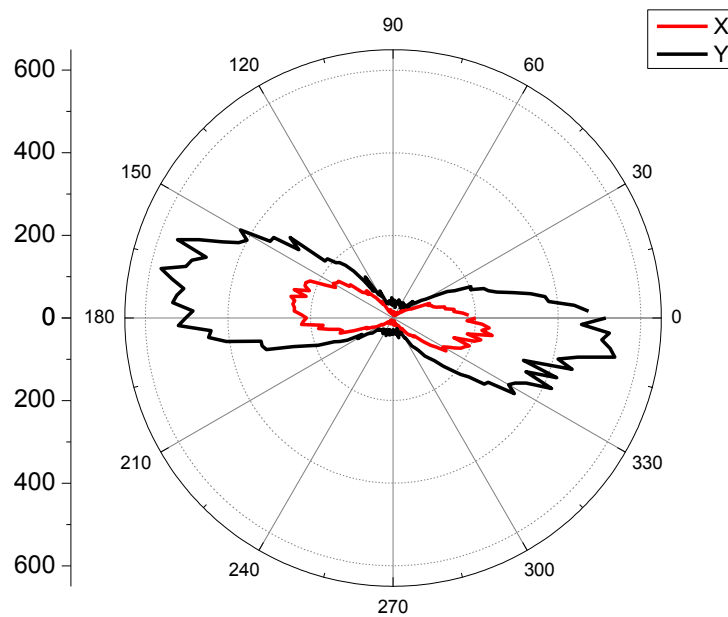
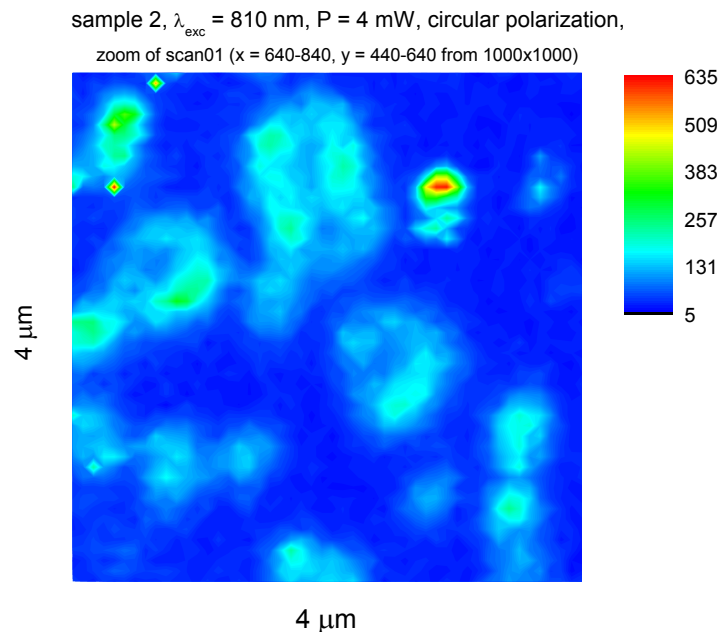


Figure 3.14: Experimentally obtained polarization analysis of the emission observed for NR2.

Clearly, the polarization response reveals a dipolar character of the emission pattern, which is typical for metallic nanoparticles of the size much below the excitation wavelength ( $< \lambda/10$ ). The origin of this polarization response can be attributed to the high anisotropy of the nanorod [29].

While doing the experiment we came across with the problems that prevent us to see the better SH signals.

- 1) The first problem may come from the thin film of the NRs. There is the possibility that nanoparticles form aggregates and the resultant structure of nanosystem is different from that in solution.
- 2) The second problem is associated with the incident power and the high repetition rate. The incident power we used in our experiment ranges from several  $\mu\text{W}$  to several mW. However, even with the lowest power the sample undergoes gradual destruction, resulting in more diffused images after a few scans, as shown in figure 3.15. It is possible that the repetition rate of our laser system (80 MHz) is too high, not allowing for an efficient heat dissipation. Gold nanoparticles convert the energy of surface plasmon resonance to heat and transfer it to the environment within a few picoseconds, however the further dissipation across the polymer matrix may encounter



*Figure 3.15: Zoom of the sample after measurements of the spectra.*

a barrier due to the low thermal conductivity of PVA ( $0.2 \text{ Wm}^{-1}\text{K}^{-1}$ ) and the very small thickness of the layer. This may cause the accumulation of heat in small volumes within the sample, resulting in melting of polymer matrix and diffusion of studied nanoobjects and/or deformation of nanoparticles themselves. Using a laser system with lower repetition rates should solve these stability problems. Another solution will be to deposit AuNPs directly on the substrate without using a polymer matrix. This solution is currently being explored in collaboration with Wroclaw University of Technology.

- 3) A third problem may come from the BG38-39 bandpass filter: the transmission of BG 39 is 10-20 % at the SH frequencies. Furthermore, the transmission of SH signal could have been reduced twice more by additional BG38 filter. This prevented to efficiently detect the SHG by the less sensitive spectrometer, while more sensitive APDs were able to produce the SH images of the nanoparticles during the scans.
- 4) The last problem is the incident wavelength. The experiment with incident wavelength close to resonance would definitely provide better SH signal. The future work will continue to see the signal at 1064 nm incident wavelength.

### **3.10: Mixture of AuNRs with DAST derivative**

Few investigations have been conducted so far on nanoparticles grafted with the NLO chromophores, resulting in an observed enhancement of the chromophore SHG signal. Exaltation of SHG from ultrathin dye layers when deposited on fractal gold surfaces was observed [44]. NLO-active chromophores have been anchored onto AuNPs in order to combine the NLO properties of both the core and ligand components of thiolate-stabilized AuNPs [45], and an increase of hyperpolarizability has been observed. Functionalization of AuNSs with DAST derivatives has already been done in our laboratory with the collaborators from Institut Lavoisier in Versailles University, in a non-resonant regime [46].

The synthesis of a 4-dimethylamino-*N*-methyl-4-stilbazolium tosylate (DAST) derivative bearing thiol end groups liable to attach the chromophore on a gold surface has been done by

Dr. Eddy Dumas from Institut Lavoisier de Versailles. The synthesis of this DAST derivative, especially to get rid of the impurities, was quite complicated and this problem took too much time to be solved in time due to which we are not able to explore more in this area. The final product is shown in the Figure 3.16. We used this product and mixed it with AuNRs.

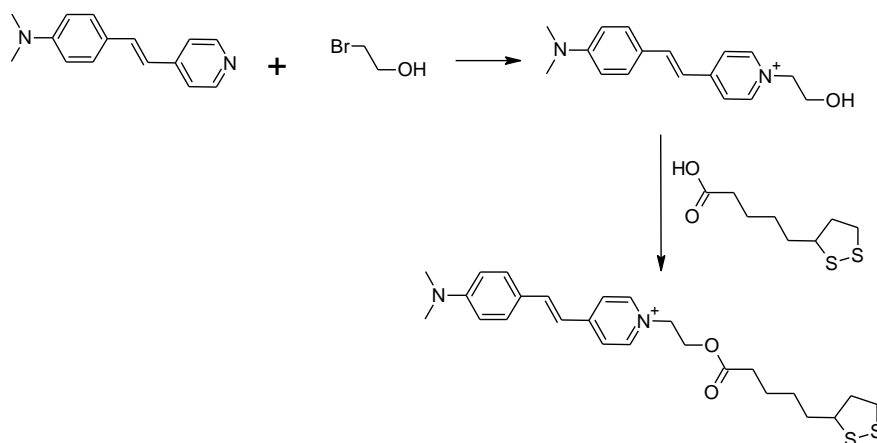


Figure 3.16: DAST used to mix it with AuNRs.

### **3.10.1: Preparation**

Firstly, the DAST are dissolved in ethanol. Then we mixed DAST solution with solution of AuNRs. We used diluted concentrations of NRs and DAST ( $0.1-0.4 \times 10^{-4}$  M). Absorption spectra for all the samples are recorded in water at room temperature.

### **3.10.2: Linear properties**

The UV-VIS spectra of DAST, NR-4, and a mixture of NR4 with DAST derivative are shown in Figure 3.17,  $\lambda_{\text{max}}$  values are shown in Table 3.5. The absorption maximum for the ICT band of DAST is centered at 471 nm whereas NR-4 shows two SPR bands at 518 nm and 691 nm. NR4 mixed with DAST shows two broad bands in the visible region which corresponds to ICT band of DAST and LgSPR band of NR4. These bands are slightly shifted from the maxima observed for ICT, which is shifted to 465 nm, whereas that of the LgSPR band is shifted to 667nm. There is an overlap of the ICT band of DAST and the TrSPR band of NR4. The shift of the SPR band and ICT broad band shows that the mixing of DAST with NR4, leads to significant electronic interactions between both entities, and confirmed the influence of NR4 on DAST derivative.

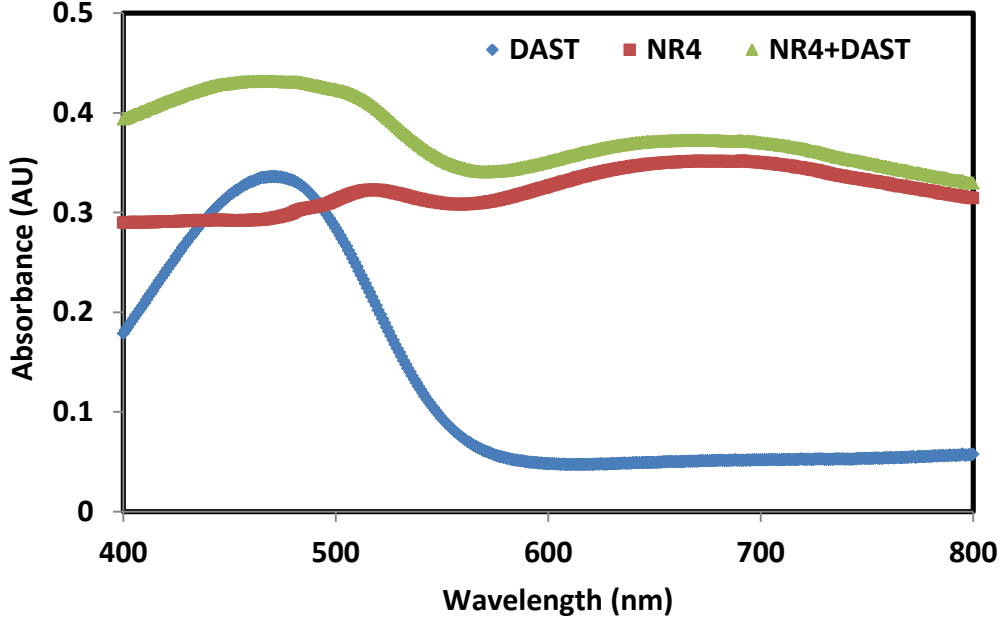


Figure 3.17: UV-Visible absorption spectra of DAST, NR4 and mixture of NR4 with DAST.

### 3.10.3: NLO properties

The measured  $\beta$  values of DAST, NR4 and mixture of NR4 with DAST are given in Table 3.5. The number of attached DAST per nanorods is calculated by assuming a surface area of  $0.322 \text{ nm}^2$  for DAST. The concentrations of the free and attached DAST are inferred, along with the  $\beta$  value of attached DAST, by applying equations 13 and 14.

$$C_{DAST}^{free} = C_{DAST}^{total} - C_{NR} \times N_{DAST}^{attached} \text{ per NR} \quad (13)$$

$$\langle \beta_{DAST}^{attached} \rangle = \frac{(p-1)N_{water} \langle \beta_{water}^2 \rangle - N_{DAST}^{free} \langle \beta_{DAST}^2 \rangle - N_{NR} \langle \beta_{NR}^2 \rangle}{N_{DAST}^{attached}} \quad (14)$$

Where

$$p = \frac{\text{slope of the mixed (NR,DAST)}}{\text{slope of the water}} \quad (15)$$

The  $\beta$  value obtained for isolated DAST is  $70 \times 10^{-30}$  esu. The  $\beta$  value obtained from the mixture of NR4 with DAST is  $556 \times 10^{-30}$  esu which is 8 times higher than the  $\beta$  value observed for the isolated DAST. The influence of NR4 on DAST is clearly evidenced from these results. This result is consistent with the work done by previous researchers, e.g.

exaltation of SHG from ultrathin dye layers deposited on fractal gold surfaces [44], large first hyperpolarizability from the dye when anchored to the surface of the gold nanoparticles [45], and three times higher  $\beta$  value of DAST derivative when attached with the gold nanosphers [46].

Table 3.5: First hyperpolarizability ( $\beta$ ) of Au per atom obtained from DAST, NR4 and mixture of NR4 with DAST.

| Sample           | $\lambda_{\max}$<br>(nm) | Conc.<br>( $\times 10^{-4}$ ) M | $C_{particle}$<br>( $\times 10^{-9}$ ) | $N_{DAST}^{attached}$<br>per NR | $C_{DAST}^{free}$<br>( $\times 10^{-5}$ ) | $C_{DAST}^{attached}$<br>( $\times 10^{-5}$ ) | $\beta_{DAST}^{attached}$<br>( $\times 10^{-30}$ )<br>esu |
|------------------|--------------------------|---------------------------------|--|---------------------------------|---|---|---|
| DAST             | 471                      | DAST = 0.363                    | -                                      |                                 | -   | -   | 70  |
| NR-4<br>AR = 2.5 | 518,<br>691              | Au = 2.5                        | 1.25                                   |                                 | -   | -   | 85  |
| NR4+<br>DAST     | 465,<br>667              | Au = 5<br>DAST= 0.181           | -                                      | 4224                            | 1.28                                      | 0.528   | Attached<br>556   |

In other experiments, DAST is also mixed with NR3 and NR1. The UV-Vis spectra also shows broad band in visible region but the shift of the ICT  $\lambda_{\max}$  occurred to longer wavelengths [Figure 3.17 and 3.18] opposite to what we observed in Figure 3.17. The LgSPR band of NR3 shows a bathochromic shift when mixed with DAST derivatives whereas the TrSPR overlaps with ICT band of the DAST [Figure 3. 18].

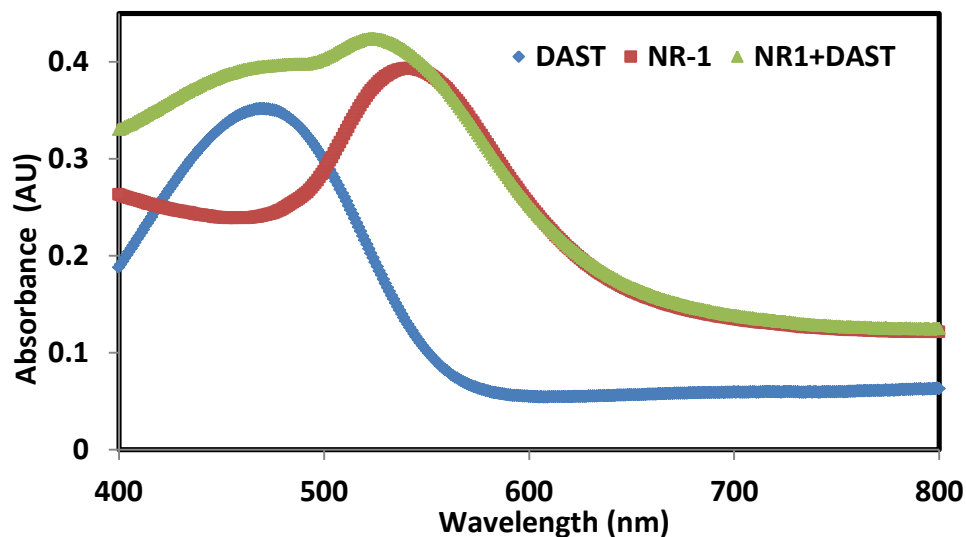


Figure 3.18: UV-Visible absorption spectra of DAST, NR1 and mixture of NR1 with DAST.

The DAST  $\beta$  value obtained from the mixture of NR3 with DAST is  $530 \times 10^{-30}$  esu, and that of DAST with NR1 is  $420 \times 10^{-30}$  esu which is 6 times higher than the  $\beta$  value observed for the pure DAST [Table 3.6 and 3.7].

Table 3.6: First hyperpolarizability ( $\beta$ ) of Au per atom obtained from DAST, NR1 and mixture of NR1 with DAST.

| Sample           | $\lambda_{\max}$<br>(nm) | Conc.<br>( $\times 10^{-4}$ ) M | $C_{\text{particle}}$<br>( $\times 10^{-9}$ ) | $N_{\text{DAST}}^{\text{attached}}$<br>per NR | $C_{\text{DAST}}^{\text{free}}$<br>( $\times 10^{-5}$ ) | $C_{\text{DAST}}^{\text{attached}}$<br>( $\times 10^{-5}$ ) | $\beta_{\text{DAST}}^{\text{attached}}$<br>( $\times 10^{-30}$ ) esu |
|------------------|--------------------------|---------------------------------|---|---|---|---|--|
| DAST             | 471                      | DAST = 0.45                     | -   |   | -   | -   | 70   |
| NR-1<br>AR = 1.7 | 541                      | Au = 2.5                        | 0.938   |   | -   | -   | 48   |
| NR1+<br>DAST     | 486,<br>524              | Au = 2.5<br>DAST= 0.225         | -   | 4826  | 1.80  | 0.45  | Attached<br>419  |

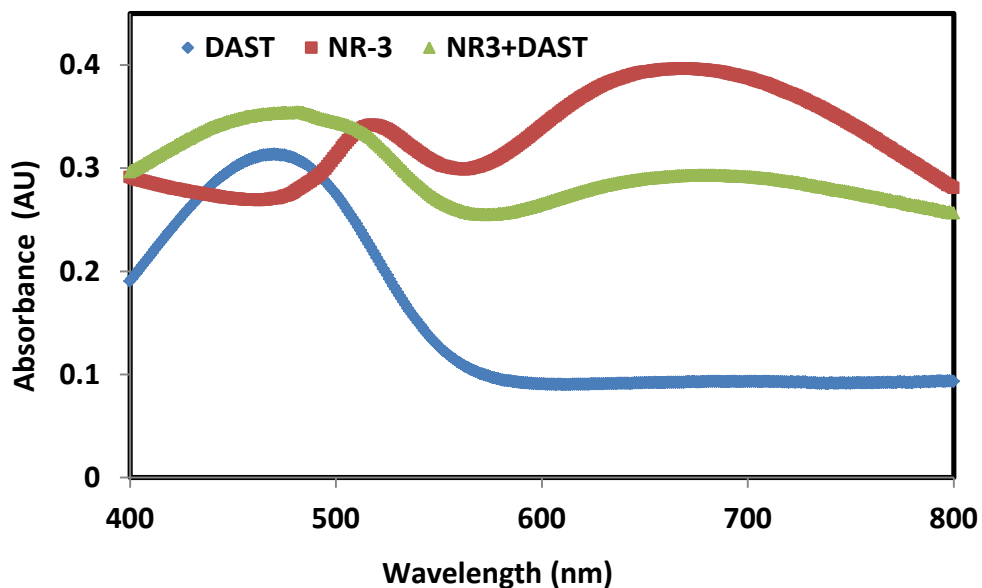


Figure 3.19: UV-Visible absorption spectra of DAST, NR3 and mixture of NR3 with DAST.

Table 3.7: First hyperpolarizability ( $\beta$ ) of Au per atom obtained from DAST, NR3 and mixture of NR3 with DAST.

| Sample            | $\lambda_{\max}$<br>(nm) | Conc.<br>( $\times 10^{-4}$ ) M | $C_{particle}$<br>( $\times 10^{-9}$ ) | $N_{DAST}^{attached}$<br>per NR | $C_{DAST}^{free}$<br>( $\times 10^{-5}$ ) | $C_{DAST}^{attached}$<br>( $\times 10^{-5}$ ) | $\beta_{DAST}^{attached}$<br>( $\times 10^{-30}$ ) esu |
|-------------------|--------------------------|---------------------------------|--|---------------------------------|---|---|--|
| DAST              | 470                      | DAST = 0.363                    | -                                      |                                 | -   | -   | 70   |
| NR-3<br>AR = 2.25 | 517,<br>665              | Au = 2                          | 0.956                                  |                                 | -   | -   | 75   |
| NR3+<br>DAST      | 481,<br>682              | Au = 4<br>DAST= 0.363           | -                                      | 4258                            | 3.2                                       | 0.407   | Attached<br>530  |

In all cases, a strong enhancement of the NLO response has been observed. The obtained results also show their dependence with nanorod aspect ratios (Figure 3.20). As we increase the AR the NLO response of the DAST derivative increases.

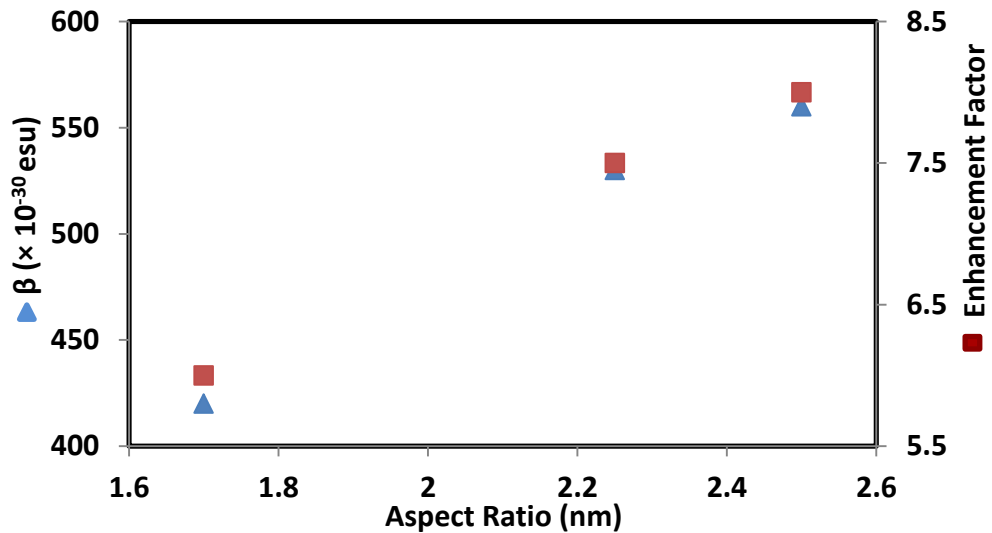


Figure 3.20:  $\beta_{DAST}^{attached}$  with NRs and enhancement factor versus AR of the AuNRs

This is the first trial to observe the enhancement of the NLO response of DAST by simply mixing the NRs with DAST. The next promising future work would be a really controlled functionalization of DAST or metal complexes with NRs.

## **References**

- [1] Hoang-Thi, K., Ph.D. thèses, LPQM, ENS Cachan, 2008.
- [2] Vance, F. W., Lemon, B. I. and Hupp, J. T., *J. Phys. Chem. B*, 1998, 102, 10091.
- [3] Bellona, J., Mustafa, M., Remit, H., Mariner, J.-L., Decorum, M.-O., *New J. Chem.*, 1998, 22, 1239-1255.
- [4] Bellona, J., Remit, H., In *Radiation Chemistry: From Basics to Applications in Material and Life Sciences*; Spothem-Maurizot, M., Mostafavi, M., Douki, T., Belloni, J., Ed., EDP Sciences: Les Ulis, France, 2008, Vol. 97, 116.
- [5] Krishnaswamy, R., Remita, H., Imperor-Clerc, M., Even, C., Davidson, P., Pansu, B., *Chem. Phys. Chem.*, 2006, 7, 1510.
- [6] Ksar, F., Surendran, G., Ramos, L., Keita, B., Nadjo, L., Prouzet, E., Beaunier, P., Hagege, A., Audonnet, F., Remita, H. *Chem. Mater.*, 2009, 21, 1612.
- [7] Zhang, J., Liu, M., Zhang, A., Lin, K., Song, C., Guo, X. *Solid State Sci.* 2010, 12, 267.
- [8] Tornblom, M., Henriksson, U., *J. Phys. Chem. B*, 1997, 101, 6028.
- [9] Baxendale, J. H., and Busi, F., *The study of fast processes and transient species by electron pulse radiolysis*, NATO ASI Series 86, D. Reidel, Town 1982.
- [10] Remita, H., Lampre, I., Mostafavi, M., Balanzat, E., Bouffard, S., *Radiation Physics and chemistry*, 2005, 72 (5), 575-586.
- [11] Abidi, W., Selvakanan, P. R., Guillet, Y., Lampre, I., Beaunier, P., Pansu, B., Palpant B., and Remita, H., *J. Phys. Chem. C*, 2010, 114, 14794.
- [12] Treguer, M., de Cointet, C., Remita, H., Khatouri, J., Mostafavi, M., Amblard, J., and Belloni, J., *J. Phys. Chem. B*, 1998, 102, 4310-4321.
- [13] Abidi, W., Remita, H., *Recent Patents on Engineering*, 2010, 4 (3), 170-188.
- [14] Buxton, G. V., In: *Spothem-Maurizot, M., Mostafavi, M., Douki, T., Belloni, J., Eds. Radiation Chemistry: From basics to applications in material and life sciences*. L'Editeur: EDP Sciences, 2008, 3-16.
- [15] Ferradini, C., Pucheault, J., *Biologie de l'action des rayonnements ionisants*, Masson, Paris 1983.
- [16] Belloni, J., *Catal Today*, 2006, 113, 141-156.

- [17] Buxton, G.V., Greenstock C. L., Helman, W. P., Ross, A. B., J Phys Chem., 1988, 17, 513-883.
- [18] Schwarz, H. A., Dodson R.W., J Phys. Chem., 1989, 93, 409-414.
- [19] Swallow, A. J., Radiation chemistry: an introduction. Wiley: New York 1973.
- [20] Schwarz, H. A., J Chem Educ., 198, 58, 101-105.
- [21] Abidi W., and Remita, H., Recent Patent on Engineering, Special Issue: Light-driven reactions and materials in the environmental technology, 2010, 4, 170.
- [22] Dey, G. R., El Omar, A. K., Jacob, J. A., Mostafavi M., and Belloni, J., J. Phys. Chem. A, 2011, 115, 383.
- [23] Hubert, F., Testard F., and Spalla, O., Langmuir, 2008, 24, 9219.
- [24] Hubert, F., Testard, F., G. Rizza and Spalla, O., Langmuir, 2010, 26, 6887.
- [25] Smith, D. k., Korgel, B. A. Langmuir, 2008, 24, 644.
- [26] Smith, D. K., Miller, N.R., Korgel, B. A. Langmuir, 2009, 25, 9518.
- [27] Millstone, J. E., Wei, W., Jones, M. R., Yoo, H., Mirkin, C. A., Nano Lett., 2008, 8, 2526.
- [28] Rayavarapu, R. G., Ungureanu, C., Krystek, P., van Leeuwen, T. G., Manohar, S., Langmuir, 2010, 26, 5050.
- [29] Galletto, P., Brevet, P.F., Girault, H.H., Antoine, R., Broyer, M., Chem. Commun., 1999, 581.
- [30] Russier-Antoine, I., Benichou, E., Bachelier, G., Jonin, C., and Brevet, P. F., J. Phys. Chem. C, 2007, 111 (26), 9044–9048.
- [31] Nappa, J., Revillod, G., Russier-Antoine, I., Benichou, E., Jonin, C., Brevet, P. F., Phys. Rev. B, 2005, 71, 165407.
- [32] Maker, P. D., Phys. Rev. A, 1970, 1, 923.
- [33] Christophe Dhenaut thesis, 1995, LPQM, ENS Cachan.
- [34] Oudar, J. L. and Chemla, D. S., J. Chem Phys. 1977, 66, 2664.
- [35] Johnson, R. C., Li, J., Hupp, J. T., Schatz, G. C., Chem. Phys. Lett., 2002, 356, 534-540.
- [36] Nappa J., Revillod, G., Abid J.-P., Russier-Antoine, I., Jonin C., Benichou E., G. H. H. and Brevet P. F., Faraday Discuss., 2004, 125, 145-156.
- [37] Brasselet, S., Zyss J., JOSA B, 1998, 15, 1, 257-288.

- [38] Butet, J., Duboisset, J., Bachelier, G., Russier-Antoine, I., Benichou, E., Jonin, C., and Brevet, P-F., *Nano Lett.* 2010, 10, 1717–1721.
- [39] Brasselet, S., Zyss J., *C. R. Physique* 8, 2007, 165–179.
- [40] Lippitz, M., van Dijk, M. A., Orrit, M., *Nano Lett.*, 2005, 5, 799.
- [41] Jin, R., Jureller, J. E., Kim, H. Y., Scherer, N. F., *J. Am. Chem. Soc.*, 2005, 127, 12482.
- [42] Zielinski, M., Oron, D., Chauvat, D., and Zyss, J., *Small*, 2009, 5 (24), 2835–2840.
- [43] Slablab, A., Xuan, L. Le, Zielinski, M., Wilde, Y. de, Jacques, V., Chauvat, D., and Roch, J.-F., *Optics Express*, 20 (1), 220.
- [44] Anceau, C., Brasselet, S., Zyss J., and Gadenne, P., *Opt. Lett.*, 2003, 28, 9, 713-715.
- [45] Vargas-Baca, I., Brown, A. P., Andrews, M. P., Galstian, T., Li, Y., Vali, H., Kuzyk, M. G., *Can. J. Chem.* 2002, 80, 1625-1633.
- [46] Dumur, F., Guerlin, A., Dumas, E., Miomandre, F., Hoang-Thi, K., Perriat, P., Ledoux-Rak, I., Zyss, J., and Mayer, C. R., Institut Lavoisier de Versailles, PPSM, and LPQM ENS Cachan Laboratoire MATEIS, INSA-Lyon, [unpublished data].

## Conclusions and Perspectives

This thesis presented the NLO techniques used for the detection of the molecular quadratic nonlinear optical (NLO) responses of Organometallic, photochromic, and lanthanides complexes. The technique used for these measurement was either EFISH or HLS at 1910 nm. This thesis also includes the NLO response of AuNPs, measured by HLS at 1.064 nm. The important conclusion of this thesis is summarized below:

- The cyclometallated 1,3-di(2-pyridyl)benzene platinum(II) complexes is a new family of organometallic chromophores in which the response is easily tuneable by a rational approach, where the Pt atom plays the role of a central bridge of the transfer process from the donor to the acceptor moieties of the molecular structure.
- Ethynylferrocene appears as a strong electron releasing organometallic end group as compare to the purely organic or organometallic analogues substituents, with a stronger electron releasing power than for example, ferrocene, OMe or amino group. Incorporating the electron-rich acetylide  $d^6$ -transition metal end groups “*trans*-Cl-( $\eta^2$ -dppe)<sub>2</sub> RuC≡C” and “( $\eta^2$ -dppe)( $\eta^5$ -C<sub>5</sub>Me<sub>5</sub>)FeCu≡C” at the periphery of triarylisocyanurate derivatives constitutes a quite efficient means to significantly enhance the hyperpolarizability of the resulting octupoles. These new trinuclear organometallics belong to the most active octupolar quadratic NLO-phores reported to date and ally a remarkable transparency to their good activities.
- A series of dithienylethene (DTE)-containing 2,2-bipyridine ligands with different metal such as Zn, Ru, Re, Cu, and Fe complexes have been designed and synthesized in an dipolar chromophore featuring two photochromic DTE units, tetrahedral chromophore featuring four photochromic DTE units, and in an octahedral chromophore featuring six photochromic DTE units. Their photochromic, photophysical, and quadratic nonlinear optical properties have been studied. Large hyperpolarizability is observed after UV irradiation and subsequent formation of the ring-closed isomers. The significant enhancements clearly evidence the delocalization

of the  $\pi$ -electron system and the occurrence of strong push–pull in the closed forms of the chromophores.

- A bis-(phthalocyaninato) Eu, Dy, and Lu sandwich complex with ABAB, AB3, B4, and A4 phthalocyanine bearing electron-donor (thioalkyl) groups on two opposite rings was synthesized and its  $\beta$  value measured. An exceptionally large  $\beta$  value is reported for octupolar molecules.
- AuNRs and AuNSs are homogeneously synthesized by radiolysis. The TEM images show that they are well dispersed in the solution. HLS intensity collected from the solution of AuNRs is significantly higher than the solution of the AuNSs. The first hyperpolarizability has been measured and it increases with the increase of the aspect ratio. The HLS intensity is enhanced by the transverse and longitudinal SPR band. The observed depolarization ratio reveals a strongly anisotropic behavior from the AuNRs. With the help of NLO microscopy we are able to observe a faint SH signal at 640 nm. The polarization response reveals a highly dipolar character of the nanorod emission which can be attributed to increase anisotropy of electronic fluctuations inside the rod, resulting in dipolar instantaneous electronic distributions that would be responsible for HLS emission. Eight times enhancement of the  $\beta$  value of DAST dye has been observed when mixed with nanorods. The observed results also show their dependency upon the aspect ratio. As we increase the AR the NLO response of the DAST derivative increases.

### **Recommendations for Future Research about AuNPs**

The knowledge and the experience gained from the preliminary experiments done in this project open new opportunities to further research in the nonlinear optical properties of AuNPs.

The possible pathways to continue the present work are as follows:

- 1) Functionalization of AuNRs with NLO dyes, metal complexes, complexes of photochromic molecules etc.

- 2) SHG from other shapes of AuNPs such as, pyramid. In order to observe the influence of their narrow SPR band on SHG and to explore more octupolar gold NPs.
- 3) To observe the SHG of a single NR from Nonlinear scanning microscopy at different wavelength.

## List of Publications

1. Ayhan M. M., **Singh A.**, Hirel, C. Gürek A. G., Ahsen V., Jeanneau E., Ledoux I., Zyss J., Andraud C. and Bretonnière Y., “*ABAB Homoleptic Bis (phthalocyaninato) lutetium(III) Complex: Toward the Real Octupolar Cube and Giant Quadratic Hyperpolarizability*”, *J. Am. Chem. Soc.*, (2012), *134* (8), pp 3655–3658. DOI: 10.1021/ja211064a
2. Argouarch, G., Veillard, R., Roisnel, T., Amar, A., Boucekkine, A., **Singh A.**, Ledoux I., and Paul F., “*Donor-substituted Triaryl-1, 3, 5-Triazines-2, 4, 6 Triones: Octupolar NLO-phores with a Remarkable Transparency–Nonlinearity Trade-off*”, *New J. Chem.*, (2011), *35*, 2409-2411. <http://dx.doi.org/10.1039/C1NJ20442D>
3. Aubert, V., Ordronneau L., Escadeillas M., Williams J. A. G., Boucekkine A., Coulaud E., Dragonetti C., Righetto S., Roberto D., Ugo R., Valore A., **Singh A.**, Zyss J., Ledoux I., Le Bozec H., and Guerchais V., “*Linear and Nonlinear Optical Properties of Cationic Bipyridyl Iridium (III) Complexes: Tunable and Photoswitchable*”, *Inorg. Chem.*, (2011), *50*, 5027–5038. <http://dx.doi.org/10.1021/ic2002892>
4. Ordronneau, L., Nitadori, H., Ledoux, I., **Singh, A.**, Williams, J. A. G., Akita, M., Guerchais, V., and Le Bozec, H., “*Photochromic Metal Complexes: Photoregulation of both the Nonlinear Optical and Luminescent Properties*” *Inorg. Chem.*, (2012), *51* (10), 5627–5636, DOI: 10.1021/ic2025457
5. Trujillo, A., Veillard, R., Argouarch, G., Roisnel, T., **Singh, A.**, Ledoux, I., Paul, F., 2012, Dalton Transactions. “*Triaryl-1, 3, 5-triazinane-2, 4, 6-triones functionalized with electron-rich Fe (ii) and Ru (ii) acetylide complexes: new organometallic octupoles with large hyperpolarizabilities*”, *Dalton Trans.*, 2012, 41, 7454.
6. Rossi, E., Colombo, A., Dragonetti, C., Righetto, S., Roberto, D., Ugo, R., Valore, A., Williams, J. A. G., Lobello, M. G., Angelis, D. F., Fantacci, S., Ledoux-Rak, I., **Singh, A.**, and Zyss J., “*Tuning the dipolar second-order non-linear optical properties of cyclometallated platinum(II) complexes with tridentate N^C^N-binding ligands*”, Accepted for JACS.

7. Nitadori, H., Ordronneau, L., Boixel, J., Jacquemin, D., Boucekkine, A., Singh, A., Akita, M., Ledoux, I., Guerschais, V., and Le Bozec, H., “*Photoswitching of the Second-order nonlinearity of a tetrahedral octupolar multi DTE-based copper (I) complex*”, Chem. Commun., 2012, 48, 10395-10397,  
<http://pubs.rsc.org/en/content/articlepdf/2012/cc/c2cc34999j>

## Related Publications with Author’s Contribution

1. Ennaceur N., Jarraya K., **Singh A.**, Ledoux I., Mhiri T. “*Phase transitions, ferroelectric behavior and second-order nonlinear optics of a new mixed sodium dihydrogen phosphate–arsenate*”. Journal of Physics and Chemistry of Solids 73, (2012), 418–422.  
<http://dx.doi.org/10.1016/j.jpics.2011.11.006>
2. Huriye A., Malval J.-P., Morlet-Savary F., **Singh A.**, Toupet L., Ledoux I., Zyss J., and Le Bozec H., “*The synthesis of tetrahedral bipyridyl metallo-octupoles with large second- and third-order nonlinear optical properties*”, Dyes and Pigments, 92, (2012), 681-688.  
<http://dx.doi.org/10.1016/j.dyepig.2011.06.013>
3. Fortuna C. G., Bonaccorso C., Qamar F., **Anu A.**, Ledoux I., and Musumarra G., “*Synthesis and NLO properties of new trans 2-(thiophen-2-yl) vinyl heteroaromatic iodides*”, Org. Biomol. Chem., (2011), 9, 1608, DOI: 10.1039/c0ob00046a
4. Draper, S. M., “*The Synthesis and Characterisation of Novel Ferrocenyl Polyphenylenes*”, Dalton Trans., (2012), 41, 8850,  
<http://pubs.rsc.org/en/content/articlepdf/2012/dt/c2dt30542a>
5. Shi, W.-J., Lo, P.-C., **Singh, A.**, Ledoux-Rak, I., Ng, D. K.P., “*Synthesis and second-order nonlinear optical properties of push-pull BODIPY derivatives*”, Tetrahedron, 2012, 68 (42), 8712-8718, <http://www.sciencedirect.com/science/article/pii/S0040402012012628#>

## Summer School and Conference Proceedings

- **Oral Presentation:** Réunion plénière 2012 du GDR Or-Nano Nanoparticules d'or : de la théorie à l'application Espace Mendès France, Poitiers, 19-21 Mars 2012, on “Comparison between the second harmonic response from the gold nanosphere and different aspect ratios of the gold nanorods”. [http://www.insp.upmc.fr/webornano/gdr-nanoparticules-or/reunion\\_pleniere\\_programmeP.html](http://www.insp.upmc.fr/webornano/gdr-nanoparticules-or/reunion_pleniere_programmeP.html)
- **Poster Presentation :** The Nanotech Revolution from Science To Society : A Time for Passion and A Time for Reason, JSPS Meeting, Institut d'Alembert, LPQM,ENS Cachan, 12<sup>th</sup>-13<sup>th</sup> December 2011, Poster on “ Nonlinear optical properties of gold nanorods: the role of aspect ratio”. <http://www.ida.ens-cachan.fr/version-francaise/seminaires-et-colloques/france-japan-workshop/>
- **Poster Presentation:** International Conference on Fiber Optics and Photonics, 11<sup>th</sup>-15<sup>th</sup> Dec 2010 and also presented a poster on “The Role of Surface Plasmon Resonance of Gold Nanoparticles to the Enhancement of Second Harmonic Generation”.[http://www.iitg.ernet.in/photonics2010/programPoster13\\_1.html](http://www.iitg.ernet.in/photonics2010/programPoster13_1.html)
- **Poster Presentation:** Advances in Molecular Nonlinear Optics Information Technology and Life Sciences (AMARIS'10), 24<sup>th</sup> – 28<sup>th</sup> May 2010, ENS Cachan, France-P-90. Poster on “Enhancement of Second Harmonic Generation of Stilbazolium Dyes by Covalent Linkage with Gold Nanoparticles”. <http://www.ida.ens-cachan.fr/version-francaise/seminaires-et-colloques/conference-amaris-10/>
- **Summer School** on “Plasmonics 2”, held at Porquerolles island, Hyères, France, 3-7 Oct 2011 also present there a Poster on “Shape and size dependence of the surface plasmon enhanced second harmonic response of gold nanospheres and rods”.
- **Summer School** organized by C'nano IdF, 20-25 June 2010 and also presents there a Poster on “Synthesis of new organometallic octupolar chromophores and their nonlinear optical properties”.
- **Summer school** organized by Centre of Nanosciences Ile De France (C'nano IdF) from 21-26 June 2009 and also presents there a Poster and also presents there a Poster.